Molecular Conformation and Dynamics of Conjugated Polymers using Neutron and X-ray Scattering and Simulations

Caitlyn M. Wolf

A dissertation

submitted in partial fulfillment of the

requirements for the degree of

Doctor of Philosophy

University of Washington

2020

Reading Committee:

Lilo D. Pozzo, Chair

Christine K. Luscombe

David A. C. Beck

Program Authorized to Offer Degree:

Chemical Engineering

University of Washington

Abstract

Molecular Conformation and Dynamics of Conjugated Polymers using Neutron and X-ray Scattering and Simulations

Caitlyn M. Wolf

Chair of the Supervisory Committee:

Professor Lilo D. Pozzo

Department of Chemical Engineering

Conjugated polymers (CPs) are advantageous materials for lower-cost and flexible organic electronic devices, such as organic photovoltaics (OPVs), organic light-emitting diodes (OLEDs), organic field-effect transistors (OFETs), bioelectronics, chemical sensors, flexible displays, and wearable electronics. Their pi-conjugated backbones enable charge transport along the chain or through the pi-orbital overlap of neighboring chains. The molecular dynamics and morphology in the crystalline and amorphous phases of both pure and blended CPs have a direct impact on these mechanisms and therefore, the macroscopic performance of the material. A thorough understanding of this relationship is important for the future development of improved materials and devices. In this work, we utilize neutron and X-ray scattering together with molecular dynamics (MD) simulations and density functional theory (DFT) for a powerful combined experimental and theoretical approach to probing the structure and dynamics in poly(3-hexylthiophene) (P3HT) and other polythiophenes. We first utilize quasi-elastic neutron scattering (QENS) to perform a critical assessment of MD simulation force fields for P3HT. Although these models capture system-level dynamics well, they fail to accurately represent characteristic motions along the polymer backbone which play a critical role in charge transport processes. Next, we utilize density functional theory (DFT) to explore the non-bonded, intermolecular interactions of P3HT and use MD simulations to understand their influence on in-silico dynamics. With selective deuteration, characteristic relaxation times are extracted from QENS data for a set of P3HT polymers and oligomers to probe the effect of molecular weight and crystallinity on backbone and side-chain dynamics. Pure CPs are still susceptible to limited environmental stability and low mechanical durability (e.g. cracking), but blending CPs with a commodity polymer, e.g. polystyrene, can improve the lifetime and mechanical robustness of these materials while maintaining electronic performance at low amounts of the conjugated material. In our final study, small-angle neutron scattering (SANS) and wide-angle X-ray scattering (WAXS) are used to characterize phase separation and self-assembly in these polythiophene-polystyrene blends, and correlate phase morphology with macroscopic conductivity.

TABLE OF CONTENTS

LIST OF FIGURES

LIST OF TABLES

ACKNOWLEDGEMENTS

I would first like to acknowledge my advisor, Professor Lilo Pozzo, for her mentorship over these past five years of graduate school. Without her continued support and advocacy, I would not be the researcher that I am today. Thank you, Lilo, for always believing in me and inspiring me.

I also wish to acknowledge Professor Elizabeth Nance for her support. Thank you for such wonderful memories and experiences while planning the annual Women in Chemical Engineering Industry Event. Many thanks to Professor David Beck for his guidance and encouragement as I dived into the data science community. Thank you for an incredibly rewarding experience as a teaching assistant in DIRECT. The opportunity to teach my first lecture, that I also prepared myself, on database management systems, is a memory I will forever value. And thank you to my committee members and all of the talented collaborators I have had the opportunity to work with over the years.

Thank you to Dr. David Li and Dr. Yuyin Xi, my “Accountabilabuddies”. David, I am forever grateful for your mentorship and your friendship in both the best and worst of times. Yuyin, thank you for always taking the time to answer my questions. Thank you to my family and friends Apryl Ridl, Jasmine Reed, Victor Hu, and Sonja Dunakey for your endless support. I also thank past and present Pozzo group members, especially Dr. Yi-Ting Lee, Dr. Katie Weigandt, Dr. Greg Newbloom, Kacper Lachowski, Sage Scheiwiller, and Ryan O’Hara. And thank you to my graduate cohort, especially Brittany Bishop, Brian Gerwe, and Jon Witt.

I acknowledge the financial support of an NSF IGERT fellowship DGE-1258485 in big data and data science, a University of Washington Clean Energy Institute graduate fellowship, and grants DE- SC0010282 and DE-SC0019911 from the Department of Energy, Office of Basic Energy Sciences. I acknowledge the support of the National Institute of Standards and Technology, U.S. Department of Commerce, in providing the neutron research facilities used in this work. Access to the High-Flux Backscattering Spectrometer, Spin Echo Spectrometer, and NG-3 45m Very Small-Angle Neutron Scattering instrument was provided by the Center for High Resolution Neutron Scattering, a partnership between the National Institute of Standards and Technology and the National Science Foundation (NSF) under Agreement No. DMR-1508249. This work also used neutron scattering resources at the Spallation Neutron Source, a DOE Office of Science User Facility operated by the Oak Ridge National Laboratory. Moreover, resources of the Advanced Photon Source, a U.S. Department of Energy (DOE) Office of Science User Facility operated for the DOE Office of Science by Argonne National Laboratory under Contract No. DE-AC02-06CH11357 were utilized in this work. This work was facilitated though the use of advanced computational, storage, and networking infrastructure provided by the Hyak supercomputer system and funded by the STF at the University of Washington. We also acknowledge the National Science Foundation's Division of Material Research (DMR) for funding the small angle X-ray scattering instrument that was used in this work (DMR 0817622). Finally, this work benefited from the use of the SasView application, originally developed under NSF award DMR-0520547. SasView contains code developed with funding from the European Union’s Horizon 2020 research and innovation programme under the SINE2020 project, grant agreement No 654000.

DEDICATION

To my parents, Steve and Shelly Wolf, for their steady love and support.

Chapter 1. INTRODUCTION

It was only a little over a century ago, in 1895, that Wilhelm Conrad Röntgen made the discovery of X-rays,[1,2] a form of electromagnetic radiation that has since become a common part of our lives, from medical imaging and treatments to airport security. Soon to follow was a debate on the wave- or particle-nature of these X-rays, and it would not be until 1912 that Max von Laue, Walter Friedrich, and Paul Knipping performed the first X-ray diffraction experiment on a sample of copper sulfate.[1–3] Shortly after, Lawrence Bragg explained the resulting diffraction spots as an indication of the material's internal crystal structure with the development of the fundamental equation we now know as Bragg's law[2,3]:

$$2d \sin \theta = n\lambda \tag{1.1}$$

where d is the distance between scattering planes, θ is the angle between the incident beam and the scattering plane (or between the diffracted beam and the plane), n is an integer, and λ is the wavelength of the incident radiation source. Within another year, Lawrence's father, William H. Bragg, built the first X-ray spectrometer[2], and it was not until the 1920s that small-angle X-ray scattering (SAXS) was used to study the internal structures of non-crystalline (amorphous) materials.[4] In 1932 James Chadwick then made the discovery of the neutron,[5–7] which would launch the development of reactors over the following two decades and the rapid growth of neutron research and scattering experiments.[6–8] Then in the 1970's, a milestone in polymer science and neutron scattering was made when Henri Benoit and Julia Higgins applied some of the first small-angle neutron scattering (SANS) experiments to confirm Paul Flory's theory that polymers in the melt would follow a random coil conformation that scaled with the squared root of chain length.[6,9,10] Since then, SANS has continued to provide valuable information regarding the structural nature of polymer systems, ranging from the radius of gyration or size-scales of large aggregates and the Guassian conformation of the polymer molecules down to the persistence length or correlation length of the chain.[7] With use of inelastic and quasi-elastic neutron scattering (QENS) methods, researchers can also probe polymer dynamics, e.g. chain vibrations, rotations, and diffusion, at time scales ranging from picoseconds to microseconds.[7,11,12] Today, both X-ray and neutron scattering remain as powerful material characterization techniques for not only polymer science but a wide breadth of fields ranging from archaeology to zoology.

1.1 CONJUGATED POLYMERS

Since their finding in the 1970's, conjugated polymers (CPs) have been realized as a promising material for a wide range of organic electronic device applications, including organic photovoltaics (OPVs), organic light-emitting diodes (OLEDs), organic field-effect transistors (OFETs), bioelectronics, chemical sensors, and flexible displays.[13–26]. OPVs have now been able to achieve efficiencies over 17%[27,28], and while the efficiencies of more traditional, inorganic solar cells can reach over twice that, organic devices offer advantages of lower cost and flexibility.[19,23] Sirringhaus et al. notes the significant advancement of OFET devices, with charge mobility increasing over three orders of magnitude in a quarter of a decade and surpassing silicon devices by one order of magnitude.[29] Moreover, OLEDs are already present in phone screens, TVs, and displays today, and are favored for additional applications of flexible or wearable devices.[30]

Some of the most studied and well-characterized CPs are the polythiophenes, especially poly(3-hexylthiophene) (P3HT).[20,31] Although materials with higher charge mobility (e.g. donor-acceptor CPs) have become prominent, P3HT has served as a model polymer for the field with vast amounts of information available in the literature.[20] Shown in Figure 1.1 is the molecular structure for P3HT as well as other polythiophenes used in this work. The typical CP structure involves a π-conjugated backbone comprised of monomeric units such as acetylene, aniline, thiophene, pyrrole, fluorene and phenylene vinylene.[32] Alkyl side chains are often added along the backbone to increase the polymer's solubility, enabling solution processing and the opportunity for rapid, roll-to-roll processing of these devices.[33–35] However, modifications in either of these structural regimes (side chains or backbone) has significant impact on the macroscopic properties and performance of the material, such as charge transport.

Two types of charge transport mechanisms can occur in these materials. Charges can either travel along the π-conjugated backbone of the chain (i.e. intra-chain charge transfer) or through the π-orbital stacking of nearby conjugated units (i.e. inter-chain charge transfer) in both the ordered (i.e. crystalline) and disordered (i.e. amorphous) phases of the material. In the crystalline phases, charge transport can occur directly along the backbone or pi-stacking directions of the crystal structure, and intra-chain charge transfer mechanisms (backbone direction) are associated with a charge mobility orders of magnitude higher than that of inter-chain charge transfer (pi-stacking direction). However, transfer in the amorphous phases rely on either local charge delocalization along a chain backbone or through the pi-orbital overlap of looping or passing chains.[36] Therefore, it is the morphology between the crystalline and amorphous phases that dictate the limiting rate of the macroscopic conductivity.[35–37] For example, the work of Gu et al. explored the effect of adding higher molecular weight chains, or tie-chains, on the charge mobility of P3HT. At small amounts, the macroscopic performance was limited by the charge transport expected for the amorphous phase. However, by adding a critical mole fraction of tie-chains at 10^{-3} , extended charge transport pathways that linked the crystalline regimes were created, and they improved the macroscopic performance to expected charge mobilities of the ordered phase.[36] Connecting the molecular and phase morphology of these materials to electronic performance as well as developing a thorough understanding of that structure-function relationship play a significant role in the advancement of conjugated materials and organic electronic devices.

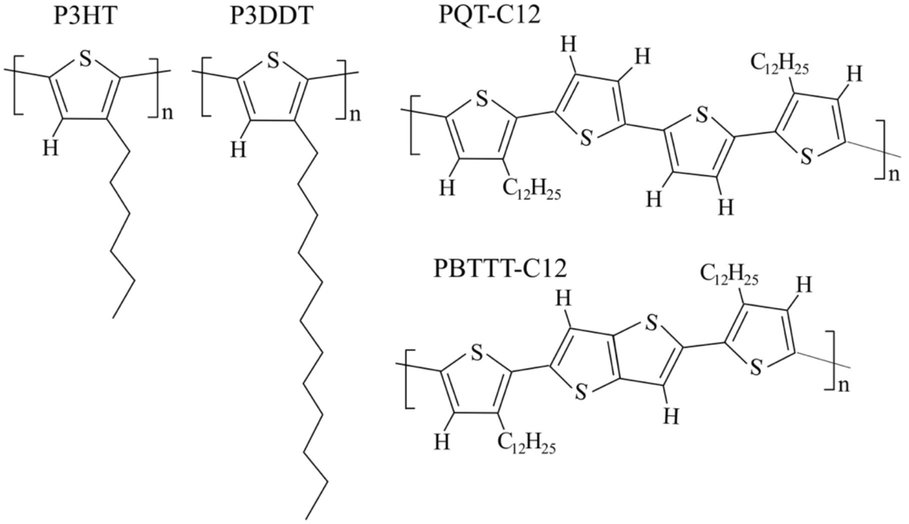

Figure 1.1. Molecular structure of poly(3-hexylthiophene) (P3HT), poly(3-dodecylthiophene) (P3DDT), poly(3-3’’’-didodecyl quarter thiophene) (PQT-C12), and poly[2,5-bis(3-dodecylthiophen-2-yl)thieno[3,2-b]thiophene] (PBTTT-C12).

X-rays have been shown as a valuable tool for probing the crystalline and amorphous phases of CPs. It was X-ray diffraction that enabled researchers to determine the now well-known lamellar crystalline structure of the poly(3-alkylthiophenes)[38,39], which is shown in the Figure 1.2 for P3HT. Balko and coworkers showed how temperature-series SAXS and wide-angle X-ray scattering (WAXS) data can be used determine the degree of crystallinity for a set of monodisperse P3HT samples at varying molecular weight. Their results demonstrated how folding of the longer chains reduced the crystallinity in the material at high molecular weigths.[40] Another group used grazing-incidence X-ray scattering (GISAXS, GIWAXS) to determine the minimum sizes of

P3HT and PCBM phases in OPV active layers for improved device performance.[41] Goffri et al. also used grazing-incidence X-ray diffraction to understand the effect of crystallinity in conjugated and insulated polymer blends on OFET device performance. They found that utilizing a semi-crystalline insulating component rather than an amorphous one encouraged crystallization in the conjugated phase and improved charge transport.[42]

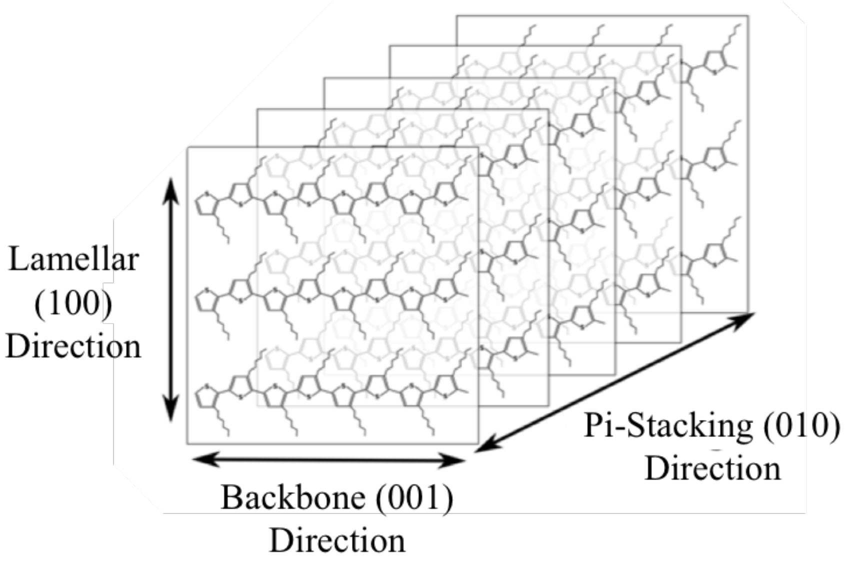

Figure 1.2. Lamellar crystalline structure of poly(3-hexylthiophene) (P3HT).

Neutron scattering is advantageous for the analysis of polymeric materials due to the ability to achieve contrast between two or more organic phases (see further discussion of contrast variation in Chapter 2). Therefore, it has been used to study the conformation, dynamics, and self-assembly behavior of CPs in both the solid- and solution-state. McCulloch et al. monitored the decreasing persistence length in dilute solutions of poly(3-alkylthiophene) as temperature and regioregularity were increased using small-angle neutron scattering (SANS).[43] CPs have also been known to self-assemble into nanofiber networks that enable improved charge mobility in the material. The work of Bastianini and coworkers used SANS to monitor the formation of P3HT nanofibers in solution over time, observing a transition from polymer coils, to rods, lamellae, and finally nanofibers, and they found the speed and extent at which these nanofibers formed to be incredible sensitive to temperature.[44] QENS was utilized by Obrzut et al. to correlate increased side-chain motions in P3HT with an increase in chain disorder and decrease in conductivity.[45] Additionally, Guilbert and coworkers applied QENS to blends of P3HT and PCBM to understand the system dynamics in the picosecond time scale above and below the P3HT glass transition temperature, finding that the blend of these two materials contributed to decreased P3HT dynamics and enhanced PCBM dynamics.[46]

1.2 MOLECULAR MODELLING

While X-ray and neutron scattering methods have both been valuable to understanding CP behavior, researchers have also taken a theoretical approach to studying the relationship between morphology and performance in these materials. Alder and Wainright demonstrated one of the earliest applications of molecular dynamics (MD) simulations with a simplified hard sphere system in 1957.[47–49] Since then, advancements in the algorithms and approaches for MD and *ab-initio* simulations has grown molecular modelling into an expansive field for studying the *in-silico* behavior of many materials, and polymers are no exception. Molecular modelling includes both quantum and classical simulation approaches to capturing polymer properties across multiple orders of magnitude. At the smallest length and time scales, density functional theory (quantum mechanics) can probe bond lengths and vibrations, molecular conformations and electron orbitals. At intermediate length and time scale, atomistic MD simulations (classical mechanics) can explore Rouse motions, radii of gyration, and backbone fluctuations. And at the largest length and time scales, coarse-grained MD can investigate phase separation, diffusion, and reptation.

Many works in the literature have already employed MD and *ab-initio* simulations to understand the behaviors of CPs and how they affect charge transport mechanisms. The work by McMahon and coworkers used a combination of atomistic MD simulations and *ab-initio* calculations to understand the effect of regioregularity on charge traps along the polymer chain and revealed that these traps do not preferentially appear in 'defect-rich' regions of low regioregularity.[50] MD allowed them access to 'snapshots' of the P3HT chain conformation across large time scales that could then be used as input configurations for more computationally expensive quantum-mechanical methods. Tapping and coworkers implemented a similar approach, but used coarse-grained MD simulations together with an exciton model, to track the movement of an exciton from the surface to core of aggregated P3HT nanofibers in solution.[51] From a purely quantum-mechanical approach, Marchiori and Koehler used density functional theory (DFT) to explore how different conformations and polarizations between P3HT and PCBM play a significant role on the charge transfer process between these donor and acceptor materials.[52] Although all modelling approaches are implementing an approximation of complex quantum mechanical interactions, these works show how developed and validated systems can still help researchers explore and understand molecular behaviors that are not readily accessible with experiments alone. However, when possible, implementing a combined experimental and theoretical approach can be an even more powerful method than either one alone.

1.3 A PARALLEL SCATTERING AND MOLECULAR MODELLING APPROACH

Neutron scattering is one experimental method that has been proposed to study soft matter in parallel with molecular modelling techniques, especially for QENS and MD simulations.[12] These techniques cover similar time and length scales, and so QENS can not only be used to validate molecular modelling parameters, but simulations can also be used to uncover *in-silico* features to help to understand experimental results. Neutron and X-ray scattering have only been used together with molecular modeling to understand the conformation, molecular dynamics, and charge transport mechanisms in CPs on a few occasions.[34,53–56] Guilbert and coworkers have utilized a combined MD and QENS approach to both pure P3HT and P3HT/PCBM blends. With use of MD simulations, the group was able to show that their previous QENS results[46] of dampened P3HT dynamics and enhanced PCBM dynamics were a result of P3HT chains wrapping around the PCBM molecules.[54] The group also found that MD simulations recreated system dynamics well when compared to QENS results for P3HT and poly(3-octylthiophene) (P3OT), providing them with both experimental and *in-silico* insight into dynamics on the order of picoseconds to nanoseconds.[53] In a more recent work, the group utilized both QENS and neutron diffraction together with both MD and *ab-initio* simulations to characterize the dynamics in the picosecond to nanosecond time scales in regio-regular (semi-crystalline) and regio-random (amorphous) P3HT.[55] Zhan et al. utilized MD simulations together with both QENS and SANS experiments of poly(3-alkylthiophenes) to show how longer side chain lengths increase motion along the chain's backbone.[56] While these works have provided examples in the context of CPs, they all demonstrate the value in a combined experimental and theoretical approach to understanding structure-function relationships in materials.

1.4 OVERVIEW

In this work, we utilize both elastic and quasi-elastic neutron and X-ray scattering experiments together with MD simulations and density functional theory to understand the molecular conformation and dynamics in polythiophenes. In Chapter 2, we review the fundamentals of neutron and X-ray scattering, and provide a more detailed look into methods of wide-angle X-ray scattering, small-angle neutron scattering, and quasi-elastic neutron scattering. We additionally cover experimental tools of differential scanning calorimetry and UV-visible spectroscopy. In Chapter 3, we provide a discussion on computational methods of molecular dynamics simulations and density functional theory, and how these results can be compared directly with those from scattering. Chapter 4 provides a quantitative assessment of available MD simulation force fields for P3HT using QENS and WAXS. An *in-silico* analysis also highlights the effects of modifications to force field parameters on the simulated backbone conformation and dynamics as they relate to charge transport mechanisms. In Chapter 5, we discuss preliminary QENS data that is used to compare relaxation times of backbone and side-chain dynamics in regio-regular and regio-random forms of P3HT polymers and oligomers. Furthermore, density functional theory provides insights into the limitations of MD simulation force fields at capturing non-bonded interactions in P3HT oligomers. Chapter 6 includes a thorough investigation into the phase conformation and molecular self-assembly in polythiophene and polystyrene blends using SANS and WAXS measurements. Different blend conformations are also related to their macroscopic conductivity. Finally, we provide in the appendix (Chapter 7) a review of Python tools for improving and semi-automating the analysis and fitting of neutron and X-ray scattering data, discussion on the considerations surrounding a repository for SANS data, and supplementary neutron scattering data for additional polythiophene systems.

1.5 REFERENCES

(1) Assmus, A. Early History of X Rays http://www.slac.stanford.edu/pubs/beamline/25/2/25-2-assmus.pdf.

(2) Clarke, I. The History of X-Ray Crystallography https://arts.leeds.ac.uk/museum-of-hstm/research/william-thomas-astbury/the-history-of-x-ray-crystallography/.

(3) ChemViews. 100th Anniversary of the Discovery of X-Ray Diffraction. 2012.

(4) Chu, B.; Hsiao, B. S. *Small-Angle X-Ray Scattering of Polymers*. *Chem. Rev.* **2001**, *101* (6), 1727–1762. https://doi.org/10.1021/cr9900376.

(5) Mason, T. E.; Gawne, T. J.; Nagler, S. E.; Nestor, M. B.; Carpenter, J. M. *The Early Development of Neutron Diffraction: Science in the Wings of the Manhattan Project*. *Acta Crystallogr. Sect. A Found. Crystallogr.* **2013**, *69* (1), 37–44. https://doi.org/10.1107/S0108767312036021.

(6) Neutron Scattering https://www.iop.org/publications/iop/2011/file_47455.pdf.

(7) *Polymers and Neutron Scattering*; Higgins, J. S., Benoit, H. C., Eds.; Oxford University Press Inc.: New York, 1994.

(8) Rush, J. J.; Cappelletti, R. L. The NIST Center for Neutron Research: Over 40 Years Serving NIST/NBS and the Nation.

(9) Higgins, J. S. *Neutron Scattering from Polymers: Five Decades of Developing Possibilities*. *Annu. Rev. Chem. Biomol. Eng.* **2016**, *7* (1), 1–28. https://doi.org/10.1146/annurev-chembioeng-080615-034429.

(10) BENOIT, H.; DECKER, D.; HIGGINS, J. S.; PICOT, C.; COTTON, J. P.; FARNOUX, B.; JANNINK, G.; OBER, R. *Dimensions of a Flexible Polymer Chain in the Bulk and in Solution*. *Nat. Phys. Sci.* **1973**, *245* (140), 13–15. https://doi.org/10.1038/physci245013a0.

(11) Sakai, V. G.; Arbe, A. *Quasielastic Neutron Scattering in Soft Matter*. *Curr. Opin. Colloid Interface Sci.* **2009**, *14* (6), 381–390. https://doi.org/10.1016/j.cocis.2009.04.002.

(12) Arbe, A.; Alvarez, F.; Colmenero, J. *Neutron Scattering and Molecular Dynamics Simulations: Synergetic Tools to Unravel Structure and Dynamics in Polymers*. *Soft Matter* **2012**, *8* (32), 8257. https://doi.org/10.1039/c2sm26061a.

(13) Someya, T.; Bao, Z.; Malliaras, G. G. *The Rise of Plastic Bioelectronics*. *Nature* **2016**, *540* (7633), 379–385. https://doi.org/10.1038/nature21004.

(14) Etxebarria, I.; Ajuria, J.; Pacios, R. *Solution-Processable Polymeric Solar Cells: A Review on Materials, Strategies and Cell Architectures to Overcome 10%*. *Org. Electron.* **2015**, *19*, 34–60. https://doi.org/10.1016/j.orgel.2015.01.014.

(15) Pandey, M.; Kumari, N.; Nagamatsu, S.; Pandey, S. S. *Recent Advances in the Orientation of Conjugated Polymers for Organic Field-Effect Transistors*. *J. Mater. Chem. C* **2019**, *7* (43), 13323–13351. https://doi.org/10.1039/C9TC04397G.

(16) Anantha-Iyengar, G.; Shanmugasundaram, K.; Nallal, M.; Lee, K.-P.; Whitcombe, M. J.; Lakshmi, D.; Sai-Anand, G. *Functionalized Conjugated Polymers for Sensing and Molecular Imprinting Applications*. *Prog. Polym. Sci.* **2019**, *88*, 1–129. https://doi.org/10.1016/j.progpolymsci.2018.08.001.

(17) Fidanovski, K.; Mawad, D. *Conjugated Polymers in Bioelectronics: Addressing the Interface Challenge*. *Adv. Healthc. Mater.* **2019**, *8* (10), 1900053. https://doi.org/10.1002/adhm.201900053.

(18) Wang, M.; Baek, P.; Akbarinejad, A.; Barker, D.; Travas-Sejdic, J. *Conjugated Polymers and Composites for Stretchable Organic Electronics*. *J. Mater. Chem. C* **2019**, *7* (19), 5534–5552. https://doi.org/10.1039/C9TC00709A.

(19) Mehmood, U.; Al-Ahmed, A.; Hussein, I. A. *Review on Recent Advances in Polythiophene Based Photovoltaic Devices*. *Renew. Sustain. Energy Rev.* **2016**, *57*, 550–561. https://doi.org/10.1016/j.rser.2015.12.177.

(20) Harrelson, T. F.; Moulé, A. J.; Faller, R. *Modeling Organic Electronic Materials: Bridging Length and Time Scales*. *Mol. Simul.* **2017**, *43* (10–11), 730–742. https://doi.org/10.1080/08927022.2016.1273526.

(21) Li, G.; Chang, W.-H.; Yang, Y. *Low-Bandgap Conjugated Polymers Enabling Solution-Processable Tandem Solar Cells*. *Nat. Rev. Mater.* **2017**, *2* (8), 17043. https://doi.org/10.1038/natrevmats.2017.43.

(22) Sirringhaus, H. *25th Anniversary Article: Organic Field-Effect Transistors: The Path Beyond Amorphous Silicon*. *Adv. Mater.* **2014**, *26* (9), 1319–1335. https://doi.org/10.1002/adma.201304346.

(23) Mazzio, K. a.; Luscombe, C. K. *The Future of Organic Photovoltaics*. *Chem. Soc. Rev.* **2014**, *44* (1), 78–90. https://doi.org/10.1039/c4cs00227j.

(24) Huynh, T. P.; Sharma, P. S.; Sosnowska, M.; D'Souza, F.; Kutner, W. *Functionalized Polythiophenes: Recognition Materials for Chemosensors and Biosensors of Superior Sensitivity, Selectivity, and Detectability*. *Prog. Polym. Sci.* **2015**, *47*, 1–25. https://doi.org/10.1016/j.progpolymsci.2015.04.009.

(25) Alvarez, A.; Costa-Fernández, J. M.; Pereiro, R.; Sanz-Medel, A.; Salinas-Castillo, A. *Fluorescent Conjugated Polymers for Chemical and Biochemical Sensing*. *TrAC Trends Anal. Chem.* **2011**, *30* (9), 1513–1525. https://doi.org/10.1016/j.trac.2011.04.017.

(26) Li, Z.; Chueh, C.-C.; Jen, A. K.-Y. *Recent Advances in Molecular Design of Functional Conjugated Polymers for High-Performance Polymer Solar Cells*. *Prog. Polym. Sci.* **2019**, *99*, 101175. https://doi.org/10.1016/j.progpolymsci.2019.101175.

(27) NREL Best Research-Cell Efficiency Chart https://www.nrel.gov/pv/cell-efficiency.html (accessed Jun 11, 2020).

(28) Green, M. A.; Dunlop, E. D.; Hohl-Ebinger, J.; Yoshita, M.; Kopidakis, N.; Ho-Baillie, A. W. Y. *Solar Cell Efficiency Tables (Version 55)*. *Prog. Photovoltaics Res. Appl.* **2020**, *28* (1), 3–15. https://doi.org/10.1002/pip.3228.

(29) Sirringhaus, H. *25th Anniversary Article: Organic Field-Effect Transistors: The Path Beyond Amorphous Silicon*. *Adv. Mater.* **2014**, *26* (9), 1319–1335. https://doi.org/10.1002/adma.201304346.

(30) Sekine, C.; Tsubata, Y.; Yamada, T.; Kitano, M.; Doi, S. *Recent Progress of High Performance Polymer OLED and OPV Materials for Organic Printed Electronics*. *Sci. Technol. Adv. Mater.* **2014**, *15* (3), 034203. https://doi.org/10.1088/1468-6996/15/3/034203.

(31) Etxebarria, I.; Ajuria, J.; Pacios, R. *Solution-Processable Polymeric Solar Cells: A Review on Materials, Strategies and Cell Architectures to Overcome 10%*. *Org. Electron.* **2015**, *19*, 34–60. https://doi.org/10.1016/j.orgel.2015.01.014.

(32) Alvarez, A.; Costa-Fernández, J. M.; Pereiro, R.; Sanz-Medel, A.; Salinas-Castillo, A. *Fluorescent Conjugated Polymers for Chemical and Biochemical Sensing*. *TrAC Trends Anal. Chem.* **2011**, *30* (9), 1513–1525. https://doi.org/10.1016/j.trac.2011.04.017.

(33) Mei, J.; Bao, Z. *Side Chain Engineering in Solution-Processable Conjugated Polymers*. *Chem. Mater.* **2014**, *26* (1), 604–615. https://doi.org/10.1021/cm4020805.

(34) Newbloom, G. M.; Hoffmann, S. M.; West, A. F.; Gile, M. C.; Sista, P.; Cheung, H. K. C.; Luscombe, C. K.; Pfaendtner, J.; Pozzo, L. D. *Solvatochromism and Conformational Changes in Fully Dissolved Poly(3-Alkylthiophene)S*. *Langmuir* **2015**, *31* (1), 458–468. https://doi.org/10.1021/la503666x.

(35) Lan, Y.-K.; Huang, C.-I. *A Theoretical Study of the Charge Transfer Behavior of the Highly Regioregular Poly-3-Hexylthiophene in the Ordered State*. *J. Phys. Chem. B* **2008**, *112* (47), 14857–14862. https://doi.org/10.1021/jp806967x.

(36) Gu, K.; Snyder, C. R.; Onorato, J.; Luscombe, C. K.; Bosse, A. W.; Loo, Y.-L. *Assessing the Huang–Brown Description of Tie Chains for Charge Transport in Conjugated Polymers*. *ACS Macro Lett.* **2018**, *7* (11), 1333–1338. https://doi.org/10.1021/acsmacrolett.8b00626.

(37) Lan, Y.-K.; Huang, C.-I. *Charge Mobility and Transport Behavior in the Ordered and Disordered States of the Regioregular Poly(3-Hexylthiophene)*. *J. Phys. Chem. B* **2009**, *113* (44), 14555–14564. https://doi.org/10.1021/jp904841j.

(38) Prosa, T. J.; Winokur, M. J.; Moulton, J.; Smith, P.; Heeger, A. J. *X-Ray Structural Studies of Poly(3-Alkylthiophenes): An Example of an Inverse Comb*. *Macromolecules* **1992**, *25* (17), 4364–4372. https://doi.org/10.1021/ma00043a019.

(39) Kuei, B.; Gomez, E. D. *Chain Conformations and Phase Behavior of Conjugated Polymers*. *Soft Matter* **2016**, *114*, 10087–10088. https://doi.org/10.1039/C6SM00979D.

(40) Balko, J.; Lohwasser, R. H.; Sommer, M.; Thelakkat, M.; Thurn-Albrecht, T. *Determination of the Crystallinity of Semicrystalline Poly(3-Hexylthiophene) by Means of Wide-Angle X-Ray Scattering*. *Macromolecules* **2013**, *46* (24), 9642–9651. https://doi.org/10.1021/ma401946w.

(41) Chiu, M.; Jeng, U.; Su, C.; Liang, K. S.; Wei, K. *Simultaneous Use of Small- and Wide-Angle X-ray Techniques to Analyze Nanometerscale Phase Separation in Polymer Heterojunction Solar Cells*. *Adv. Mater.* **2008**, *20* (13), 2573–2578. https://doi.org/10.1002/adma.200703097.

(42) Goffri, S.; Müller, C.; Stingelin-Stutzmann, N.; Breiby, D. W.; Radano, C. P.; Andreasen, J. W.; Thompson, R.; Janssen, R. A. J.; Nielsen, M. M.; Smith, P.; Sirringhaus, H. *Multicomponent Semiconducting Polymer Systems with Low Crystallization-Induced Percolation Threshold*. *Nat. Mater.* **2006**, *5* (12), 950–956. https://doi.org/10.1038/nmat1779.

(43) McCulloch, B.; Ho, V.; Hoarfrost, M.; Stanley, C.; Do, C.; Heller, W. T.; Segalman, R. A. *Polymer Chain Shape of Poly(3-Alkylthiophenes) in Solution Using Small-Angle Neutron Scattering*. *Macromolecules* **2013**, *46* (5), 1899–1907. https://doi.org/10.1021/ma302463d.

(44) Bastianini, F.; Pérez, G. E.; Hobson, A. R.; Rogers, S. E.; Parnell, A. J.; Grell, M.; Gutiérrez, A. F.; Dunbar, A. D. F. *In−situ Monitoring Poly(3-Hexylthiophene) Nanowire Formation and Shape Evolution in Solution via Small Angle Neutron Scattering*. *Sol. Energy Mater. Sol. Cells* **2019**, *202*, 110128. https://doi.org/10.1016/j.solmat.2019.110128.

(45) Obrzut, J.; Page, K. A. *Electrical Conductivity and Relaxation in Poly(3-Hexylthiophene)*. *Phys. Rev. B* **2009**, *80* (19), 195211. https://doi.org/10.1103/PhysRevB.80.195211.

(46) Guilbert, A. A. Y.; Zbiri, M.; Jenart, M. V. C.; Nielsen, C. B.; Nelson, J. *New Insights into the Molecular Dynamics of P3HT:PCBM Bulk Heterojunction: A Time-of-Flight Quasi-Elastic Neutron Scattering Study*. *J. Phys. Chem. Lett.* **2016**, *7* (12), 2252–2257. https://doi.org/10.1021/acs.jpclett.6b00537.

(47) Alder, B. J.; Wainwright, T. E. *Phase Transition for a Hard Sphere System*. *J. Chem. Phys.* **1957**, *27* (5), 1208–1209. https://doi.org/10.1063/1.1743957.

(48) Sutmann, G. Classical Molecular Dynamics. In *Quantum Simulations of Complex Many-Body Systems: From Theory to Algorithms, Lecture Notes*; Grotendorst, J., Marx, D., Muramatsu, A., Eds.; 2002; pp 211–254.

(49) Hernandez, E. R. Molecular Dynamics: from basic techniques to applications (A Molecular Dynamics Primer).

(50) McMahon, D. P.; Cheung, D. L.; Goris, L.; Dacuña, J.; Salleo, A.; Troisi, A. *Relation between Microstructure and Charge Transport in Polymers of Different Regioregularity. J. Phys. Chem. C* **2011**, *115* (39), 19386–19393. https://doi.org/10.1021/jp207026s.

(51) Tapping, P. C.; Clafton, S. N.; Schwarz, K. N.; Kee, T. W.; Huang, D. M. *Molecular-Level Details of Morphology-Dependent Exciton Migration in Poly(3-Hexylthiophene) Nanostructures. J. Phys. Chem. C* **2015**, *119* (13), 7047–7059. https://doi.org/10.1021/acs.jpcc.5b00705.

(52) Marchiori, C. F. N.; Koehler, M. *Density Functional Theory Study of the Dipole across the P3HT : PCBM Complex: The Role of Polarization and Charge Transfer. J. Phys. D. Appl. Phys.* **2014**, *47* (21), 215104. https://doi.org/10.1088/0022-3727/47/21/215104.

(53) Guilbert, A. A. Y.; Urbina, A.; Abad, J.; Díaz-Paniagua, C.; Batallán, F.; Seydel, T.; Zbiri, M.; García-Sakai, V.; Nelson, J. *Temperature-Dependent Dynamics of Polyalkylthiophene Conjugated Polymers: A Combined Neutron Scattering and Simulation Study. Chem. Mater.* **2015**, *27* (22), 7652–7661. https://doi.org/10.1021/acs.chemmater.5b03001.

(54) Guilbert, A. A. Y.; Zbiri, M.; Dunbar, A. D. F.; Nelson, J. *Quantitative Analysis of the Molecular Dynamics of P3HT:PCBM Bulk Heterojunction. J. Phys. Chem. B* **2017**, *121* (38), 9073–9080. https://doi.org/10.1021/acs.jpcb.7b08312.

(55) Guilbert, A. A. Y.; Zbiri, M.; Finn, P. A.; Jenart, M.; Fouquet, P.; Cristiglio, V.; Frick, B.; Nelson, J.; Nielsen, C. B. *Mapping Microstructural Dynamics up to the Nanosecond of the Conjugated Polymer P3HT in the Solid State. Chem. Mater.* **2019**, *31* (23), 9635–9651. https://doi.org/10.1021/acs.chemmater.9b02904.

(56) Zhan, P.; Zhang, W.; Jacobs, I. E.; Nisson, D. M.; Xie, R.; Weissen, A. R.; Colby, R. H.; Moulé, A. J.; Milner, S. T.; Maranas, J. K.; Gomez, E. D. *Side Chain Length Affects Backbone Dynamics in Poly(3-Alkylthiophene)S. J. Polym. Sci. Part B Polym. Phys.* **2018**, *56* (17), 1193–1202. https://doi.org/10.1002/polb.24637.

Chapter 2. EXPERIMENTAL METHODS AND RELATED THEORY

2.1 X-RAY AND NEUTRON SCATTERING

Neutron and X-ray scattering are powerful characterization techniques with applications ranging from polymer science and colloidal materials to geology. They provide access to molecular structure and dynamics in the material's bulk at length and time scales ranging from Angstroms to micrometers and from femtoseconds to microseconds.[1,2] In this section, we first review the scattering fundamentals, including elastic and inelastic scattering, coherent and incoherent scattering (2.1.1), scattering length density and cross section (2.1.2) and contrast variation (2.1.3). We then discuss common elastic scattering techniques of wide-angle X-ray scattering (2.2.1), as well as small-angle (2.2.2), very-small-angle (2.2.3), and ultra-small-angle (2.2.4) neutron scattering. Selected models and form factors for analyzing small-angle scattering data are also provided in section 2.2.5. Finally, we provide relevant data reduction methods and instrumentation for quasi-elastic neutron scattering techniques of backscattering (2.3.1), time-of-flight (2.3.2), and spin echo (2.3.3) spectroscopy. Each of these X-ray and neutron scattering instruments are designed to access specific structural and dynamic windows in materials, as shown in Figure 2.1.

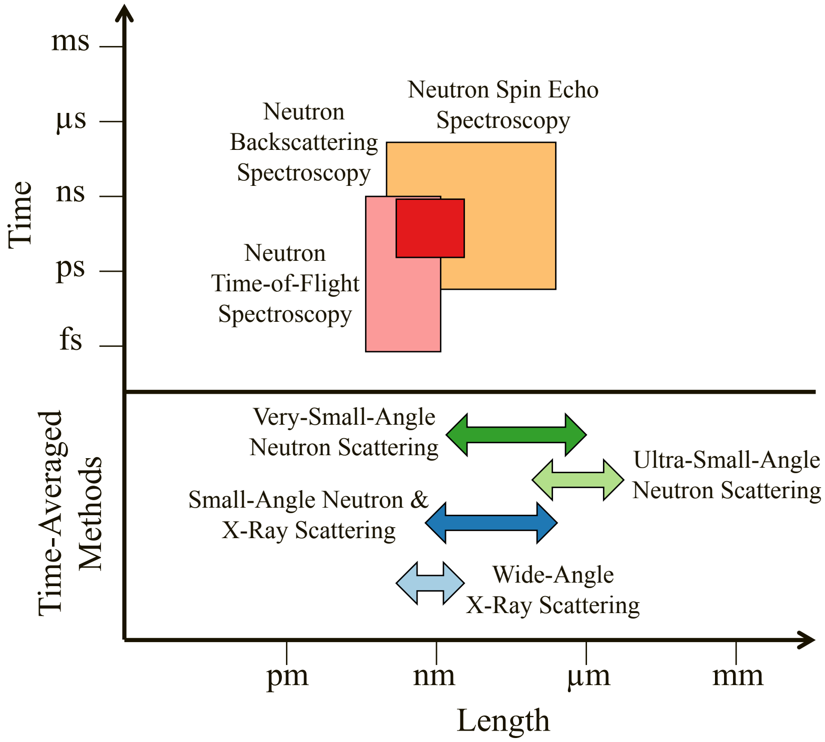

Figure 2.1. Time and length scales of neutron and X-ray scattering methods used in this work.[3–7]

While scattering instrumentation can vary wildly, they all rely on the same scattering fundamentals. A sample of interest is placed in the path of an incident beam of radiation, i.e. neutrons or X-rays. It will either pass through the sample unaffected (referred to as transmission), be absorbed, or scatter as a result of structural and dynamic fluctuations within a material. If the scattered beam only changes in momentum (direction), it is defined as an elastic scattering event, but if the scattered beam changes in both momentum and energy, it is defined as an inelastic scattering event. Figure 2.2 provides a schematic for both of these interactions.

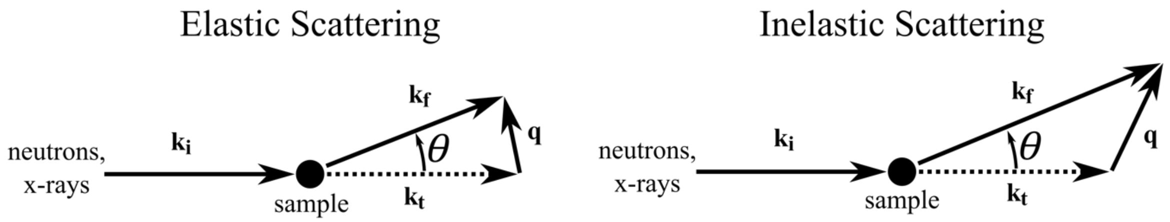

Figure 2.2. Schematic of elastic and inelastic scattering events.

The relationship between the incident beam, $\boldsymbol{k_i}$, the scattered beam, $\boldsymbol{k_f}$, and the scattering vector, $\boldsymbol{q}$, is defined with the following formula[2]:

$$\boldsymbol{q} = \boldsymbol{k_f} - \boldsymbol{k_i} \tag{2.1}$$

In an elastic scattering event, the incident and scattered beams have equal magnitudes, and the following relationships hold[2]:

$$\left|\boldsymbol{k_f}\right| = \left|\boldsymbol{k_i}\right| = \frac{2\pi}{\lambda} \tag{2.2}$$

$$|\boldsymbol{q}| = \frac{4\pi}{\lambda}\sin\left(\frac{\theta}{2}\right) = \frac{2\pi n}{d} \tag{2.3}$$

where λ is the wavelength of incident beam, θ is the scattering angle, and d is a characteristic length scale in the system. This last part of eq. 2.3 is more commonly known as Bragg's law in the diffraction community. In an inelastic scattering event, the incident and scattered beams have unequal energies, and the following relationships can be defined[2]:

$$|\boldsymbol{q}| = k_i^2 + k_f^2 - 2k_ik_f\cos\theta \tag{2.4}$$

$$\Delta E = \frac{h}{4\pi m}\left(k_f^2 - k_i^2\right) \tag{2.5}$$

where ΔE is the energy change, h is Planck's constant, and m is the mass of the radiation particle (e.g. neutron mass).

2.1.1 *Scattering Length Density and Cross Section*

The intensity of a scattering event between the incident beam and the scattering medium (e.g. atom) is quantified by the scattering length, b, which is also defined as the change in beam wave amplitude.[1,2] Scattering length is typically discussed in the context of scattering length density (SLD), which is determined by the sum of scattering lengths per unit volume of a material. The square of the scattering length is directly related to the scattering cross section, σ, which can be defined as the probability of a scattering event.[2] The value of the scattering length is dependent on both the type of incident radiation and the specific scattering medium. X-rays interact with an atom's electron cloud, and therefore, X-ray scattering lengths vary proportionally with the atomic radius and number, i.e. they tend to grow uniformly across the periodic table. Conversely, neutrons interact with the atomic nucleus and vary randomly across the periodic table.[1,2] These differing interactions between either X-rays or neutrons and the material play an important role in choosing an appropriate scattering technique. In some situations, these interactions can be manipulated (contrast variation) to create sufficient contrast, which is discussed more thoroughly in section 2.1.3.

2.1.2 *Coherent and Incoherent Scattering*

The scattering cross section can be broken down into both its coherent and incoherent components which arise from the ordered and disordered fluctuations of scattering length density within a material. Coherent scattering includes information about both the structure and pair-correlated motions within a material, while incoherent scattering captures the self-motions.[1,2,8,9] Coherent and incoherent cross sections can be defined with the following equations[1,2]:

$$\sigma_{coh} = 4\pi\langle b\rangle^2 \tag{2.6}$$

$$\sigma_{inc} = 4\pi(\langle b^2\rangle - \langle b\rangle^2) \tag{2.7}$$

where σ_{coh} and σ_{inc} are the coherent and incoherent cross sections , respectively, and b is the scattering length. As previously discussed, the scattering length, b, is related to the scattered wave's amplitude, and so for neutron scattering specifically, Higgins and Benoit define b^2 as "the probability that a neutron will be scattered per nucleus, per incident neutron, per solid angle".[2] When determining the cross section, $4\pi b^2$ averages over all scattering angles from the scattering particle and so it represents the total probability of a scattering event occurring. When isotopes with identical scattering length densities are spatially correlated, they can result in constructive interference of the scattered waves at particular angles that depend on that distance (see Bragg's law in eq.2.3) which provides information about the structure or the pair-correlated motions of those isotopes. However, random fluctuations in scattering length density, such as randomly placed isotopes of different scattering lengths, only result in destructive interference. While incoherent scattering does not provide structural information, inelastic scattering events can provide information about the self-motions of those scatterers.[2] Higgins and Benoit also note that isotopes are not the only origin of the incoherent neutron scattering; rather, the spins of the nucleus (scatterers) and the neutrons can also make significant contributions, especially for hydrogen whose scattering lengths differ greatly based on the spin state. The spin state will determine the interaction between the nucleus and the neutron, and so similar to randomly placed isotopes, random occurrences of the different spin states result in additional incoherent scattering. For fully hydrogenated materials, this limits the structural information that can be extracted with neutron scattering due to a high incoherent background in the scattering signal.[2] However, this high incoherent signal can be useful for extracting the self-motion, such as diffusion, by use of quasi-elastic and inelastic scattering methods.

2.1.3 *Contrast Variation*

Scattering arises from the fluctuations of SLD, or contrast, between different phases within a material.[1] Ensuring that there is both sufficient and informative contrast within a system is an important part of the experimental design for neutron and X-ray scattering. It not only dictates the scattering intensity but also how one can analyze and interpret the results. Recalling that the X-ray scattering lengths are proportional to atomic radius, contrast can be limited for systems with similar atomic compositions, such as in polymer blends. However, neutron scattering can be particularly advantageous for these types of systems by use of contrast variation.

There is a significant difference in the neutron scattering lengths of hydrogen and its isotope deuterium. As seen in Table 2.1, the hydrogen cross section is an order of magnitude higher than that of all other common isotopes encountered in this work. By selectively replacing hydrogen with deuterium in one of the material's phases or components, the SLD can be modified in such a way as to increase contrast while having minimal effects on the system. An example of this is in a blend of two polymers such as poly(3-hexylthiophene) (P3HT) and polystyrene (PS). The SLD for these two materials are $0.676\text{x}10^{-6}$ Å^{-2} and $1.493\text{x}10^{-6}$ Å^{-2}, respectively. However, by fully deuterating the PS phase (PS-D8), the SLD is increased to $6.464\text{x}10^{-6}$ Å^{-2}, which enables the characterization of one organic phase (P3HT) within another organic matrix (PS-D8), a task that can be difficult with more common microscopy techniques (e.g. AFM, TEM, optical microscopy) or with X-ray scattering. We can also consider contrast variation when probing the dynamics in a pure material, such as P3HT, with quasi-elastic neutron scattering. In the fully hydrogenated material, the scattering signal will be dominated by the self-motions (incoherent scattering) of the hydrogens, the majority of which are located on the alkyl side chain. Alternatively, we could replace the hydrogens with deuterium which would allow us to probe the pair-correlated motions resulting from a higher coherent scattering contribution. Furthermore, we could selectively replace the hydrogens in the side chains with deuterium and leave the hydrogen atoms along the backbone. The side chains now contribute both pair-motions from the coherent scattering and also some self-motions from the incoherent scattering (see Table 2.1). However, due to the high incoherent scattering from the backbone's remaining hydrogens, the signal from the self-motions of the chain's backbone are maximized in the scattering intensity.

Table 2.1. Coherent and incoherent neutron scattering cross section of hydrogen, deuterium, carbon, and sulfur.[10,11]

Element/Isotope	**Coherent Cross Section (10^{-24} cm^2)**	**Incoherent Cross Section (10^{-24} cm^2)**	**Total Cross Section (10^{-24} cm^2)**
Hydrogen	1.7568	80.26	82.02
Deuterium	5.592	2.05	7.64
Carbon	5.551	0.001	5.551
Sulfur	1.0186	0.007	1.026

2.2 ELASTIC SCATTERING

Elastic scattering experiments focus solely on momentum (direction) changes to extract information about structural features within the sample, such as a crystal structure or the shape of colloidal particles.[1,2] Data is collected as a 2D image of scattering intensity on an image plate or detector. Then, based on the configuration of the instrument, that information is converted to scattering intensity, I, as a function of the scattering vector, q. The presence of structural features at particular length scales cause an increase in the coherent structure factor, or scattering signal, above the incoherent background at the corresponding q-values. Elastic scattering methods of wide-angle X-ray scattering (WAXS) (2.2.1), small-angle neutron scattering (SANS) (2.2.2), very-small-angle neutron scattering (VSANS) (2.2.3), and ultra-small-angle neutron scattering (USANS) (2.2.4) are all discussed in greater detail below.

2.2.1 *Wide-Angle X-Ray Scattering (WAXS)*

In this work, WAXS is used to investigate the crystallinity and intermolecular structure of conjugated polymers at length scales between Angstroms to a hundred nanometers. Much of the WAXS data was collected utilizing a line-collimated transmission configuration, as shown in Figure 2.3. In line-collimation mode, the X-ray beam is collimated into a slit shape before reaching the sample position. After interacting with the sample, the beam is either transmitted through and blocked by the beam stop, or is scattered and captured at the image plate (detector) position. While this configuration does offer increased flux in comparison to a point-collimation source, instrumental ‘smearing’ of the signal needs to be accounted for when reducing and analyzing the data. The scattering vector, q, is determined by the vertical position of the scattered beam in relation to the beam vector, as shown in the left panel of Figure 2.3. However, the beam does not necessarily scatter in the vertical direction only; it can travel radially from the position at which the beam passes through the sample as long as the proper scattering angle, θ, is maintained (e.g. horizontally), resulting in the uncertainty of the Q-value at each detector position. Smearing can be accounted for, however, during the reduction process (desmearing) or it can be included as part of the model when fitting and analyzing data by characterizing the beam dimensions (length and width).

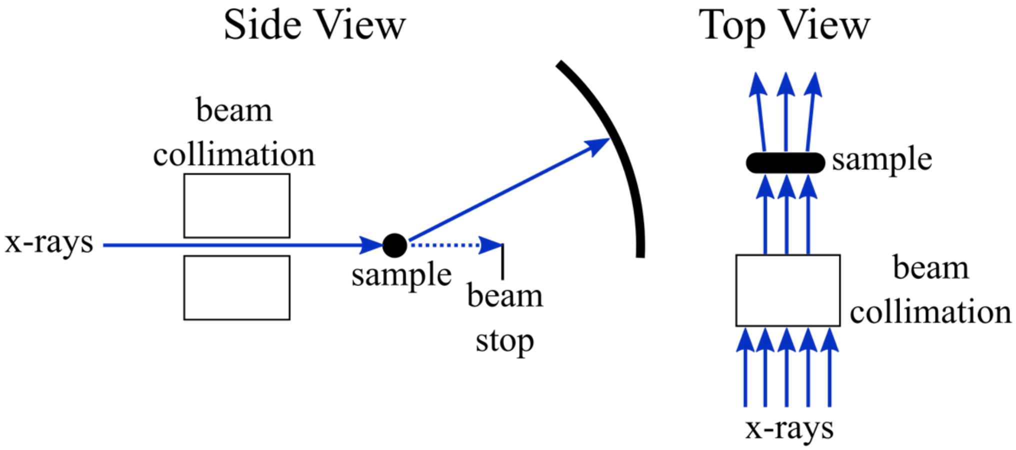

Figure 2.3. Schematic of wide-angle X-ray scattering (WAXS) experimental setup in line-collimation mode.

An example of WAXS data for blends of RRe-P3HT and deuterated PS is shown in Figure 2.4. Fully amorphous materials (e.g. PS) will show broad peaks (e.g. Q-values of approximately 0.75 and 1.4 Å^{-1} for PS) that correspond to polydisperse correlation distances within the material. However, semi-crystalline materials will display a combination of broad peaks from the amorphous phase and sharper peaks from the crystalline phase. For RRe-P3HT, two crystalline peaks appear at Q-values of approximately 0.35 and 1.7 Å^{-1} which correspond to the lamellar and π-stacking distances of the crystal structure, respectively. Additional discussion about how WAXS results can be compared to results from molecular dynamics simulations can be found in Chapter 3. By converting these Q-values into real space using eq. 2.3, the crystal spacing can be extracted. However, additional information about the nature of the crystalline regimes are contained within the peak characteristics. For example, the height of each of these peaks corresponds to the degree of crystallization in their respective directions. By comparing the relative heights of the lamellar and pi-stacking peaks across different samples, one can understand the preferred crystallization direction within a material, as we demonstrate later in Chapter 6.

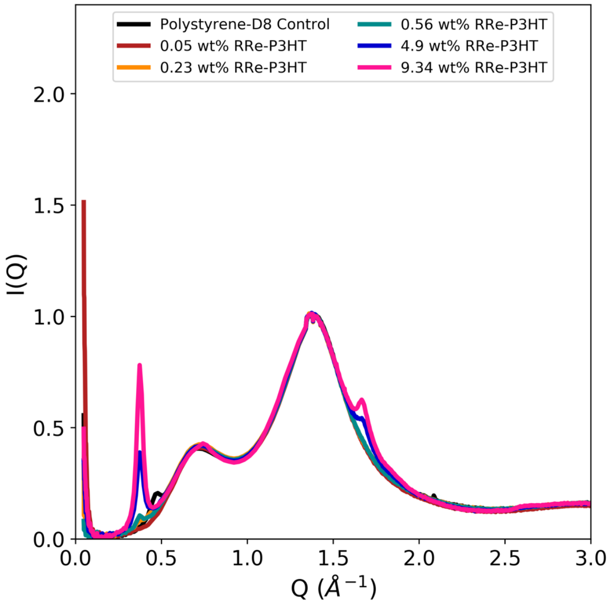

Figure 2.4. Wide-angle X-ray scattering (WAXS) data for solid polymer blends of regio-regular poly(3-hexlthiophene) (RRe-P3HT) and deuterated polystyrene (PS-D8).s

2.2.2 *Small-Angle Neutron Scattering (SANS)*

Small-angle neutron scattering (SANS) is one of the most popular neutron methods for investigating length scales of ~1 nm to 500 nm in materials.[1] In this work, SANS measurements were performed at the National Institute of Standards and Technology (NIST) Center for Neutron

Research (NCNR) in Gaithersburg, MD on the NGB and NG7 30m SANS instruments.[12] Instrument configurations were set to capture scattering vectors between 0.003 – 0.3 Å^{-1}. A schematic of the experimental setup is shown in Figure 2.5. The velocity selector is used to monochromate the incoming neutron beam which is then collimated and focused with guides and attenuators. Neutrons passed through the sample that scatter then travel through the vacuum chamber to either the beam stop or the detectors. Because the majority of neutrons are transmitted through the material unaffected, the beam stop is used to block the intense main beam, protect the detector, and minimize saturation. However, the geometry of the beam stop and its positioning relative to the detectors also determine the smallest scattering vector that can be observed. Additionally, the detectors can be positioned at various configurations to capture different ranges of scattering vectors. A closer detector will capture wider angles while a farther detector can more easily resolve smaller angles.

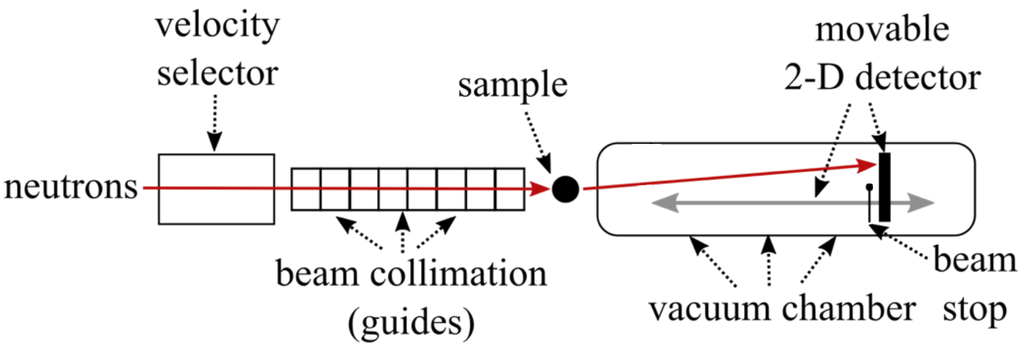

Figure 2.5. Schematic of the Small-Angle Neutron Scattering instruments (NGB and NG7 30m) at the NIST Center for Neutron Research (NCNR).[12]

The intensity measured from a SANS experiment is directly related to the differential cross section, or neutrons scattered per scattering angle. The differential cross section includes both incoherent and coherent cross sections, as shown by the following formulas[1,2]:

$$\left[\frac{\delta\sigma}{\delta\Omega}(q)\right]_{coh} = \langle b\rangle^2 \Sigma_{j,k=1}^{N}\langle e^{iq\cdot r_{jk}}\rangle \tag{2.8}$$

$$\left[\frac{\delta\sigma}{\delta\Omega}\right]_{inc} = N(\langle b^2\rangle - \langle b\rangle^2) \tag{2.9}$$

$$\frac{\delta\sigma}{\delta\Omega}(q) = \left[\frac{\delta\sigma}{\delta\Omega}(q)\right]_{coh} + \left[\frac{\delta\sigma}{\delta\Omega}\right]_{inc} \tag{2.10}$$

where Ω is the scattering angle, N is the total number of particles, and r_{jk} is the position vector between particles j and k.

The detectors capture a 2D image of the neutrons that are scattered radially from the sample within the accessible scattering angles. The 2D form of the scattering intensity can be useful for capturing any alignment that may develop within the scattering medium, but for isotropic samples, these images will be radially uniform. Therefore, we radially average the data during reduction to obtain a 1D profile of scattering intensity as a function of the scattering vector, q. This intensity can be further broken down using the following formula[13]:

$$\frac{\delta\sigma}{\delta\Omega}(q) = n\Delta\rho^2 V^2 P(q) S(q) + background \tag{2.11}$$

where I is the scattering intensity, n is the number density of scattering particles, $\Delta\rho^2$ is the scattering contrast determined by the squared difference between scattering length density of the particles and the matrix or solvent, V is the volume of particles, P is the form factor which arises from shapes of the scattering particles, S is the structure factor which arises from particle-particle correlations and is equal to 1 in the dilute limit, and $background$ accounts for the flat background intensity that is usually dominated by incoherent scattering from the sample, but could also include contributions from air, solvent, or sample holders. Various form factors and structure factors have been defined for a wide variety of scattering structures, such as spheres, cylinders, fractals and network models. By fitting these models to the measured scattering intensity profiles, they can be used to extract quantitative structural information about the material, e.g. a sphere's radius. A more thorough description of these form factors can be found in Section 2.2.5.

2.2.3 *Very Small-Angle Neutron Scattering (VSANS)*

The very small-angle neutron scattering (VSANS) technique is used to reach lower scattering angles than accessed with traditional SANS instruments. VSANS measurements were performed at the NCNR in Gaithersburg, MD on the NG3 VSANS instrument. A longer chamber length and a high resolution detector at the farther distance enables a minimum q of 0.0002 Å^{-1}.[7] Rather than utilizing a single movable detector, the VSANS instrument also utilizes three detectors to obtain data across the entire q-range simultaneously.[14] This is advantageous for kinetic studies as there is no lost time moving the detector to different positions or restricting the experiment to a narrow q-range of a single detector.[15,16] The detector arrangement is shown in Figure 2.6. There are additional features of the instrument design that enable the low-q range of the VSANS instrument, however, we note that this work did not utilize the high resolution features and instead collected data across a q-range more comparable with that of the SANS instruments previously discussed. Nevertheless, the VSANS instrument did allow us to efficiently capture a large set of high-quality data for our work.

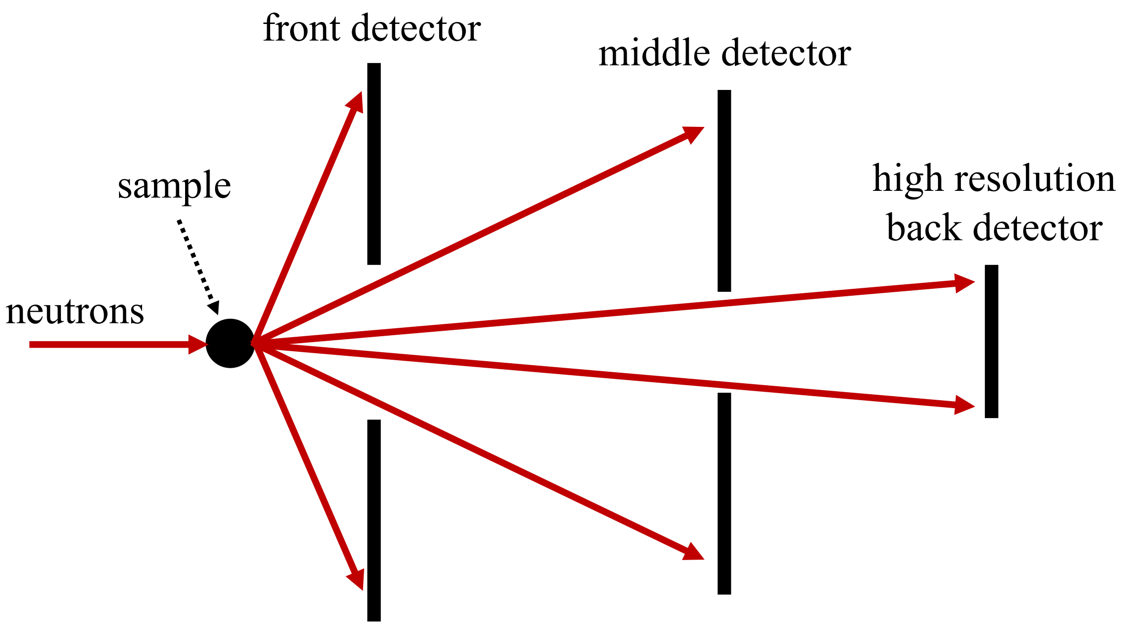

Figure 2.6. Schematic of the Very Small-Angle Neutron Scattering instruments (NG-3) at the NIST Center for Neutron Research (NCNR).[14]

2.2.4 *Ultra-Small-Angle Neutron Scattering (USANS)*

An ultra-small-angle neutron scattering (USANS) instrument can reach even lower q-values than either traditional SANS or VSANS instrumentation (minimum q of 0.00003 Å^{-1}). All USANS measurements were performed at the NCNR in Gaithersburg, MD on the BT-5 VSANS instrument. Unlike other SANS instruments, the USANS instrument is a double-crystal diffractometer. Neutrons of wavelength 2.38 Å are selected from the source at the sapphire and graphite filters. The beam is further focused by the premonochromator and the monochromator. Neutrons then pass through the sample and are either transmitted or scattered. Those transmitted neutrons are counted by the transmission detector. The analyzer is then arranged at a specific position to reflect neutrons that are scattered from the sample at a specific scattering angle. The scattered neutrons are then detected at the main detector position. This means that unlike traditional SANS instruments, the USANS instrument measures scattering intensity one specific q-value at a time. In both the analyzer and monochromator, Si(220) crystals are used to reflect the neutron beam, and so with careful control of the analyzer position and the small wavelength, extremely small scattering angles can be achieved.

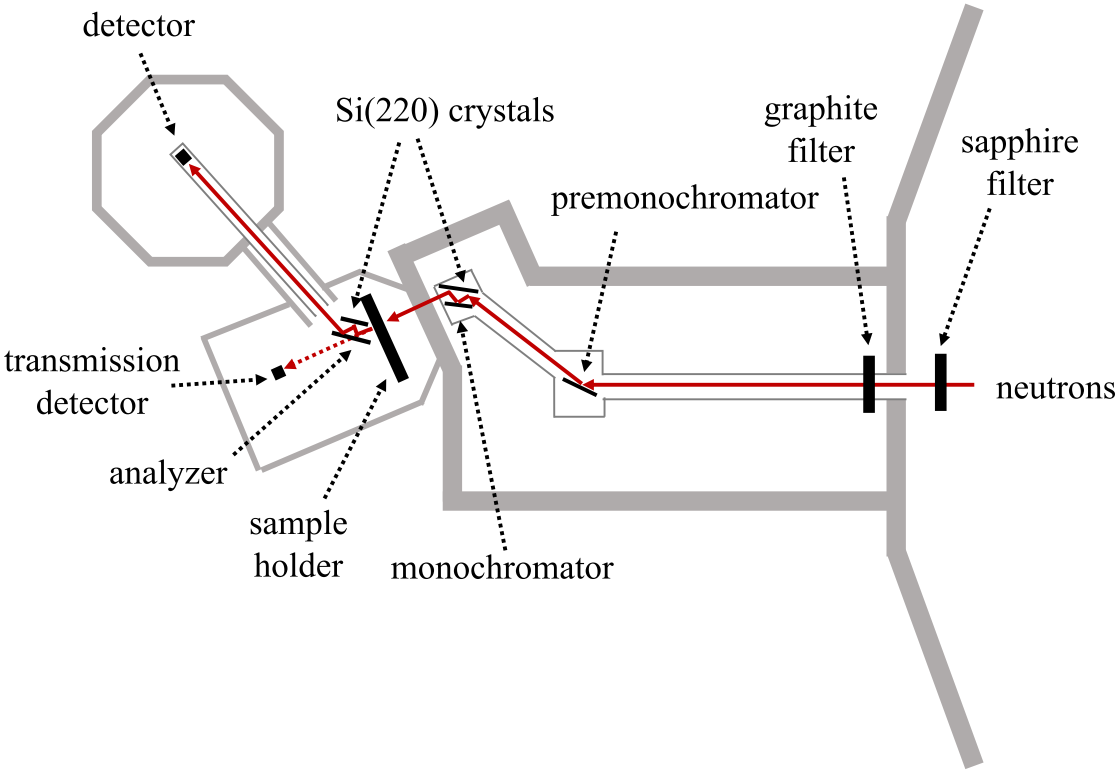

Figure 2.7. Schematic of the Ultra-Small-Angle Neutron Scattering instrument (BT-5) at the NIST Center for Neutron Research (NCNR).[17]

2.2.5 *Selected Models and Form Factors for Small-Angle Scattering*

As previously discussed, hundreds of models and form factors have been developed for small-angle scattering data as a means to quantitatively describe the sample conformation. In this section, we discuss selected models and form factors used in this work to characterize polymers in both solution- and solid-state. The application of these models for blends of polythiophenes and polystyrene is discussed in greater detail in Chapter 6.

An excellent first approach to analyzing the internal structure of a sample is to probe the structure's dimensionality and interface with a Porod analysis[18]. The scattering intensity, I, can be modeled by[19]:

$$I_{Porod}(q) = \frac{C_{Porod}}{q^m} + background \tag{2.12}$$

where C_{Porod} is the Porod constant, m is the Porod exponent, and $background$ is a constant value largely contributed to by incoherent scattering. Exponents can vary from 1, 2 and 4, which are generally indicative of 1-dimensional (rods) , 2-dimensional (sheets), or 3-dimensional structures, respectively.[13] At the high-q limit, the scattering is dominated by interfaces and the Porod analysis enables quantification of the interfacial properties. Not only can this describe a rough (exponent of 3) or sharp/smooth (exponent of 4) interface, but it can also be used to determine an interfacial concentration, $\frac{S}{V}$, in the sample[1]:

$$C_{Porod} = 2\pi\Delta\rho^2 \frac{S}{V} \tag{2.13}$$

Power-law exponents in the low- to mid-q regions can also be used to classify the aggregation of particles into various types of fractals or networks. In general, power-law models can be defined as[19,20]:

$$I_{Power-Law}(q) = \frac{A}{q^n} \tag{2.14}$$

where A is an arbitrary scaling parameter and n is the power-law exponent.

A more general, application of the Porod analysis is the Guinier-Porod model[19,21,22]. It not only captures the dimensionality of the scattering objects (Porod, high-q region) but also their size (Guinier, low-q region). It is defined as[19,21,22]:

$$I_{Guinier-Porod}(q) = \begin{cases} \frac{G}{q^s} \exp\left[-\frac{q^2 R_g^2}{3-s}\right] & q \leq q_1 \\ \frac{D}{q^m} & q \geq q_1 \end{cases} \tag{2.15}$$

$$q_1 = \frac{1}{R_g}\sqrt{\frac{(m-s)(3-s)}{2}} \tag{2.16}$$

$$D = \frac{G}{R_g^{m-s}} \exp\left[\frac{s-m}{2}\right]\left(\frac{(m-s)(3-s)}{2}\right)^{\frac{m-s}{2}} \tag{2.17}$$

where G and D are scale factors, and R_g is the radius gyration of the scattering structures (size). Below q_1, the system follows a Guinier model, where the variable s varies in the range $0 \leq s \leq 2$ and describes the dimensionality of the structures within the sample. A value of 0 corresponds to 3-dimensional objects, a value of 1 is indicative of 1-dimensional objects (rods), and a value of 2 is indicative of 2-dimensional objects (sheets).[19,21] Above q_1, the system follows the Porod model as defined in eq. 2.12.

The Porod, power law, and Guinier-Porod models discussed thus far have provided a more generalized, yet descriptive, approach to analyzing the nature of a sample's internal structure. However, form factors can provide even more characterization of specific shapes within a material, ranging from simple spheres or cylinders to even more complex materials such as core-multi-shell particles. For spherical scattering objects, the scattering intensity can be defined as[19,21]:

$$I_{sphere}(q) = vV_{sphere}\Delta\rho^2\left[3\,\frac{\sin(\mathrm{qR_{sphere}}) - qR_{sphere}\cos(qR_{sphere})}{\left(qR_{sphere}\right)^3}\right]^2 \tag{2.18}$$

where v is the volume fraction of the spherical phase in the sample, V_{sphere} is the sphere volume, and R_{sphere} is the sphere radius. With knowledge of the sample's SLD values and volume fractions, the spherical form factor allows researchers to extract the sphere size and polydispersity in their system. Similarly, a form factor for ellipsoids of rotation can be defined as[19,23]:

$$I_{ellipsoid}(q) = vV_{ellipsoid}\Delta\rho^2\int_0^{\frac{\pi}{2}}\left[3\,\frac{\sin(qR_{ellipsoid}) - qR_{ellipsoid}\cos(qR_{ellipsoid})}{\left(qR_{ellipsoid}\right)^2}\right]\sin(\alpha)\,d\alpha \tag{2.19}$$

$$V_{ellipsoid} = \left(\frac{4}{3}\right)\pi R_{polar}R_{equatorial}^2 \tag{2.20}$$

$$R_{ellipsoid} = \sqrt{R_{equatorial}^2\sin^2(\alpha) + R_{polar}^2\cos^2(\alpha)} \tag{2.21}$$

where the ellipsoids are characterized by polar and equatorial radii, R_{polar} and $R_{equatorial}$, respectively. Finally, a system comprised of rigid cylinders follows the form factor[19,24–26]:

$$I_{cylinder}(q) = \frac{v}{V_{cylinder}}\int_0^{\frac{\pi}{2}}F^2(q,\alpha)\sin(\alpha)\,d\alpha \tag{2.22}$$

$$F(q,\alpha) = 2\Delta\rho\,\frac{V_{cylinder}\sin\left(\frac{1}{2}qL_{cylinder}\,cos(\alpha)\right)}{\frac{1}{2}qL_{cylinder}\cos(\alpha)}\,\frac{J_1\left(qR_{cylinder}\sin(\alpha)\right)}{qRsin(\alpha)} \tag{2.23}$$

$$V_{cylinder} = \pi R_{cylinder}^2 L_{cylinder} \tag{2.24}$$

where the cylinder is characterized by a cross sectional radius, $R_{cylinder}$, and length, $L_{cylinder}$. Finally, J_1 is the Bessel function of the first kind.

2.3 QUASI-ELASTIC NEUTRON SCATTERING

Inelastic neutron scattering experiments collect information about both momentum and energy changes due to a scattering event. It is through this additional energy information that dynamics within the material (e.g. rotations, vibrations, and translations) can be uncovered. More specifically, a quasi-elastic neutron scattering (QENS) experiment collects scattering data at the smaller energy changes caused by translations and rotations in the material.[2] The scattering intensity collected during a QENS experiment is directly proportional to the double differential cross section, or neutrons scattered per scattering angle and per energy change.[1,2,9] The coherent and incoherent contributions to the double differential cross section can be defined by the following equations[1]:

$$\frac{\delta^2\sigma}{\delta\Omega\delta\omega} = N\frac{k_f}{k_i}\left(\left(\langle b^2\rangle - \langle b\rangle^2\right)S_{inc}(q,\omega) + \langle b\rangle^2 S_{coh}(q,\omega)\right) \tag{2.25}$$

$$S_{inc}(q,\omega) = \frac{1}{2\pi N}\int dt\left\langle \Sigma_j \mathrm{e}^{\mathrm{i}\left(\mathrm{q}\cdot\left(\mathrm{r_j(t)}-\mathrm{r_j(0)}\right)-\omega t\right)}\right\rangle \tag{2.26}$$

$$S_{coh}(q,\omega) = \frac{1}{2\pi N}\int dt\left\langle \Sigma_{j,k} \mathrm{e}^{\mathrm{i}\left(\mathrm{q}\cdot\left(\mathrm{r_k(t)}-\mathrm{r_j(0)}\right)-\omega t\right)}\right\rangle \tag{2.27}$$

where ω is frequency (related to the neutron energy), t is time, and all other variables remain as previously defined. The incoherent contribution tracks the location of a single particle at a particular time relative to its initial position, i.e. self-motions within the sample. The coherent contribution tracks the location of one particle at a particular time relative to the initial position of another particle, i.e. pair-correlated motions within the sample.[1,9] Frequently, data from QENS measurements is presented as scattering intensity, I, versus time scale, t, for a particular scattering vector, q. However, data is typically collected in the energy domain and so this requires a Fourier transform to the time domain and the deconvolution of the instrument resolution[27]:

$$I(q,t) = \frac{\int S(q,\omega) e^{i\omega t} d\omega}{\int R(q,\omega) e^{i\omega t} d\omega} \tag{2.28}$$

where $R(q,\omega)$ is the resolution function. Moreover, QENS data in the time domain can be fit using a stretched exponential or Kohlrausch–Williams–Watts (KWW) function to extract a characteristic relaxation time, τ, that describes the captured system dynamics. This function is defined as[8]:

$$I(q,t) = I_o(q) \exp - \left[\frac{t}{tau(q)}\right]^{\beta} \tag{2.29}$$

where b is a stretching parameter of the decay and I_O accounts for dynamics (decays) occurring at shorter time scales than the instrument's range.

Finally, we note that QENS instruments can also be operated in an 'elastic mode' that only tracks changes in the elastic scattering signal (within the resolution of the instrument) as a function of temperature (fixed window scan). Reductions in the elastic scattering intensity are related to increases in the inelastic or quasi-elastic scattering contributions. Similar to differential scanning calorimetry (section 2.4) this can be useful for probing different phases of the material's dynamics. The elastic signal can be analyzed directly, or transformed into a mean squared displacement using the Debye-Waller factor[28]:

$$S(q, \omega = 0) = \exp\left[-\frac{q^2 < u^2 >}{3}\right] \quad (2.30)$$

where $< u^2 >$ is the mean squared displacement. The elastic signal at the lowest temperature is used as a reference point for a system with no motions (i.e. mean squared displacement is equal to zero).

2.3.1 *Backscattering Spectroscopy*

Extremely small energy changes in scattered neutrons need to be resolved to capture slower polymeric motions (e.g. backbone fluctuations) on the order of a nanosecond. A backscattering spectrometer is able to capture the needed high energy resolutions (~ 1 μeV) by utilizing a monochromator to reflect the beam at nearly 180°. At these high Bragg angles, the range in wavelength (resolution) of reflected neutrons is incredibly narrow.[1,2] In this work, backscattering experiments were performed using either the High Flux Backscattering Spectrometer (HFBS)[3] at the NCNR or the Backscattering Spectrometer (BASIS)[4] at the Spallation Neutron Source (SNS) at the Oak Ridge National Laboratory (ORNL).

A schematic of the experimental setup for HFBS is shown in Figure 2.8. The incident neutron beam (a continuous source at the NCNR) is guided to the instrument with the neutron guides. It is then focused at the phase space transform chopper and sent to the doppler drive and monochromator. The monochromator is made from Si(111) crystals that are oriented in such a way to reflect the beam back to the instrument at an angle of 180° with a wavelength of approximately 6.2 Å. The neutrons finally pass through the sample and are then scattered towards more Si(111) crystals at the analyzer. Only the neutrons that have passed through the sample without a change in energy (wavelength at 6.2 Å) are again reflected back from the analyzers through the sample to the He-3 detectors. In this event, only the elastically scattered neutrons are detected. In order to capture the inelastically scattered neutrons that have undergone small energy change, a doppler effect is used at the monochromator position to slightly change the wavelength of the reflected neutrons. Therefore, a small energy change due to an inelastic scattering event must occur for the neutrons to recover a wavelength of 6.2 Å, be reflected at the analyzers, and reach the detectors. In this way, the instrument can ‘scan’ a small range of energy changes surrounding the elastic scattering peak (i.e. corresponding to no energy change) and capture the slower motions at time scales of ~100 ps to 1 ns.[2,3] The instrument is also capable of performing elastic scans in which it only collects the elastic scattering data while another variable, usually the sample temperature, is changed.[3]

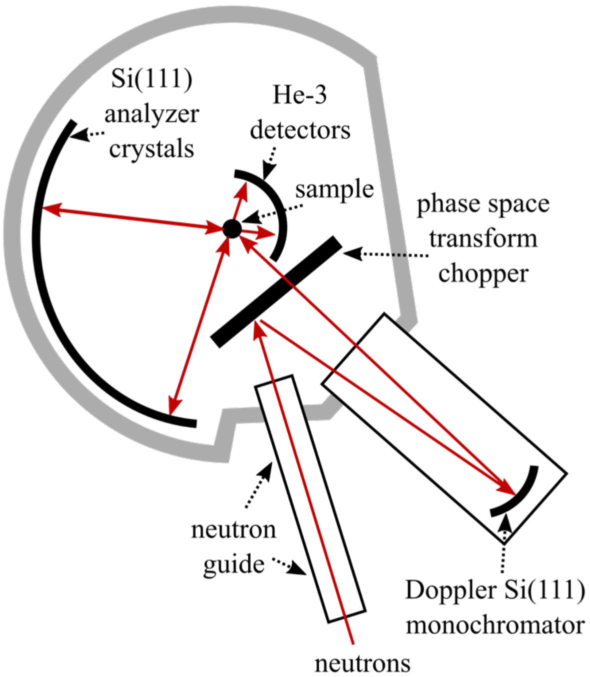

Figure 2.8. Schematic of the High Flux Backscattering Spectrometer (HFBS) at the NIST Center for Neutron Research (NCNR).[3]

The experimental setup for BASIS is shown in Figure 2.9. BASIS at the SNS utilizes similar backscattering fundamentals as HFBS, but with a few key differences. Incoming neutrons from the spallation source arrive in pulses. Therefore, the BASIS instrument uses choppers and the neutron time-of-flight (i.e. velocity) to create well-defined neutron pulses with particular wavelengths (energies). After the neutron pulse interacts with the sample and reaches the analyzer, they are reflected back towards the detectors. However, BASIS carefully focuses the analyzers to He-3 detectors located both above and below the sample position. This eliminates the need for neutrons to pass through the sample twice as they do at HFBS. Although the BASIS resolution is not quite as high as that of HFBS, BASIS is able to capture a wider energy range and therefore, wider dynamic time scales of ~10 ps to 1 ns.[2,4]

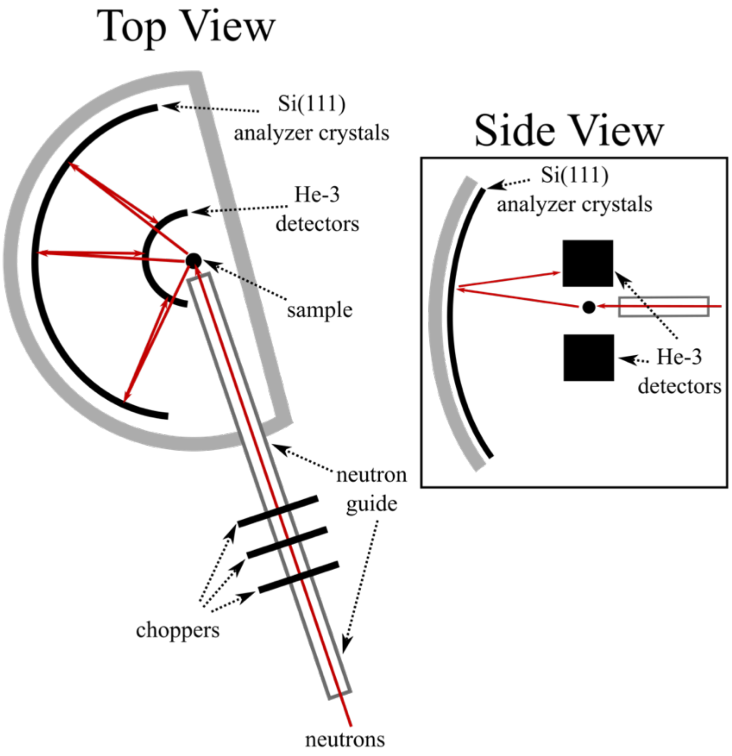

Figure 2.9. Schematic of the Backscattering Spectrometer (BASIS) at the Spallation Neutron Source (SNS) at the Oak Ridge National Laboratory (ORNL).[4]

2.3.2 *Time-of-Flight Spectroscopy*

Time-of-flight spectrometers use knowledge of the time passed between a scattering event and detector impact (direction and velocity) to resolve the neutron's final momentum and energy.[2] These instruments are able to capture the quicker motions in a material at time scales ~0.1 – 10 ps. All time-of-flight experiments were performed using the Disk Chopper Spectrometer (DCS) at the NCNR,[6] and a schematic of the experimental setup is shown in Figure 2.10.[6]

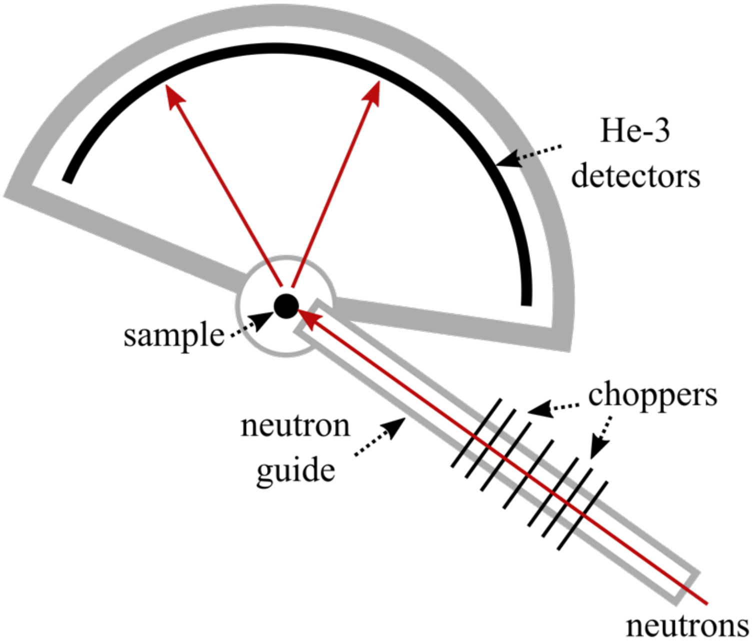

Figure 2.10. Schematic of the Disk Chopper Spectrometer (DCS) at the NIST Center for Neutron Research (NCNR).[6]

At the DCS instrument, the continuous beam of neutrons supplied from the reactor must first be segmented into well-defined, monochromatic neutron pulses by a series of choppers. This gives the instrument knowledge of the time of neutron-sample impact. After sample interactions, neutrons are scattered in various directions towards the He-3 detectors. Based on the energy of the incoming neutrons selected at the choppers (i.e. their velocity) and their time reaching the sample, their time-of-arrival at the detector position should be known for elastic scattering events. However, if inelastic scattering (energy change) occurs, their time-of-flight from the sample position to the detectors is either faster or slower than expected. Based on this time differential, the energy change can be determined. The operation of the choppers can be controlled in such a way as to change the incident beam energy, resolution (energy width) and flux, giving the researchers some flexibility in the time and length scales captured.[2,6]

2.3.3 *Spin-Echo Spectroscopy*

Neutron spin echo uses the spin of the neutron to track energy changes from inelastic scattering., which allows the instrument to have extremely high energy resolution and probe dynamics with time scales from ~1 ps – 100 ns.[2,8] All spin echo experiments were performed on the Neutron Spin Echo Spectrometer (NSE) at the NCNR.[5] A schematic of the experiment setup for NSE is shown in Figure 2.11.[5] Neutrons with a particular energy are roughly selected from the source at the velocity selector. The width of wavelengths for the selected neutrons is rather wide at the spin echo instrument, as this does not impact the energy resolution as it does on other spectrometers. The polarizer ensures that the neutron spins are all parallel to the neutron path direction. At the first $\frac{\pi}{2}$ flipper, the neutron spin is flipped perpendicular (up) to the path. At this point, precession of the neutron begins. The precession segments are equal-length solenoids generating a magnetic field. Each neutron will precess at the same frequency (Larmor precession frequency), but depending on the neutron velocity, i.e. time spent in the precession segment of the instrument, some neutrons will complete more precessions than others. Near the sample, neutron spins are rotated 180° around the upward direction, reversing the distribution of neutron spins in the beam. Assuming the neutrons interacted elastically with the sample and are moving at the same velocity, the path through the second precession field will cause the spins to return to the original upward position by the end. Neutrons then pass through a second $\frac{\pi}{2}$ flipper to return the spins parallel to the path. If the neutrons interacted inelastically with the sample, their change in velocity will not allow their spin to return to the upward position, and therefore, will not be returned parallel to the beam path after the second $\frac{\pi}{2}$ flipper. Only neutrons with a spin parallel to the beam are allowed to pass through the analyzer and reach the detector, where the intensity measured decreases with the occurrence of inelastic scattering. An important note here is that the spin echo instrument directly measures the coherent contribution to the structure factor. Since 2/3 of the total incoherent scattering is due to neutron spin flips, it is able to remove that contribution. Additionally, the instrument collects data at different scattering angles by physically moving the latter half of the instrument (sample to detector) radially about the sample position (region of movement).[2,5,8] The spin echo instrument is different from other quasi-elastic techniques as it collects data directly in time, not in energy. By tuning one of the solenoids, one can account for small changes in the energy of the neutron. Inelastically scattered neutrons, with a time-scale related to the magnetic field, are then returned to their upward position by the end of their path and reach the detector position. Moreover, this is advantageous for removing contributions to the scattering signal from instrument resolution. Instead of performing a complex deconvolution in energy, it is now a simple division in time.[2,5,8]

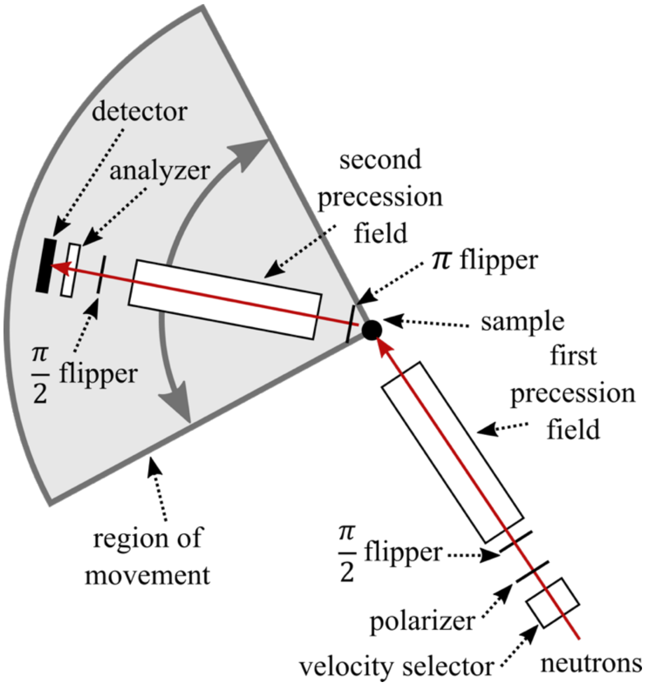

Figure 2.11. Schematic of the Neutron Spin Echo Spectrometer (NSE) at the NIST Center for Neutron Research (NCNR).[5]

2.4 DIFFERENTIAL SCANNING CALORIMETRY (DSC)

Differential scanning calorimetry (DSC) is a useful technique for finding phase changes, glass transition temperatures, and melting temperatures of polymers. More broadly, this technique records the heat transferred to/from a sample of known mass while heating/cooling at a constant rate (e.g. 5 K/min). Inflection points and maxima/minima in the data indicate a transition point within the material. Moreover, by integrating the area under the curve, one can determine the enthalpy change for that phase transition.[29] In this work, DSC is used to determine the glass transition temperature (inflection) and the crystalline to amorphous melting temperature (maxima) of conjugated polymers. An example of this can be seen in Figure 2.12 for regio-regular and regio-random P3HT.

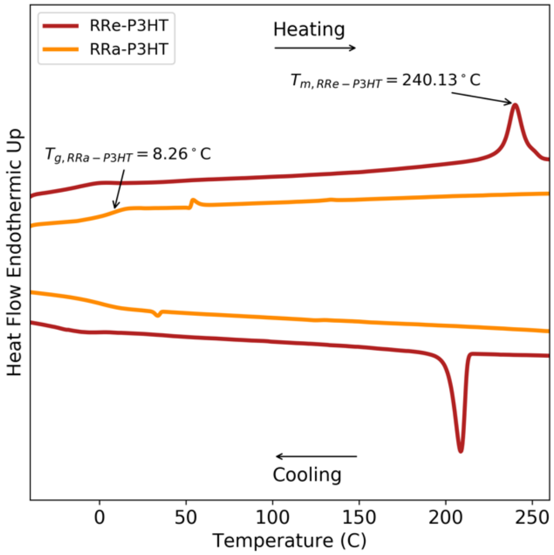

Figure 2.12. Differential scanning calorimetry (DSC) data for regio-regular and regio-random poly(3-hexylthiophene) (RRe-P3HT, RRa-P3HT). The glass transition is noted by T_g and the melting temperature by T_m.

2.5 ULTRAVIOLET-VISIBLE (UV-VIS) SPECTROSCOPY

The absorption spectra from ultraviolet-visible spectroscopy (UV-Vis) of polymer solutions can be used to not only determine concentration but also infer structural information about the material based on the peak absorbance location (wavelength) or intensity.[30] When fully dissolved in solution, poly(3-hexylthiophene) (P3HT), for example, will show a single absorption peak at approximately 450 nm[30–32]. However, as P3HT crystallization or conformation changes begin to occur in solution, there is a shift of the peak to higher wavelengths or the appearance of additional peaks.[31] The absorbance peak intensity can be related to concentration by the Beer-Lambert law[33]:

$$A(\lambda) = \epsilon(\lambda) l c \tag{2.31}$$

where A is the absorbance, ϵ is the extinction coefficient, l is the path length and c is the concentration. By calculating the extinction coefficient at a particular wavelength for a fully dissolved system with known concentration and pathlength, the concentration for unknown systems can be determined as long as the system remains in the fully dissolved (linear) regime. In this work, we utilize UV-Vis to determine the accurate amount of conjugated polymer in polythiophene-polystyrene blends. Shown in Figure 2.13 is the absorption spectra for blends of regio-regular P3HT and polystyrene at varying ratios dissolved in chlorobenzene at a constant total concentration. Since the absorption peak intensity is sensitive to the concentration of the P3HT component, we can use samples of well-known P3HT:PS ratios to determine the unknown composition of others. This is further discussed in Chapter 6.

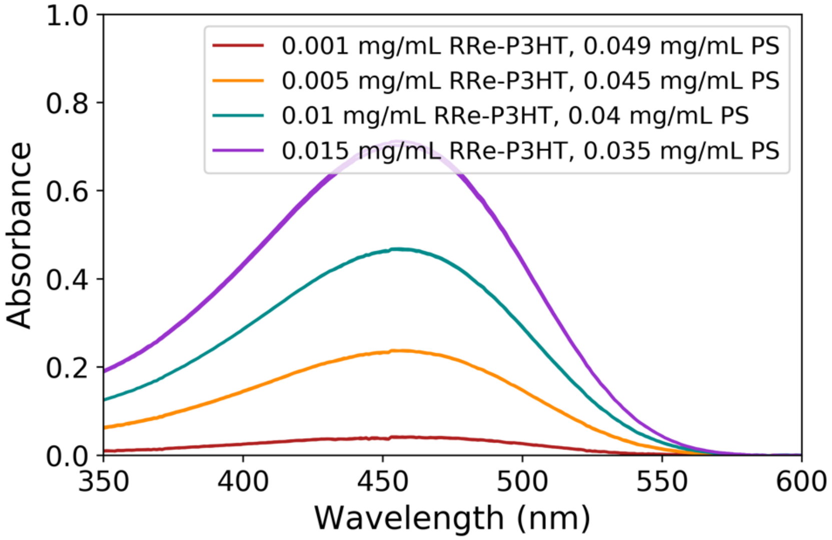

Figure 2.13. UV-Vis spectrum for blends of regio-regular poly(3-hexylthiophene) (RRe-P3HT) and polystyrene dissolved in chlorobenzene.

2.6 REFERENCES

(1) *Neutrons, X-Rays and Light: Scattering Methods Applied to Soft Condensed Matter*, First.; Lindner, P., Zemb, T., Eds.; Elsevier Science B.V: Amsterdam, 2002.

(2) *Polymers and Neutron Scattering*; Higgins, J. S., Benoit, H. C., Eds.; Oxford University Press Inc.: New York, 1994.

(3) Meyer, A.; Dimeo, R. M.; Gehring, P. M.; Neumann, D. A. *The High-Flux Backscattering Spectrometer at the NIST Center for Neutron Research*. *Rev. Sci. Instrum.* **2003**, *74* (5), 2759–2777. https://doi.org/10.1063/1.1568557.

(4) Mamontov, E.; Herwig, K. W. *A Time-of-Flight Backscattering Spectrometer at the Spallation Neutron Source, BASIS*. *Rev. Sci. Instrum.* **2011**, *82* (8), 085109. https://doi.org/10.1063/1.3626214.

(5) Rosov, N.; Rathgeber, S.; Monkenbusch, M. Neutron Spin Echo Spectroscopy at the NIST Center for Neutron Research. In *Scattering from polymers: characterization by x-rays, neutrons, and light*; Cebe, P., Hsaio, B. S., Lohse, D. J., Eds.; American Chemical Society: Washington, D.C., 2000; pp 103–116.

(6) Copley, J. R. D.; Cook, J. C. *The Disk Chopper Spectrometer at NIST: A New Instrument for Quasielastic Neutron Scattering Studies*. *Chem. Phys.* **2003**, *292* (2–3), 477–485. https://doi.org/10.1016/S0301-0104(03)00124-1.

(7) 45-meter VSANS Instrument @ Guide NG-3 https://ncnr.nist.gov/equipment/msnew/ncnr/vsans-design-features.html (accessed May 31, 2020).

(8) Richter, D.; Monkenbusch, M.; Arbe, A.; Colmenero, J. *Neutron Spin Echo in Polymer Systems*; Springer Berlin Heidelberg: Berlin, Heidelberg, 2005. https://doi.org/10.1007/b106578.

(9) Arbe, A.; Alvarez, F.; Colmenero, J. *Neutron Scattering and Molecular Dynamics Simulations: Synergetic Tools to Unravel Structure and Dynamics in Polymers*. *Soft Matter* **2012**, *8* (32), 8257. https://doi.org/10.1039/c2sm26061a.

(10) Sears, V. F. *Neutron Scattering Lengths and Cross Sections*. *Neutron News* **1992**, *3* (3), 26–37. https://doi.org/10.1080/10448639208218770.

(11) Munter, A. Neutron scattering lengths and cross sections https://www.ncnr.nist.gov/resources/n-lengths/ (accessed Sep 1, 2017).

(12) Glinka, C. J.; Barker, J. G.; Hammouda, B.; Krueger, S.; Moyer, J. J.; Orts, W. J. *The 30 m Small-Angle Neutron Scattering Instruments at the National Institute of Standards and Technology*. *J. Appl. Crystallogr.* **1998**, *31* (3), 430–445. https://doi.org/10.1107/S0021889897017020.

(13) Hammouda, B. *Probing Nanoscale Structures - The SANS Toolbox.*; National Institute for Standards and Technology Center for Neutron Research: Gaithersburg, MD, 2016.

(14) VSANS Detectors https://ncnr.nist.gov/equipment/msnew/ncnr/vsans-detectors.html (accessed May 31, 2020).

(15) Lee, Y.-T.; Li, D. S.; Pozzo, L. D. *Kinetic Analysis of Ultrasound-Induced Oil Exchange in Oil-in-Water Emulsions through Contrast Variation Time-Resolved Small-Angle Neutron Scattering*. *Langmuir* **2019**. https://doi.org/10.1021/acs.langmuir.9b02424.

(16) Lee, Y.-T.; Pozzo, L. D. *Contrast-Variation Time-Resolved SANS Analysis of Oil Exchange Kinetics Between Oil-in-Water Emulsions Stabilized by Anionic Surfactants*. *Langmuir* **2019**. https://doi.org/10.1021/acs.langmuir.9b02423.

(17) Barker, J. G.; Glinka, C. J.; Moyer, J. J.; Kim, M. H.; Drews, A. R.; Agamalian, M. *Design and Performance of a Thermal-Neutron Double-Crystal Diffractometer for USANS at NIST*. *J. Appl. Crystallogr.* **2005**, *38* (6), 1004–1011. https://doi.org/10.1107/S0021889805032103.

(18) Porod, G. *Die Röntgenkleinwinkelstreuung von Dichtgepackten Kolloiden Systemen*. *Kolloid-Zeitschrift* **1951**, *124* (2), 83–114. https://doi.org/10.1007/BF01512792.

(19) Doucet, M.; King, S.; Butler, P.; Kienzle, P.; Parker, P.; Krzywon, J.; Jackson, A.; Richter, T.; Gonzales, M.; Nielsen, T.; Ferraz, L. R. *SasView (Version 5.0.1)*. 2020.

(20) Newbloom, G. M.; Kim, F. S.; Jenekhe, S. A.; Pozzo, D. C. *Mesoscale Morphology and Charge Transport in Colloidal Networks of Poly(3-Hexylthiophene)*. *Macromolecules* **2011**, *44* (10), 3801–3809. https://doi.org/10.1021/ma2000515.

(21) Hammouda, B. *A New Guinier–Porod Model*. *J. Appl. Crystallogr.* **2010**, *43* (4), 716–719. https://doi.org/10.1107/S0021889810015773.

(22) Hammouda, B. *Analysis of the Beaucage Model*. *J. Appl. Crystallogr.* **2010**, *43* (6), 1474–1478. https://doi.org/10.1107/S0021889810033856.

(23) Feigin, L. A.; Svergun, D. I. *Structure Analysis by Small-Angle X-Ray and Neutron Scattering*; Plenum Press: New York, 1987.

(24) Pedersen, J. S. *Analysis of Small-Angle Scattering Data from Colloids and Polymer Solutions: Modeling and Least-Squares Fitting*. *Adv. Colloid Interface Sci.* **1997**, *70*.

(25) Fournet, G. *Scattering Functions for Geometrical Forms*. *Bull. French Soc. Mineral. Crystallogr.* **1951**, *74*.

(26) Onsager, L. *The Effects of Shape on the Interaction of Colloidal Particles*. *Ann. N. Y. Acad. Sci.* **1949**, *51* (4), 627–659.

(27) Colmenero, J.; Arbe, A. *Recent Progress on Polymer Dynamics by Neutron Scattering:*

From Simple Polymers to Complex Materials. *J. Polym. Sci. Part B Polym. Phys.* **2013**, *51* (2), 87–113. https://doi.org/10.1002/polb.23178.

(28) Zhan, P.; Zhang, W.; Jacobs, I. E.; Nisson, D. M.; Xie, R.; Weissen, A. R.; Colby, R. H.; Moulé, A. J.; Milner, S. T.; Maranas, J. K.; Gomez, E. D. *Side Chain Length Affects Backbone Dynamics in Poly(3-Alkylthiophene)S*. *J. Polym. Sci. Part B Polym. Phys.* **2018**, *56* (17), 1193–1202. https://doi.org/10.1002/polb.24637.

(29) Chen, S. A.; Ni, J. M. *Structure/Properties of Conjugated Conductive Polymers. 1. Neutral Poly(3-Alkythiophene)S*. *Macromolecules* **1992**, *25* (23), 6081–6089. https://doi.org/10.1021/ma00049a001.

(30) Böckmann, M.; Schemme, T.; de Jong, D. H.; Denz, C.; Heuer, A.; Doltsinis, N. L. *Structure of P3HT Crystals, Thin Films, and Solutions by UV/Vis Spectral Analysis*. *Phys. Chem. Chem. Phys.* **2015**, *17* (43), 28616–28625. https://doi.org/10.1039/C5CP03665H.

(31) Samanta, K.; Guenet, J.-M.; Malik, S. *Intermingled Network of Syndiotactic Polystyrene/Poly(3-Hexylthiophene)*. *Macromolecules* **2019**, *52* (22), 8569–8576. https://doi.org/10.1021/acs.macromol.9b01512.

(32) Xi, Y.; Pozzo, L. D. *Electric Field Directed Formation of Aligned Conjugated Polymer Fibers*. *Soft Matter* **2017**, *13* (21), 3894–3908. https://doi.org/10.1039/C7SM00485K.

(33) Newbloom, G. M. Engineering the Multi-Length Scale Structure of Self-Assembled Conjugated Polymer Networks, University of Washington, 2014.

Chapter 3. COMPUTATIONAL METHODS AND RELATED THEORY

3.1 MOLECULAR DYNAMICS SIMULATIONS

A molecular dynamics (MD) simulation is a computational modeling technique that uses classical mechanics to track the motion of particles (e.g. atoms) as a function of time. It utilizes a force field to provide a functional form and parameters to define all bonded and non-bonded interactions between particles. It then solves the equations of motion (3.1.2) to move each particle at every timestep in response to the 'force' that is applied by the surrounding particles. While it is an approximation of complex quantum mechanical interatomic and intermolecular interactions, MD simulations are still able to provide *in-silico* insight into molecular motions and structures at time scales ranging between picoseconds to milliseconds and length scales between Angstroms to micrometers that are not readily accessible by experiments alone. Thousands of functional forms and parameter sets for MD force fields have been developed across many types of materials, from small molecules to polymers, but not all force fields can be applied to all materials and they should be carefully selected for each system of interest. In this section, we review the fundamentals of MD simulations, including force fields (3.1.1), integrators (3.1.2), and NPT and NVT ensembles (3.1.3). An advantage of MD is that these simulations cover similar length and time scales as neutron and X-ray scattering techniques[1], enabling a direct validation between theoretical and experimental systems as discussed in sections 3.1.4 and 3.1.5. Finally, we provided examples of *in-silico* structure and dynamics that can be extracted from MD simulations in section 3.1.6.

3.1.1 *Force Field*

An MD force field defines the bonded and non-bonded interactions between atoms in the system, and they can range in both their functional form and their parameter sets. At the base level, a Class I force field is represented by the following equations[2–4]:

$$\mathrm{V} = \mathrm{V}_{\mathrm{bonded}} + V_{non-bonded} \tag{3.1}$$

$$\mathrm{V}_{\mathrm{bonded}} = \Sigma_{\mathrm{bonds}} \tfrac{1}{2} K_{b,ij}\left(b_{ij} - b_{o,ij}\right)^2 + \Sigma_{angles} \tfrac{1}{2} K_{\theta,ijk}\left(\theta_{ijk} - \theta_{o,ijk}\right)^2 +$$

$$\Sigma_{impropers} \tfrac{1}{2} K_{\zeta,ijkl}\left(\zeta_{ijkl} - \zeta_{o,ijkl}\right)^2 + \Sigma_{dihedrals} \tfrac{1}{2} K_{\phi,ijkl}\left(1 + \cos\left(n\phi_{ijkl} - \delta_n\right)\right) \tag{3.2}$$

$$\mathrm{V}_{non-bonded} = \Sigma_{pairs}\left[4\epsilon_{ij}\left(\left(\frac{\sigma_{ij}}{r_{ij}}\right)^{12} - \left(\frac{\sigma_{ij}}{r_{ij}}\right)^{6}\right) + \frac{q_i q_j}{\kappa r_{ij}}\right] \tag{3.3}$$

where V is the total potential energy of bonded ($\mathrm{V}_{\mathrm{bonded}}$) and non-bonded ($\mathrm{V}_{\mathrm{non-bonded}}$) contributions. In the bond contribution to the bonded potential function (Σ_{bonds}) , $\mathrm{K}_{\mathrm{b,ij}}$ is the bond spring constant, b_{ij} is the bond length, and $b_{o,ij}$ is the equilibrium bond length between bonded atoms i and j. In the angle contribution to the bonded potential function (Σ_{angles}) , $\mathrm{K}_{\theta,\mathrm{ijk}}$ is the angle spring constant, θ_{ijk} is the angle, and $\theta_{o,ijk}$ is the equilibrium angle between linearly bonded atoms i, j and k. In the improper angle contribution to the bonded potential function ($\Sigma_{\mathrm{impropers}}$), $\mathrm{K}_{\zeta,\mathrm{ijkl}}$ is the improper spring constant for atoms i, j, k and l bonded in a trigonal pyramid or trigonal planar structure. ζ_{ijkl} is the improper angle and $\zeta_{o,ijkl}$ is the equilibrium improper angle between the plane formed by atoms i, j and k and the plane formed by atoms i, j and l where atom k is bonded to all atoms i, j and l. In the dihedral angle contribution to the bonded potential function ($\Sigma_{\mathrm{dihedrals}}$) , $\mathrm{K}_{\phi,\mathrm{ijkl}}$ is the dihedral potential constant for linearly bonded atoms (in order) i, j, k and l. ϕ_{ijkl} is the dihedral angle and $\phi_{o,ijkl}$ is the equilibrium dihedral angle between the plane formed by atoms i, j and k and the plane formed by atoms j, k and l. The phase is represented by δ_n for potential maximum/minimum n. The non-bonded potential includes contributions from the 12/6 Lennard-Jones and Coulombic potential functions. ϵ_{ij}, σ_i, and σ_j are the Lennard-Jones parameters, q_i and q_j are the atomic partial charges, κ is the dielectric constant, and r_{ij} is the distance between non-bonded atoms i and j. For a more interactive exploration of an atomistic MD force field, visit https://interactive-md-ff.herokuapp.com/. These force field parameters are typically determined with a combination of quantum mechanical simulations and experimental fitting to bulk material properties (e.g. density). Therefore, each parameter set is very specific to each specific or class of materials depending on the development process.

3.1.2 *Velocity-Verlet Integrator*

At the start of each MD simulation, each atom is placed in an initial position and given a starting velocity. The integrator, such as the velocity-Verlet algorithm, is then responsible for updating each atom's position and velocity at every timestep based on the 'force' they experience due to the bonded and non-bonded interactions with neighboring atoms. This force acting upon atom i can be calculated by integrating the potential energy defined by the force field[2]:

$$\mathbf{F}_i = \frac{\delta V}{\delta \boldsymbol{r}_i} \tag{3.4}$$

where $\mathbf{F}_i$ is the force vector acting on atom i and $\boldsymbol{r}_i$ is position vector of atom i. Using Newton's second law of motion and Taylor series expansion of the equations of motion, the velocity-Verlet integrator solves for the position vector, $\boldsymbol{r}_n$, and the velocity vector, $\boldsymbol{v}_n$, for each atom at step n with[5]:

$$\boldsymbol{F}_{n-1} = m_i \boldsymbol{a}_{n-1} \tag{3.5}$$

$$\boldsymbol{r}_n = \boldsymbol{r}_{n-1} + \boldsymbol{v}_{n-1}\Delta t + \frac{\boldsymbol{a}_{n-1}}{2}\Delta t^2 = \boldsymbol{r}_{n-1} + \boldsymbol{v}_{n-1}\Delta t + \frac{\boldsymbol{F}_{n-1}}{2m}\Delta t^2 \tag{3.6}$$

$$\boldsymbol{v}_n = \boldsymbol{v}_{n-1} + \frac{\boldsymbol{F}_n + \boldsymbol{F}_{n-1}}{2m}\Delta t \tag{3.7}$$

where $\boldsymbol{F}_{n-1}$ is the force vector at the step $n-1$, m_i is the mass of atom i, and $\boldsymbol{a}_{n-1}$ is the acceleration of atom i. Finally, the timestep Δt can be defined as $t_n - t_{n-1}$.

3.1.3 *NVT and NPT Ensembles*

In this work, we utilize both the canonical (NVT) and isothermal-isobaric (NPT) ensembles. An MD simulation under the NVT ensemble is held with constant volume and temperature, while a simulation under the NPT ensemble is held with constant pressure and temperature. More specifically, we utilize Nose-Hoover non-Hamiltonian integrators to control temperature (thermostat) and to control pressure (barostat). The thermostat applies additional variables to the integrator that act as a heat bath to the system, controlling atom kinetic energies and therefore, temperature. The barostat works similarly in that it modifies the simulation box dimensions (volume) to control system pressure.[2]

3.1.4 *Comparison between Molecular Dynamics and Quasi-Elastic Neutron Scattering*

MD simulations can be directly compared to quasi-elastic neutron scattering (QENS) dynamics data through the intermediate scattering function (see Chapter 2). This is accomplished by calculation of the coherent and incoherent contributions to the dynamic structure factor[6,7]:

$$I_{inc}(q,t) = \frac{1}{\sum_{j=1}^{N_{species}} n_j b_{j,inc}^2} \sum_{\alpha=1}^{N} b_{\alpha=1}^2 \langle e^{-i\vec{q}\cdot\overrightarrow{r_\alpha}(0)} e^{-i\vec{q}\cdot\overrightarrow{r_\alpha}(t)} \rangle \tag{3.8}$$

$$I_{coh}(q,t) = \frac{1}{\sum_{j=1}^{N_{species}} n_j b_{j,coh}^2} \sum_{\alpha,\beta\geq\alpha}^{N} b_{\alpha,coh} b_{\beta,coh} \langle e^{-i\vec{q}\cdot\overrightarrow{r_\alpha}(0)} e^{-i\vec{q}\cdot\overrightarrow{r_\beta}(t)} \rangle \tag{3.9}$$

$$I(q,t) = \frac{\sum_{j=1}^{N_{species}} n_j b_{j,inc}^2 I_{inc}(q,t) + \sum_{j=1}^{N_{species}} n_j b_{j,coh}^2 I_{coh}(q,t)}{\sum_{j=1}^{N_{species}} n_j b_{j,inc}^2 + \sum_{j=1}^{N_{species}} n_j b_{j,coh}^2} \tag{3.10}$$

where $N_{species}$ is the total number of atom types (i.e. isotopes), n_j is the number of atoms of isotope j, N is the total number of atoms, $b_{i,inc}$ and $b_{i,coh}$ are the incoherent and coherent scattering lengths of isotope j, $b_{\alpha,inc}$ and $b_{\alpha,coh}$ are the incoherent and coherent scattering lengths of atom α, a is the scattering vector, and $r_\alpha(t)$ and $r_\beta(t)$ are the positions of atoms α and β at a time t. To compare with QENS elastic scans, a net mean squared displacement (MSD) at an appropriate time scale based on the instrument's resolution, or dynamic window, can be determined by:

$$MSD = \langle \frac{1}{\sum_{\alpha=1}^{N}(\sigma_{\alpha,inc}+\sigma_{\alpha,coh})} \sum_{\alpha=1}^{N} \left(\sigma_{\alpha,inc} + \sigma_{\alpha,coh}\right) \cdot (\|\overrightarrow{r_\alpha}(\tau + \tau_O) - \overrightarrow{r_\alpha}(\tau_O)\|_F)^2 \rangle_{\tau_O} \tag{3.11}$$

where N is the total number of atoms, , $\sigma_{\alpha,inc}$ and $\sigma_{\beta,inc}$ are the incoherent and coherent scattering cross sections, $\overrightarrow{r_\alpha}(\tau_O)$ is the positional vector at time τ_O and $\overrightarrow{r_\alpha}(\tau_O + \tau)$ is the positional vector at a time $\tau_O + \tau$ of atom α.

3.1.5 *Comparison between Molecular Dynamics and Wide-Angle X-ray Scattering*

The *in-silico* structure from MD simulations can be compared to results from WAXS measurements (see Chapter 2) by use of the static structure factor. This can be calculated by the following formula^{6,7}:

$$S(Q) = \frac{1}{\sum_{j=1}^{N_{species}} n_j Z_j^2} \sum_{\alpha,\beta\geq\alpha}^{N} Z_\alpha Z_\beta \left\langle e^{-i\vec{Q}\cdot\overrightarrow{r_\alpha}} e^{-i\vec{Q}\cdot\overrightarrow{r_\beta}} \right\rangle \tag{3.12}$$

where $N_{species}$ the total number of atom types (i.e. isotopes), N is the total number of atoms, Z_α and Z_β are the atomic numbers of atoms α and β, Q is the scattering vector, and r_α and r_β are the positions of atoms α and β.

3.1.6 *In-Silico Structure and Dynamics from MD Simulations*

MD simulations enable researchers to explore specific structural and dynamic properties of materials that would not be readily accessible by experiments alone. In this work, we use MD to extract bulk properties and *in-silico* information of conjugated polymers relevant to charge transport mechanisms in these materials. In this section we provide the formulas for calculating these properties in the context of poly(3-hexylthiophene) (P3HT), a conjugated polymer comprised of a thiophene backbone and alkyl side chains, and a more thorough discussion of these analyses and their results can be found in Chapter 4. However, we want to emphasize these approaches of autocorrelation functions, mean squared relative displacements, and radial distribution functions can be extended to many more materials.

The dihedral autocorrelation function (DACF) can probe the mobility of the P3HT backbone by tracking the dihedral angle between the thiophene rings as a function of time as shown in the following equation[8]:

$$DACF(\tau) = \frac{\langle \cos\phi(\tau+\tau_o)\cos\phi(\tau_o)\rangle - \langle \cos\phi(\tau_o)\rangle^2}{\langle \cos\phi(\tau_o)\cos\phi(\tau_o)\rangle - \langle \cos\phi(\tau_o)\rangle^2} \tag{3.13}$$

where ϕ is the dihedral angle of interest (between thiophene rings in our example), τ_o is the initial reference time, and τ is time. Similarly, the mean squared relative displacement (MSRD) can monitor fluctuations in the distance between thiophene rings on nearby chains following:

$$MSRD_{thio} = \langle \frac{1}{N_{\alpha\beta}} \sum_{\alpha=1,\beta>\alpha}^{N_{\alpha\beta}} \left(\left\| (\overrightarrow{r_\beta}(\tau_O + \tau) - \overrightarrow{r_\alpha}(\tau_O + \tau)) - (\overrightarrow{r_\beta}(\tau_O) - \overrightarrow{r_\alpha}(\tau_O) \right\|_F \right)^2 \rangle \quad (3.14)$$

where $N_{\alpha\beta}$ is the total number of thiophene pairs, r_α, r_β are the position vectors to rings α and β, respectively, τ_O is the initial reference time, and τ is the time scale of interest. Finally, the radial distribution function, $G(r)_{thio}$, was used to determine the distribution of thiophene rings throughout the material with the following equation:

$$G(r)_{thio} = \langle \frac{N_{r,thio}}{\frac{4}{3}\pi((r+\Delta r)^3 - (r-\Delta r)^3)} \cdot \frac{1}{\rho_{thio}} \rangle_{N_{thio}} \qquad (3.15)$$

where $N_{r,thio}$ is the number of thiophene rings at a certain distance $r \pm \Delta r$ from the reference point, ρ_{thio} is the density of thiophene rings, and N_{thio} is the total number thiophene rings.

3.2 DENSITY FUNCTIONAL THEORY

While MD simulations take a classical approach to modelling materials, density functional theory (DFT) and other *ab-initio* methods take a quantum approach. DFT is motivated by finding an accurate approximation to the Schrödinger equation to determine the total electronic energy as well as the behavior and properties of the system. In DFT, the total electronic energy of the system, E_{total}, can be defined as function of the electron density[9,10]:

$$E_{total}[n(r)] = E_T[n(r)] + E_V[n(r)] + E_J[n(r)] + E_Q[n(r)] \quad (3.16)$$

where $n(r)$ is the electron density which is a function of electron location (r), E_T is the kinetic energy, E_V is the potential energy due to classical attraction between the electrons and the nucleus, E_J is the potential energy due to classical repulsion between electrons, and E_Q is the quantum-mechanical exchange and correlation energy between electrons.

The potential energy contributions (E_V and E_J) can be defined with the functionals for Coulombic interactions, but it is difficult to develop accurate functionals for the kinetic and quantum contributions. In the Kohn-Sham implementation of DFT, most commonly used today, the kinetic energy is first approximated by a system with non-interacting electron density.[9] A non-empirical or semi-empirical exchange-correlation energy is then used to both correct the kinetic energy approximation and account for the quantum-mechanical electron-electron interactions. Hundreds of these 'functionals' have been developed at varying levels of accuracy, starting with a Hartree approximation at the lowest accuracy (does not include any exchange or correlation corrections) and approaching chemical accuracy with additional descriptors of the electron density $(n, \nabla n, \nabla^2 n)$ and/or kinetic energy density.[9] It is important to use a functional that is appropriate and sufficiently accurate for your molecular system while also balancing computational expense. For example, a noteworthy limitation of DFT is its inability to accurately capture long-range dispersion interactions[9,10], which play a significant role in the intermolecular interactions of the conjugated materials of this work. Therefore, a functional that specifically includes additional dispersion corrections, e.g. B3LYP-D3(BJ), would need to be chosen for these systems.

In this work, DFT is used to probe the non-bonded interactions between two P3HT oligomeric chains at variable degree of polymerization. This can be accomplished by calculating the system energy as well as the self-energy for each chain at a series of distances (d) between the two chains:

$$E_{non-bonded}(d) = E_{system}(d) - 2E_{single-chain}(d) \tag{3.17}$$

The resulting non-bonded energy can then be fit to an appropriate functional form, such as the Lennard-Jones equation, to extract information about the strength of the interaction. However, it is important to note that the non-bonded energy includes contributions from Coulombic interactions, steric repulsion, and van der Waals forces.

3.3 REFERENCES

(1) Arbe, A.; Alvarez, F.; Colmenero, J. *Neutron Scattering and Molecular Dynamics Simulations: Synergetic Tools to Unravel Structure and Dynamics in Polymers*. *Soft Matter* **2012**, *8* (32), 8257. https://doi.org/10.1039/c2sm26061a.

(2) González, M. A. *Force Fields and Molecular Dynamics Simulations*. *École thématique la Société Française la Neutron.* **2011**, *12*, 169–200. https://doi.org/10.1051/sfn/201112009.

(3) Allen, M. P. Introduction to Molecular Dynamics Simulation. In *Computational Soft Matter: From Synthetic Polymers to Proteins*; 23, 2004; pp 1–28.

(4) Moreno, M.; Casalegno, M.; Raos, G.; Meille, S. V.; Po, R. *Molecular Modeling of Crystalline Alkylthiophene Oligomers and Polymers*. *J. Phys. Chem. B* **2010**, *114* (4), 1591–1602. https://doi.org/10.1021/jp9106124.

(5) Frenkel, D.; Smit, B. *Understanding Molecular Simulation: From Algorithms to Applications*, 2nd ed.; Academic Press: San Diego, 2002.

(6) Pellegrini, E.; Calligari, P.; Calandrini, V.; Hinsen, K.; Kneller, G. R. *NMOLDYN User's Guide Version 3.4*; 2009.

(7) T., R.; K., M.; K., H.; Kneller, G. R. *NMoldyn : A Program Package for a Neutron Scattering*. *J. Comput. Chem.* **2003**, *24* (5), 657–667. https://doi.org/10.1002/jcc.10243.

(8) Yimer, Y. Y.; Tsige, M. *Static and Dynamic Properties of Poly(3-Hexylthiophene) Films at Liquid/Vacuum Interfaces*. *J. Chem. Phys.* **2012**, *137* (20), 204701. https://doi.org/10.1063/1.4767395.

(9) Mardirossian, N.; Head-Gordon, M. *Thirty Years of Density Functional Theory in Computational Chemistry: An Overview and Extensive Assessment of 200 Density Functionals*. *Mol. Phys.* **2017**, *115* (19), 2315–2372. https://doi.org/10.1080/00268976.2017.1333644.

(10) Baseden, K. A.; Tye, J. W. *Introduction to Density Functional Theory: Calculations by Hand on the Helium Atom*. *J. Chem. Educ.* **2014**, *91* (12), 2116–2123. https://doi.org/10.1021/ed5004788.

Chapter 4. MOLECULAR DYNAMICS FORCE FIELDS FOR POLY(3-HEXYLTHIOPHENE): A NEUTRON AND X-RAY SCATTERING APPROACH

This chapter contains work from the following publication and the author would like to acknowledge the contributions of the coauthors:

Wolf, C. M*.; Kanekal, K*. H.; Yimer, Y. Y.; Tyagi, M.; Omar-Diallo, S.; Pakhnyuk, V.; Luscombe, C. K.; Pfaendtner, J.; Pozzo, L. D. *Assessment of Molecular Dynamics Simulations for Amorphous Poly(3-Hexylthiophene) Using Neutron and X-Ray Scattering Experiments*. *Soft Matter* **2019**, *15* (25), 5067–5083.
https://doi.org/10.1039/C9SM00807A.
**these authors contributed equally to this work*

4.1 INTRODUCTION

In Chapter 1, we motivated the advantages of using conjugated polymers (CPs) for more flexible, low-cost and solution processible organic electronic devices, such as organic photovoltaics (OPVs), field effect transistors (OFETs) or bioelectronics. The backbone and side-chain architecture of these materials can be used to tune their performance and solubility[1,2], but the wide-scale implementation of these technologies rely on a more complete understanding of the structure-function relationship. It is known that molecular morphology in conjugated polymers is closely connected to the overall charge mobility of the material.[3,4] Charge transport can occur either along the π-conjugated backbone (i.e. intra-chain charge transfer) or through the pi-orbital overlap of stacked conjugated rings on neighboring chains (i.e. inter-chain charge transfer). The work of Lan et al. reviewed the charge mobility of these two mechanisms in poly(3-hexylthiophene) (P3HT).

They note that although charge transport occurs more efficiently along the backbone in ordered (i.e. crystalline) regimes, it is the relationship between the ordered and disordered (i.e. amorphous) regimes that dictate the limit of the macroscopic charge mobility.[5] We also discussed how molecular modeling tools can be useful for probing CPs on molecular and atomistic levels. McMahon and coworkers utilized similar MD and quantum methods to evaluate the electronic properties of P3HT, and how it was affected by torsion angles along the backbone and regio-regularity defects in P3HT. They determined that the regio-regularity defects (e.g. head-to-head arrangement of neighboring monomers) did not have as significant of an effect on the charge traps within the material as was previously thought.[6] Schwarz, et al. used coarse-grained molecular dynamics simulations to study the temperature dependent structure and self-assembly behavior of P3HT in anisole. They were able to match the computed size of polymer aggregates to experimental values.[7] Jones and coworkers also used both classical and quantum simulations to find that higher annealing temperature improved ordering and charge mobility in P3HT. They found that longer chains improved mobility by creating tie chains between crystalline regimes (across the amorphous phase),[8] a behavior that was also explored in the work of Gu et al.[9] Chaudhari, et al. utilized MD and *ab-initio* methods compared with experimental nuclear magnetic resonance (NMR) data to determine the preferred crystal structure of a donor-acceptor polymer (DPP-DTT).[10] These computational approaches have all provided researchers with valuable *in-silico* information that can be difficult to extract with experiments alone. However, this also emphasizes the importance of using well-developed and validated models for the specific system of interest. For conjugated polymers specifically, there is still disagreement in the literature regarding the proper approach for parameterization of force fields and simulation procedures.

X-ray and neutron scattering have already shown their value in probing the molecular conformation and dynamics in conjugated materials. Mo and coworkers used X-ray scattering to probe the crystal structure of polythiophenes and found increased ordering due to higher annealing temperatures.[11] Parnell and coworkers used small-angle and wide-angle x-ray scattering (SAXS, WAXS) to study the phase separation behavior of P3HT:PCBM blends used in traditional OPVs. The authors concluded that instead of a two-phase system, the annealed layer was actually comprised of separate crystalline P3HT and PCBM phases plus an additional mixed amorphous phase.[12] McCulloch et al. used grazing-incidence X-ray scattering to investigate the crystal structure of poly(2,5-bis(3-alkylthiophen-2-yl)thieno[3,2-b]thiophene) (PBTTT).[13,14] In the work of Obrzut et al., QENS showed P3HT relaxations that corresponded to an activation of side chain motions at 175 K.[15] Guilbert and coworkers also quasi-elastic neutron scattering (QENS) and investigated P3HT:PCBM blends above and below the P3HT glass transition temperature. The authors found that P3HT dynamics were hindered while PCBM dynamics were enhanced by blending of the two materials.[16]

X-ray and neutron scattering methods are ideal for a powerful combined experimental and theoretical approach together with MD simulations as they all access similar length and time scales.[17,18] Moreover, these length and time scales are relevant for charge transport mechanisms in conjugated materials. However, utilizing scattering experiments together with molecular modeling has only been applied to conjugated polymers a limited number of times, as we reviewed in Chapter 1. In this chapter, we apply QENS and WAXS experiments together with atomistic MD simulations to a model amorphous conjugated polymer, regio-random P3HT, to assess the performance and limitations of five published force fields. *In-silico* parameters regarding the backbone and pi-stacking conformation and dynamics allow us to investigate the effect of different force field parameters in the modeled system, while Marcus theory relates those properties to charge transport mechanisms. Contrast variation is then used to deconvolute backbone and side-chain dynamics in QENS data for P3HT and relate those back to the modeled systems. Finally, we apply these simulations to poly(3-dodecylthiophene) (P3DDT), a similar molecule with longer alkyl side chains, to understand the applicability of these force fields to additional materials.

4.2 MATERIALS & METHODS

4.2.1 *Materials: Poly(3-hexylthiophene) and Poly(3-dodecylthiophene)*

Much of the work in this chapter utilized a single batch of regio-random poly(3-hexylthiophene) (RRa-P3HT) and another batch of regio-regular poly(3-dodecylthiophene) (P3DDT). Both materials were purchased from Rieke Metals and used as received. For the last part of this work that utilized contrast variation, a pair of similar hydrogenated and partially deuterated regio-random P3HT materials were synthesized by the Luscombe research group at the University of Washington in Seattle. Additional details of the synthesis procedure can be found in the work of Wolf et al.[21] The first material will be referred to as P3HT-H14, which is a fully hydrogenated material. The second will be referred to as P3HT-D13, which was deuterated along the hexyl side-chain while leaving the hydrogen along the backbone (attached directly to the thiophene ring). Values for molecular weight and polydispersity of all polymers are shown in Table 4.2. When using GPC with a polystyrene standard to determine the molecular weight of conjugated polymers, the value can be easily overestimated, and so in this work, we utilized the procedure outlined in Liu et al.[22] to correct the molecular weights for all our samples.

Table 4.2. Molecular weight (M_W) and polydispersity (PDI) of regio-random poly(3-hexylthiophene) and poly(3-dodecylthiophene) used in this work. RRa-P3HT and P3DDT were purchased from Rieke Metals, and P3HT-14 and P3HT-D13 were synthesized by the Luscombe research group at the University of Washington.

P3HT Batch	**M_W (kDa)**	**PDI**
RRa-P3HT	31	1.5
P3HT-H14	22	3.3
P3HT-D13	21	3.1
P3DDT	14	1.5

4.2.2 *Wide-Angle X-Ray Scattering*

WAXS measurements were performed with a line-collimated transmission mode Anton-Paar X-Ray scattering instrument with a Cu-Kα source generating an X-ray beam with a wavelength of 1.54 Å. Measurements were collected under vacuum and temperature was controlled with a TCS300 Anton-Paar sample holder. A thermocouple was also used at the sample location to correct for temperature gradients between the sample holder, sample frame, and polymer material. The polymer was pressed into a film with a thickness of approximately 1 mm that was held in between two Mylar films. These layers were held together with Aluminum frames as shown in Figure 4.1. Fujifilm image plates were used to collect the data which was later extracted using a PerkinElmer Cyclone image plate reader. Finally, the SAXSQuant software was used to reduce the scattering images and account for background corrections.

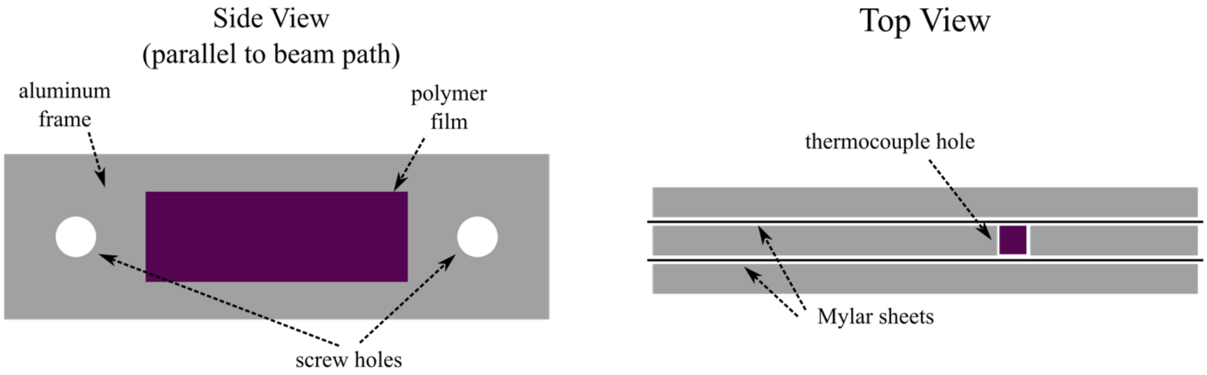

Figure 4.1. Schematic of a wide-angle X-ray scattering experiment sample used for a thick polymer film.

4.2.3 *Quasi-Elastic Neutron Scattering*

QENS measurements were taken using the Disk Chopper Spectrometer (DCS)[23] at the National Institute of Standards and Technology (NIST) Center for Neutron Research (NCNR), the Backscattering Spectrometer (BASIS)[24] at the Spallation Neutron Source (SNS) at the Oak Ridge National Laboratory (ORNL), and the High-Flux Backscattering Spectrometer (HFBS)[25] at the NCNR to access short-, medium-, and long-time scale dynamics, respectively. Measurements were collected at specified temperatures under vacuum using a top loading closed cycle refrigerator (CCR) sample environment and all resolution measurements were taken at 50 K. To create the QENS samples, thick films of polymer were applied to aluminum foil that was subsequently folded and shaped cylindrically into a pouch that fit along the inner wall of the standard cylindrical aluminum sample canisters. For the P3HT-H14 and P3HT-D13 samples, a thin lead wire was used to seal the edges and prevent the material from leaking. A schematic of the QENS sample is shown in Figure 4.2. For neutron diffraction measurements of P3DDT, the Diffuse Scattering Spectrometer at the Institute Laue-Langevin in Grenoble, France was utilized. Samples for this measurement were created following the QENS sample procedure outlined here.

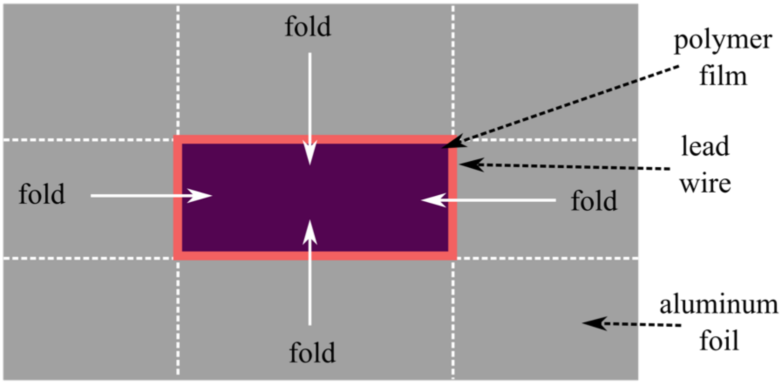

Figure 4.2. Schematic of a quasi-elastic neutron scattering sample used for a thick polymer film. Lead wire was optional and not used in all samples.

Data reduction for both QENS dynamics measurements and elastic scans were performed using the Data Acquisition and Visualization Environment (DAVE) software[26] (NCNR) or the Mantid software[27] (SNS). Elastic scans were performed at a rate of 2 K/minute. For a more thorough discussion of data collection and reduction for QENS experiments, please see Chapter 2, section 2.3.

4.2.4 *Molecular Dynamics Simulations*

The LAMMPS Molecular Dynamics software[28] was used for all MD simulations in this work. Each simulation box included 64 polymer chains that were spaced in a grid formation at uniform distances corresponding to an initial density of 0.0671 g/cm^3. Chain lengths were either 60 and 41 monomers for the RRa-P3HT and P3HT-H14/-D13 systems, respectively. Regio-regularity of the simulated chains followed the distributions extracted from nuclear magnetic resonance (NMR) data, as shown in Figure 4.3. A starting distribution of cis- and trans-conformations of the thiophene rings along the backbone was generated from a Metropolis algorithm and the relevant dihedral potential from each force field.

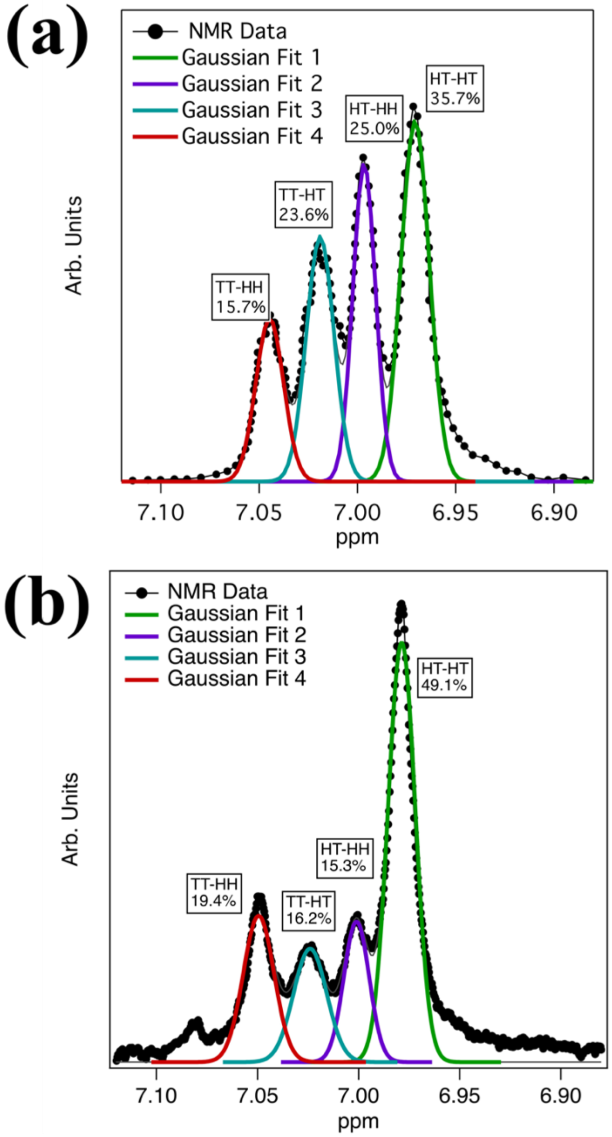

Figure 4.3. Nuclear magnetic resonance (NMR) data for RRa-P3HT (a) and P3HT-H14 (b). Gaussian fits of the NMR peaks correspond to head-tail trimer configurations outlined in Chen et. al.[29] The P3HT-D13 material was assumed to have a similar distribution to that of P3HT-H14 for simulations.

All simulations were first equilibrated for 2 ns at 600 K, followed by an additional equilibration at either 473 K or 523 K for 4 ns for the RRa-P3HT and P3HT-H14/-D13 systems, respectively. Each system was then cooled with a series of 200 ps runs at temperature steps every 10 K. For simulations where dynamics data was extracted, the system was started from the relevant cooling step for a 4 ns equilibration followed by a 5 ns production run. For mean squared displacement calculations, a 200 ps equilibration followed by a 1.5 ns production run was started at every cooling step for the desired temperature points. All simulations were performed with the NPT ensemble utilizing a velocity-Verlet algorithm with a 1 fs timestep and 0.001 atm pressure. The low pressure was used to approximate the vacuum conditions during QENS measurements. The Nose-Hoover barostat and thermostats were used to maintain pressure and temperature, respectively, with characteristic time constants of $\tau_{pressure}$ = 1 ps and $\tau_{temperature}$ = 0.1 ps. A particle-particle/particle-mesh (pppm) Ewald algorithm[30] was used for long range Coulombic interactions. Lennard-Jones interactions utilized a cutoff distance of 12 Å, and were scaled at 0.0, 0.0, and 0.5 for 1-2, 1-3, and 1-4 bonds, respectively.

nMolDyn[31] (Versions 3 and 4) was used to calculate the static and dynamic structure factors from the simulation results to enable direct comparison with scattering data (see extended discussion in Chapter 3, sections 3.1.4 and 3.1.5). The static structure factor was calculated from 0 to 2.5 $Å^{-1}$ and the dynamic structure factor from 0.3 to 1.9 $Å^{-1}$.

4.2.5 *Molecular Dynamics Force Fields*

In this work, we investigate five published force fields from the literature that have been developed for P3HT extracted from the work of Bhatta, et al.[19], Huang, et al.[7], and Moreno, et al. (three variations)[20]. To account for the effects of conjugation, these researchers all performed partial re-parameterizations of the classical OPLS-AA[32–34] force field. This first included a modification to the dihedral potential between monomers (thiophene rings) along the backbone of the chain as well as the dihedral between the thiophene ring and alkyl side chain. Finally, partial charges were determined with *ab-initio* methods. For the Bhatta[19] force field specifically, we utilized a modified form as steric interactions during *ab-initio* calculations caused an extreme and non-physical torsion potential along the alkyl side chain near the thiophene ring. Therefore, *ab-initio* calculations for these dihedrals were done again following the procedure in the original work[19] but with the rest of the alkyl side chain removed to parameterize more accurate potentials. These results compared to the relevant torsion potentials in the other force fields are shown in Figure 4.4. We will refer to this modified version of the Bhatta force field as Mod. Bhatta throughout the remainder of this work. Moreover, the Moreno force field variations will be referred to as FF1, FF2, and FF3.

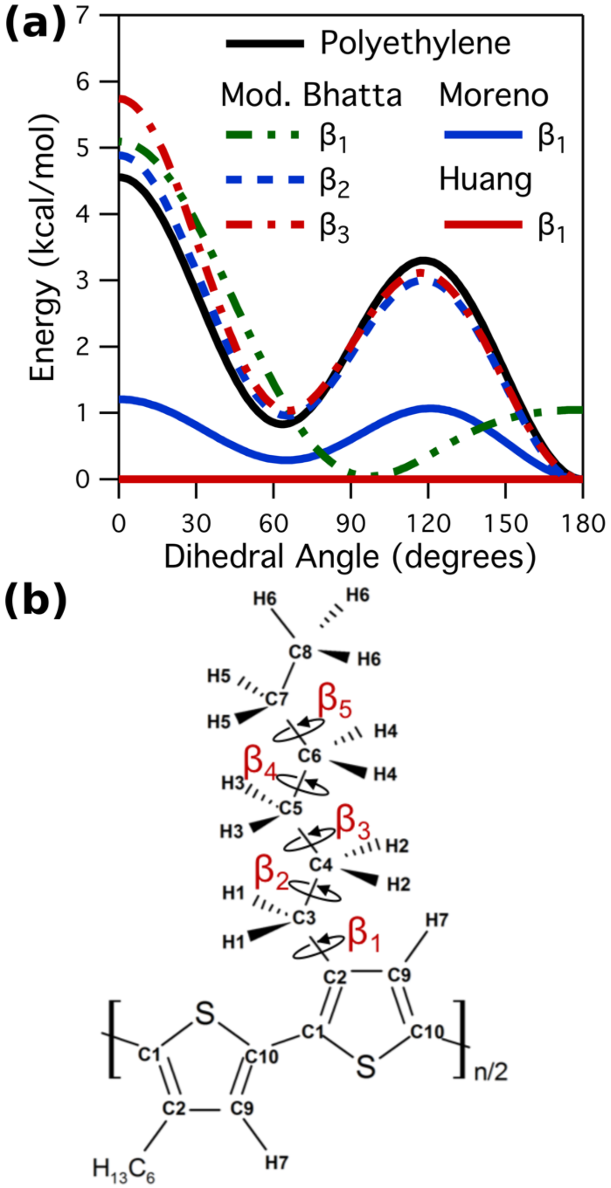

Figure 4.4. (a) Torsion potentials for the first three bonds in the side-chain for force fields developed by Bhatta and coworkers[19], Huang and coworkers[7], and Moreno and coworkers[20]. Dashed lines correspond to the re-calculation (this work) of the torsion potentials from Bhatta et al. For all side-chain torsion potentials other than the first (β_2 - β_5), the Huang FF and the Moreno FFs used the polyethylene torsion potential from OPLS-AA[32–34], represented by the black line. (b) Atomic structure and class labels for a P3HT dimer; β_1 - β_5 represent the torsion angles in the hexyl side chain.

Shown in Figure 4.5 are the dihedral potentials for the angle between thiophene rings along the backbone. There is a high energetic barrier at 90 degrees that encourages a planar conformation, either in the cis-conformation at 0 degrees or the trans-conformation at 180 degrees. The difference in energetic barrier as well as the energetic preference for a cis- or trans-conformation of the thiophene rings is a results of the different approaches utilized by the authors in parameterizing this potential. The work of Bhatta et al.[19] performed *ab-initio* calculations of a P3HT decamer at the B3LYP/6-31+G(d,p) level of theory. A combined MD and DFT approach was used to determine the potential for the Huang force field.[7] Finally, Moreno et al. performed their *ab-initio* calculations for quarterthiophene at the B3LYP/6-311G(d,p) level of theory.[20]

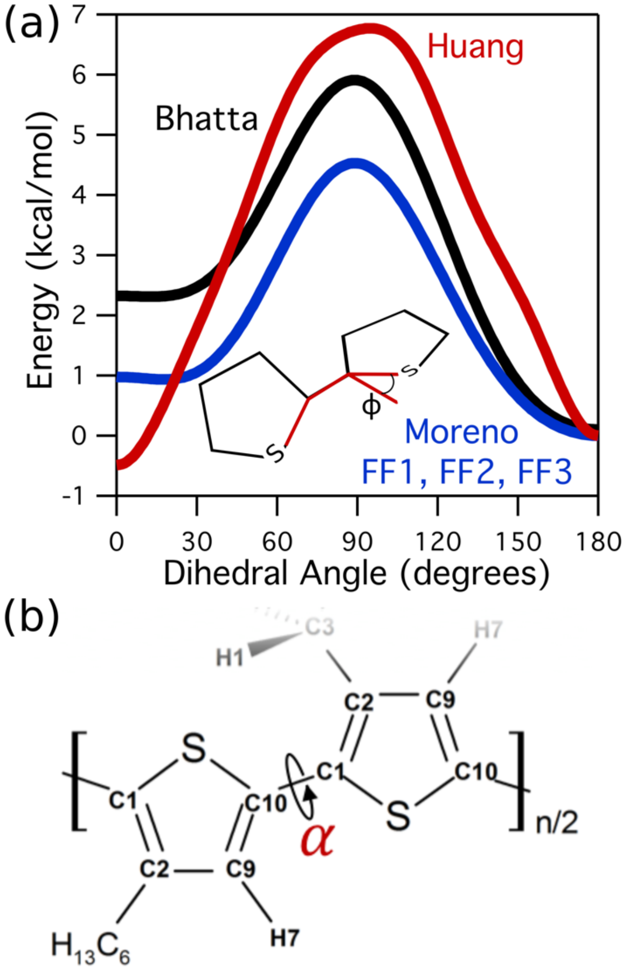

Figure 4.5. (a) Backbone torsion potentials for force fields developed by Bhatta and coworkers[19], Huang and coworkers[7], and Moreno and coworkers[20]. (b) Atomic structure and class labels along the backbone for a P3HT dimer; α represents the torsion angle between thiophene rings.

These researchers also implemented re-parameterization of the partial charges at different levels of theory, MP2/6-31+G(d,p) in Bhatta et al.[19], MP2/aug-cc-pVTZ in Huang et al.[7], and B3LYP/6-311G(d,p) in Moreno FF2.[20] The Moreno FF1 extracted partial charges from the OPLS force field directly, while Moreno FF3 utilized an averaging of partial charges between the FF1 and FF2 sets. All partial charges for these force fields are provided below in Table 4.3.

Table 4.3. Atomistic partial charges used for the thiophene rings and the first side-chain methyl group for force fields developed by Bhatta and coworkers[19], Huang and coworkers[7], and Moreno and coworkers[20]. Shaded rows indicate disagreement on the sign of the partial charge across the force fields.

Atom	Bhatta	Huang	Moreno FF1	Moreno FF2	Moreno FF3
S1	−0.2171	−0.1496	0.0180	−0.1200	−0.0510
C1	−0.0441	0.0748	−0.0090	0.0000	−0.0045
C2	0.0318	−0.1817	0.0000	−0.0300	−0.0150
C3	0.1278	0.0617	−0.1200	0.0300	−0.0450
C4	−0.0926	−0.1200	−0.1200	−0.1200	−0.1200
C5	0.0189	−0.1200	−0.1200	−0.1200	−0.1200
C6	0.0289	−0.1200	−0.1200	−0.1200	−0.1200
C7	−0.1396	−0.1200	−0.1200	−0.1200	−0.1200
C8	−0.0670	−0.1800	−0.1800	−0.1800	−0.1800
C9	−0.3128	−0.1817	−0.1150	−0.1800	−0.1475
C10	0.1762	0.0748	−0.0090	0. 0000	−0.0045
H1	0.0039	0.0600	0.0600	0.0600	0.0600
H2	0.0290	0.0600	0.0600	0.0600	0.0600
H3	0.0036	0.0600	0.0600	0.0600	0.0600
H4	0.0069	0.0600	0.0600	0.0600	0.0600
H5	0.0536	0.0600	0.0600	0.0600	0.0600
H6	0.0200	0.0600	0.0600	0.0600	0.0600
H7	0.2356	0.1817	0.1150	0.1800	0.1475

4.2.6 *Molecular Dynamics Trajectory Result Analysis*

As briefly mentioned above, the static and dynamic structure factors were used to compare results from MD simulations to the scattering data using the equations provided in Chapter 3. For mean squared displacement calculations, (eq. 3.11), a time scale of 1 ns with an averaging over the 1.5 ns production run was implemented. Density was determined with a time average using the following equation:

$$\rho = \langle \frac{1}{x_\tau y_\tau z_\tau} \sum_{\alpha=1}^{N} m_\alpha \rangle_{\tau_o} \tag{4.1}$$

where $\boldsymbol{N}$ is the total number of atoms, $\boldsymbol{m_\alpha}$ is the mass of atom $\boldsymbol{\alpha}$, and $\boldsymbol{x_\tau}$, $\boldsymbol{y_\tau}$ and $\boldsymbol{z_\tau}$ are the simulation box dimensions (volume) at a time step of $\boldsymbol{\tau_o}$.The dihedral autocorrelation function (DACF) tracked the twisting motions between P3HT monomers and was calculated using eq. 3.13 where 180° dihedral angle corresponds to a fully trans conformation of thiophene rings along the backbone. The mean squared relative displacement (not the net MSD) tracked distances between thiophene rings and was calculated with eq. 3.14 where thiophene pairs were determined by thiophene rings on different polymer chains or rings far away on the same chain to account for looping chains. Finally, the radial distribution function was calculated for the thiophene-thiophene distances in the simulation trajectories using eq. 3.15.

4.3 RESULTS & DISCUSSION

4.3.1 *Force Field Validation: X-Ray and Neutron Scattering, Density, and Glass Transition Temperature*

A collection of X-ray and neutron scattering data, together with metrics of density and glass transition temperature, were first used to evaluate the performance differences and validate the investigated force fields. Shown in Figure 4.6 are the WAXS results at varying temperatures compared to the static structure factor calculated from the simulated systems. The first broad peak at approximately 0.4 Å^{-1} and the second broad peak at approximately 1.4 Å^{-1} are indicative of lamellar and pi-stacking distance correlations in an amorphous system, respectively. All of the modeled systems were able to capture the location of these peaks well, meaning they are all able to capture the intermolecular structural correlations of P3HT. The first peak does present at a lower intensity relative to the second in the simulations as compared to the experimental results, but this is due to a limited simulation box size. Larger simulations would enable longer-range correlations and increase the peak at low-q. Unfortunately, these results indicate that WAXS alone is insufficient as a sole validation metric for these systems.

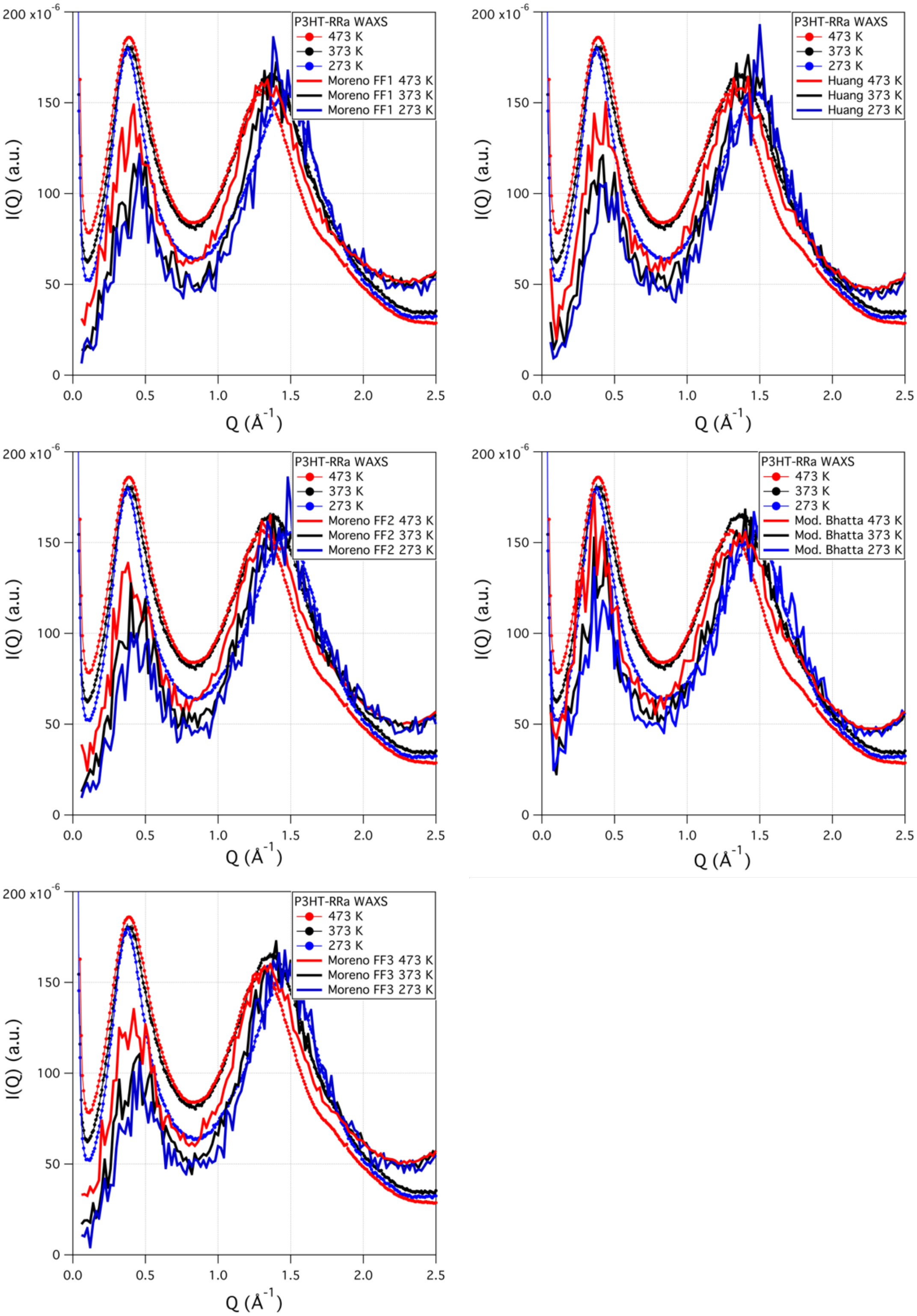

Figure 4.6. Experimental WAXS data at 273 K, 373 K, and 473 K for RRa-P3HT. Static structure factors were calculated from simulations using the Mod. Bhatta[19], Huang[7], and Moreno FF1, FF2, and FF3[20] force fields.

Shown in Figure 4.7 and Figure 4.8 are the QENS dynamics results at 273 K and 473 K, respectively, compared to the simulations results. At these temperatures and time scales, we are observing fluctuations along the chain's backbone as well as rotations and fluctuations along the alkyl side chain. With this metric, we now begin to see performance differences across the modeled systems. At 273 K, the Mod. Bhatta force field shows the largest deviation from experiments at the highest q-values which correspond to the shorter length scales in the system. At 473 K, we also observe further deviation from the experimental data across all models, especially at the longest time scales. The Moreno and Huang force fields begin to fail at the smaller q-values (longest time scales) while the Mod. Bhatta force field shows even more deviation across most ranges of time and length scales. A chi-squared, χ^2, value was determined for all of these systems to provide a more quantitative approach to comparing the performance of these models to the experimental QENS data. These are showed in Figure 4.9 and we find that the Huang and Moreno force fields perform better than the Mod. Bhatta force field across broader ranges of time and length scales.

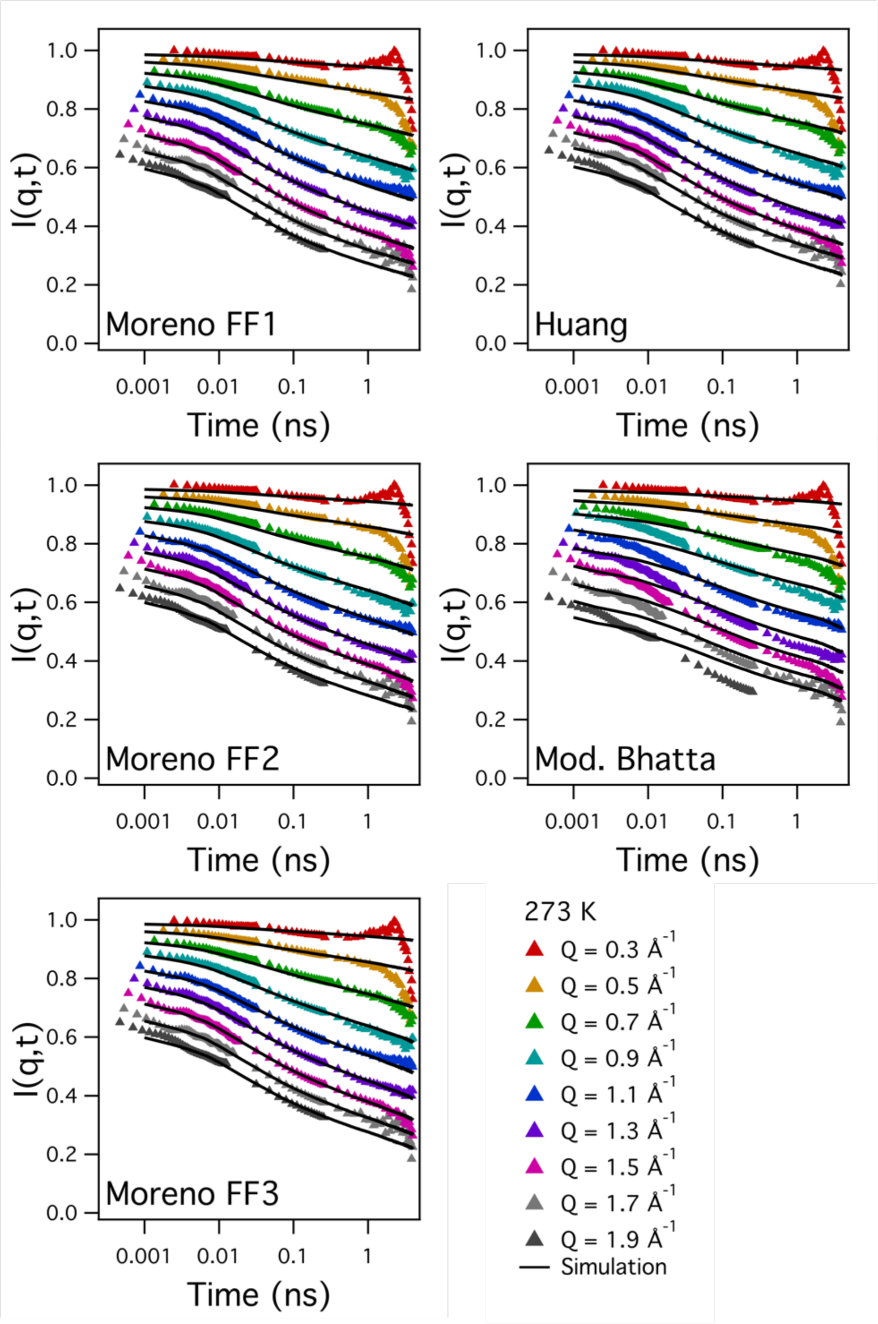

Figure 4.7. Experimental quasi-elastic neutron scattering data collected at 273 K for RRa-P3HT on the HFBS[25] and DCS[23] instruments at the NCNR and the BASIS[24] instrument at the SNS at ORNL. Dynamic structure factor results are calculated from simulations using the Mod. Bhatta[19], Huang[7], and Moreno FF1, FF2, and FF3[20] force fields.

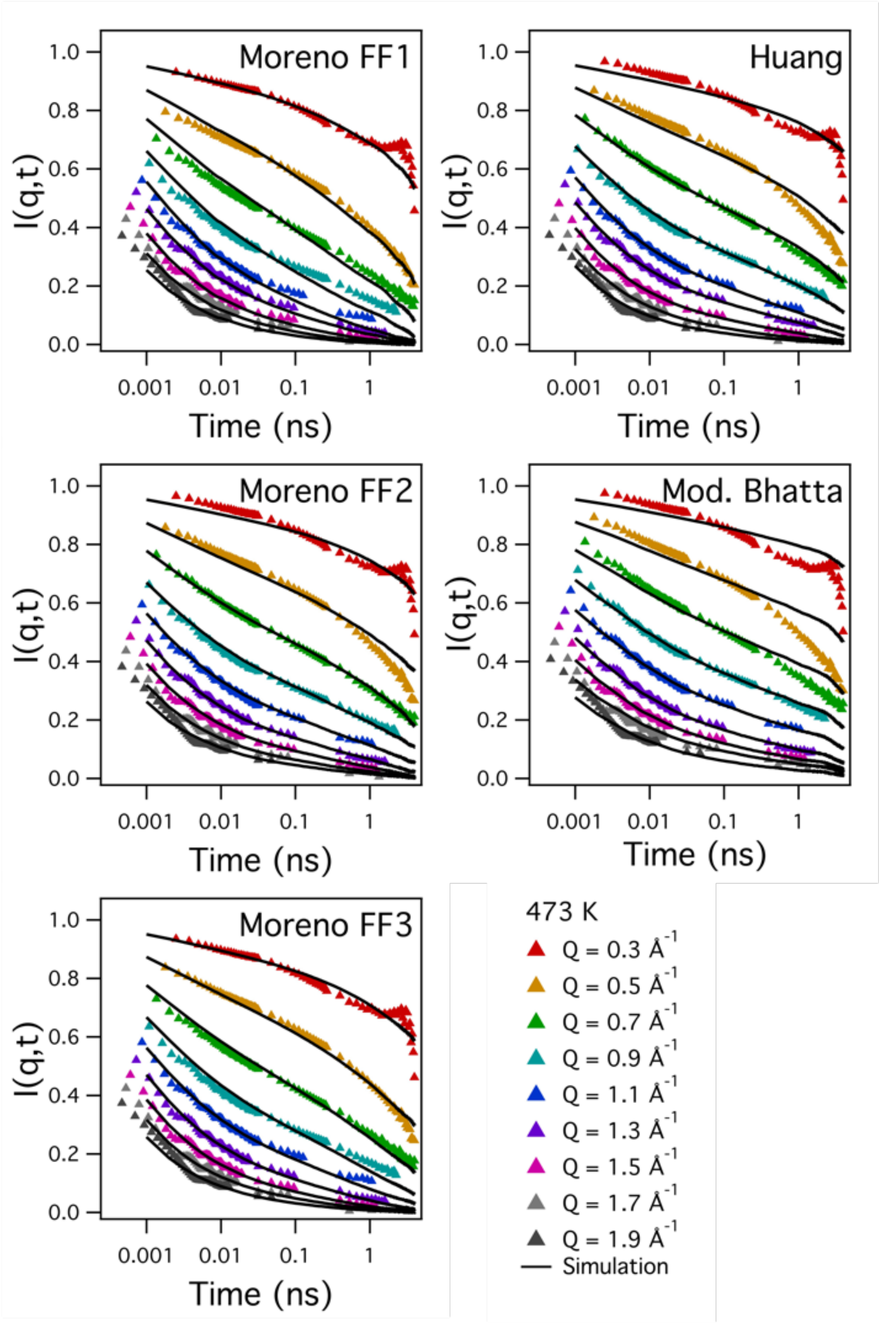

Figure 4.8. Experimental quasi-elastic neutron scattering data collected at 473 K for RRa-P3HT on the HFBS[25] and DCS[23] instruments at the NCNR and the BASIS[24] instrument at the SNS at ORNL. Dynamic structure factor results are calculated from simulations using the Mod. Bhatta[19], Huang[7], and Moreno FF1, FF2, and FF3[20] force fields.

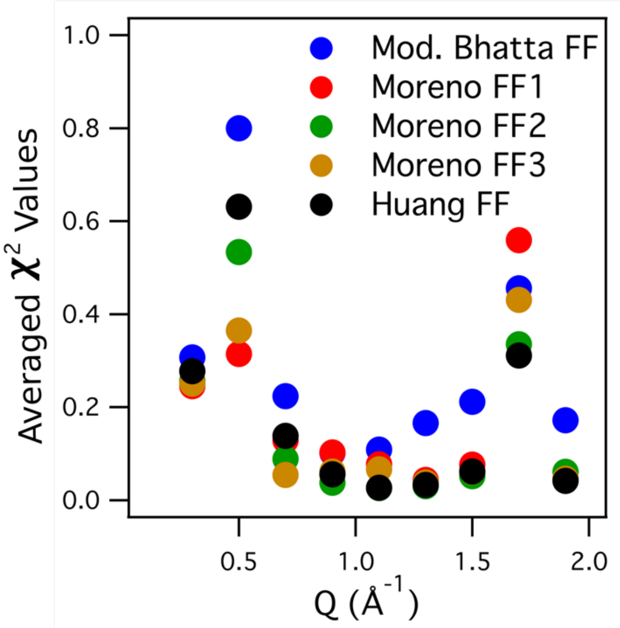

Figure 4.9. Average χ^2 values between experimental QENS data and simulation results (dynamic structure factor) using the Mod. Bhatta[19], Huang[7], and Moreno FF1, FF2, and FF3[20] force fields.

Shown in Figure 4.10 and Table 4.4 are the results comparing density and glass transition temperature in the experimental and theoretical systems. In all modeled systems, the density was significantly underestimated, especially for the Mod. Bhatta force field, however this system was able to capture the most accurate glass transition temperature. We do note that the Mod. Bhatta force field, however, did utilize the glass transition temperature as a validation metric during development of their force field.

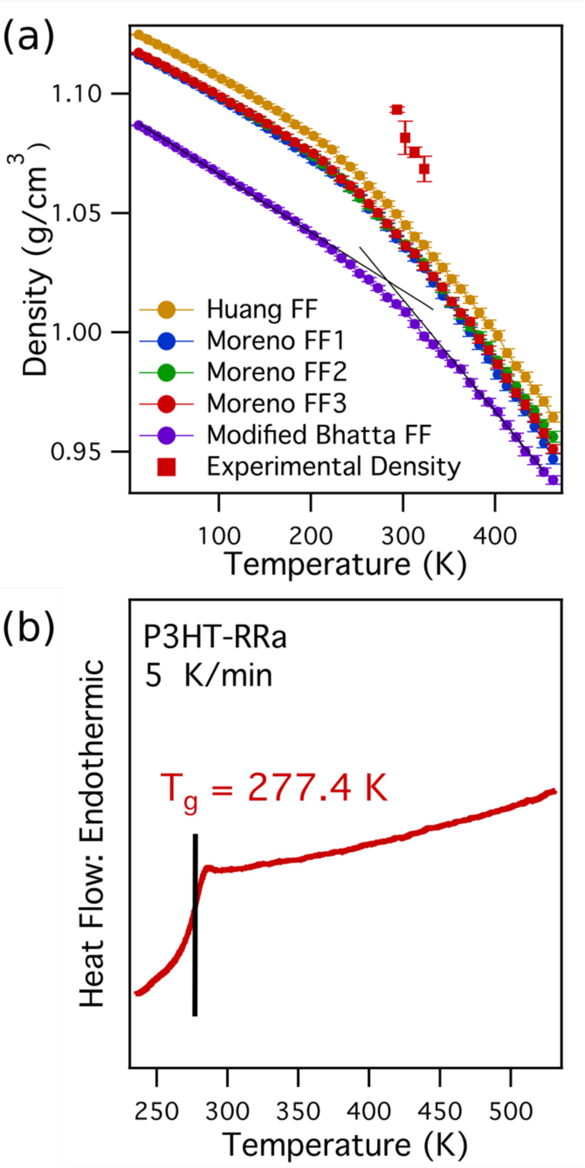

Figure 4.10. (a) Experimentally determined density of RRa-P3HT and simulated results for the Mod. Bhatta[19], Huang[7], and Moreno FF1, FF2, and FF3[20] force fields at various temperatures between 13 and 473 K. (b) Differential scanning calorimetry (DSC) data taken at a rate of 5 K/min for RRa-P3HT. Glass transition temperature is shown on the plot.

Table 4.4. Computationally determined glass transition temperature using the Mod. Bhatta[19], Huang[7], and Moreno FF1, FF2, and FF3[20] force fields. Percent errors are calculated by comparing to the experimental value of 277.4 K.

Force Field	**Mod. Bhatta**	**Huang**	**Moreno FF1**	**Moreno FF2**	**Moreno FF3**
Glass Transition Temperature (K)	283 ± 15	319 ± 15	254 ± 15	247 ± 15	252 ± 15
% Error to Experimental Value (277.4 K)	2.02%	15.0%	8.44%	11.0%	9.16%

4.3.2 *In-Silico Parameters Relevant for Charge Transport Mechanisms*

An advantage of simulations is that one can explore parameters *in-silico* that are not accessible by experiments alone. To further evaluate the effect of force field parameters on the modeled P3HT system, past work focused on features of the simulation that would directly affect charge transport mechanisms. This is especially important if molecular dynamics snapshots are to be used to study the electronic properties of these materials in the future.

Marcus theory is commonly used to describe the charge transfer rate, k_{ct}, which is directly proportional to the charge mobility in the material.[5] It can be defined with the following equation[5]:

$$k_{ct} = \frac{2\pi}{\hbar^2} I_t^2 \sqrt{\frac{1}{4\lambda\pi k_B T}}\, e^{-\frac{(\Delta G+\lambda)^2}{4\lambda k_B T}} \tag{4.2}$$

where I_t is the transfer integral, ΔG is the change in free energy, T is temperature, k_B is the Boltzmann constant, $\hbar$ is Planck's constant, and λ is the reorganization energy. Lan et al. applied this relationship to investigate changes in the transfer integral due to changes in either the distance between stacked thiophene rings (pi-orbital overlap) or the torsion between two thiophene rings (backbone conjugation) for P3HT.[5] These results of transfer integral versus thiophene-thiophene distance and torsion angle[5] are shown in Figure 4.11 with corresponding fits to the data. From these figures, it becomes clear how a closer arrangement of thiophene rings for inter-chain charge transfer and a completely planar and trans-conformation of thiophene rings along the backbone for intra-chain charge transfer are favored for charge mobility within the material.

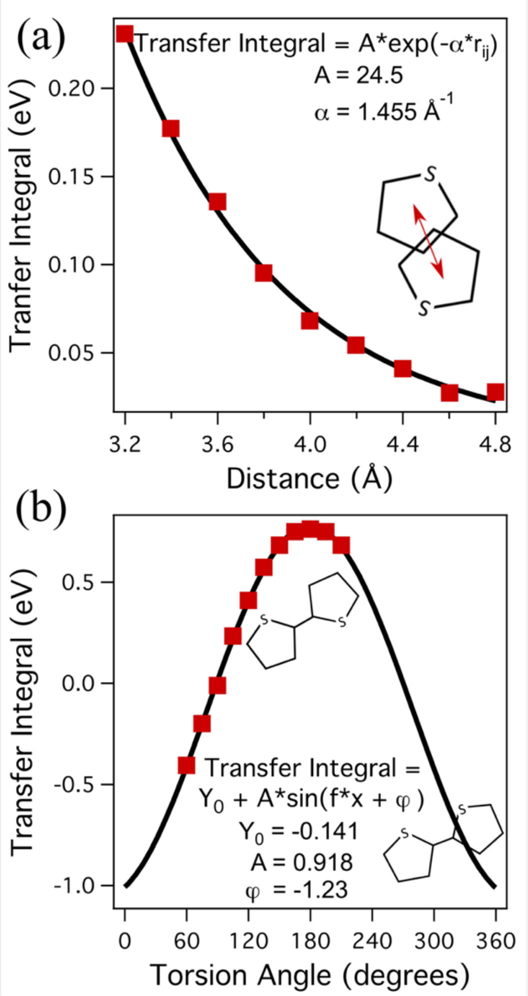

Figure 4.11. Transfer integral data versus distance between thiophene rings on neighboring chains (a) and versus dihedral angle between thiophene rings along the backbone (b) taken from the work of Lan et al.[5] Fits to the data are shown on the plot.

To evaluate what effect different force field parameters had on thiophene-thiophene distance and backbone dihedral angles from Figure 4.11, each of these parameters were investigated *in-silico.* Figure 4.12 shows the radial distribution function and the mean-squared relative displacement ($MSRD_{thio}$) of the distance between stacked thiophene rings on neighboring chains. The radial distribution function provides information about the preferential ordering of these rings within the system. While there are minimal differences in the thiophene-thiophene distance across force fields, the Moreno FF1 does show preference for a slightly closer arrangement. Considering the results shown in Figure 4.11, it can be reasonably assumed that the Moreno FF1 would give results of a higher charge transfer integral. The $MSRD_{thio}$ gives an indication of the relative motions of thiophene rings in the system. Again, by referencing Figure 4.11, these fluctuations can be expected to have a direct impact on the charge integral. The Moreno FF1, while preferring a closer arrangement, does show the most motion of thiophene pairs within the material. This is in contrast to the Mod. Bhatta force field, which shows the least amount of movement. The Moreno FF1, FF2 and FF3 show significantly different results in the $MSRD_{thio}$, but interestingly, their only differences in parameters are in the atomic partial charges (Figure 4.5 and Table 4.3). Therefore, atomic partial charges are expected to take part in affecting the stacked thiophene-thiophene interactions.

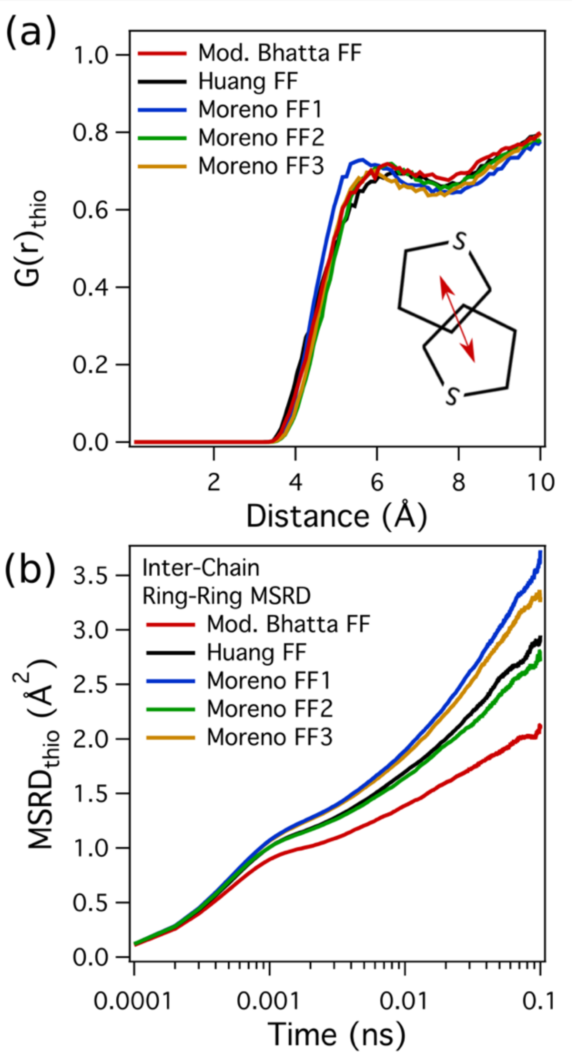

Figure 4.12. (a) Radial distribution function and (b) the mean-squared relative displacement (MSRD$_{thio}$) of the thiophene-thiophene inter-chain distance for simulations of RRa-P3HT using the Mod. Bhatta[19], Huang[7], and Moreno FF1, FF2, and FF3[20] force fields.

Figure 4.13 shows the torsion population and autocorrelation function for the dihedral angle between neighboring monomers along the backbone. The torsion populations demonstrate that the Huang force field is the only one to strictly enforce a more planar backbone configuration at 0 and 180˚ while the other force fields have distributions focused at slightly offset angles of 30 and 150˚. This is a result of the high energetic barrier in the torsion potential at 90˚ for the Huang force field compared to the others, as shown in Figure 4.5, that forces more dihedrals into a fully planar conformation. Additionally, preferences for a cis or trans conformations of the thiophene rings become apparent across different force fields. While the Huang, Mod. Bhatta, and Moreno FF2 force field give preference to a trans conformation, the others give preference to the cis conformation. This is especially interesting when again considering the three Moreno force fields. The torsion potential is identical across all three, and only atomic partial charges are changed among them. Therefore, these results indicate that not only do the torsion potentials have an impact on the backbone structure, but the partial charges do as well. The autocorrelation function provides information about the fluctuations in these dihedral conformations. Two main groupings of the force fields become apparent. One group, made up of the three Moreno force fields, demonstrates more twisting and motions along the backbone. This is not completely unexpected as the energy barrier in the Moreno torsion potential (Figure 4.5) is the lowest among all force fields. However, these results again show the effect of partial charges, as the three Moreno force field dihedral autocorrelation functions begin to deviate at longer time scales. When looking at these results through the lens of Marcus theory and Figure 4.11, the choice of force field becomes an important decision for evaluating inter-chain charge transfer of the material. The Huang force field is expected to give results with higher transfer integrals as more dihedrals are present in fully planar configurations with minimal motions. The Moreno force fields are expected to give lower transfer integral values due to the higher amount of backbone fluctuations that would make and break the conjugation. Moreover, the Moreno FF2 is expected to favor charge transfer (compared to Moreno FF1 and FF3) as more trans- than cis-configurations of the thiophene rings are present in the torsion populations.

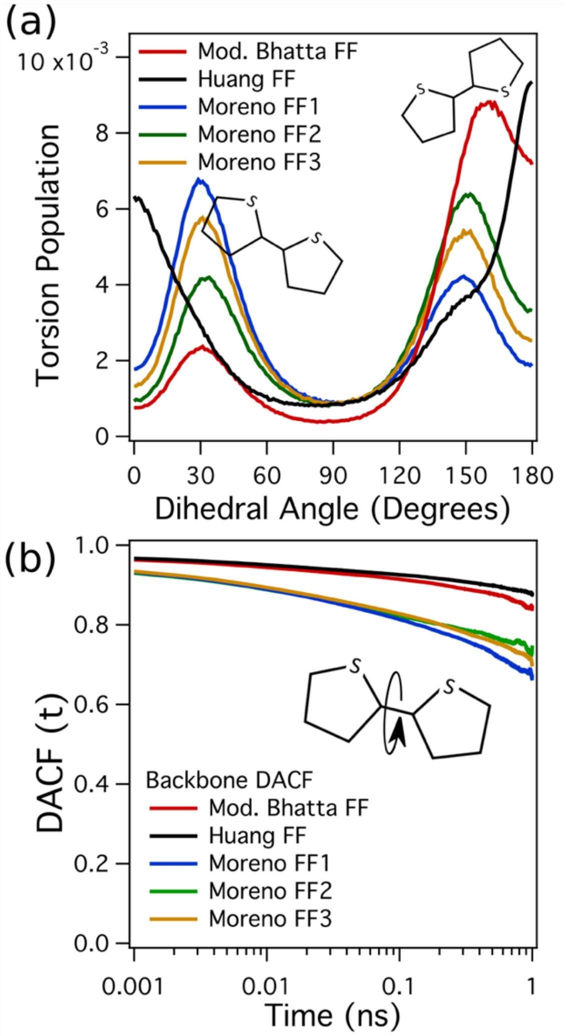

Figure 4.13. (a) Torsion population and (b) dihedral autocorrelation function of the thiophene-thiophene intra-chain dihedral angle for simulations of RRA-P3HT using the Mod. Bhatta[19], Huang[7], and Moreno FF1, FF2, and FF3[20] force fields.

4.3.3 *Deconvolution of P3HT Backbone and Side-Chain Dynamics*

Up until now, all results have been representative of the entire system, which includes contributions of both backbone and side chain motions within the material. Due to the high scattering cross section of hydrogen, the side chains would have contributed to 91% of the QENS signal. Therefore, we utilized fully hydrogenated (P3HT-H14) and partially deuterated (P3HT-

D13) versions of regio-random P3HT to separate the contribution of the backbone motions. By replacing all hydrogens on the side chain with deuterium, while simultaneously leaving one hydrogen connected to the thiophene ring on the backbone, the side chain contribution is lowered from 91% to only 56% of the QENS signal.

Experimentally determined net MSD for P3HT-H14 and P3HT-D13, determined from fixed window scans, are shown in Figure 4.14. The P3HT-H14 sample showed significant system motion almost immediately after it began warming up from 50 K, indicative of the faster side chain motions relaxing at the lower temperatures. However, the deuterated sample showed minimal motion until after 400 K when the slower backbone motions were finally activated. Simulated MSD results were determined for the Huang, Mod. Bhatta, and Moreno FF2 force fields, and are also provided in the remaining subplots of Figure 4.14. Although the general shape across the temperature range was captured by the modelled systems, motions were significantly overestimated for all force fields. We can reason that the low densities in the simulations are connected to the wider ranges of motion allowed in these systems. However, the Mod. Bhatta force field did present the lowest MSD as well as the lowest density, indicating that the underlying complex interactions of the system that stem from a variety of force field parameters. Additionally, none of the force fields were able to capture the significant difference between hydrogenated and deuterated systems, meaning that the systems are not accurately capturing the individual motions of backbone and side chain structural regimes. The Moreno, Mod. Bhatta, and Huang force fields were all re-parameterized with different quantum methods and procedures, and utilized significantly different parameters of backbone and side chain torsion and atomic partial charges. While some of the bulk dynamics were captured reasonably well, as shown by comparisons to standard QENS dynamics data, these latest results emphasize the need for improved modeling methods to accurately capture the important backbone motions with critical roles in charge transport mechanisms of these materials.

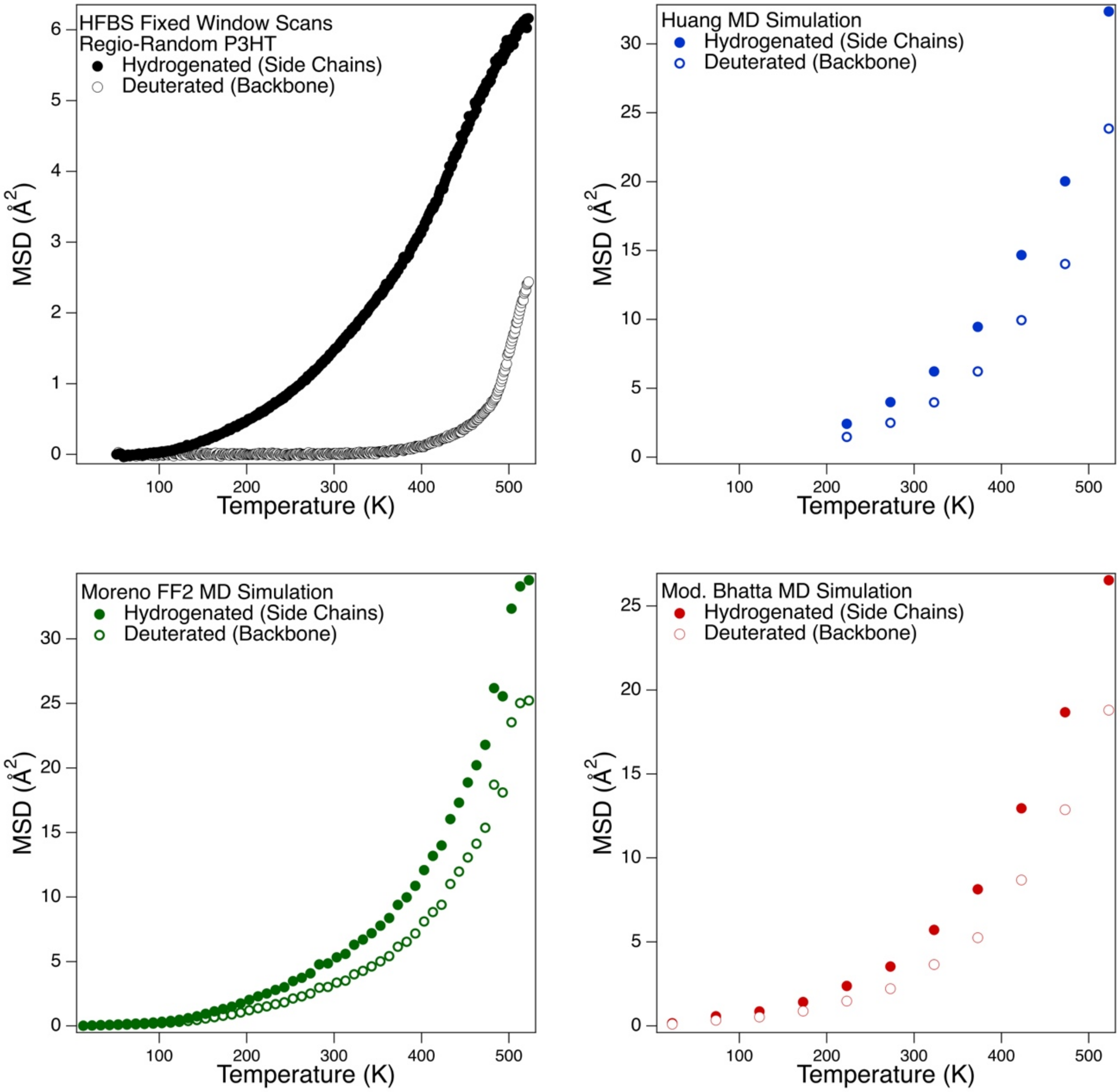

Figure 4.14. Mean squared displacement of fully hydrogenated and partially deuterated (side-chain only) regio-random P3HT calculated from fixed window scans captured on the HFBS[25] instrument at the NCNR. Also shown are calculated net MSD from simulations using the Moreno et al. (FF2 only)[20], Huang et al.[7] and Mod. Bhatta et al. [19] force fields.

4.3.4 *Application of Moreno FF2 Models to P3DDT*

To assess the transferability of these models to other polythiophenes, we performed simulations of P3DDT using the Moreno FF2 force field as it performed well overall at capturing the characteristic dynamic and structural characteristics captured with QENS and WAXS experiments. Shown in Figure 4.15 are experimental WAXS, neutron diffraction, and QENS results for P3DDT compared to the corresponding simulation results. The structure of the simulated system is captured reasonably well, with only a minor disagreement in the second peak representing of pi-stacking correlations in the system shown in the WAXS results. The structural correlations in the material are captured reasonably well when considering the neutron diffraction and WAXS data, with some slight disagreement in the pi-stacking peak in the X-ray data. The simulated system slightly underestimates this distance (shift to higher-q). However, when comparing the QENS results with the modeled system, we find that the Moreno FF2 is only able to capture the dynamics well at shorter time scales. This is comparable to the P3HT results where the slower dynamics were more difficult to capture with MD simulations. Overall, these results show that these models are not easily transferable between materials, even similar ones such as P3HT and P3DDT, and call for careful parameterization of these force fields.

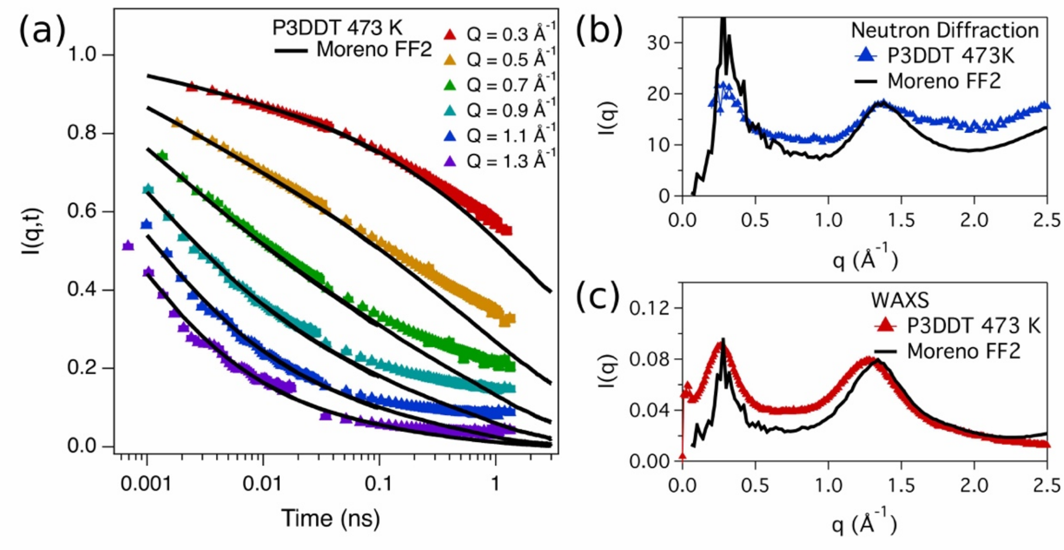

Figure 4.15. Quasi-elastic neutron scattering results (a) compared to calculated dynamic structure factor molecular dynamics simulations of P3DDT using Moreno FF2[20]. Also provided are neutron diffraction (b) and wide-angle x-ray scattering (c) results compared to the calculated static structure factor from the same system.

4.4 CONCLUSIONS

In this work, we have provided a critical assessment of three published force fields, Moreno et al.[20] (FF1, FF2, and FF3), Huang et al.[7], and Bhatta et al.[19] for amorphous P3HT. All models were able to capture the structural features shown in experimental WAXS data well. However, only the Huang and Moreno force fields were able to capture the dynamics shown in experimental QENS data across a wide range of temperatures, scattering vectors, and time scales. The Mod. Bhatta deviated from the system dynamics at longer time and length scales specifically. We found the although all systems underestimated the experimental density, the Huang force field was the closest. Moreover, the Mod. Bhatta force field reproduced the most accurate glass transition temperature.

Conformation and fluctuations along the backbone dihedrals between monomers and thiophene-thiophene distances were used to explore the effect of force field parameters on these *in-silico* properties relevant to charge transport mechanisms in the material. Differences in the dihedral potentials resulted in a more planar backbone conformation in the Huang force field simulations, while there was a slightly offset configuration at 30 and 150 degrees in the Moreno and Mod. Bhatta systems. Interestingly, the Moreno force fields also showed differences in a preference for cis- or trans-conformations between thiophene rings, despite having identical torsion potentials. We observe similar effects in the dihedral autocorrelation function and observe difference in the dynamics across all force fields, including the three variants of the Moreno system. Similar differences in the thiophene-thiophene differences also emphasize the effects of not only torsion potential but also the partial charges on the *in-silico* structure and dynamics of these models.

We also explored the different motions present in the backbone and side chain regimes of the polymer by using hydrogenated and partially deuterated samples of P3HT. We were able to experimentally capture the slower backbone motions that relax at much higher temperatures compared to the quicker side chain motions that relax at lower temperatures. However, the modeled systems significantly overestimated the dynamics of the material, and the contrast between the backbone and side chain motions was not well-captured. Accurately capturing the backbone motions of the material is critical if the MD trajectory results are used evaluate electronic performance. Even for a well-studied, model conjugated polymer, P3HT, the currently available force fields for conjugated materials are unable to accurately or consistently capture the dynamics relevant to charge transport mechanisms within the material.

Finally, we applied the Moreno FF2 force field to a P3DDT system to test the transferability of these parameters. The modeled system was able to capture the structure reasonably well, as with P3HT, but failed to capture the dynamics present in QENS results at longer time scales and higher scattering vectors. This is again indicative of the model's ability to capture the side chain motions while failing to capture the slower backbone fluctuations accurately. These backbone motions are particularly important as they directly impact charge transport calculations within the system, and conclude that force fields for conjugated polymers cannot be easily generalized.

4.5 REFERENCES

(1) Newbloom, G. M.; Hoffmann, S. M.; West, A. F.; Gile, M. C.; Sista, P.; Cheung, H. K. C.; Luscombe, C. K.; Pfaendtner, J.; Pozzo, L. D. *Solvatochromism and Conformational Changes in Fully Dissolved Poly(3-Alkylthiophene)S*. *Langmuir* **2015**, *31* (1), 458–468. https://doi.org/10.1021/la503666x.

(2) Mei, J.; Bao, Z. *Side Chain Engineering in Solution-Processable Conjugated Polymers*. *Chem. Mater.* **2014**, *26* (1), 604–615. https://doi.org/10.1021/cm4020805.

(3) Lan, Y.; Huang, C.-I. *Charge Mobility and Transport Behavior in the Ordered and Disordered States of the Regioregular Poly(3-Hexylthiophene)*. *J. Phys. Chem. B* **2009**, *113* (44), 14555–14564. https://doi.org/10.1021/jp904841j.

(4) Chang, M.; Lim, G.; Park, B.; Reichmanis, E. *Control of Molecular Ordering, Alignment, and Charge Transport in Solution-Processed Conjugated Polymer Thin Films*. *Polymers (Basel).* **2017**, *9* (12), 212. https://doi.org/10.3390/polym9060212.

(5) Lan, Y.-K.; Huang, C.-I. *A Theoretical Study of the Charge Transfer Behavior of the Highly Regioregular Poly-3-Hexylthiophene in the Ordered State*. *J. Phys. Chem. B* **2008**, *112* (47), 14857–14862. https://doi.org/10.1021/jp806967x.

(6) McMahon, D. P.; Cheung, D. L.; Goris, L.; Dacuña, J.; Salleo, A.; Troisi, A. *Relation between Microstructure and Charge Transport in Polymers of Different Regioregularity*. *J. Phys. Chem. C* **2011**, *115* (39), 19386–19393. https://doi.org/10.1021/jp207026s.

(7) Schwarz, K. N.; Kee, T. W.; Huang, D. M. *Coarse-Grained Simulations of the Solution-Phase Self-Assembly of Poly(3-Hexylthiophene) Nanostructures*. *Nanoscale* **2013**, *5* (5), 2017. https://doi.org/10.1039/c3nr33324h.

(8) Jones, M. L.; Huang, D. M.; Chakrabarti, B.; Groves, C. *Relating Molecular Morphology to Charge Mobility in Semicrystalline Conjugated Polymers*. *J. Phys. Chem. C* **2016**, *120* (8), 4240–4250. https://doi.org/10.1021/acs.jpcc.5b11511.

(9) Gu, K.; Snyder, C. R.; Onorato, J.; Luscombe, C. K.; Bosse, A. W.; Loo, Y.-L. *Assessing the Huang–Brown Description of Tie Chains for Charge Transport in Conjugated Polymers*. *ACS Macro Lett.* **2018**, *7* (11), 1333–1338. https://doi.org/10.1021/acsmacrolett.8b00626.

(10) Chaudhari, S. R.; Griffin, J. M.; Broch, K.; Lesage, A.; Lemaur, V.; Dudenko, D.; Olivier, Y.; Sirringhaus, H.; Emsley, L.; Grey, C. P. *Donor–Acceptor Stacking Arrangements in Bulk and Thin-Film High-Mobility Conjugated Polymers Characterized Using Molecular Modelling and MAS and Surface-Enhanced Solid-State NMR Spectroscopy*. *Chem. Sci.* **2017**, *8* (4), 3126–3136. https://doi.org/10.1039/C7SC00053G.

(11) Mo, Z.; Lee, K. B.; Moon, Y. B.; Kobayashi, M.; Heeger, A. J.; Wudl, F. *X-Ray Scattering from Poly(Thiophene): Crystallinity and Crystallographic Structure*.

Macromolecules **1985**, *18* (10), 1972–1977. https://doi.org/10.1021/ma00152a028.

(12) Parnell, A. J.; Cadby, A. J.; Mykhaylyk, O. O.; Dunbar, A. D. F.; Hopkinson, P. E.; Donald, A. M.; Jones, R. A. L. *Nanoscale Phase Separation of P3HT PCBM Thick Films As Measured by Small-Angle X-Ray Scattering*. *Macromolecules* **2011**, *44* (16), 6503–6508. https://doi.org/10.1021/ma2007706.

(13) McCulloch, I.; Heeney, M.; Bailey, C.; Genevicius, K.; Macdonald, I.; Shkunov, M.; Sparrowe, D.; Tierney, S.; Wagner, R.; Zhang, W.; Chabinyc, M. L.; Kline, R. J.; McGehee, M. D.; Toney, M. F. *Liquid-Crystalline Semiconducting Polymers with High Charge-Carrier Mobility*. **2006**, *5* (April).

(14) Chabinyc, M. L.; Toney, M. F.; Kline, R. J.; McCulloch, I.; Heeney, M. *X-Ray Scattering Study of Thin Films of Poly(2,5-Bis(3-Alkylthiophen-2-Yl)Thieno[3,2- b]Thiophene)*. *J. Am. Chem. Soc.* **2007**, *129* (11), 3226–3237. https://doi.org/10.1021/ja0670714.

(15) Obrzut, J.; Page, K. A. *Electrical Conductivity and Relaxation in Poly(3-Hexylthiophene)*. *Phys. Rev. B* **2009**, *80* (19), 195211. https://doi.org/10.1103/PhysRevB.80.195211.

(16) Guilbert, A. A. Y.; Zbiri, M.; Jenart, M. V. C.; Nielsen, C. B.; Nelson, J. *New Insights into the Molecular Dynamics of P3HT:PCBM Bulk Heterojunction: A Time-of-Flight Quasi-Elastic Neutron Scattering Study*. *J. Phys. Chem. Lett.* **2016**, *7* (12), 2252–2257. https://doi.org/10.1021/acs.jpclett.6b00537.

(17) Arbe, A.; Alvarez, F.; Colmenero, J. *Neutron Scattering and Molecular Dynamics Simulations: Synergetic Tools to Unravel Structure and Dynamics in Polymers*. *Soft Matter* **2012**, *8* (32), 8257. https://doi.org/10.1039/c2sm26061a.

(18) Boldon, L.; Laliberte, F.; Liu, L. *Review of the Fundamental Theories behind Small Angle X-Ray Scattering, Molecular Dynamics Simulations, and Relevant Integrated Application*. *Nano Rev.* **2015**, *6* (1), 25661. https://doi.org/10.3402/nano.v6.25661.

(19) Bhatta, R. S.; Yimer, Y. Y.; Perry, D. S.; Tsige, M. *Improved Force Field for Molecular Modeling of Poly(3-Hexylthiophene)*. *J. Phys. Chem. B* **2013**, *117* (34), 10035–10045. https://doi.org/10.1021/jp404629a.

(20) Moreno, M.; Casalegno, M.; Raos, G.; Meille, S. V.; Po, R. *Molecular Modeling of Crystalline Alkylthiophene Oligomers and Polymers*. *J. Phys. Chem. B* **2010**, *114* (4), 1591–1602. https://doi.org/10.1021/jp9106124.

(21) Wolf, C. M.; Kanekal, K. H.; Yimer, Y. Y.; Tyagi, M.; Omar-Diallo, S.; Pakhnyuk, V.; Luscombe, C. K.; Pfaendtner, J.; Pozzo, L. D. *Assessment of Molecular Dynamics Simulations for Amorphous Poly(3-Hexylthiophene) Using Neutron and X-Ray Scattering Experiments*. *Soft Matter* **2019**, *15* (25), 5067–5083. https://doi.org/10.1039/C9SM00807A.

(22) Liu, J.; Loewe, R. S.; McCullough, R. D. *Employing MALDI-MS on Poly(Alkylthiophenes): Analysis of Molecular Weights, Molecular Weight Distributions,*

End-Group Structures, and End-Group Modifications. *Macromolecules* **1999**, *32* (18), 5777–5785. https://doi.org/10.1021/ma9905324.

(23) Copley, J. R. D.; Cook, J. C. *The Disk Chopper Spectrometer at NIST: A New Instrument for Quasielastic Neutron Scattering Studies*. *Chem. Phys.* **2003**, *292* (2–3), 477–485. https://doi.org/10.1016/S0301-0104(03)00124-1.

(24) Mamontov, E.; Herwig, K. W. *A Time-of-Flight Backscattering Spectrometer at the Spallation Neutron Source, BASIS*. *Rev. Sci. Instrum.* **2011**, *82* (8), 085109. https://doi.org/10.1063/1.3626214.

(25) Meyer, A.; Dimeo, R. M.; Gehring, P. M.; Neumann, D. A. *The High-Flux Backscattering Spectrometer at the NIST Center for Neutron Research*. *Rev. Sci. Instrum.* **2003**, *74* (5), 2759–2777. https://doi.org/10.1063/1.1568557.

(26) Azuah, R. T.; Kneller, L. R.; Qiu, Y.; Tregenna-Piggott, P. L. W.; Brown, C. M.; Copley, J. R. D.; Dimeo, R. M. *DAVE: A Comprehensive Software Suite for the Reduction, Visualization, and Analysis of Low Energy Neutron Spectroscopic Data*. *J. Res. Natl. Inst. Stand. Technol.* **2009**, *114* (6), 341. https://doi.org/10.6028/jres.114.025.

(27) Arnold, O.; Bilheux, J. C.; Borreguero, J. M.; Buts, A.; Campbell, S. I.; Chapon, L.; Doucet, M.; Draper, N.; Ferraz Leal, R.; Gigg, M. A.; Lynch, V. E.; Markvardsen, A.; Mikkelson, D. J.; Mikkelson, R. L.; Miller, R.; Palmen, K.; Parker, P.; Passos, G.; Perring, T. G.; Peterson, P. F.; Ren, S.; Reuter, M. A.; Savici, A. T.; Taylor, J. W.; Taylor, R. J.; Tolchenov, R.; Zhou, W.; Zikovsky, J. *Mantid - Data Analysis and Visualization Package for Neutron Scattering and μ SR Experiments*. *Nucl. Instruments Methods Phys. Res. Sect. A Accel. Spectrometers, Detect. Assoc. Equip.* **2014**, *764*, 156–166. https://doi.org/10.1016/j.nima.2014.07.029.

(28) Plimpton, S. *Fast Parallel Algorithms for Short-Range Molecular Dynamics*. *J. Comput. Phys.* **1995**, *117* (1), 1–19, http://lammps.sandia.gov. https://doi.org/10.1006/jcph.1995.1039.

(29) Chen, T. A.; Rieke, R. D. *The First Regioregular Head-to-Tail Poly(3-Hexylthiophene-2,5-Diyl) and a Regiorandom Isopolymer: Nickel versus Palladium Catalysis of 2(5)-Bromo-5(2)-(Bromozincio)-3-Hexylthiophene Polymerization*. *J. Am. Chem. Soc.* **1992**, *114* (25), 10087–10088. https://doi.org/10.1021/ja00051a066.

(30) Hockney, R. W.; Eastwood, J. W. *Computer Simulation Using Particles*, 1st ed.; Bristol: Adam Hilger, 1988.

(31) T., R.; K., M.; K., H.; Kneller, G. R. *NMoldyn : A Program Package for a Neutron Scattering*. *J. Comput. Chem.* **2003**, *24* (5), 657–667. https://doi.org/10.1002/jcc.10243.

(32) Jorgensen, W. L.; Tirado-Rives, J. *Potential Energy Functions for Atomic-Level Simulations of Water and Organic and Biomolecular Systems*. *Proc. Natl. Acad. Sci.* **2005**, *102* (19), 6665–6670. https://doi.org/10.1073/pnas.0408037102.

(33) Jorgensen, W. L.; McDonald, N. A. *Development of an All-Atom Force Field for Heterocycles. Properties of Liquid Pyridine and Diazenes*. *J. Mol. Struct. THEOCHEM* **1998**, *424* (1–2), 145–155. https://doi.org/10.1016/S0166-1280(97)00237-6.

(34) Jorgensen, W. L.; Maxwell, D. S.; Tirado-Rives, J. *Development and Testing of the OPLS All-Atom Force Field on Conformational Energetics and Properties of Organic Liquids*. *J. Am. Chem. Soc.* **1996**, *118* (45), 11225–11236. https://doi.org/10.1021/ja9621760.

Chapter 5. INTERMOLECULAR INTERACTIONS AND CHAIN DYNAMICS IN POLY(3-HEXYLTHIOPHENE) FROM NEUTRON SCATTERING AND DENSITY FUNCTIONAL THEORY

The author would like to acknowledge the contributions of our collaborators Viktoria Pakhnyuk, Lorenzo Guio, and Christine Luscombe to this work. Additionally, the work presented here is only provided in a preliminary state, but discussion of ongoing and future work is included.

5.1 INTRODUCTION

In the last chapter, we discussed the limitations of five molecular dynamics (MD) force fields proposed in the literature (Mod. Bhatta[1], Huang[2], and Moreno FF1, FF2 and FF3[3]) for a model conjugated polymer, poly(3-hexylthiophene) (P3HT). Researchers built upon the classical OPLS[4] force field, making modifications to the atomic partial charges, dihedral potential between backbone thiophene rings, and the dihedral potential between the side chain and backbone to account for the effects of conjugation on the chain dynamics. However, we saw how variations in these parameters across force fields affected fluctuations of thiophene-thiophene distances and twisting along the backbone, both parameters that would significantly influence any *in-silico* calculations of charge transport mechanisms in the material. The simulated systems did capture the overall system dynamics well when compared with quasi-elastic neutron scattering (QENS) dynamics measurements, but these signals were dominated by the signal from the alkyl side chains, which we would expect the simulations to recreate reasonably well. However, when comparing backbone and side-chain dynamics to results from QENS elastic scans for hydrogenated (dominated by side-chain motions) and partially deuterated (dominated by backbone motions)

P3HT, we found that the simulated materials failed to capture characteristic motions of the backbone, again, a behavior that would significantly affect any charge transport mechanisms in the material. In response to these force field limitations, we started considering other classical force field parameters may be affected by the π-conjugation in the material, including the non-bonded interaction parameters of the Lennard-Jones potential.

Many of the MD force fields for conjugated polymers utilize classical Lennard-Jones parameters. In the Moreno[3], Huang[2], and Bhatta[1] force fields investigated in our previous work[5], Lennard-Jones parameters were taken from the OPLS force field[6] parameters for small molecules of thiophene and benzene. There have been only a handful of examples in the literature where researchers reconsidered the Lennard-Jones parameters for CPs. For example, DuBay et al. were cautious of overestimating the repulsive force at the shorter intermolecular distances for conjugated systems that could have slightly closer conformations.[7] They utilized a buffered 14/7 version, rather than the standard 12/6 form, which was similar to the standard parameters apart from the slightly lower repulsive force at short distances. Marcon and coworkers were motivated by their expectation of more polarizable systems with stronger dispersion forces in the conjugated materials, as well as an underestimated density by almost 10% in their simulated system of crystalline oligothiophenes. In response, they utilized a Buckingham potential with modified carbon parameters that increased the depth of the attractive well by 39%.[8]

Israelachvili begins a discussion of intermolecular behavior by stating, "…electromagnetic forces – the source of all intermolecular interactions – determine the properties of solids, liquids, and gases," in their book titled *Intermolecular and Surface Forces*.[9] The book provides an in-depth review of all forms of these interactions with either electrostatic or quantum mechanical origins. There are strong intermolecular forces with electrostatic origins, including many of the different atomic bonds as well as Coulombic forces or charge-charge interactions. Electrostatic behavior also results in the polarization of molecules, including the interactions between atoms, ions, nonpolar and uncharged molecules, and the introduction of dipole/induced-dipole interactions. This then extends into interactions between polar molecules, such as hydrogen bonds, ion-dipole forces or dipole/dipole interactions. From the quantum mechanical origins, there are London or dispersion forces, which are induced-dipole/induced-dipole interactions that originate from the motion of electrons. Together, London/dispersion forces, dipole/dipole and dipole/induced-dipole interactions make up the van der Waals forces. Finally, they note the steric repulsion forces that originate due to the electron clouds. Together, the van der Waals forces and steric repulsion make up the components to the well-known Lennard-Jones or other pair potentials used to capture the combined resulting attraction and repulsion between atoms and molecules.[9] Marcon and coworkers already pointed out the effect of electron delocalization in conjugated materials that would lead to more polarizability and therefore, stronger dispersion forces.[8] In as early as 1951, Davies et al. took a theoretical approach to understanding polarizability in long π-conjugated chains (polyacetylene) and found a power law dependence with molecular weight that relied on the ability of electrons to travel along the chain (electron delocalization). In a more recent study, Schmit and Levine proposed the existence of an additional binding force between polyacetylene chains that was a result of electronic tunneling between approaching molecules.[10]

From the perspective of electronic performance in these materials, electron delocalization is what enables charge transport mechanisms to occur, either along the π-conjugated backbone (intra-chain charge transfer) or through the π-orbital overlap of nearby chains (inter-chain charge transfer). For example, we consider the active layer in a common organic photovoltaic (OPV) device of P3HT (donor material) and PCBM (acceptor). As photoabsorption occurs, an electron is excited from the highest occupied molecular orbital (HOMO level) in P3HT to the lowest unoccupied molecular orbital (LUMO level), creating an exciton, or electron and hole pair. This electron must then travel through the donor (P3HT) via inter- and intra-chain charge transfer mechanisms until it reaches the interface between the donor and acceptor materials. Here, exciton dissociation occurs, enabling the electron to continue through the acceptor material to the cathode and the electron hole through the donor material to the anode. If recombination of the electron and hold pair occur at any stage during this process, this results in a penalty to the device's performance.[11,12] Marchiori et al. further investigated the effect of polarizability and dipoles in the charge transport and exciton dissociation mechanisms in P3HT and PCBM materials. They used density functional theory (DFT) to probe different molecular conformations between P3HT and PCBM and the resulting induced dipoles created by the electrostatic interactions between molecules. They found that in the lowest energy conformation, the induced dipole was actually in a preferred orientation that encouraged exciton dissociation at the interface, which is favorable for charge transport and device performance. The researchers also emphasized that the long-range polarization effects of these molecules are especially influential on this behavior.[11]

These findings all point to the impact of π-conjugation on the polarizability in these materials, which would have a direct influence on the van der Waals forces in the material. Moreover, representing these intermolecular interactions as accurately as possible is critical to understanding the relationship between molecular conformation and dynamics on the performance of conjugated polymers, especially as they have been shown to have a direct influence on the charge transport mechanisms. In this work, we utilize neutron scattering together with DFT and MD simulations to probe the current limitations of MD force fields for capturing the non-bonded interactions in conjugated polymers. Well-characterized P3HT oligomers allow us to make direct comparisons between these three approaches, and investigate the backbone and side-chain dynamics at the low molecular weight limit. Moreover, quasi-elastic neutron scattering (QENS) allows us to probe the effects of crystallinity and molecular weight on the backbone and side-chain dynamics in regio-regular (semi-crystalline) and regio-random (amorphous) forms of P3HT.

5.2 MATERIALS & METHODS

5.2.1 *Regio-Random and Regio-Regular Poly(3-hexylthiophene) Polymers and Oligomers*

Fully hydrogenated (H14) and partially deuterated (side-chains only, D13) forms of P3HT were synthesized by the Luscombe group at the University of Washington. As we saw in Chapter 4, deuterating the side chain while leaving a single hydrogen along the thiophene ring of the backbone enabled us to maximize the signal from the backbone dynamics relative to those of the side-chains. Hydrogenated and deuterated pairs of regio-regular (semi-crystalline) and regio-random (amorphous) P3HT, RRe-P3HT and RRa-P3HT, respectively, were synthesized to probe the effect of crystallinity on the backbone and side-chain dynamics. The molecular weight (M_n) and dispersity of these samples is shown in Table 5.5. We make note that the length of the RRe-P3HT-H14 sample is only half that of the other samples, which we expect to have a significant effect on the chain dynamics. Therefore, future work will include synthesis of a RRe-P3HT-H14 sample at a matching molecular weight (approximately 12 kDa) to complete our dataset and allow us to make direct comparisons between the systems. Here, we present the data as is to begin our analysis of the backbone and side-chain dynamics in semi-crystalline and amorphous polymer systems. Differential scanning calorimetry (DSC) data for these samples was collected using a TA Instruments (New Castle, DE, USA) Q200 with aluminum sample pans and this data is provided in Figure 5.1. The melting temperature for RRe-P3HT-H14 was determined to be 484 K and for RRe-P3HT-D13 at 495 K. The glass transition temperature for RRa-P3HT-H14 was determined to be at 272 K and for RRa-P3HT-D13 at 280.24 K. Finally, three P3HT oligomer samples were synthesized to explore the dynamics at the limit of low chain lengths. Moreover, utilizing oligomer samples was advantageous for making direct comparisons of experimental data, MD simulations, and DFT calculations with reasonable computational cost. The three oligomer samples will be referred to as P3HT-H14-12mer, P3HT-H14-9mer, and P3HT-D13-8mer to note their hydrogenated or partially deuterated composition as well as their chain length (8mer = 8 monomer length).

Table 5.5. Molecular weight (M_n) and polydispersity (PDI) of hydrogenated (H14) and partially deuterated (side-chains, D13) regio-random (RRa) and regio-regular (RRe) poly(3-hexylthiophene) (P3HT) used in this work. These materials were synthesized by the Luscombe research group at the University of Washington.

P3HT Batch	**M_W (kDa)**	**PDI**
RRe-P3HT-H14	5.5	1.3
RRe-P3HT-D13	11.5	1.1
RRa-P3HT-H14	13.1	6.9
RRa-P3HT-D13	13.1	6.3

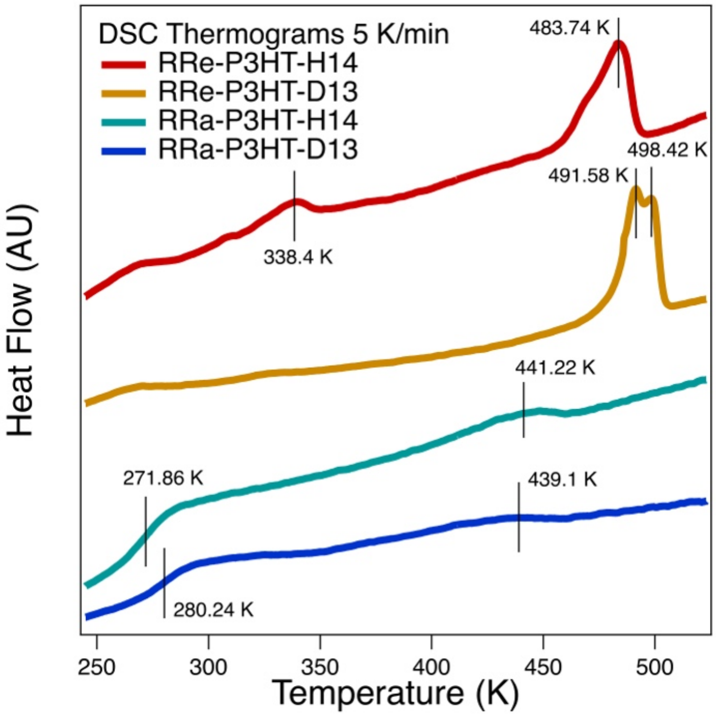

Figure 5.1. Differential scanning calorimetry (DSC) data for hydrogenated (H14) and partially deuterated (side-chains, D13) regio-regular (RRe) and regio-random (RRa) poly(3-hexylthiophene) (P3HT) samples. Shown is the second heating step for a full heat/cool/heat cycle.

5.2.2 *Quasi-Elastic Neutron Scattering Measurements*

QENS measurements were taken using the High-Flux Backscattering Spectrometer (HFBS)[13] at the NCNR following the procedure outlined in Chapter 4. For the oligomer samples specifically, samples were drop cast onto the aluminum foil and a lead wire barrier was not used as previously described. However, all other processing conditions remain unchanged. Data reduction, including the Fourier transformation to the time domain, were done using the Data Acquisition and Visualization Environment (DAVE) software.[14] Elastic scans were collected at rates of either 1 or 2 K/min between 50 and 523 K (polymers) or 50 and 448 K (oligomers). For an extended discussion of the data collection and treatments for QENS experiments, please refer to section 2.3

in Chapter 2. To extract relaxation times, τ, and stretching parameters, β, from the QENS dynamics data, we utilized equation 2.29 for the Kohlrausch–Williams–Watts (KWW) function.

5.2.3 *Molecular Dynamics Simulations*

Molecular dynamics (MD) simulations were performed following the procedure outlined in Chapter 4 for the P3HT-H14/-D13 samples and any modifications to that procedure are provided here. Crystalline simulations were modified to start an initial density of approximately 1 g/cm^3. Chain length for the polymers was 74 monomers while the oligomers followed a chain length distribution to reproduce the system's polydispersity as shown in Figure 5.2.

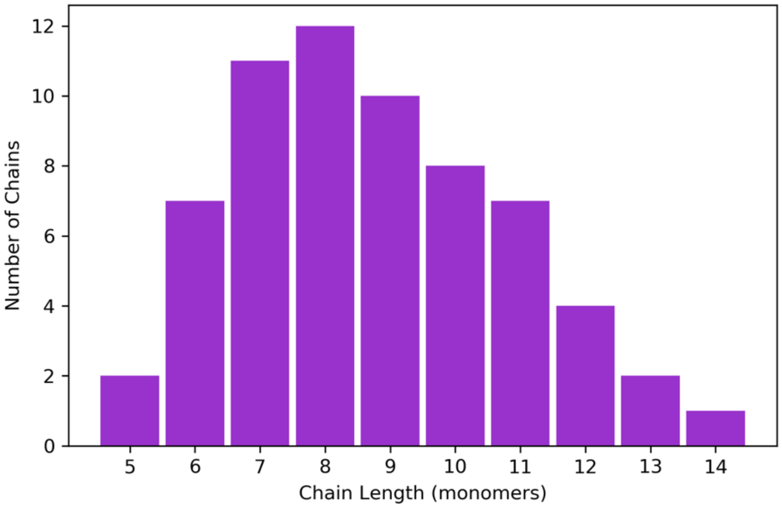

Figure 5.2. Distribution of chain lengths for oligomer simulations.

In this work, we only utilize the Moreno FF2[3] force field. Amorphous simulations implemented a Metropolis algorithm and the force field's backbone dihedral potential to define an initial distribution of cis- and trans-conformations along the backbone. Equilibration was performed at 600 K for 4 ns followed by an additional equilibration at 523 K for 4 ns. During the subsequent cooling step, 200 ps runs every 10 K were performed until a temperature of 13 K was reached. At temperatures where dynamics data was to be collected, the system was restarted from the appropriate cooling step, equilibrated for another 4 ns and then a production run was completed for 5 ns. In the crystalline simulations, the system was first equilibrated at 273 K for 8 ns prior to the cooling step down to 13 K. The system was then warmed up at the same rate until 523 K. For all mean squared displacement calculations, simulations were restarted at the appropriate cooling/warming step, equilibrated for 200 ps and then a production run for 1.8 ns was performed.

5.2.4 *Density Functional Theory*

Density functional theory (DFT) energy calculations were ran for pairs of P3HT oligomers at lengths of dimers, tetramers, hexamers, and octamers using the Gaussian 16 software[15]. The B3LYP functional[16,17] and 6-311++g(d,p) basis set were chosen for providing a balance between computational cost and accuracy for conjugated materials, as investigated by the work of Zhugayevych et al.[18] For dispersion corrections, we utilize the Grimme D3 method[19] with Becke-Johnson damping[20]. Counterpoise corrections[21,22] were applied to isolate the non-bonded interactions between the two chains. The conformation of each chain was held in place following the most stable polymorph ('BDa') from the work of Zhugayevych et al.[18] and the distance between chains was extracted from the pi-stacking vector of the provided crystal structure. To 'scan' non-bonded energies as a function of distance, one chain was translated along this vector to a new position for energy calculations. For comparison, the non-bonded energy was also calculated at identical positions for all atom pairs on different chains within the cutoff distance defined above using the classical Moreno FF2[3] parameters.

5.3 PRELIMINARY RESULTS AND DISCUSSION

5.3.1 *Intermolecular Interactions from Quantum and Classical Molecular Modelling*

We first explored the non-bonded interactions in P3HT using partial charges and Lennard-Jones values extracted from the Moreno FF2[23] parameter set. Shown in Figure 5.3 are the individual Coulombic and Lennard-Jones contribution as well as the total non-bonded energy normalized by chain length between pairs of P3HT oligomers at lengths between 2 and 12 monomers. We find that the Lennard-Jones interactions are the most dominating force, while the Coulombic interactions only provide a significant repulsive force at short intermolecular distances. If we investigate the total non-bonded energy, we find that the depth of the well, representative of the attractive force between to molecules, converges to an approximately constant value per monomer after a chain length of about 6 monomers. Conversely, shown in Figure 5.4 are the non-bonded energies calculated from DFT compared directly with those from the MD force field. Here we find that the interaction strength (well depth) does not converge after a hexamer length, rather, it continues to diverge from the classical results. This would suggest that the force field is currently underestimating the non-bonded interaction strength, especially for longer chain P3HT. Work in progress includes a set of MD simulations for P3HT polymers with scaled energy Lennard-Jones terms along the backbone to recreate the appropriate interaction strength and explore its effects on the backbone and side-chain dynamics.

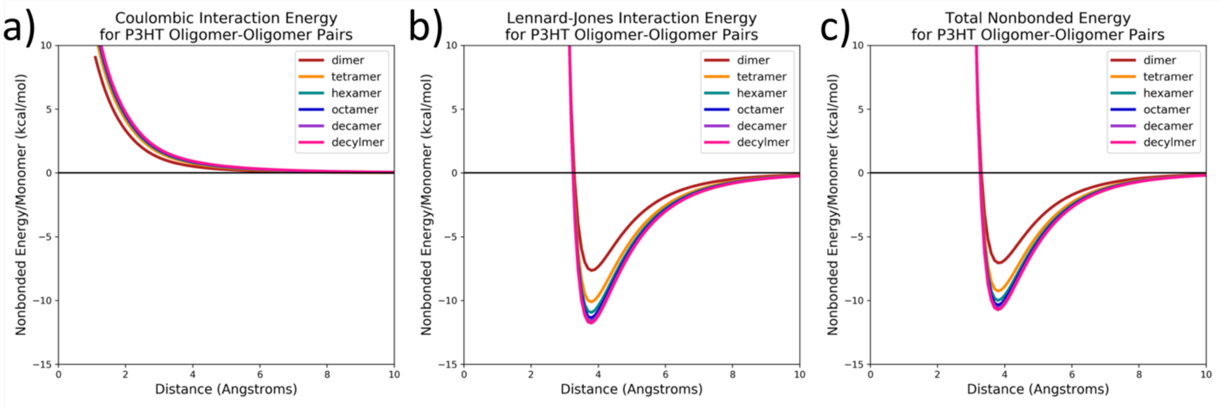

Figure 5.3. (a) Coulombic interactions, (b) Lennard-Jones interactions, and (c) total non-bonded interactions between two P3HT oligomers between 2 and 12 monomers long determined with parameters extracted from the work of Moreno et al.[23] (FF2) and normalized to chain length. Conformation of P3HT chains followed the 'BDa' polymorph from the work of Zhugayevych et al.[18]

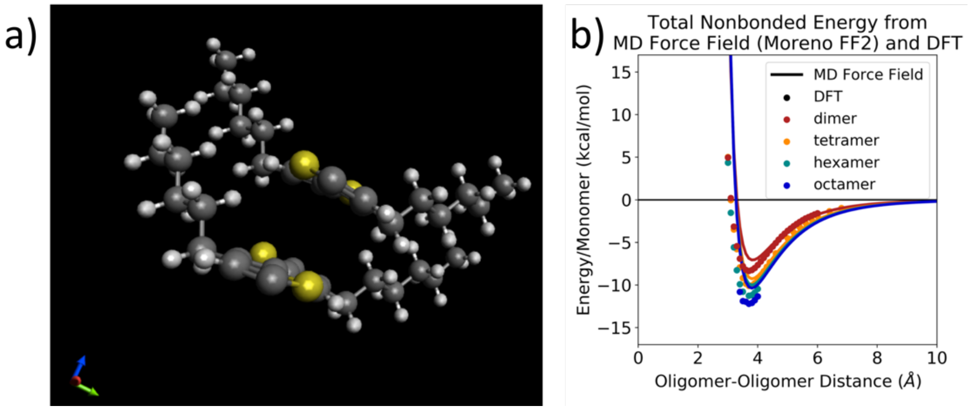

Figure 5.4. (a) Simulation image from density functional theory (DFT) calculations of two P3HT dimers. The conformation of the chains followed the 'BDa' polymorph from the work of Zhugayevych et al.[18] (b) Total non-bonded energy calculated from molecular dynamics simulation force fields (parameters from the work of Moreno et al.[23] (FF2) compared to the non-bonded energy calculated using DFT simulations for pairs of P3HT oligomers ranging in length from 2 to 8 monomers.

5.3.2 *Effect of Crystallinity and Chain Length on Backbone and Side-Chain Dynamics*

QENS measurements of hydrogenated and partially deuterated P3HT pairs allows us to maximize the signals from the side-chain and backbone regions of the molecule, respectively. Shown in Figure 5.5 are elastic scans from hydrogenated and deuterated regio-regular (semi-crystalline) and regio-random (amorphous) P3HT polymers and oligomers. For the polymer materials, we find that the side chain dynamics are similar in both the amorphous and semi-crystalline systems, suggesting that the crystalline structure still allows significant motions of the side chains. Moreover, these side-chains begin relaxing at incredible low temperatures below 200 K. However, the backbone dynamics do not significantly begin until after 440 K. Moreover, we do find a sharp transition point in the backbone dynamics of the RRe-P3HT-D13 sample that corresponds well with the melting temperature of the material. In the oligomer systems, we find a less significant difference in the dynamics of the side-chain and backbone regimes, most likely due to the shorter backbone length that could lead to relaxation of the thiophenes at lower temperatures. In the oligomer side chains, we observe a sharp transition between phases at approximately 225 and 350 K for the 12mer and 9mer, respectively. In future work, these phase transitions will be compared with data collected from differential scanning calorimetry to further understand the phase transition happening at this point.

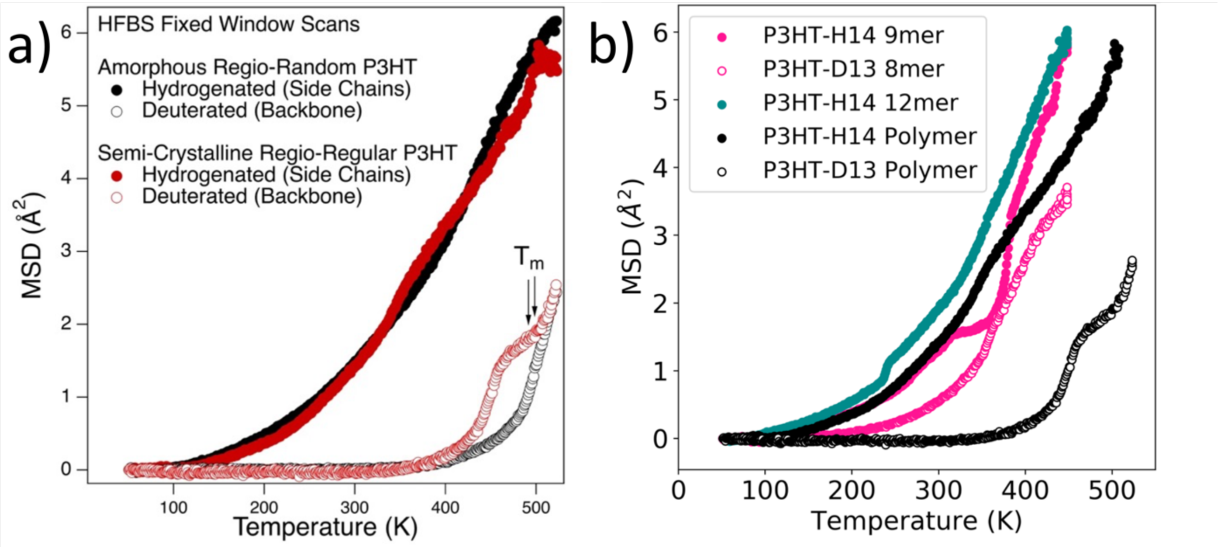

Figure 5.5. Fixed window scans (elastic scans) collecting during warming on the High Flux Backscattering Spectrometer (HFBS)[13] at the NIST Center for Neutron Research for (a) hydrogenated and partially deuterated regio-regular and regio-random poly(3-hexylthiophene) (P3HT) and (b) hydrogenated and partially deuterated P3HT oligomers. In panel (b), also shown for reference is the polymer data for the RRe-P3HT-H14 and RRe-P3HT-D13 samples from panel (a). On panel (b) the melting peaks for RRe-P3HT-D13 determined from differential scanning calorimetry (DSC) are also provided for reference.

The QENS dynamics data begins to tell us more information about the time scales at which motions are occurring in the backbone and side-chains of these polymers and oligomers. Provided in Figure 5.6 are the dynamics data for all samples at 273 K with the corresponding KWW fits. Extracted relaxation times from the fits are also provided in the figure. The flat profiles of the QENS data for the oligomers and the partially deuterated polymer samples indicate that there is very little motion happening within the accessible time scales of the instrument and suggest that any dynamics are occurring at much longer times as noted by their high intensities. The only dynamics we are able to observe and model with the KWW function are those of the RRe-P3HT-H14 and RRa-P3HT-H14 samples whose signals are dominated by side-chain fluctuations. The relaxation times for these samples are very similar at this temperature, indicating that the side-chain dynamics are not significantly influenced by the crystallinity of the polymer. We do start to notice more dynamics occurring in the accessible time window for these same samples at 373 K, as shown in Figure 5.7. At this temperature, the oligomer samples begin to display more motions as the material begins to melt. In the hydrogenated materials, the relaxation times for all materials are very similar, with the time scales for the oligomers presenting at slightly lower values (faster times) than the polymeric samples. This could perhaps be due to longer chain lengths in the polymer samples that are restricting the motion of the alkyl side chains compared to the oligomeric materials. This difference is more significant as we begin to look at the backbone dynamics in the deuterated samples at 373 K. In the mean squared displacement data, polymeric backbones do not show significant relaxation until after 400 K. However, the oligomeric backbones begin to show a similar relaxation at much lower temperatures, around 300 K. This corresponds to the longer relaxation times in the polymers and shorter relaxation times in the oligomers at 373 K. At 448 K and 473 K, shown in Figure 5.8 and Figure 5.9, we see similar results. However, interestingly the backbone motions in the regio-regular sample are still somewhat confined compared to those of the regio-random material. If we consider the DSC data for this material, the crystalline regimes would not have been fully melted at this temperature in the regio-regular samples, resulting in slower relaxation times that are consistent with our results. Future include a deeper investigation into these results as well as consider the simulation data to provide a more thorough explanation of these behaviors.

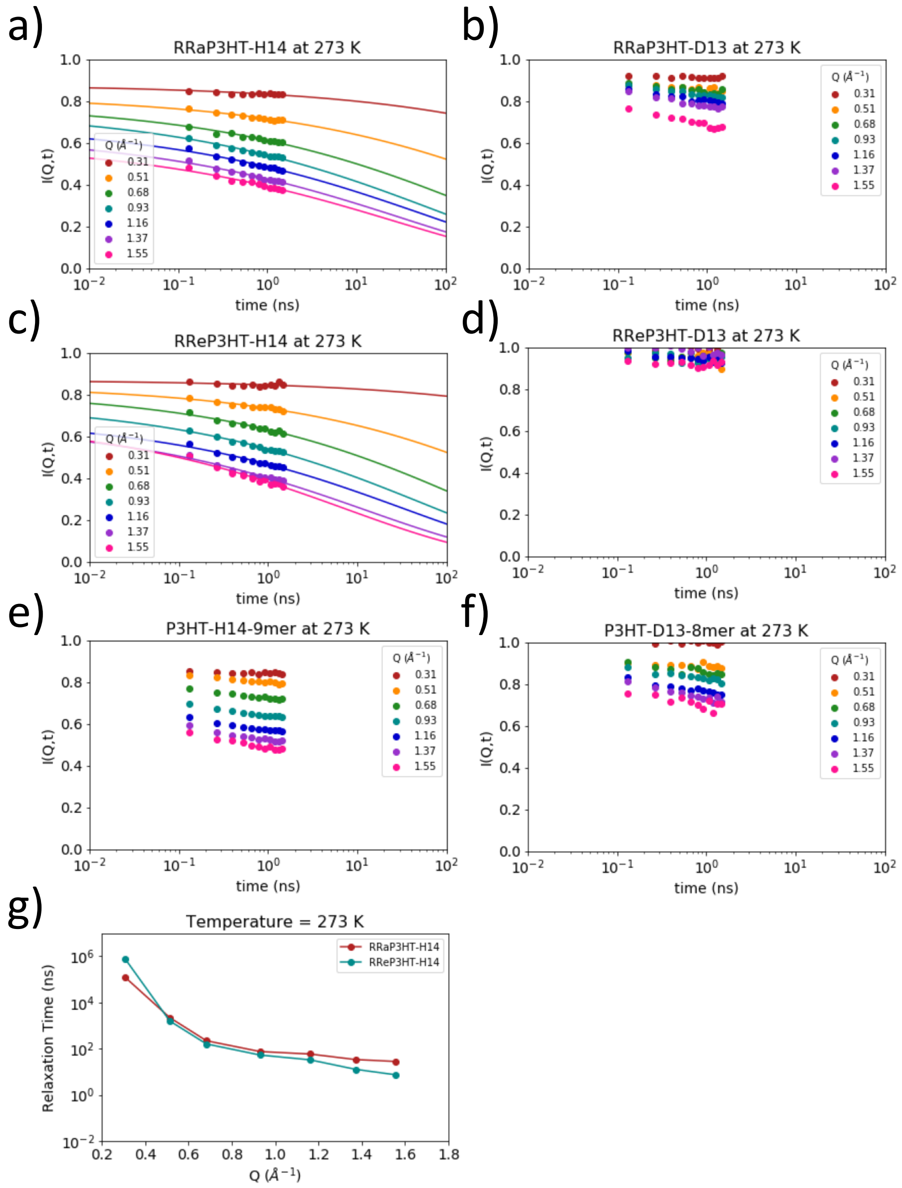

Figure 5.6. QENS data collected at 273 K for hydrogenated (a,c,e) and partially deuterated (b,d,f) forms of P3HT oligomers (e,f) as well as regio-regular (c,d) and regio-random (a,b) polymers. Data shown in markers was collected using the high-flux backscattering spectrometer (HFBS). (g) Relation times, τ, extracted from fits of the KWW function to the data (when possible with limited data ranges). The corresponding fits are shown as lines overlaid on the data on panels (a-f).

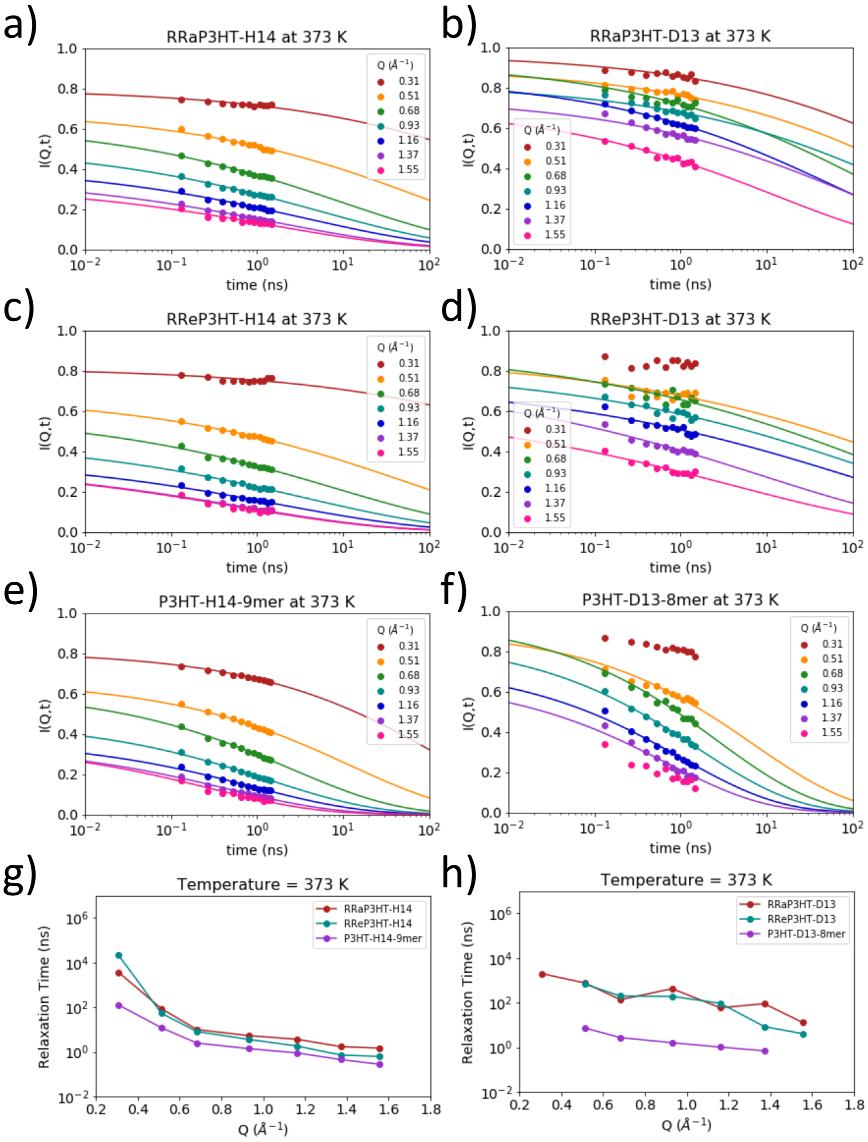

Figure 5.7. QENS data collected at 373 K for hydrogenated (a,c,e) and partially deuterated (b,d,f) forms of P3HT oligomers (e,f) as well as regio-regular (c,d) and regio-random (a,b) polymers. Data shown in markers was collected using the high-flux backscattering spectrometer (HFBS). (g,h) Relation times, τ, extracted from fits of the KWW function to the data (when possible with limited data ranges). The corresponding fits are shown as lines overlaid on the data on panels (a-f).

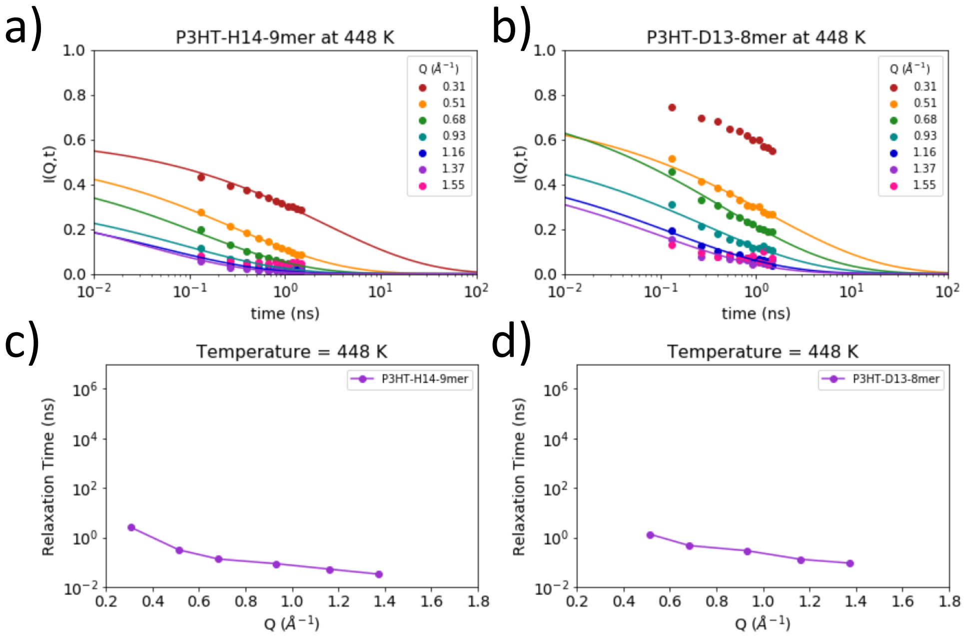

Figure 5.8. QENS data collected at 448 K for hydrogenated (a) and partially deuterated (b) forms of P3HT oligomers. Data shown in markers was collected using the high-flux backscattering spectrometer (HFBS). (c,d) Relation times, τ, extracted from fits of the KWW function to the data (when possible with limited data ranges). The corresponding fits are shown as lines overlaid on the data on panels (a-b).

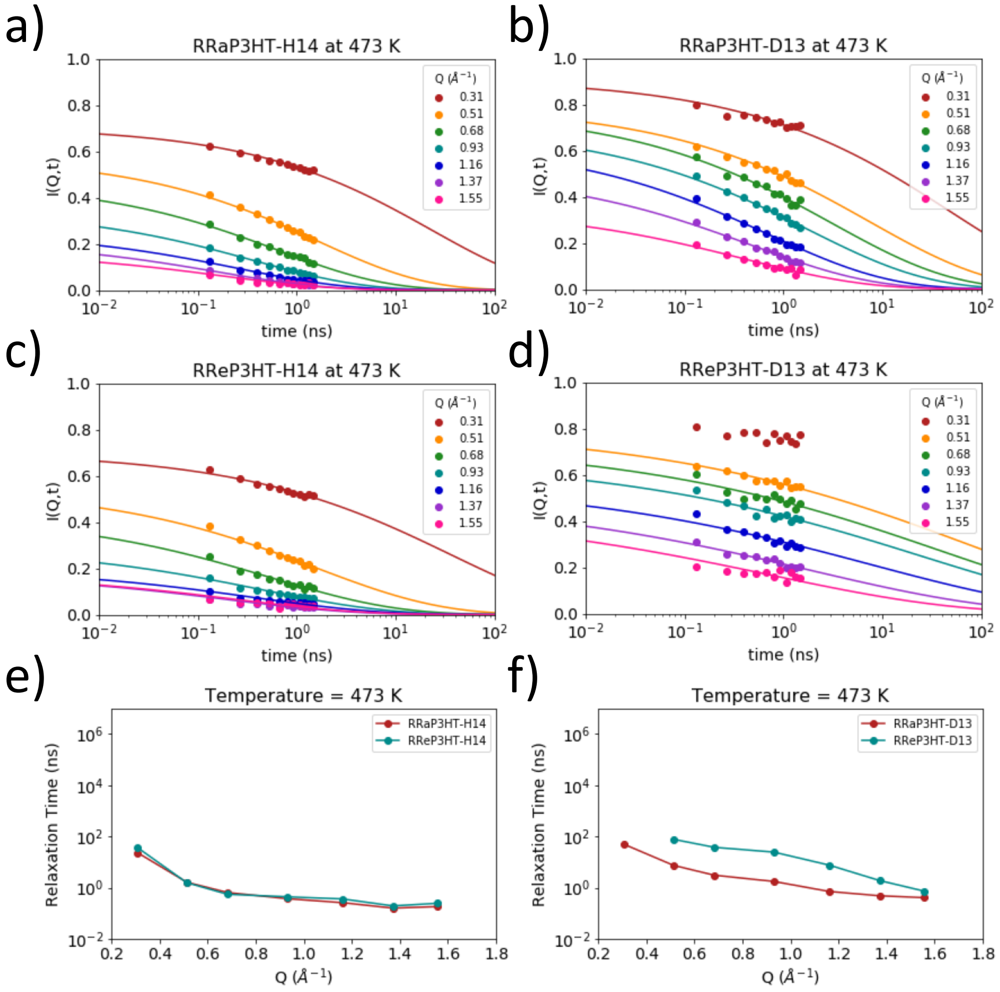

Figure 5.9. QENS data collected at 473 K for hydrogenated (a,c) and partially deuterated (b,d) forms of P3HT polymers, either regio-regular (c,d) or regio-random (a,b). Data shown in markers was collected using the high-flux backscattering spectrometer (HFBS). (e,f) Relation times, τ, extracted from fits of the KWW function to the data (when possible with limited data ranges). The corresponding fits are shown as lines overlaid on the data on panels (a-d).

5.4 CONCLUSIONS AND FUTURE WORK

Our preliminary investigation into the non-bonded interaction parameters of MD force fields for P3HT has found that the system is currently underestimating the intermolecular interactions as determined by DFT calculations. Simulations for P3HT oligomers and polymers are currently running with scaled backbone Lennard-Jones energy parameters to understand how modifying the interaction strength to more closely match that from quantum mechanical calculations affects the system conformation and dynamics. QENS measurements also allowed us to experimentally probe the effect of crystallinity and molecular weight on the backbone and side-chain dynamics in P3HT oligomers and polymers. Using the KWW function, we can extract quantitative descriptions of these motions through the relaxation time and elastic incoherent structure factor. Ongoing work includes a more thorough analysis of these relaxation times, including the use of simulations to help provide molecular motivations for these behaviors.

5.5 REFERENCES

(1) Bhatta, R. S.; Yimer, Y. Y.; Perry, D. S.; Tsige, M. *Improved Force Field for Molecular Modeling of Poly(3-Hexylthiophene)*. *J. Phys. Chem. B* **2013**, *117* (34), 10035–10045. https://doi.org/10.1021/jp404629a.

(2) Schwarz, K. N.; Kee, T. W.; Huang, D. M. *Coarse-Grained Simulations of the Solution-Phase Self-Assembly of Poly(3-Hexylthiophene) Nanostructures*. *Nanoscale* **2013**, *5* (5), 2017. https://doi.org/10.1039/c3nr33324h.

(3) Moreno, M.; Casalegno, M.; Raos, G.; Meille, S. V.; Po, R. *Molecular Modeling of Crystalline Alkylthiophene Oligomers and Polymers*. *J. Phys. Chem. B* **2010**, *114* (4), 1591–1602. https://doi.org/10.1021/jp9106124.

(4) Jorgensen, W. L.; Maxwell, D. S.; Tirado-Rives, J. *Development and Testing of the OLPS All-Atom Force Field on Conformational Energetics and Properties of Organic Liquids*. *J. Am. Chem. Soc.* **1996**, *118* (15), 11225–11236. https://doi.org/10.1021/ja9621760.

(5) Wolf, C. M.; Kanekal, K. H.; Yimer, Y. Y.; Tyagi, M.; Omar-Diallo, S.; Pakhnyuk, V.; Luscombe, C. K.; Pfaendtner, J.; Pozzo, L. D. *Assessment of Molecular Dynamics Simulations for Amorphous Poly(3-Hexylthiophene) Using Neutron and X-Ray Scattering Experiments*. *Soft Matter* **2019**, *15* (25), 5067–5083. https://doi.org/10.1039/C9SM00807A.

(6) Jorgensen, W. L.; Tirado-Rives, J. *Potential Energy Functions for Atomic-Level Simulations of Water and Organic and Biomolecular Systems*. *Proc. Natl. Acad. Sci.* **2005**, *102* (19), 6665–6670. https://doi.org/10.1073/pnas.0408037102.

(7) DuBay, K. H.; Hall, M. L.; Hughes, T. F.; Wu, C.; Reichman, D. R.; Friesner, R. A. *Accurate Force Field Development for Modeling Conjugated Polymers*. *J. Chem. Theory Comput.* **2012**, *8* (11), 4556–4569. https://doi.org/10.1021/ct300175w.

(8) Marcon, V.; Raos, G. *Molecular Modeling of Crystalline Oligothiophenes: Testing and Development of Improved Force Fields*. *J. Phys. Chem. B* **2004**, *108* (46), 18053–18064. https://doi.org/10.1021/jp047128d.

(9) Israelachvili, J. N. *Intermolecular and Surface Forces*, 3rd ed.; Elsevier Inc., 2011.

(10) Schmit, J. D.; Levine, A. J. *Statistical Model for Intermolecular Adhesion in Pi-Conjugated Polymers*. *Phys. Rev. Lett.* **2008**, *100* (19), 198303. https://doi.org/10.1103/PhysRevLett.100.198303.

(11) Marchiori, C. F. N.; Koehler, M. *Density Functional Theory Study of the Dipole across the P3HT : PCBM Complex: The Role of Polarization and Charge Transfer*. *J. Phys. D. Appl. Phys.* **2014**, *47* (21), 215104. https://doi.org/10.1088/0022-3727/47/21/215104.

(12) Mazzio, K. a.; Luscombe, C. K. *The Future of Organic Photovoltaics*. *Chem. Soc. Rev.*

2014, *44* (1), 78–90. https://doi.org/10.1039/c4cs00227j.

(13) Meyer, A.; Dimeo, R. M.; Gehring, P. M.; Neumann, D. A. *The High-Flux Backscattering Spectrometer at the NIST Center for Neutron Research*. *Rev. Sci. Instrum.* **2003**, *74* (5), 2759–2777. https://doi.org/10.1063/1.1568557.

(14) Azuah, R. T.; Kneller, L. R.; Qiu, Y.; Tregenna-Piggott, P. L. W.; Brown, C. M.; Copley, J. R. D.; Dimeo, R. M. *DAVE: A Comprehensive Software Suite for the Reduction, Visualization, and Analysis of Low Energy Neutron Spectroscopic Data*. *J. Res. Natl. Inst. Stand. Technol.* **2009**, *114* (6), 341. https://doi.org/10.6028/jres.114.025.

(15) Frisch, M. J.; Trucks, G. W.; Schlegel, H. B.; Scuseria, G. E.; Robb, M. A.; Cheeseman, J. R.; Scalmani, G.; Barone, V.; Petersson, G. A.; Nakatsuji, H.; Li, X.; Caricato, M.; Marenich, A. V.; Bloino, J.; Janesko, B. G.; Gomperts, R.; Mennucci, B.; Hratchian, H. P.; Ortiz, J. V.; Izmaylov, A. F.; Sonnenberg, J. L.; Williams-Young, D.; Ding, F.; Lipparini, F.; Egidi, F.; Goings, J.; Peng, B.; Petrone, A.; Henderson, T.; Ranasinghe, D.; Zakrzewski, V. G.; Gao, J.; Rega, N.; Zheng, G.; Liang, W.; Hada, M.; Ehara, M.; Toyota, K.; Fukuda, R.; Hasegawa, J.; Ishida, M.; Nakajima, T.; Honda, Y.; Kitao, O.; Nakai, H.; Vreven, T.; Throssell, K.; Montgomery Jr., J. A.; Peralta, J. E.; Ogliaro, F.; Bearpark, M. J.; Heyd, J. J.; Brothers, E. N.; Kudin, K. N.; Staroverov, V. N.; Keith, T. A.; Kobayashi, R.; Normand, J.; Raghavachari, K.; Rendell, A. P.; Burant, J. C.; Iyengar, S. S.; Tomasi, J.; Cossi, M.; Millam, J. M.; Klene, M.; Adamo, C.; Cammi, R.; Ochterski, J. W.; Martin, R. L.; Morokuma, K.; Farkas, O.; Foresman, J. B.; Fox, D. J. *Gaussian 16, Revision B.01*. Gaussian, Inc.: Wallingford CT 2016.

(16) Lee, C.; Yang, W.; Parr, R. G. *Development of the Colle-Salvetti Correlation-Energy Formula into a Functional of the Electron Density*. *Phys. Rev. B* **1988**, *37* (2), 785–789. https://doi.org/10.1103/PhysRevB.37.785.

(17) Becke, A. D. *Density‐functional Thermochemistry. III. The Role of Exact Exchange*. *J. Chem. Phys.* **1993**, *98* (7), 5648–5652. https://doi.org/10.1063/1.464913.

(18) Zhugayevych, A.; Mazaleva, O.; Naumov, A.; Tretiak, S. *Lowest-Energy Crystalline Polymorphs of P3HT*. *J. Phys. Chem. C* **2018**, *122* (16), 9141–9151. https://doi.org/10.1021/acs.jpcc.7b11271.

(19) Grimme, S.; Antony, J.; Ehrlich, S.; Krieg, H. *A Consistent and Accurate Ab Initio Parametrization of Density Functional Dispersion Correction (DFT-D) for the 94 Elements H-Pu*. *J. Chem. Phys.* **2010**, *132* (15), 154104. https://doi.org/10.1063/1.3382344.

(20) Grimme, S.; Ehrlich, S.; Goerigk, L. *Effect of the Damping Function in Dispersion Corrected Density Functional Theory*. *J. Comput. Chem.* **2011**, *32* (7), 1456–1465. https://doi.org/10.1002/jcc.21759.

(21) Simon, S.; Duran, M.; Dannenberg, J. J. *How Does Basis Set Superposition Error Change the Potential Surfaces for Hydrogen‐bonded Dimers?* *J. Chem. Phys.* **1996**, *105* (24), 11024–11031. https://doi.org/10.1063/1.472902.

(22) Boys, S. F.; Bernardi, F. *The Calculation of Small Molecular Interactions by the Differences of Separate Total Energies. Some Procedures with Reduced Errors*. *Mol. Phys.* **1970**, *19* (4), 553–566. https://doi.org/10.1080/00268977000101561.

(23) Moreno, M.; Casalegno, M.; Raos, G.; Meille, S. V.; Po, R. *Molecular Modeling of Crystalline Alkylthiophene Oligomers and Polymers*. *J. Phys. Chem. B* **2010**, *114* (4), 1591–1602. https://doi.org/10.1021/jp9106124.

Chapter 6. BLEND MORPHOLOGY IN POLYTHIOPHENE-POLYSTYRENE COMPOSITES FROM NEUTRON AND X-RAY SCATTERING

This chapter contains material from the following manuscript submitted for publication and the author would like to acknowledge the contributions of all coauthors:

> Wolf, C. M.; Guio, L., Scheiwiller, S. C., O'Hara, R., Luscombe, C., Pozzo, L. D. *Blend Morphology in Polythiophene-Polystyrene Composites from Neutron and X-ray Scattering*. **2020** (submitted)

6.1 INTRODUCTION

In our work thus far, we have discussed the advantages of conjugated polymers (CPs) for more flexible and lower-cost organic electronic devices, such as organic photovoltaics (OPVs), bioelectronics, flexible displays, and more. We know that the morphology and conformation in the disordered and ordered phases of CPs impact the charge transport and macroscopic performance. Gu et al. explored the impact of tie chains (high molecular weight chains) in pure P3HT. These tie chains at a critical mole fraction of 10^{-3} were able to create charge transport pathways connecting the high-mobility crystalline regimes that improved the material's overall charge mobility.[1] Self-assembly and crystallization of CPs into nanofibers or nanoribbons has also been used as a strategy to improve charge transport. These nanofibers have been shown to grow in length, rather than width, to form fiber networks that create charge transport pathways effective across longer distances in the bulk.[2] Past work in our group has explored multiple approaches to controlling this self-assembly including solvent quality (solubility), solvent mixtures, electric fields and ultrasound.[2–5] However, there are still performance limitations in current materials and devices, including significant environmental degradation and low mechanical durability (e.g. cracking), that limits the wide-scale implementation of these technologies.[6–10]

In order to improve the environmental stability and mechanical durability of these materials while keeping charge transport abilities, researchers have investigated blends of CPs in a matrix of an insulating commodity polymer, such as polystyrene or polyethylene.[11–19] In the work of Goffri et al. researchers found that using blends of regio-regular poly(3-hexylthipohene) (RRe-P3HT) and either isostatic polystyrene (PS), or high-density or linear low-density polyethylene (PE), in the active layer of OFETs maintained performance at P3HT amounts as low as 5-10 wt% or 3-5 wt%, respectively. They found that annealing these blends at a temperature below the crystallization of P3HT but above that of the PS or PE furthered the degree of phase separation in the liquid state, encouraged crystallization of the P3HT, and promoted the accumulation of P3HT at the interface of the film.[12] In another work, Kumar and coworkers demonstrated that blends of RRe-P3HT and PE had improved environmental stability when compared to pure RRe-P3HT after four months of light and air exposure.[13] This was also demonstrated for RRe-P3HT and PS blends after one week of air exposure by Qiu et al,[15] and these authors also note how tuning of the solvent processing conditions of these blends can maintain comparable device performance down to 1 wt% of P3HT.[14] While many of these blends utilize P3HT, a model CP, researchers have also begun extending this approach to high-performance donor-acceptor CPs.[16–18]

The relationship between morphology and electronic performance in conjugated and commodity polymer blends is just as important as in the pure materials. Researchers have found two primary mechanisms for how an insulator material can maintain or improve charge mobility in these blends even at low amounts of the CP. The first is by encouraging vertical phase separation and an enrichment of the conjugated component at the interface, which is an ideal conformation in the OFET architecture. Alternatively, insulating materials can promote the crystallization or self-assembly of the CP into favorable morphologies, i.e. nanofiber networks, for bulk charge transport.[13] Kumar and coworkers found that they could control the length-scales at which phase separation occurred in these materials by blending RRe-P3HT with either a PE homopolymer or P3HT-PE block copolymer. While the block copolymer resulted in phase separation at smaller length scales, which improved charge transport mechanisms across the bulk, the homopolymer enabled large-scale phase separation and the enrichment of P3HT at the film interface. At small amounts of PE (80 wt% P3HT), OFET device performance was actually improved compared to a pure P3HT active later and at small amounts of P3HT down to 25 wt%, a comparable device performance was maintained.[13] The influence of solvent quality and solvent mixing on the final solid-state morphology in P3HT-PS blends was explored by Cho and coworkers.[14,15] Marginal solvents could be used to form a P3HT nanofiber network dispersed in the PS matrix that still maintained device performance down to 3 wt% P3HT[15], while mixing solvents to modulate the solvent quality (solubility) and aging of the solution could be used to improve the crystallinity and accumulation of P3HT at the film interface, maintaining device performance down to 1 wt%.[14] Han et al. also found that choosing a solvent with a high boiling point was useful for increasing the drying time of the blend and encouraging phase separation for improved devices.[19]

These works all point to a complex system of polymer-polymer and polymer-solvent interactions that strongly influence the final conformation and charge transport behavior of the blends. Therefore, it is important that these self-assembly mechanisms and the resulting nano-scale morphology in these blends are well characterized. However, proving the bulk conformation in polymer blends can be difficult with common microscopy techniques, such as atomic force microscopy (AFM) and optical microscopy, due to their sensitivity to surface structures and limitations for optically-opaque materials, respectively. It is also difficult to distinguish the structure of one organic phase in another using X-ray scattering due to limited contrast between the atomically-similar materials. However, contrast variation small-angle neutron scattering (CV-SANS) can be incredibly powerful for characterizing the bulk structure in polymer blends by using hydrogen and deuterium labelling, as described in Chapter 2. CV-SANS can capture the bulk morphology at length scales ranging from 1 nm to 10 μm by replacing the hydrogen atoms of one phase with deuterium to create sufficient contrast between the polymeric components. Numerous works in the literature have already demonstrated how CV-SANS can be useful for understanding CP structure in both the solution state[2–5] (deuterated solvents) and the solid state.[2–5] Researchers have been able to define the thermodynamics in polymer blends by extracting the Flory-Huggins parameter from the random phase approximation. [20] Others have been able to capture behaviors at the interface between semi-crystalline and amorphous polymers, observing the mixing of the amorphous phases between the crystalline regimes with a combined SANS and X-ray scattering approach[21] Finally, CV-SANS has been useful for kinetic investigations into spinodal decomposition of polymer blends.

In this chapter, we utilize CV-SANS to characterize the bulk conformation and self-assembly behavior in polythiophene and polystyrene blends. A set of semi-crystalline polythiophenes with differing side-chain lengths or densities along the backbone are explored, including regio-regular poly(3-hexylthiophene) (RRe-P3HT), poly(3-dodecylthiophene) (P3DDT), and poly(3,3'''-didodecyl[2,2':5',2'':5'',2'''-quaterthiophene]-5,5'''-diyl) (PQT-12), as well as an amorphous polythiophene: regio-random poly(3-hexylthiophene) (RRa-P3HT). The matrix polymer for all blends was an atactic (amorphous) PS. Solvents with a range of CP solubilities, toluene, chloroform, and bromobenzene, are used to understand the effect of processing conditions on the final blend morphology in the solid-state. CV-SANS allows us to first probe the nature of the interfaces between CP and PS phases and also quantitatively define the CP structures formed in the matrix, such as nanofibers or globular aggregates. Wide-angle X-ray scattering (WAXS) is then used to determine the nature of crystalline phases within the blends. Finally, the bulk conformation is related back to the macroscopic performance of these materials by use of conductivity measurements.

6.2 MATERIALS

A set of CPs were purchased from Rieke Metals (Lincoln, NE USA) including poly(3-dodecylthiophene) (P3DDT) (M_W=39 kg mol^{-1}, $Đ$=1.8, Product 4005-E), regio-random poly(3-hexylthiophene) (RRa-P3HT) (M_W=63 kg mol^{-1}, $Đ$=2.4, Product 4007), and regio-regular poly(3-hexylthiophene) (RRe-P3HT-2) (M_W=55 kg mol^{-1}, $Đ$=2.4, Product 4002-EE) Additionally, poly(3,3'''- didodecyl[2,2':5',2'':5'',2'''-quaterthiophene]-5,5'''- diyl) (PQT-12) (M_W=40 kg mol^{-1}, $Đ$=1.7, Product SOL4150) was purchased from Solaris Chem (Vaudreuil-Dorion, Quebec Canada). The polystyrene matrix material was purchased from Polymer Source (Dorval, Montreal, Quebec Canada) including a hydrogenated polystyrene (PS-H8) (M_W=278 kg mol^{-1}, $Đ$=1.07, Product P8610-S) and fully deuterated polystyrene (PS-D8) (M_W=305 kg mol^{-1}, $Đ$=1.08, Product P19833-dPS). All polymers were used as received.

Additionally, a regio-regular poly(3-hexylthiophene) (RRe-P3HT, M_W=22.7 kg mol^{-1}, $Đ$=1.2) was synthesized by the Luscombe group at the University of Washington for use in this work following literature procedure[22] with noted modifications and characterized by size exclusion chromatography (SEC) and nuclear magnetic resonance (NMR):

“1,3-bis(diphenylphosphino)propane (41.25 mg, 0.05 mmol) and bromo(2-methylphenyl)bis(triphenylphosphine)nickel(II) (37.72 mg, 0.1 mmol) were added to a Schlenk flask, and dried under vacuum for 30 min. After drying, anhydrous THF (2 mL) was added, and the mixture was stirred for 2 h. 2-bromo-3-hexyl-5-iodothiophene (1.45 mL, 6.6 mmol) was added to a Schlenk flask and degassed under vacuum for 30 min. Anhydrous THF (66 mL) was added to the Schlenk flask, the flask was placed in an ice bath and 1.85 M isopropylmagnesium chloride in THF(3.24 mL, 6 mmol) was added dropwise over 30 min. Following addition, the flask was returned to RT, and stirred for 1 h under darkness. The catalyst mixture was injected rapidly to the monomer flask to start the polymerization. Immediately after injection, the flask was placed in an oil bath at 45C to prevent precipitation. The polymerization proceeded for 2 h. The polymerization was quenched with the addition of HCl (3 mL, 5 M). The polymer was precipitated into methanol (1000 mL) and collected by vacuum filtration. The polymer was purified using Soxhlet extraction with methanol, acetone, and hexanes. The polymer was extracted from the thimble with chloroform, then precipitated into methanol and collected via vacuum filtration. The polymer was dried under vacuum. ^{1}H NMR spectra were obtained on a Bruker AV-500 spectrometer using $CDCl_3$ as solvent. Size exclusion chromatography (SEC) was performed using a Malvern Viscotek TDA 305 SEC with a UV and RI detector. Samples were run using THF as the eluent at a flow rate of 1 mL/min. The concentration of the polymer was 0.5 mg/mL. The molecular weight distribution is determined by SEC, and the M_n is obtained by NMR end-group analysis. Regioregularity was determined by comparing the ratio of integrations of the head-to-tail couplings against tail-to-tail and head-to-head couplings; these showed the polymers to be >99% regioregular within the

> *resolution of the NMR. 1H NMR Shifts: δ 7.43 (m, 2H), 7.24 (m, 2H), 6.98 (s, 1H), 2.80 (t, 2H (2H between the peaks at 2.8 and 2.61), J = 7.7 Hz), 2.61 (t, 2H (2H between the peaks at 2.8 and 2.61), J = 7.6), 2.49 (s, 3H), 1.71 (quint, 2H, J = 7.6 Hz), 1.48-1.38 (m, 2H), 1.37-1.30 (m, 4H), 0.91 (t, 3H, J = 7.2 Hz). For the bromo(2-methylphenyl)bis(triphenylphosphine)nickel(II) synthesis and characterization, nickel(II) Bromide (2.19 g, 10 mmol) and triphenylphosphine (5.25 g, 20 mmol) were added to a 3-neck flask with an attached condenser and dried under vacuum for 30 minutes. After drying, 15 mL anhydrous THF was added. The flask was brought to 70° C and the mixture was refluxed for 2 h. Mg turnings (0.29 g, 12 mmol) were added to a Schlenk flask and flame dried under vacuum. After drying, 1 M 2-Bromotoluene in anhydrous THF (10 mL, 10 mmol) was added dropwise to the Schlenk flask. The mixture was stirred for 1 h under darkness. The 3-neck flask was allowed to cool to RT and the Grignard solution was injected into it. The mixture was stirred for 20 minutes at RT and then quenched by pouring into methanol. The product was vacuum filtered with fine glass frit, washed with methanol, and dried under vacuum. ^{13}P NMR shifts were δ 21.97 (s, 2P).”*

Differential scanning calorimetry (DSC) was used to determine the glass transition and melting temperatures of the polymers used in this work, as well as ensure that the hydrogenated and deuterated forms of PS had similar phase behavior. This enabled the use of more cost-efficient hydrogenated PS for additional sample replicates in WAXS and conductivity measurements. DSC data was collected using a TA Instruments (New Castle, DE, USA) Q200 with aluminum sample pans. These results are shown below in Figure 6.1.

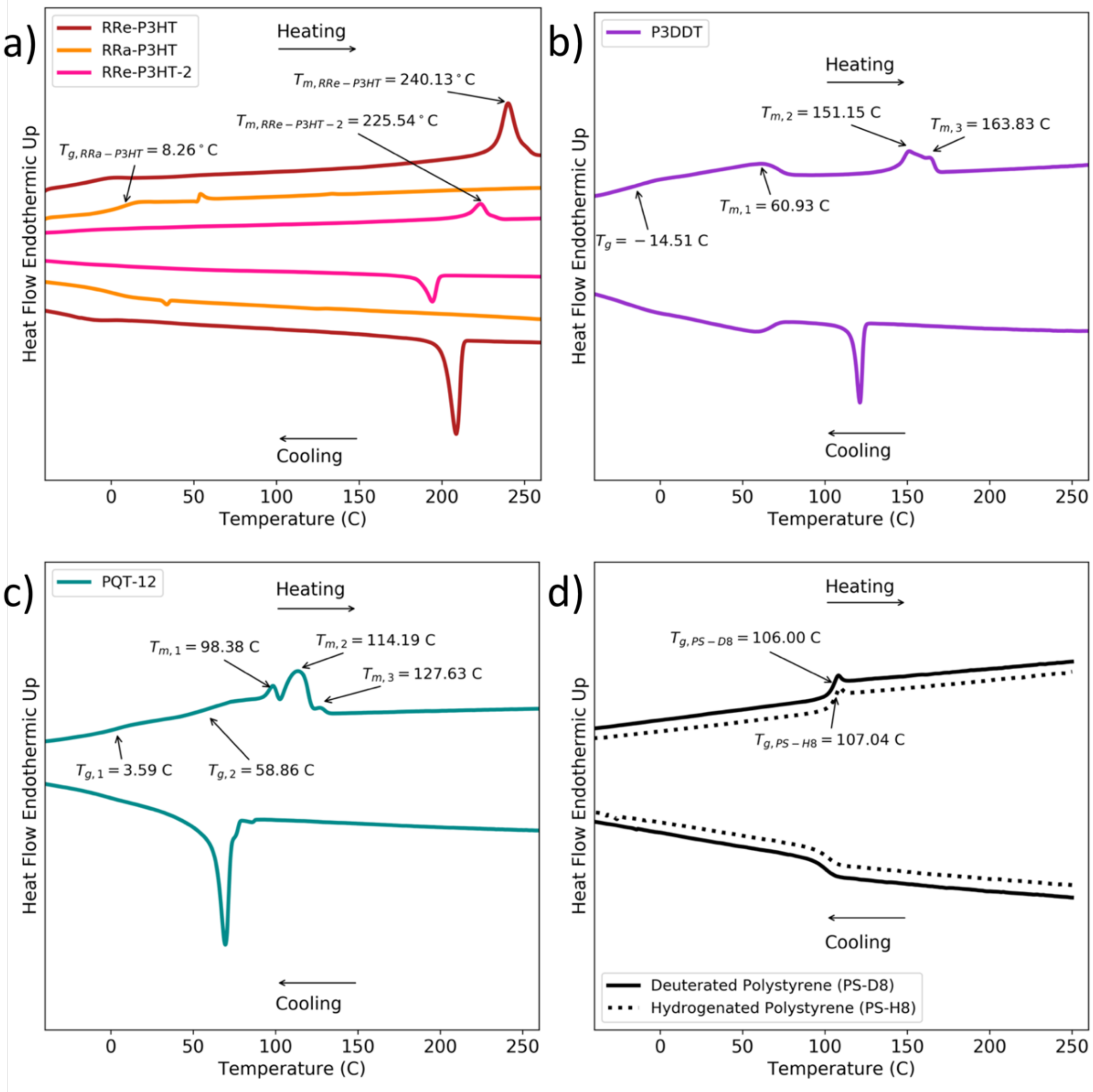

Figure 6.1. Differential scanning calorimetry (DSC) data for (a) regio-regular poly(3-hexyl thiophene) (RRe-P3HT and RRe-P3HT-2), regio-random poly(3-hexyl thiophene) (RRa-P3HT), (b) poly(3-dodecyl thiophene) (P3DDT), (c) poly(3,3'''-didodecyl[2,2':5',2'':5'',2'''-quaterthiophene]-5,5'''- diyl) (PQT-12), (d) hydrogenated polystyrene (PS-H8) and fully deuterated polystyrene-D8 (PS-D8) used in this work. Glass transition temperatures are noted by a T_g and melting temperatures are noted by a T_m. Heat flow is shown in arbitrary units. The experiment was performed with a heat/cool/heat cycle at temperature ramp rates of either 5 ºC/min (PS-H8, PS-D8, P3DDT, PQT-12) or 10 C/min (RRe-P3HT, RRe-P3HT-2, RRa-P3HT). The first heat step was performed to remove thermal history of the sample, and so data shown above is taken from the cool and second heat steps only.

For the preparation of solid samples, creation of solution samples, and UV-Vis measurements, solvents of chloroform, toluene, and chlorobenzene were purchased from Fisher Chemical (Waltham, MA USA), bromobenzene was purchased form Aldrich Chemistry (St. Louis, MO USA), and fully deuterated toluene (toluene-D8) was purchased from Cambridge Isotope Laboratories, Inc. (Tewksbury, MA USA). All solvents were used as received.

6.3 METHODS

6.3.1 *Sample Preparation*

A diagram showing the complete sample preparation process for solid polythiophene-polystyrene blends is shown below in Figure 6.2. For each sample, a CP of either RRe-P3HT, RRa-P3HT, P3DDT, or PQT-12 was dissolved in solution with either PS-D8 or PS-H8 at a total polymer concentration of 50 mg/mL. The ratio of CP and PS varied to correspond to final, solid-state P3HT concentrations ranging from 0.1 to 50 wt%. The fully deuterated PS-D8 was utilized to create sufficient contrast in samples that would be characterized using SANS. The solvents used in this initial solution-state included toluene, chloroform, and bromobenzene as they provided a range of solvent quality for the CPs. Toluene can be described as a moderate solvent for P3HT, chloroform a good solvent, and bromobenzene an excellent solvent. These solutions were then cast onto a watch glass on a hot plate at 50 °C to evaporate the majority of the solvent. Bromobenzene solutions took approximately 3 hours to dry, toluene solutions took approximately 30 minutes, and chloroform solutions took approximately 12 minutes. To investigate the effect of drying time, a set of samples noted with the keywords 'Slow Dry' were dissolved in chloroform and allowed to dry on the watch glass at room temperature, taking approximately 38 minutes to evaporate the chloroform. Additional residual solvent was removed by placing the sample in a 50 °C vacuum oven for 12-24 hours. Finally, the solid samples were shaped with 2-3 cycles in a heat press set at 150 °C, which was above the glass transition of the PS and below the melting temperature of RRe-P3HT. Precision metal shims were used as a spacer to ensure that any bubbles in the film would be removed and the material would form a smooth, uniform disc with a thickness of 0.01 inches (254 μm). For each cycle, samples were broken and pressed for 5 or 2 minutes for initial and final presses, respectively.

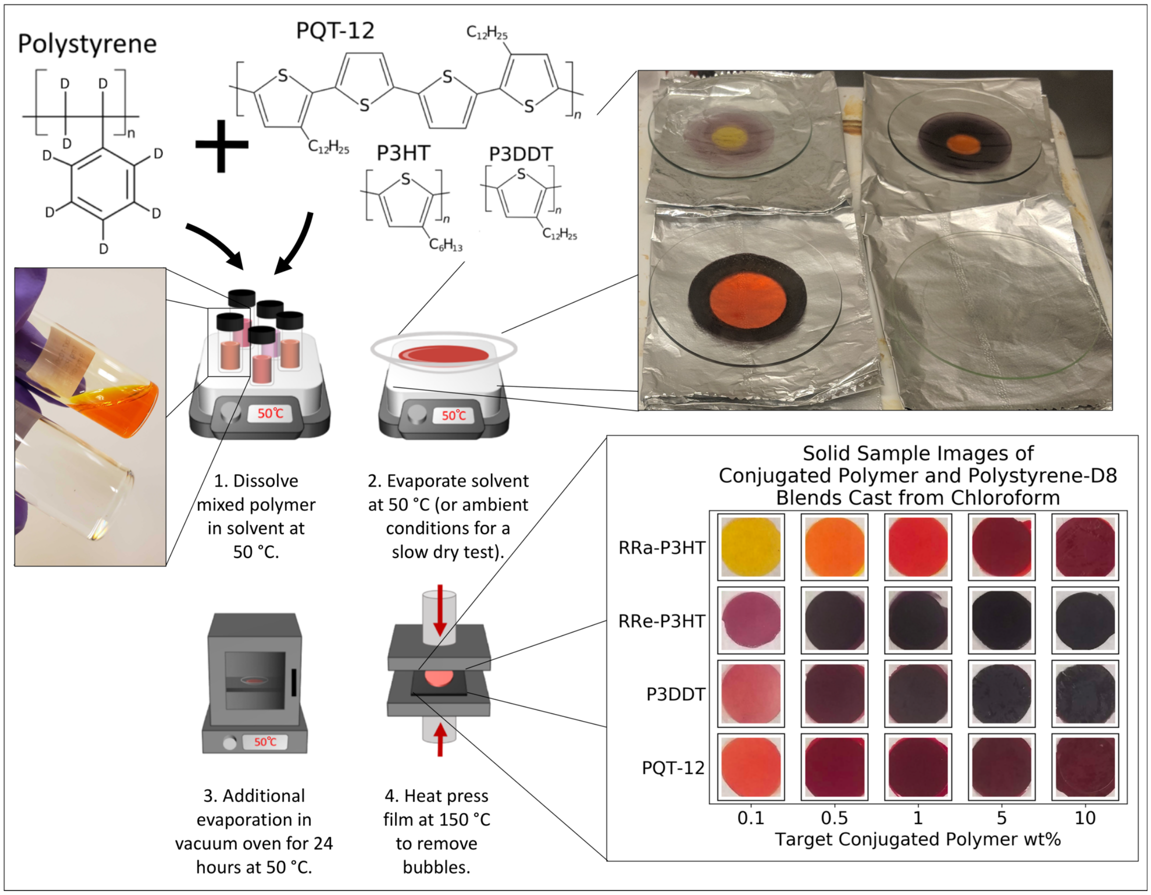

Figure 6.2. Sample preparation schematic for solid polymer blend films comprised of a CP with PS-D8 or PS-H8 (not shown). CPs used in this work included RRe-P3HT, RRa-P3HT, P3DDT, and PQT-12. The concentration of CP in the solid blend was targeted between 0.1 – 50 wt%. On the left is a representative image of the polymer blends fully dissolved in solvent. All samples were cast onto the watch glass for solvent evaporation in this state, and a color change was observed upon drying as shown in the top right image. On the lower right are images of solid CP and PS-D8 blends taken after they were fully dried and pressed.

To explore the polymer-polymer and polymer-solvent interactions in the solution state with and without the presence of PS, a small set of samples dissolved in toluene were characterized with SANS. The preparation process for these samples followed that of the solid samples up until the point of casting onto a watch glass. Two samples were comprised of RRe-P3HT at 5 mg/mL and either PS-D8 or PS-H8 dissolved at 45 mg/mL, matching the total 50 mg/mL starting concentration in the solution-state and corresponding to a 10 wt% RRe-P3HT sample in the solid-state. Additionally, three control samples were made comprised of (1) RRe-P3HT at 5 mg/mL, (2) PS-H8 at 45 mg/mL, and (3) PS-D8 at 45 mg/mL, allowing us to isolate the different polymer behaviors with and without polystyrene in solution.

6.3.2 *Small-Angle and Ultra-Small Angle Neutron Scattering*

Both SANS and USANS measurements were conducted at the National Institute of Standards and Technology (NIST) Center for Neutron Research (NCNR) in Gaithersburg, MD to collect data across a comprehensive set of length scales. SANS data collected using the NG-3 45m Very Small-Angle Neutron Scattering and NG-7 30m Small-Angle Neutron Scattering instrument accessed a q-range of 0.002 - 0.1 $Å^{-1}$ and USANS data collected using the BT-5 Ultra-Small-Angle Neutron Scattering instrument accessed a q-range of 0.00004 - 0.003 $Å^{-1}$. The data was reduced using the NCNR SANS and USANS macros for Igor Pro.[23] This integrated the data from 2D scattering images to 1D profiles of scattering intensity, I, versus q, removed background contributions, and scaled the data to absolute intensity. Solution samples were measured in the standard titanium demountable cells with quartz windows and a pathlength of 2 mm while titanium and cadmium sample frames were used to hold the solid samples in place in the sample holder. Finally, we note that all USANS data is shown in the smeared form (accounted for numerically during modeling with SasView/sasmodels[24,25]), resulting in a seemingly discontinuous scattering profile between the USANS and SANS q-ranges. However, the USANS data of the solution samples were desmeared using the USANS reduction macros[23] for Igor Pro. Additional analysis of the SANS and USANS data was performed using the SasView/sasmodels[24,25] and bumps[26] packages for Python, which is discussed in greater detail in the Appendix provided in Chapter 7. Using Python 3 to perform our SANS analysis allowed us to preserve reproducible work among members of our team and produce scripts that could be shared with the community to promote open science. Moreover, utilizing this approach enabled partial-automation of fitting the scattering data, a task that can be a slow and inefficient process when performed manually and individually for each sample. All scripts and Jupyter notebooks used to analyze the data in this chapter are provided at https://github.com/pozzo-research-group/c-wolf-blends-morphology.[27]

A Porod analysis[28] was used to describe the interfaces and behavior between the CP and PS phases within the material, as described in Chapter 2 (section 2.2.5). However, we found that for these particular samples, the PS-D8 component contributed significantly to the scattering profile. Since at least the 1970's, multiple works have investigated short- and long-range ordering in amorphous materials at length scales between 10 to 10,000 Å, and while the molecular origins for these fluctuations have been attributed to intramolecular correlations or even larger 'nodules', these density fluctuations are significantly influenced by the thermal and mechanical history of the sample.[29–35] If we consider the pressing cycles above the glass transition temperature of the PS followed by rapid quenching, we can expect these non-equilibrated states of the amorphous material to be kinetically trapped, resulting in natural density fluctuations in the insulating phase. Therefore, we have broken up the Porod equation to include separate CP and PS components:

$$I(q) = v_{CP} \frac{C_{CP}}{q^{m,CP}} + (1 - v_{CP}) \frac{C_{PS}}{q^{m,PS}} + background \qquad (6.1)$$

where CP and PS refer to the conjugated and polystyrene phases, respectively, v_{CP} is the volume fraction of CP, and C is the Porod constant. As defined in eq. 2.13, we can extract the interfacial concentration, $\frac{S}{V}$, from the Porod constant of the conjugated polymer phase:

$$C_{CP} = 2\pi\Delta\rho^2 \frac{S}{V} \tag{6.2}$$

where $\Delta\rho^2$ is the contrast between the conjugated polymer and polystyrene materials.

To quantitatively characterize the structures formed in the bulk of these blends, such as globular aggregates or nanofibers of the CP, we can utilize a series of form factors that capture the shape of these structures, e.g. spheres and cylinders. We start defining this combined model by first considering the self- and cross-interactions between the different components of the blend[36,37]:

$$I(q) = \Sigma_{i=1}^{N}[(\rho - \rho_0)^2 F_{ii}(q)] + 2\ \Sigma_{i<j}\ [(\rho_i - \rho_0)(\rho_j - \rho_0)F_{ij}(q)] \tag{6.3}$$

where $F(q)$ is the partial scattering function and N is the number of components in the system not including the reference material, such as a solvent or background phase). In our polythiophene and PS blends, we can expect the intrinsic PS density fluctuations, free CP chains trapped in the matrix, phase aggregated CP, and self-assembled CP structures (e.g. nanofibers) to contribute to the total scattering intensity in contrast to the average SLD of the PS phase, ρ_0. The second half of eq. 6.3 accounts for the cross-interactions between each of these different scattering domains and structures, however, this would only contribute significantly if there was any correlation between the phases[37], such as a dependent position of the nanofibers and globular aggregates. However, we can expect these structures to be uniformly and independently dispersed in our samples, and so these cross-interaction terms can be removed from eq. 6.3. Finally, we can further define eq. 6.3 with a mass balance applied to the CP and PS phases:

$$I(q) = v_{CP}\Sigma_{k=1}^{K}[x_k I_{CP,k}(q)] + (1 - v_{CP})I_{PS}(q) + background \tag{6.4}$$

where x_k and $I_{CP,k}$ is the fraction of CP and scattering intensity, respectively, for conformation k of K total structures including either globular phase aggregates or nanofibers. Finally, I_{PS} is the scattering intensity that accounts for the PS density fluctuations.

The scattering of the PS phase, is modeled using a Guinier-Porod form as defined in eq. 2.15 – 2.17. The scattering of the CP phase accounts for globular phase aggregates in all models and also a contribution from nanofibers when they are present in the blend. While we do expect some CP chains could be trapped in the PS phase of the blends, we could not deconvolute its contribution to the overall scattering intensity. For the larger-scale globular phases, we utilize either a sphere (eq. 2.18) or ellipsoid (eq. 2.19-2.21) form factor, depending on the dimensionality that most accurately represents the data. There was no molecular motivation for one form factor over the other, and so frequently we refer to this phase as 'globular domains'. For those samples that also included scattering signal from the presence of nanofibers, we used a cylinder form factor (eq. 2.22-2.24). In general, these models may be referred to as 'sphere+cylinder' or 'ellipsoid+cylinder' to indicate which form factors were included in eq. 6.4, or more simply as 'Globular Domains' or 'Globular Domains + Nanofibers'. And although not explicitly stated in the naming convention, each of these models includes a Guinier-Porod contribution for the PS phase.

When fitting eq. 6.4, the parameters of R_{sphere}, R_{polar}, $R_{equatorial}$, $R_{cylinder}$, and $L_{cylinder}$ defined as the sphere, ellipsoid and cylinder radii as well as the cylinder length, were allowed to vary. The volume fraction of the conjugated polymer phase, v_{CP}, was varied following a normal distribution centered at the UV-Vis determined concentration, and the fraction of CP present in globular domains versus nanofibers, x_k, was allowed to vary uniformly between 0 and

1 when applicable. To compare between sphere and ellipsoid globular domains directly, we utilize a radius of gyration, R_g, which is defined as:

$$R_{g,sphere}^2 = \frac{3}{5} R_{sphere}^2 \tag{6.5}$$

$$R_{g,ellipsoid}^2 = \frac{1}{5}\left(R_{polar}^2 + 2R_{equatorial}^2\right) \tag{6.6}$$

The size of these globular domains showed a sharp transition from small- to large-scale aggregates, and so we utilized a logistic function to fit this data and approximate the critical concentration, C_{crit}, at which this transition occurs:

$$\ln(R_g) = B + \frac{H}{1+\exp[-W(ln(m_{CP})-ln(C_{crit}))]} \tag{6.7}$$

where B is a constant for vertical shifting, H is a constant related to the height of the transition, W is a constant for the width or steepness of the transition, m_{CP} is the mass fraction of CP in the sample, and C_{crit} is the inflection point of the transition.

Finally, the SANS and USANS data for our solution samples was analyzed with a slightly different approach. For the samples that included both the RRe-P3HT and PS-D8/PS-H8 phases, we removed the scattering contribution of the polystyrene phase by subtracting the scattering intensity of the appropriate polystyrene control sample at matching values of q. This provided the scattering intensity due to the RRe-P3HT phase specifically with the presence of PS interactions which could be compared with that of the RRe-P3HT control sample without the presence of PS interactions. In the low to mid-q regions of the data, we utilized a network power law model (eq.

2.14) to extract the power exponent which can be defined here as the fractal dimension, D_f, related to the density of nanofibers in the sample.[2]

6.3.3 *Small-Angle and Wide-Angle X-ray Scattering*

SAXS and WAXS data for the samples containing PS-D8 were collected at the 9ID beamline at the Advanced Photon Source at Argonne National Laboratory.[38–40] The instrument used an X-ray source of 21 keV and a beam size of 0.8 x 0.8 mm with a flux density of approximately 5 x 10^{12} photons/second/mm^2. SAXS and WAXS data were collected with exposure times of 10 seconds each. Samples were mounted using custom designed 3D-printed 48-sample frames[41] that enabled execution of remote experiments during COVID-19 constrained access. SAXS and WAXS data were reduced, de-smeared, and corrected to absolute intensity using the Nika package[42] for Igor Pro. This package was also used to combine the data from the SAXS and WAXS detectors to produce datasets that will be referred to as 'WAXS data' for the remainder of the work.

WAXS data for additional samples batches containing either RRe-P3HT-2 or RRa-P3HT in PS-H8 were measured using an Anton-Paar (Graz, Austria) SAXSess X-ray scattering instrument. The instrument was operated in line collimation mode with a Cu-Kα source (wavelength of 1.54 Å). Solid polymer blends were placed in a custom, 3D-printed frame to hold the sample in place and ensure the X-ray beam passed through the middle of the sample. The sample chamber was held under vacuum at ambient temperature (approx. 20 °C) during all measurements. Data was collected using Fujifilm (Greenwood, SC USA) image plates and read using a PerkinElmer Cyclone (Covina, CA USA) image plate reader. The Anton-Paar SAXSQuant software was used to reduce data from 2D scattering images to 1D plots of scattering intensity (I) versus scattering vector (Q), remove contributions from the background and desmear the data.

Analysis of WAXS data was performed using the SasView/sasmodels[24,25] and bumps[26] packages for Python. Three gaussian distributions were first used to fit the peaks representative of the PS phase in all pure control samples. An additional two gaussian distributions were added to the blend samples to fit the lamellar and pi-stacking peaks for the polythiophenes in the ranges of 0.25-0.35 Å^{-1} and 1.6-1.7 Å^{-1}, respectively. An example of the fits to the WAXS data are shown in Figure 6.3.

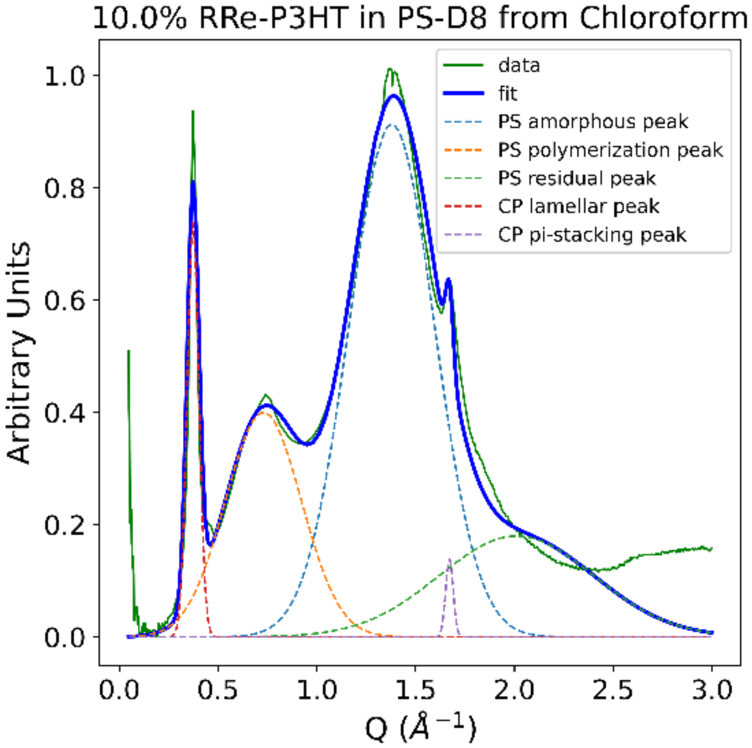

Figure 6.3. Example fit of wide-angle X-ray scattering (WAXS) data for a solid blend of RRe-P3HT and PS-D8 cast from chloroform.

6.3.4 *UV-Vis Spectroscopy*

UV-Vis spectroscopy was used to determine an accurate concentration of CP in each of the blends in the final solid state as this is important for not only analysis but also to the mass balance in eq 6.4. The concentration of the CP phase was converted to a volume fraction for all SANS data modeling using a density of 1.1 g/mL for the CP phase and a density of 1.13 g/mL for the PS-D8 phase[43–45], however we continue to refer to the CP concentration in units of wt% as to be consistent with many works in the literature[11–15,46] of CP and insulating polymer blends.

A Thermo Scientific (Waltham, MA USA) Evolution 300 UV-Visible Spectrophotometer was used for all measurements. Solid blend samples with targeted CP concentrations greater than 10 wt%, between 1 and 10 wt%, and less than 1 wt% were dissolved in chlorobenzene at 0.02, 0.1, or 1 mg/mL, respectively. This ensured that the absorbance peaks were at reasonable and characterizable intensities between 0 and 1. For samples that included PS-D8, three replicates were created for each film taken from different locations (opposite edges and center), and we found the concentration to be very uniform across the material. Each CP had a characteristic peak between 420 and 470 nm that was fit with a 2nd degree polynomial to extract an accurate peak intensity. An example for a set of RRe-P3HT and PS-D8 blends is shown in Figure 6.4.

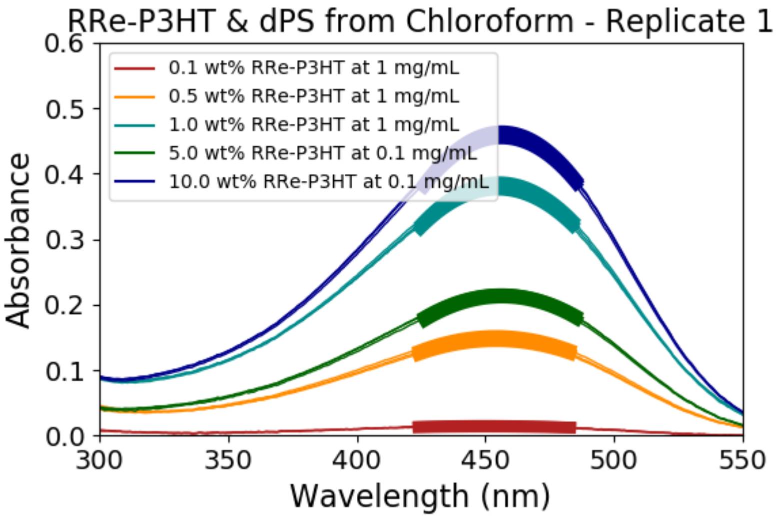

Figure 6.4. UV-Vis data for a set of blends made from RRe-P3HT and fully deuterated polystyrene (dPS/PS-D8). Conjugated polymer concentrations listed are in targeted wt% only. Three replicates are shown for each sample but are be difficult to see as the replicates overlaps well for each samples. The thick lines (centered around 450 nm) of the same color are the corresponding fit polynomials used to determine the peak absorbance and wavelength for each replicate.

For each CP and solution concentration of 0.02, 0.1 or 1 mg/mL, a calibration curve was made from samples with known CP and PS concentrations. Following the Beer-Lambert law as described in Chapter 2, we can then fit a line through these known samples and the origin to define the relationship between peak absorbance and actual concentration. Examples of these calibration curves are provided in Figure 6.5 and a comparison of actual concentrations against the target concentrations for samples comprised of a CP and PS-D8 used in this work are provided in Figure 6.6.

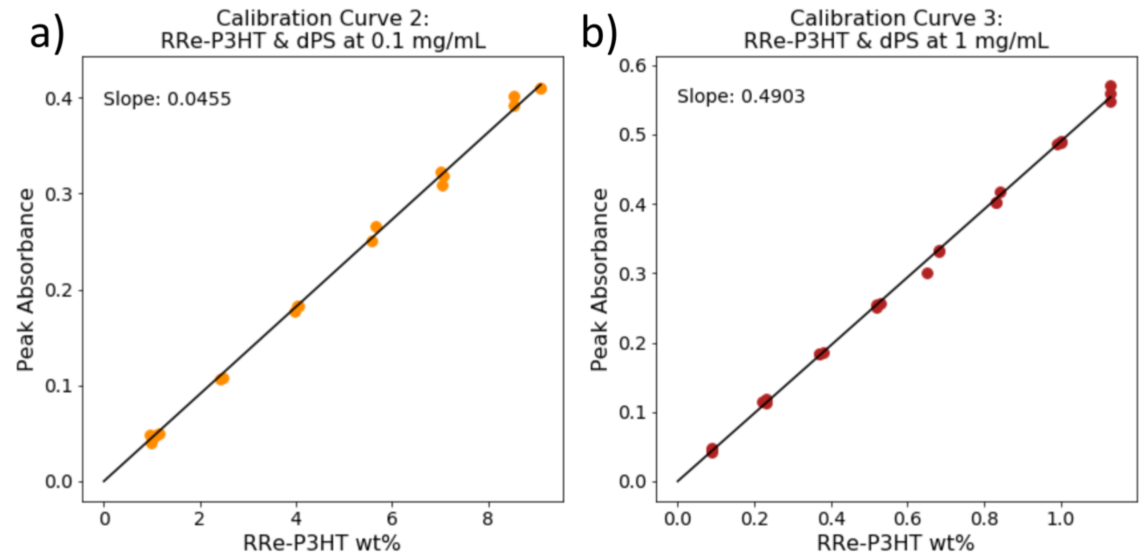

Figure 6.5. UV-Vis calibration curves for a set of blends made from RRe-P3HT and fully deuterated polystyrene (dPS/PS-D8). The calibration curve (a) was created with solutions at 0.1 mg/mL and used for samples with target concentrations between 1 and 10 wt%. The calibration curve (b) was created with solutions at 1 mg/mL and used for samples with target concentrations between 0.1 and 1 wt%. The correction was done utilizing the slopes from a linear fit that was required to pass through the origin, which are also provided on the plots above. Note that the RRe-P3HT wt% refers to the concentration in the solid state blends only.

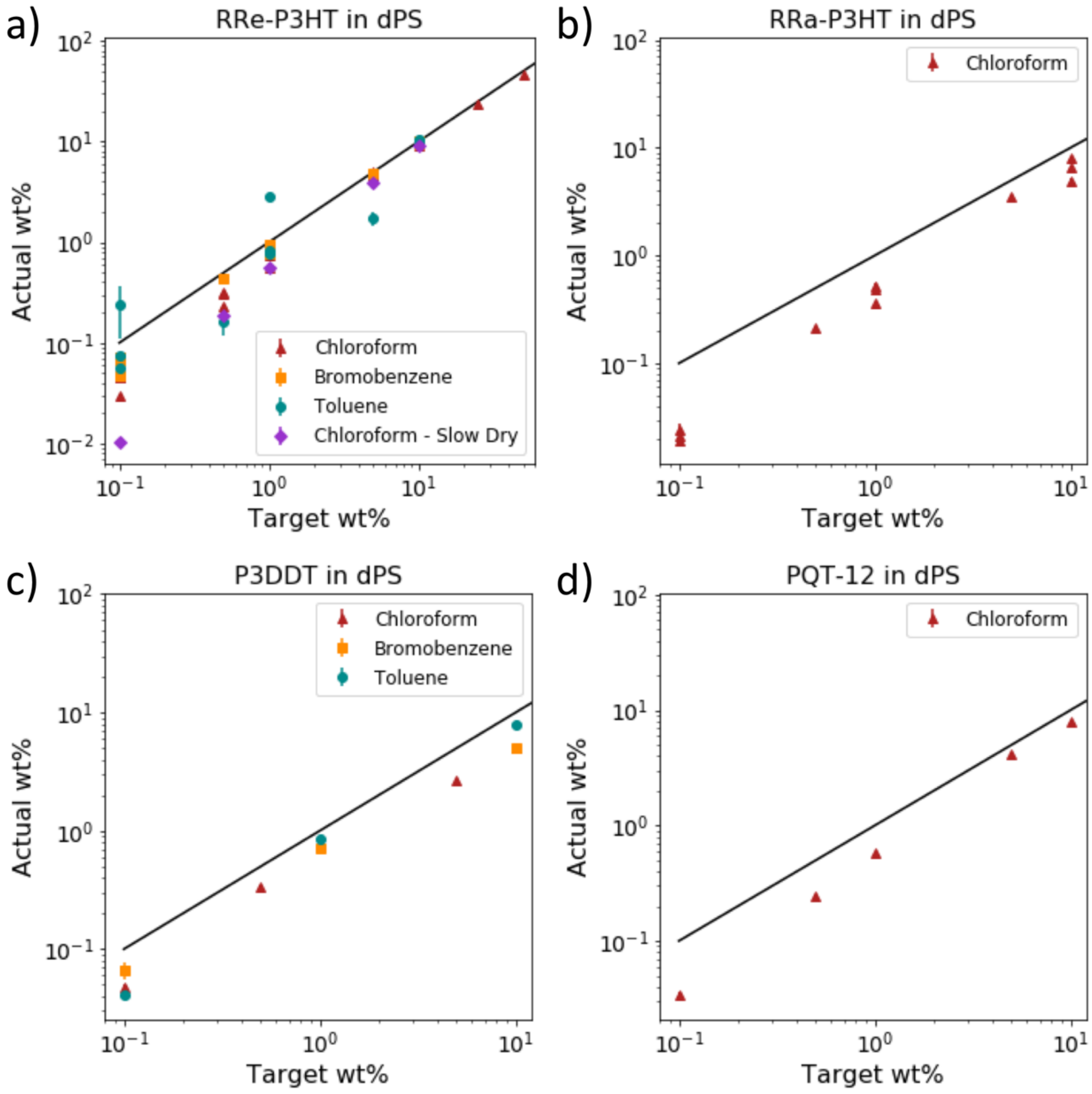

Figure 6.6. Actual conjugated polymer concentrations versus the target concentration calibrated from UV-Vis measurements for blends made from (a) RRe-P3HT, (b) RRa-P3HT, (c) P3DDT, or (d) PQT-12 in fully deuterated polystyrene-D8 (dPS/PS-D8). Original samples were cast from solutions in chloroform, bromobenzene or toluene as noted in the legends and were dried at 50 C. Samples where solvent was allowed to evaporate at ambient temperature are noted by the keywords ‘Slow Dry’. Markers represent the average and error bars represent the standard deviation determined from three replicate pieces from each sample.

6.3.5 *Conductivity Measurements*

Conductivity measurements were performed by the Luscombe group at the University of Washington with the following procedure:

> *"Conductivity measurements were performed on an Ametek (Berwyn, PA, USA) Parstat 4000a Potentiostat using RHD Instruments (Darmstadt, Germany) TSC SW closed measuring cell. The samples were first prepared by blade coating square electrodes on each side of the films with silver paste. The square electrodes had a side length of roughly 2mm. The DC current was measured across the thickness of the samples (254 um) as potential was applied ranging from 1-10 V. The conductivity was then derived using geometric calculations. For high resistance samples, the entire measuring cell was enclosed in an aluminum mesh lined enclosure to shield from electromagnetic interference."*

6.4 RESULTS AND DISCUSSION

6.4.1 *Visual Observations of Conformation Change*

Color changes of CPs have been well studied in the literature and are known to correspond to conformation changes of the polymer chains.[47,48] When fully dissolved, all blends began as a bright orange color as shown on the left side of Figure 6.2. However, as they were cast onto the watch glasses and the solvent began evaporating, many of the samples changed to a dark opaque red or purple color, as shown in the top right of Figure 6.2. This color persisted to the final, solid state of the blends, as shown in the bottom right of Figure 6.2. The transition from a bright orange to dark opaque color is indicative of more rigid, planar CP chains that then lead to aggregation or self-assembly (e.g. nanofibers). The RRa-P3HT samples were the only ones to maintain an orange or yellow color to the solid-state, suggesting that they remain amorphous at all concentrations, but the dark colors of the remaining RRe-P3HT, P3DDT, and PQT-12 samples suggest that the CPs underwent some degree of crystallization as they dried.

6.4.2 *Porod Analysis*

The SANS profiles at the high-q limit were fit with the Porod model to characterize the interfaces within the blends. A selection of these fits are shown in Figure 6.7 for RRe-PHT, RRa-P3HT, P3DDT and RRa-P3HT blends cast from solutions in chloroform. Simultaneous fits of the pure PS-D8 control samples first extracted a Porod exponent of 3.5 in the PS phase, which is indicative of rough interfaces between phases of fluctuating density, which we can expect for the kinetically-trapped amorphous material. For samples with high amounts of CP, the signal would be dominated by the interface between the conjugated and PS phases, and the Porod exponent approached a value of 4, indicative of well-defined smooth interfaces between these components. Therefore, we held the PS and CP Porod exponents constant at these values to extract the interfacial concentration.

Figure 6.8 and Figure 6.9 show the extracted interfacial concentration, $\frac{S}{V}$, for blends cast from solutions in chloroform and RRe-P3HT samples cast from different solvents, respectively. For RRa-P3HT, P3DDT and PQT-12 samples, the interfacial concentration is inversely proportional to the CP concentration, which indicates growing phase aggregates as the amount of CP is increased. The RRa-P3HT samples reach the lowest values of interfacial concentration, suggesting that the extent of phase separation in these blends is highest among the CPs investigated. For RRe-P3HT samples cast from chloroform, the interfacial concentration shows a peak, indicating an additional dependence on the degree of phase separation and the concentration. However, RRe-P3HT samples cast from either toluene or bromobenzene display a relatively constant amount of interfacial concentration, or phase aggregation.

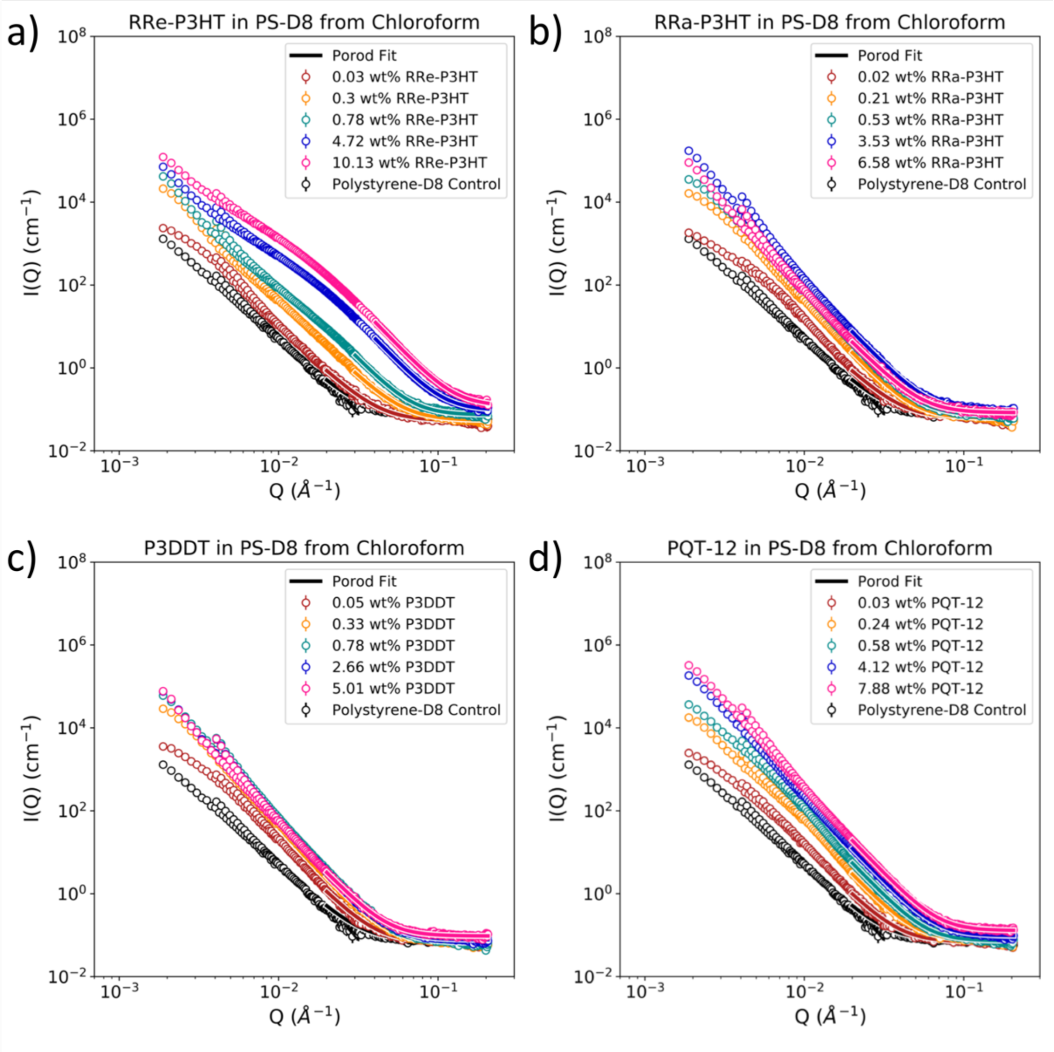

Figure 6.7. Small-angle neutron scattering (SANS) data for blends cast from solutions in chloroform. Blends are comprised of PS-D8 and either (a) RRe-P3HT, (b) RRa-P3HT, (c) P3DDT, or (d) PQT-12. Porod fits are shown as lines overlaid on top of the data at high-Q in a matching color to the scattering data shown in markers.

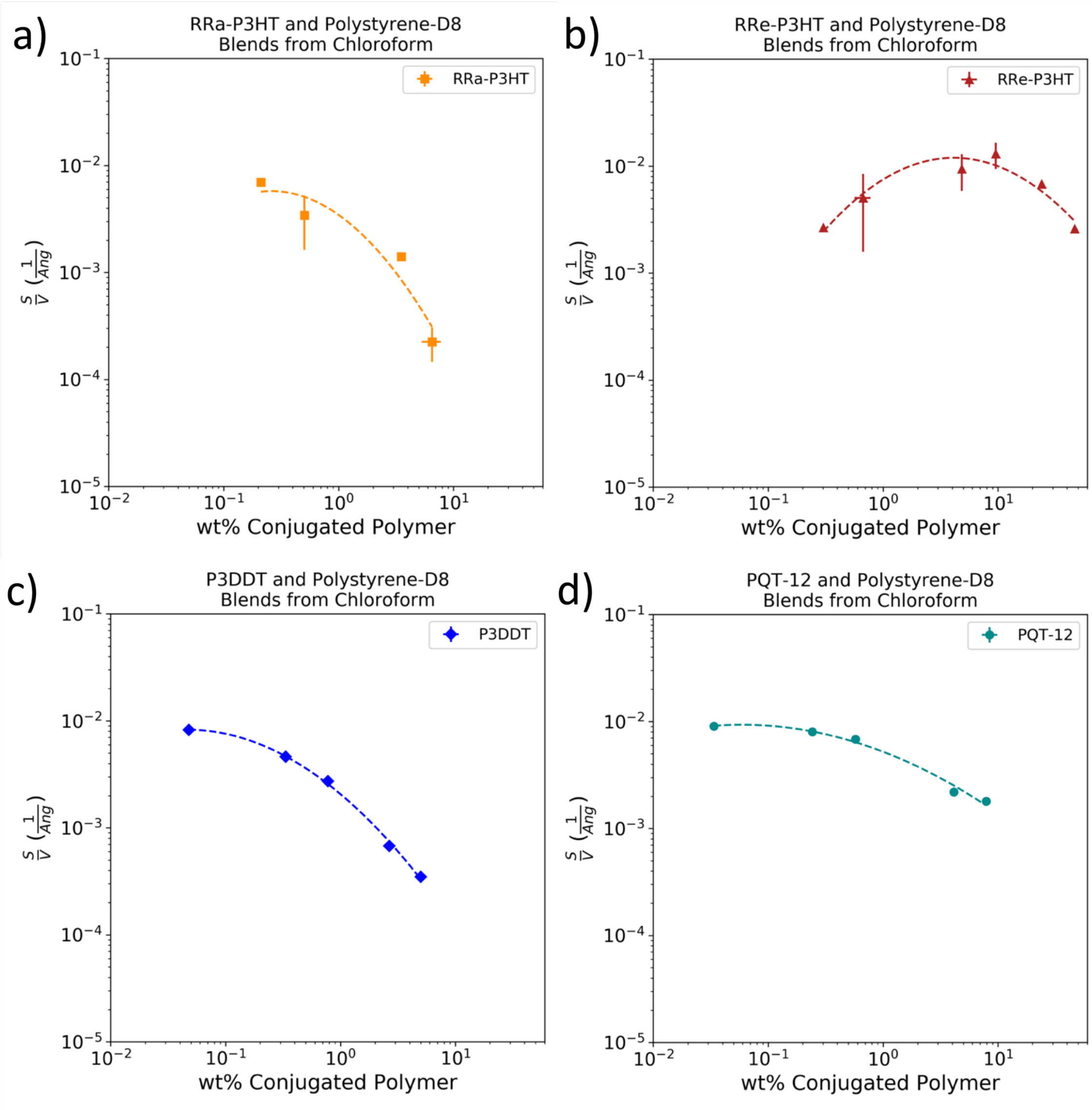

Figure 6.8. Interfacial concentration, $\frac{\mathrm{S}}{\mathrm{V}}$, for CP and PS-D8 blends cast from solutions in chloroform. CP used in each blend is either (a) RRa-P3HT, (b) RRe-P3HT, (c) P3DDT, or (d) PQT-12. When present, vertical and horizontal error bars correspond to the standard deviation of $\frac{\mathrm{S}}{\mathrm{V}}$ and CP concentration, respectively, as determined by sample replicates ($n \leq 3$). Dashed lines show polynomial fit to guide the eye only.

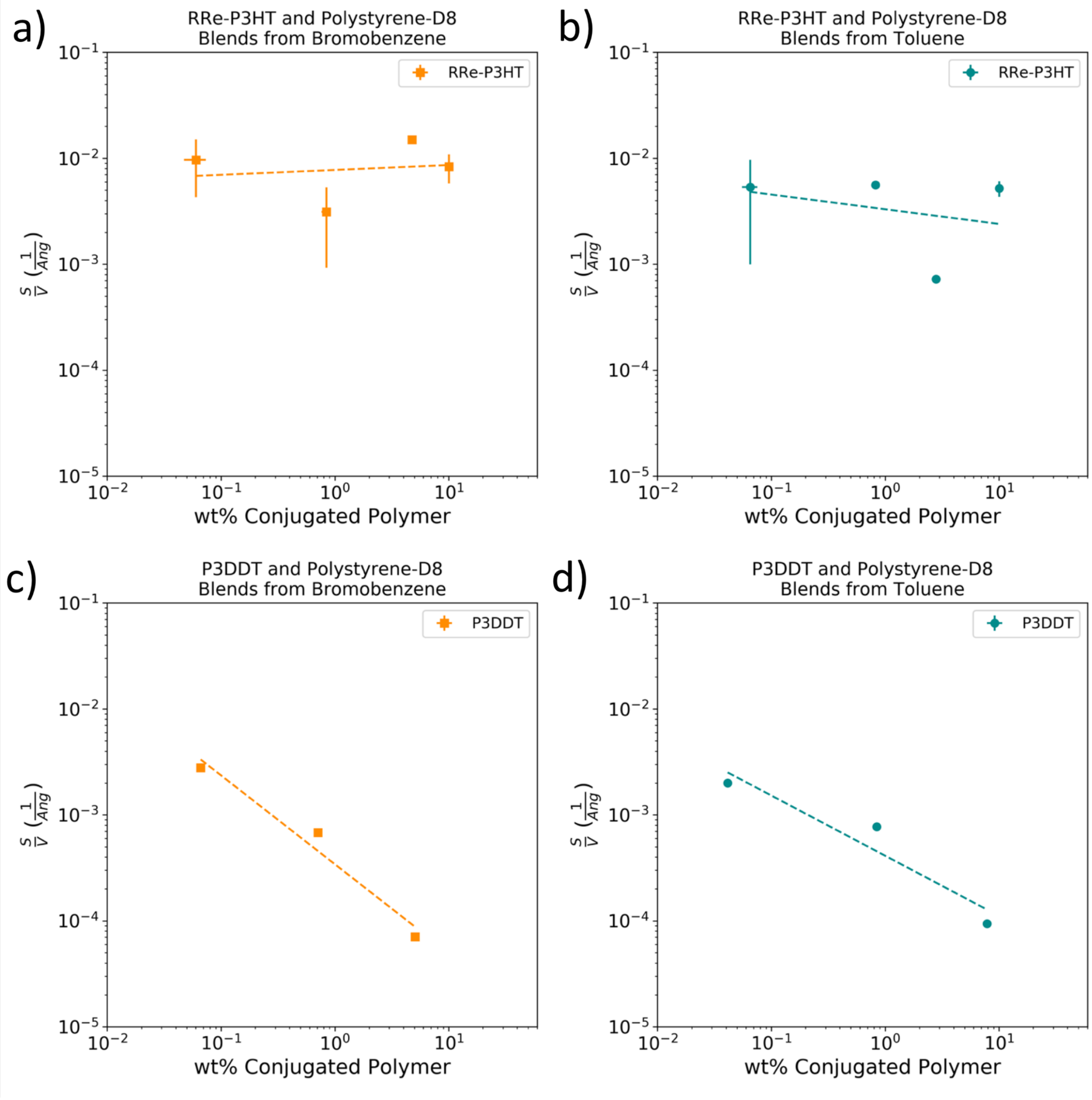

Figure 6.9. Interfacial concentration, $\frac{S}{V}$, for CP and PS-D8 blends cast from solutions in bromobenzene (a and c) or toluene (b and d). CP used in each blend is either RRe-P3HT (a and b) or P3DDT (c and d). When present, vertical and horizontal error bars correspond to the standard deviation of $\frac{S}{V}$ and CP concentration, respectively, as determined by sample replicates ($n \leq 3$). Dashed lines show a polynomial or linear fit to guide the eye only.

6.4.3 *SANS/USANS Form Factors*

Utilizing a combined, multi-component form factor for these blends allows us to model the SANS and USANS data and extract quantitative characterizations of the conformations formed by both the PS and CP phases. We first fit the data for PS-D8 control samples to a Guinier-Porod model alone, which described the density fluctuations in the PS phase. The dimensional parameter was determined to be 2.5 and the radius of gyration to be 180 Å. The parameters for the Guinier-Porod PS component of the combined model was then held constant (scaled proportionally to concentration) to reduce computational expense of the fits and the number of variable parameters.

In the SANS data for RRa-P3HT, P3DDT, and PQT-12 blends (Figure 6.10), we observe a Guinier region at low-q shifting to lower values as CP concentration rises, indicative of growing globular domains of the CP phase and either a 'sphere' or 'ellipsoid' model alone was sufficient to model the scattering profiles. In Figure 6.10d, the radius of gyration for these globular domains is plotted as a function of concentration, and we observe a steep transition between small- and large-scale phase aggregates. Using a logistic function, we can approximate the critical concentration, C_{crit}, at which this transition happens to be at least 6.5 wt% for RRa-P3HT samples, 1.4 wt % for P3DDT samples, less than 0.034 wt% for PQT-12 samples, and 1.4 wt% for RRe-P3HT samples. This behavior of growing globular domains is consistent with the results from the Porod analysis. RRa-P3HT samples display larger globular domains and a higher degree of phase separation while the PQT-12 and P3DDT samples display smaller globular domains and a lower degree of phase separation.

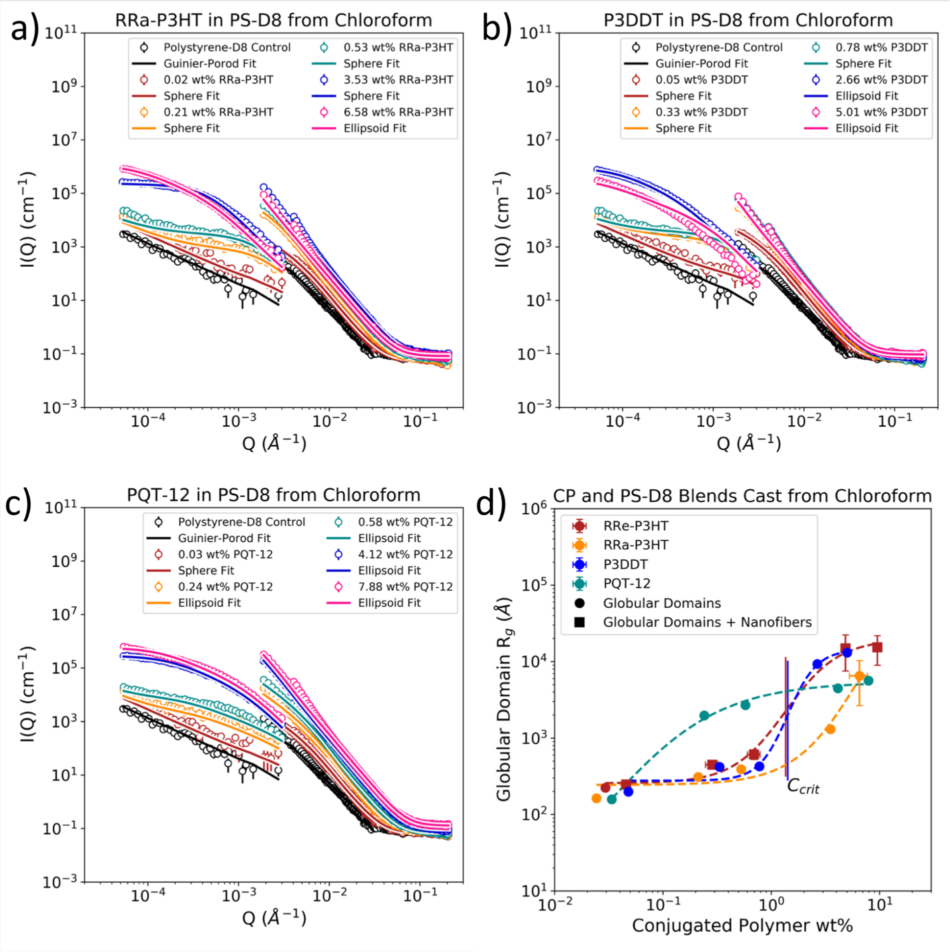

Figure 6.10. Small-angle neutron scattering (SANS) and smeared ultra-small-angle neutron scattering (USANS) data for blends made from (a) RRa_P3HT, (b) P3DDT, or (c) PQT-12 in PS-D8 cast from solutions in chloroform. The CP phase was modeled using sphere or ellipsoid fits. All of these combined models included a common Guinier-Porod fit to account for the PS-D8 phase, and a representative Guinier-Porod fit for a PS-D8 control sample is shown on all plots. Fits for remaining replicates as well as P3DDT and PS-D8 samples cast from toluene or bromobenzene are provided in the supporting information in Figures S16 and S17, respectively. (d) Radius of gyration for the globular domain phase (spheres, ellipsoids) in all replicate blends of RRa-P3HT, P3DDT, PQT-12 or RRe-P3HT in PS-D8 from chloroform. A fit of the logistic function is provided as a trendline only to guide the eye and estimate C_{crit}. When present, vertical and horizontal error bars correspond to the standard deviation of R_g and CP concentration, respectively, as determined by sample replicates ($n \leq 3$). SANS data and fits for the RRe-P3HT samples are discussed in Figure 6.11.

Similar plots for RRe-P3HT samples cast from solutions in chloroform, toluene or bromobenzene are provided in Figure 6.11, and for many of these samples, a model that only accounted for globular domains was inadequate at capturing the scattering profiles. It is known that RRe-P3HT samples tend to form nanofibers with rectangular cross-sections under favorable conditions[48–51], and considering the feature/slope change occurring in the mid- to high-*q* region of the data, an additional form factor was required to capture this structure. In this work, we utilize a cylindrical form factor rather than one with a rectangular cross section as it was still sufficient to model the rod-like structure of the nanofibers while minimizing the amount of fitting parameters. We again inspect the RRe-P3HT chains that remain in the globular domains and find a critical concentration associated with a transition from small- to large-scale aggregates to be less than 0.63 wt% for RRe-P3HT samples cast from toluene, 1.5 wt% for samples cast from chloroform, and at least 10 wt% for samples cast from bromobenzene. In the following section, we focus on the RRe-P3HT that was found present in a nanofiber form.

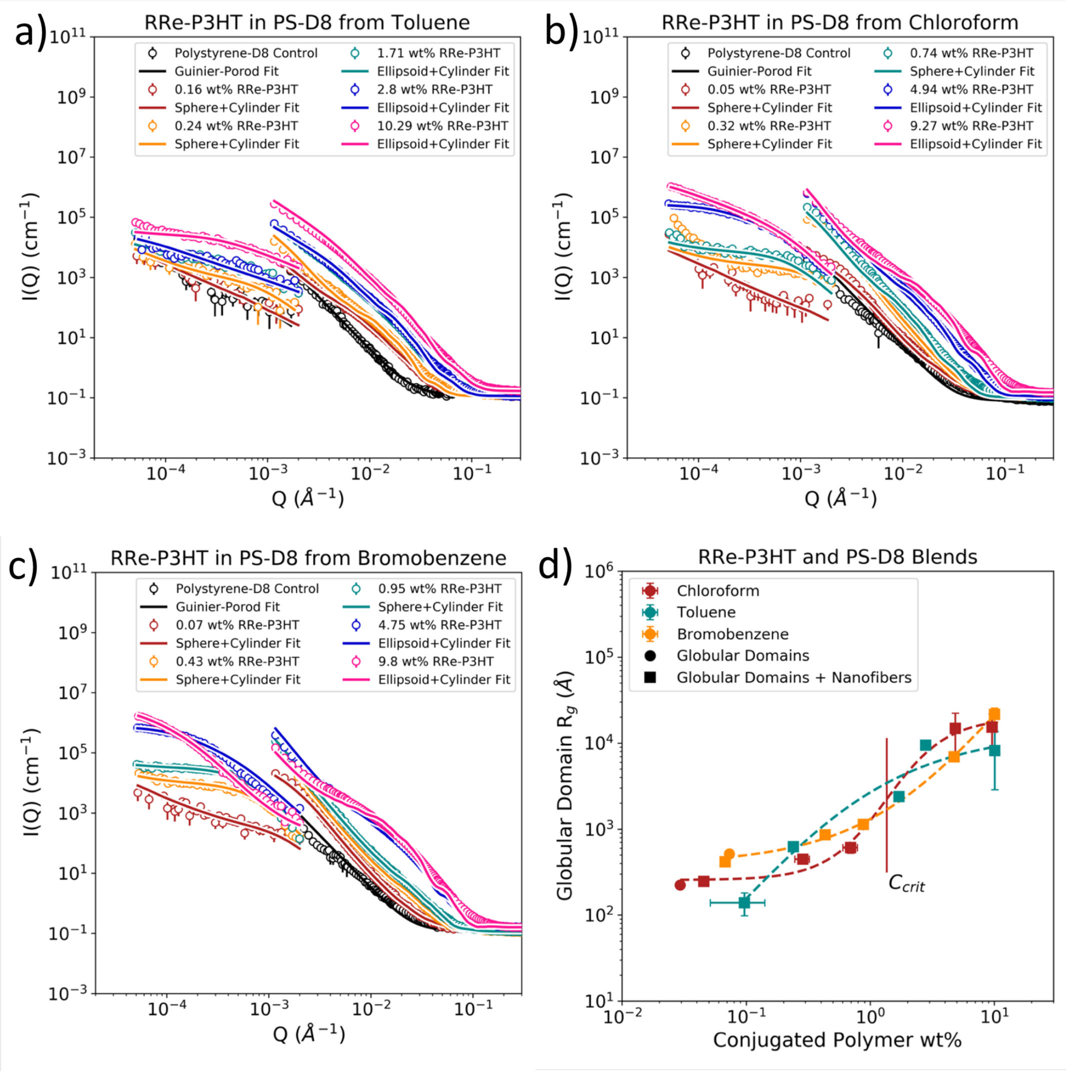

Figure 6.11. Small-angle neutron scattering (SANS) and smeared ultra-small-angle neutron scattering (USANS) data for blends made from regio-regular RRe-P3HT and PS-D8 cast from solutions in (a) toluene, (b) chloroform, or (c) bromobenzene. The CP phase was modeled using sphere, ellipsoid, sphere+cylinder or ellipsoid+cylinder fits. All of these combined models included a common Guinier-Porod fit to account for the PS-D8 phase, and a representative fit for a pure, PS-D8 control sample is also shown. Fits for remaining sample replicates are provided in Figures S18-S20 of the supporting information. (d) Radius of gyration for the globular domain phase (spheres, ellipsoids) in all replicate blends of RRe-P3HT in PS-D cast from chloroform, toluene, or bromobenzene. A fit of the logistic function is provided as a trendline only to guide the eye and estimate C_{crit}. When present, vertical and horizontal error bars correspond to the standard deviation of R_g and CP concentration, respectively, as determined by sample replicates ($n \leq 3$).

6.4.4 *Nanofiber Characterization*

By extracting the fraction of RRe-P3HT present in nanofiber form (x_k), we can observe how the use of different solvents during the film preparation process affects the final conformation in the solid state. Shown in Figure 6.12a is the concentration of nanofibers versus the total CP concentration in RRe-P3HT blends cast from solutions in chloroform, toluene, and bromobenzene. Points that lie along the diagonal line indicate that all CP is present in nanofiber form, while points that lie far away indicate that the majority of the CP chains are present in the globular domains. By comparing points at similar concentrations, we find that samples cast from solutions in toluene tend to form higher amounts of nanofibers in the final solid blends. Chloroform and bromobenzene were the quickest and slowest samples to dry, respectively, but P3HT has the lowest solubility in toluene specifically. Although the crystallization of the P3HT occurs during the drying process of these materials, this data suggests that solubility rather than drying time is the dominating factor in encouraging nanofiber growth. In Figure 6.12b, the cross sectional radius of these nanofibers is shown and we find that nanofibers formed from toluene solutions are relatively constant in size, indicating growth along the length of the fiber rather than the width. At high concentrations, nanofibers formed from solutions in bromobenzene or chloroform display a similar size while at lower concentrations we observe them to be slightly thinner.

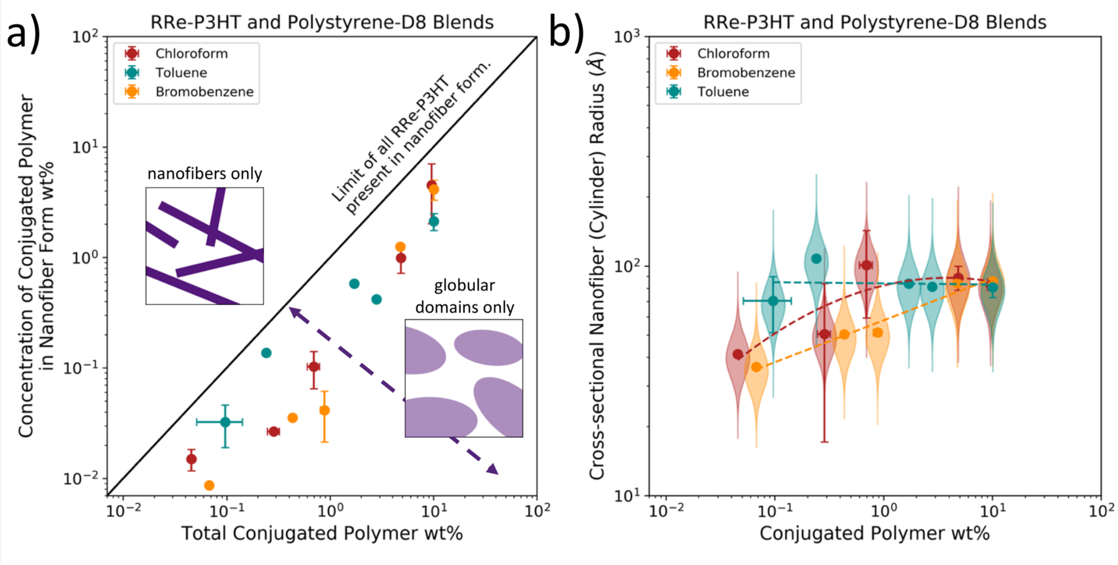

Figure 6.12. (a) Concentration of CP present in the nanofiber form and (b) cross-sectional nanofiber size (cylinder radius) versus total CP concentration in the blends of RRe-P3HT and PS-D8 cast from solutions in chloroform, toluene or bromobenzene. Dashed lines show polynomial fits to guide the eye only. The violin plot distribution for each marker shows the distribution of cylinder radii based on the polydispersity that is used in the SANS model.

WAXS was used to further characterize the preferred growth direction of the crystalline phase within these RRe-P3HT and PS blends. In Figure 6.13 we show the WAXS data for RRe-P3HT samples cast from chloroform, bromobenzene and toluene. It has been explored in past work from our group,[3] as well as many in the literature,[49,52,53] that nanofibers tend to grow lengthwise along the pi-stacking direction of the crystal. If we observe the pi-stacking peak at approximately 1.7 $Å^{-1}$, we notice growth relative to the lamellar peak at approximately 0.4 $Å^{-1}$ as the solvent quality is reduced. This would be consistent with the formation of more nanofibers (preferred pi-stacking crystallization) in the samples cast from a moderate solvent of toluene. In Figure 6.13d, we plot the pi-stacking to lamellar peak high ratio for blends of RRe-P3HT and PS-D8 as well as blends cast from RRe-P3HT-2 and PS-H8. However, we do not observe the same behavior in the

RRe-P3HT-2 samples, indicating that it is not only the polymer-solvent interactions that impact the self-assembly but also the molecular weight of the conjugated component. Regardless, this further emphasizes that the solution-state interactions have a significant impact on the final conformation in the solid state.

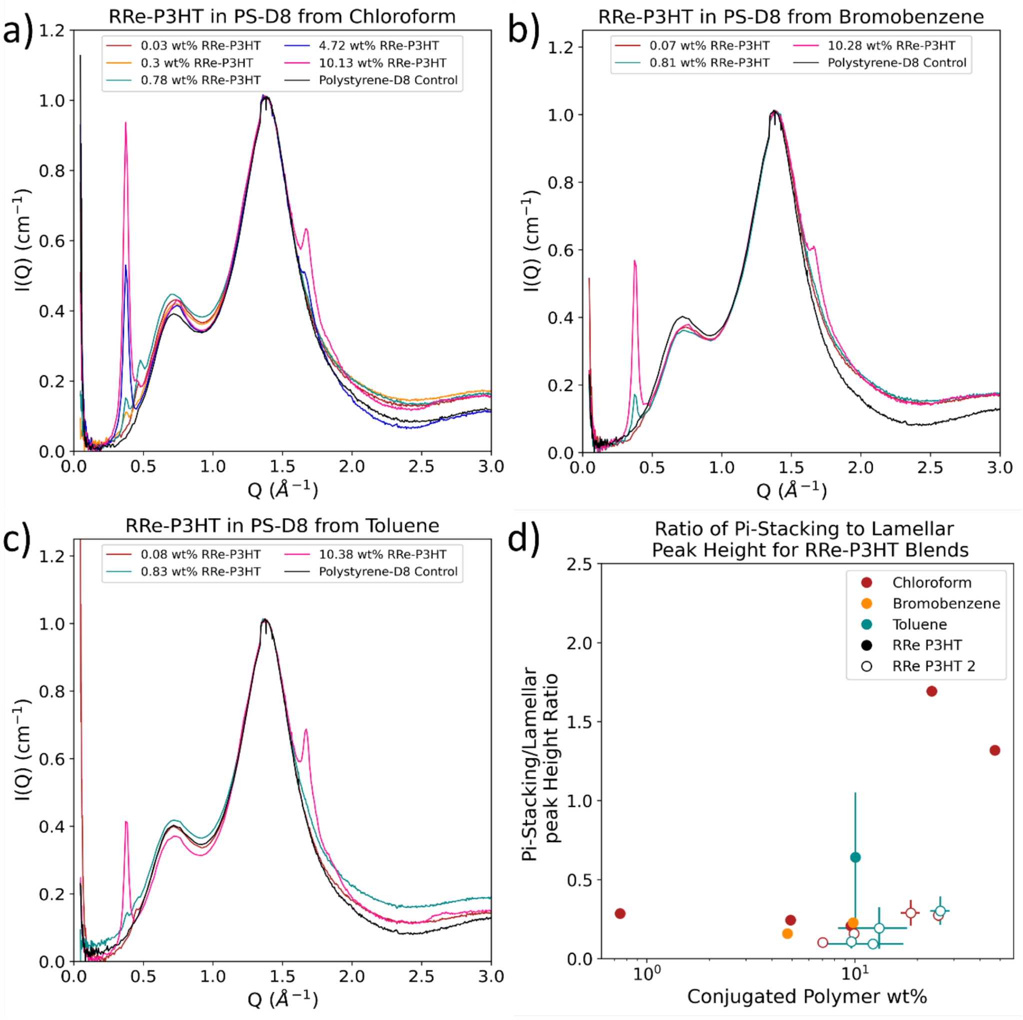

Figure 6.13. Wide-angle X-ray scattering (WAXS) data for blends comprised of RRe-P3HT and PS-D8 cast from solutions in (a) chloroform, (b) bromobenzene, and (c) toluene. (d) Pi-stacking:lamellar peak height ratio for all replicates of RRe-P3HT and PS-D8 or RRe-P3HT-2 and PS-H8 blends cast from solutions in bromobenzene, chloroform, and toluene.

6.4.5 *Blend Conductivity*

Finally, we collected conductivity data for all our blends to relate the nano-scale morphology to the macroscopic performance as provided in Figure 6.14. Many of our samples were highly insulating, most likely due to the thickness of the film and limited sensitivity of our instrumentation. Moreover, these samples were not doped, which is a common technique to improving charge transport in pure CPs.[54] As the amount of P3HT is increased in the samples, we observed significant improvement in the conductivity of the blends that correlate well with higher pi-stacking to lamellar peak ratios showed in Figure 6.13d and tells us that nanofiber formation is indeed favorable for improved charge transport. Interestingly, we can also capture similar conductivities in a small amount of P3DDT samples even though nanofiber formation was not observed for these blends specifically.

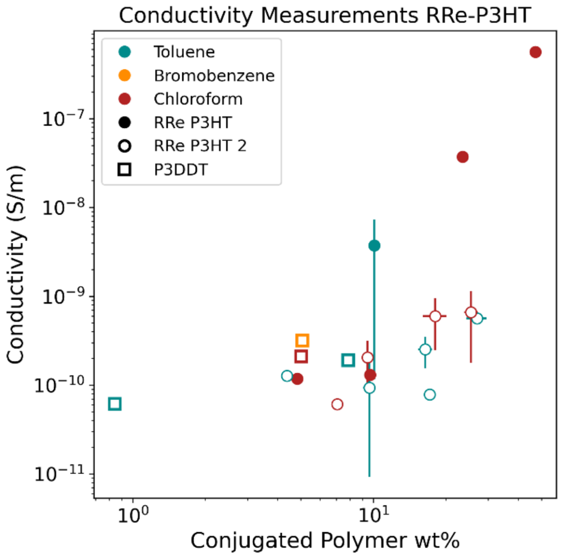

Figure 6.14. Conductivity data for blends comprised of RRe-P3HT or P3DDT in PS-D8 or blends comprised of RRe-P3HT-2 in PS-H8 cast from solutions in toluene, bromobenzene or chloroform.

6.4.6 *Blend Conformation and Morphology*

A schematic of the proposed molecular conformation and self-assembly in these polythiophene-polystyrene blends is shown in Figure 6.15 that takes into consideration results from SANS, WAXS, and conductivity measurements. The CP is present as free chains, amorphous or semi-crystalline globular domains, and/or nanofibers. For RRa-P3HT, P3DDT, and PQT-12, models with a globular domain only (sphere or ellipsoid) were sufficient to model the SANS data, as shown in Figure 6.10, indicating significantly phase separated networks that were consistent with the extracted Porod exponent of 4 (sharp interfaces). However, crystalline peaks in the WAXS data for P3DDT and PQT-12 samples indicate that the globular domains include both amorphous and crystalline phase of the CP but SANS modeling did not suggest any formation of nanofibers. Moreover, we find that the RRa-P3HT samples had the highest degree of phase separation, as shown by the largest size of globular domains when compared so either P3DDT or PQT-12 samples in both the Porod analysis and SANS modelling (Figure 6.8 and Figure 6.10, respectively).

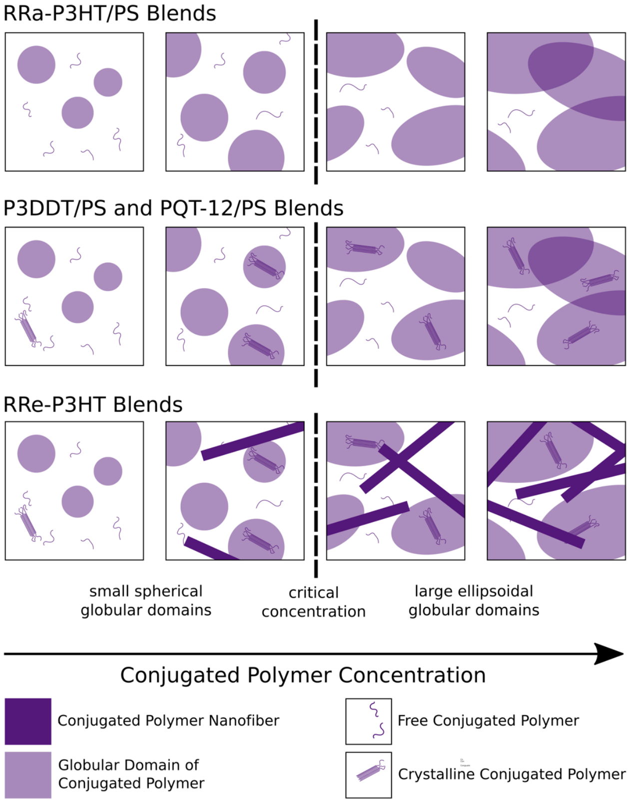

Figure 6.15. Proposed morphology of the CP phase in blends of RRe-P3HT, RRa-P3HT, P3DDT or PQT-12 and PS-D8.

Conversely, we find nanofiber formation combined with semi-crystalline globular domains in blends comprised of RRe-P3HT and PS. By using a moderate solvent (toluene), a higher amount of nanofibers can be formed in the blend compared to samples cast from good solvents, as shown in the nanofiber characterization in Figure 6.12. These nanofibers were able to form a network of charge transport pathways that could be directly correlated to the macroscopic conductivity shown in Figure 6.14 and WAXS analysis in Figure 6.13. Blends that were comprised of RRe-P3HT-2 did not display a similar electronic performance, indicating that the polymer-solvent interactions are not the only influencer on the final morphology and that molecular weight of the CP should be considered. The effect of molecular weight and chain folding in P3HT on the dimensionality and exciton coupling of nanofibers is a known phenomenon in the literature[49,51,55] and consistent with the observations in our present work. Nevertheless, our WAXS and conductivity analyses have allowed us to correlate the preferred direction of crystallization, degree of nanofiber formation, and macroscopic performance in these blends. Finally, we note the observed conductivity in the P3DDT blends despite the lack of evidence for nanofiber conformation. If we recall previous discussions on the effects of morphology and tie chains on the charge transport mechanisms in CPs, we can similarly hypothesize that the degree of phase aggregation in the semi-crystalline P3DDT is creating sufficient charge transport pathways across the bulk of the film. These results emphasize the importance of understanding these complex interactions between the molecular conformation, self-assembly, and performance in conjugated and commodity polymer blends in order to enable optimized and improved materials in the future.

Lastly, we discuss the critical concentration, C_{crit}, that marks the transition between small- and large-scale globular domains in these blends. In the RRe-P3HT samples, we find this transition to correlate well with solvent quality, indicating that the less-favorable interactions between a moderate solvent (toluene) and CP encourage a higher amount of phase separation. However, this transition in RRa-P3HT, P3DDT, and PQT-12 do not follow a similar trend based on the solubility of each CP in chloroform. Instead, the C_{crit} could be derived from not only the solvent-polymer interactions but also the molecular weights and the specific polymer-polymer interactions in the solution and solid states. The small set of solution samples exploring the behavior of RRe-P3HT dissolved in toluene with and without the presence of PS provided a preliminary look into these complex behaviors. Shown in Figure 6.16 are the SANS profiles for these samples overlaid with a fractal power law model in the mid-q range. The extracted fractal dimension for the RRe-P3HT phase increased from 1.4 without polystyrene to 2.5 and 2.6 with the presence of polystyrene, indicating a denser nanofiber network as a result of the additional polymer-polymer interactions between these materials. These differing starting conformations in the solution state would likely persist through the drying process and significantly influence the final morphology in the solid-state blends.

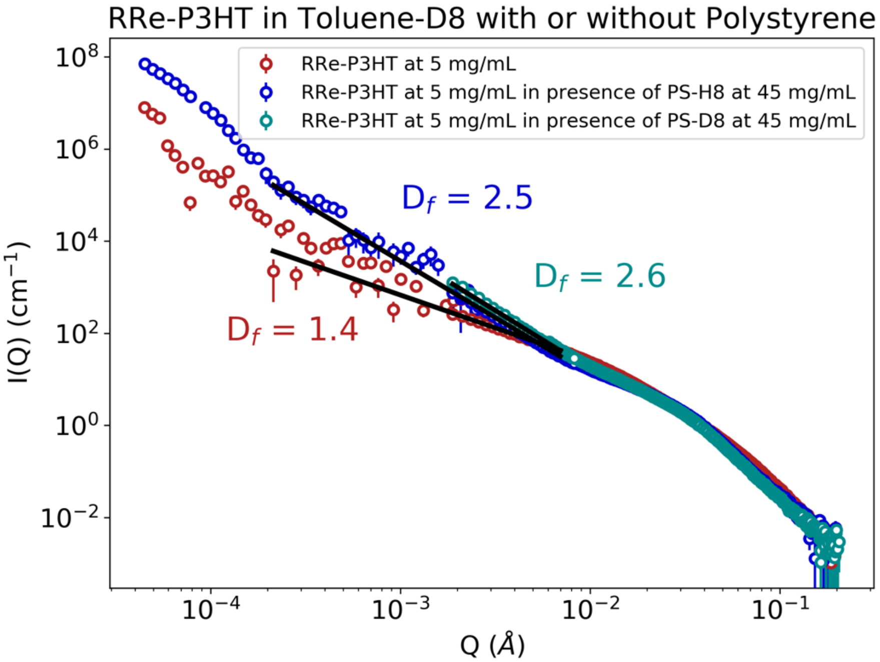

Figure 6.16. Small-angle neutron scattering (SANS) and smeared ultra-small-angle neutron scattering (USANS) data for solutions of RRe-P3HT at 5 mg/mL in toluene-D8, either with or without the presence of polystyrene (PS-H8 or PS-D8) dissolved at 45 mg/mL. The scattering contribution from the polystyrene phase has been subtracted from the blend solutions using pure solutions of either PS-H8 or PS-D8 dissolved at 45 mg/mL. The concentration of RRe-P3HT and PS-H8/PS-D8 corresponds to the starting conditions for solid blend samples at a 10 wt% of RRe-P3HT. Shown overlaid on the data in the mid-Q range is a network power law fit (black lines). Fractal dimensions (D_f) extracted from the fit are provided on the plot in corresponding color to each dataset.

6.5 CONCLUSIONS

In this work, we have used SANS, WAXS and conductivity measurements to explore the relationship between solid-state conformation in polythiophene-polystyrene blends and the macroscopic performance (charge transport). Blends of CPs and insulating commodity polymers are advantageous for reducing cost, improving mechanical durability and extending environmental stability while maintaining electronic performance in organic electronic devices. Blends comprised of RRa-P3HT and PS formed a strongly phase separated amorphous conformation, while blends comprised of P3DDT or PQT-12 with PS formed semi-crystalline globular domains of the CP phase as confirmed by Porod analysis of the SANS data and WAXS measurements. RRe-P3HT samples also formed semi-crystalline globular domains but SANS modeling showed a fraction of the CP also self-assembled into nanofiber networks. With WAXS and conductivity measurements, these nanofibers were found to grow lengthwise along the pi-stacking direction and create charge transport pathways across the bulk of the film that were favorable for charge transport. Moreover, the use of a moderate solvent (toluene) could be used to encourage a higher amount nanofiber formation at lower CP concentrations, indicating that the solution-state interactions significantly influence the final conformation in the solid films. Additional conductive samples of P3DDT and PS, however, remind us that nanofibers are not the only conformation capable of enabling charge transport in these materials. It is important that the relationship between the bulk conformation and self-assembly, processing conditions, and charge transport are well understood in conjugated and commodity polymer blends as to enable improved materials and technologies in the future.

6.6 REFERENCES

(1) Gu, K.; Snyder, C. R.; Onorato, J.; Luscombe, C. K.; Bosse, A. W.; Loo, Y.-L. *Assessing the Huang–Brown Description of Tie Chains for Charge Transport in Conjugated Polymers*. *ACS Macro Lett.* **2018**, *7* (11), 1333–1338. https://doi.org/10.1021/acsmacrolett.8b00626.

(2) Newbloom, G. M.; Kim, F. S.; Jenekhe, S. A.; Pozzo, D. C. *Mesoscale Morphology and Charge Transport in Colloidal Networks of Poly(3-Hexylthiophene)*. *Macromolecules* **2011**, *44* (10), 3801–3809. https://doi.org/10.1021/ma2000515.

(3) Xi, Y.; Wolf, C. M.; Pozzo, L. D. *Self-Assembly of Donor–Acceptor Conjugated Polymers Induced by Miscible 'Poor' Solvents*. *Soft Matter* **2019**, *15* (8), 1799–1812. https://doi.org/10.1039/C8SM02517G.

(4) Xi, Y.; Pozzo, L. D. *Electric Field Directed Formation of Aligned Conjugated Polymer Fibers*. *Soft Matter* **2017**, *13* (21), 3894–3908. https://doi.org/10.1039/C7SM00485K.

(5) Xi, Y.; Li, D. S.; Newbloom, G. M.; Tatum, W. K.; O'Donnell, M.; Luscombe, C. K.; Pozzo, L. D. *Sonocrystallization of Conjugated Polymers with Ultrasound Fields*. *Soft Matter* **2018**, *14* (24), 4963–4976. https://doi.org/10.1039/C8SM00905H.

(6) Li, Z.; Chueh, C.-C.; Jen, A. K.-Y. *Recent Advances in Molecular Design of Functional Conjugated Polymers for High-Performance Polymer Solar Cells*. *Prog. Polym. Sci.* **2019**, *99*, 101175. https://doi.org/10.1016/j.progpolymsci.2019.101175.

(7) Pandey, M.; Kumari, N.; Nagamatsu, S.; Pandey, S. S. *Recent Advances in the Orientation of Conjugated Polymers for Organic Field-Effect Transistors*. *J. Mater. Chem. C* **2019**, *7* (43), 13323–13351. https://doi.org/10.1039/C9TC04397G.

(8) Anantha-Iyengar, G.; Shanmugasundaram, K.; Nallal, M.; Lee, K.-P.; Whitcombe, M. J.; Lakshmi, D.; Sai-Anand, G. *Functionalized Conjugated Polymers for Sensing and Molecular Imprinting Applications*. *Prog. Polym. Sci.* **2019**, *88*, 1–129. https://doi.org/10.1016/j.progpolymsci.2018.08.001.

(9) Fidanovski, K.; Mawad, D. *Conjugated Polymers in Bioelectronics: Addressing the Interface Challenge*. *Adv. Healthc. Mater.* **2019**, *8* (10), 1900053. https://doi.org/10.1002/adhm.201900053.

(10) Wang, M.; Baek, P.; Akbarinejad, A.; Barker, D.; Travas-Sejdic, J. *Conjugated Polymers and Composites for Stretchable Organic Electronics*. *J. Mater. Chem. C* **2019**, *7* (19), 5534–5552. https://doi.org/10.1039/C9TC00709A.

(11) Lu, G.; Blakesley, J.; Himmelberger, S.; Pingel, P.; Frisch, J.; Lieberwirth, I.; Salzmann, I.; Oehzelt, M.; Di Pietro, R.; Salleo, A.; Koch, N.; Neher, D. *Moderate Doping Leads to High Performance of Semiconductor/Insulator Polymer Blend Transistors*. *Nat. Commun.* **2013**, *4* (1), 1588. https://doi.org/10.1038/ncomms2587.

(12) Goffri, S.; Müller, C.; Stingelin-Stutzmann, N.; Breiby, D. W.; Radano, C. P.; Andreasen, J. W.; Thompson, R.; Janssen, R. A. J.; Nielsen, M. M.; Smith, P.; Sirringhaus, H. *Multicomponent Semiconducting Polymer Systems with Low Crystallization-Induced Percolation Threshold*. *Nat. Mater.* **2006**, *5* (12), 950–956. https://doi.org/10.1038/nmat1779.

(13) Kumar, A.; Baklar, M. A.; Scott, K.; Kreouzis, T.; Stingelin-Stutzmann, N. *Efficient, Stable Bulk Charge Transport in Crystalline/Crystalline Semiconductor-Insulator Blends*. *Adv. Mater.* **2009**, *21* (44), 4447–4451. https://doi.org/10.1002/adma.200900717.

(14) Qiu, L.; Wang, X.; Lee, W. H.; Lim, J. A.; Kim, J. S.; Kwak, D.; Cho, K. *Organic Thin-Film Transistors Based on Blends of Poly(3-Hexylthiophene) and Polystyrene with a Solubility-Induced Low Percolation Threshold*. *Chem. Mater.* **2009**, *21* (19), 4380–4386. https://doi.org/10.1021/cm900628j.

(15) Qiu, L.; Lee, W. H.; Wang, X.; Kim, J. S.; Lim, J. A.; Kwak, D.; Lee, S.; Cho, K. *Organic Thin-Film Transistors Based on Polythiophene Nanowires Embedded in Insulating Polymer*. *Adv. Mater.* **2009**, *21* (13), 1349–1353. https://doi.org/10.1002/adma.200802880.

(16) Angunawela, I.; Nahid, M. M.; Ghasemi, M.; Amassian, A.; Ade, H.; Gadisa, A. *The Critical Role of Materials' Interaction in Realizing Organic Field-Effect Transistors Via High-Dilution Blending with Insulating Polymers*. *ACS Appl. Mater. Interfaces* **2020**, *12* (23), 26239–26249. https://doi.org/10.1021/acsami.0c04208.

(17) Selivanova, M.; Chuang, C.-H.; Billet, B.; Malik, A.; Xiang, P.; Landry, E.; Chiu, Y.-C.; Rondeau-Gagné, S. *Morphology and Electronic Properties of Semiconducting Polymer and Branched Polyethylene Blends*. *ACS Appl. Mater. Interfaces* **2019**, *11* (13), 12723–12732. https://doi.org/10.1021/acsami.8b22746.

(18) Li, T.; Xu, L.; Xiao, X.; Chen, F.; Cao, L.; Wu, W.; Tong, W.; Zhang, F. *Enhanced Spin Transport of Conjugated Polymer in the Semiconductor/Insulating Polymer Blend*. *ACS Appl. Mater. Interfaces* **2020**, *12* (2), 2708–2716. https://doi.org/10.1021/acsami.9b16602.

(19) Han, S.; Yu, X.; Shi, W.; Zhuang, X.; Yu, J. *Solvent-Dependent Electrical Properties Improvement of Organic Field-Effect Transistor Based on Disordered Conjugated Polymer/Insulator Blends*. *Org. Electron.* **2015**, *27*, 160–166. https://doi.org/10.1016/j.orgel.2015.09.003.

(20) Nedoma, A. J.; Robertson, M. L.; Wanakule, N. S.; Balsara, N. P. *Measurements of the Composition and Molecular Weight Dependence of the Flory−Huggins Interaction Parameter*. *Macromolecules* **2008**, *41* (15), 5773–5779. https://doi.org/10.1021/ma800698r.

(21) Russell, T. P.; Ito, H.; Wignall, G. D. *Neutron and X-Ray Scattering Studies on Semicrystalline Polymer Blends*. *Macromolecules* **1988**, *21* (6), 1703–1709. https://doi.org/10.1021/ma00184a029.

(22) Bronstein, H. A.; Luscombe, C. K. *Externally Initiated Regioregular P3HT with Controlled Molecular Weight and Narrow Polydispersity*. *J. Am. Chem. Soc.* **2009**, *131* (36), 12894–12895. https://doi.org/10.1021/ja9054977.

(23) Kline, S. R. *Reduction and Analysis of SANS and USANS Data Using IGOR Pro*. *J. Appl. Crystallogr.* **2006**, *39* (6), 895–900. https://doi.org/10.1107/S0021889806035059.

(24) Doucet, M.; King, S.; Butler, P.; Kienzle, P.; Parker, P.; Krzywon, J.; Jackson, A.; Richter, T.; Gonzales, M.; Nielsen, T.; Ferraz, L. R. *SasView (Version 5.0.1)*. 2020.

(25) Doucet, M.; King, S.; Butler, P.; Kienzle, P.; Parker, P.; Krzywon, J.; Jackson, A.; Richter, T.; Gonzales, M.; Nielsen, T.; Ferraz, L. R. *Sasmodels (Version 1.0.1)*. 2020.

(26) Kienzle, P. A.; Krycka, J.; Patel, N.; Sahin, I. *Bumps (Version 0.7.11)*. University of Maryland: College Park, MD 2011.

(27) Wolf, C. pozzo-research-group/c-wolf-blends-morphology: Initial Development (Version v0.1.0) http://doi.org/10.5281/zenodo.4035166.

(28) Porod, G. *Die Röntgenkleinwinkelstreuung von Dichtgepackten Kolloiden Systemen*. *Kolloid-Zeitschrift* **1951**, *124* (2), 83–114. https://doi.org/10.1007/BF01512792.

(29) Kozlov, G. Z.; Zaikov, G. E. *Structure of the Polymer Amorphous State*; Taylor & Francis Group, LLC: Boca Raton, FL, 2004.

(30) Furuya, H.; Mondello, M.; Yang, H.-J.; Roe, R.-J.; Erwin, R. W.; Han, C. C.; Smith, S. D. *Molecular Dynamics Simulation of Atactic Polystyrene. 2. Comparison with Neutron Scattering Data*. *Macromolecules* **1994**, *27* (20), 5674–5680. https://doi.org/10.1021/ma00098a022.

(31) Song, H. H.; Roe, R. J. *Structural Change Accompanying Volume Change in Amorphous Polystyrene as Studied by Small and Intermediate Angle X-Ray Scattering*. *Macromolecules* **1987**, *20* (11), 2723–2732. https://doi.org/10.1021/ma00177a016.

(32) Roe, R. J.; Curro, J. J. *Small-Angle x-Ray Scattering Study of Density Fluctuation in Polystyrene Annealed below the Glass Transition Temperature*. *Macromolecules* **1983**, *16* (3), 428–434. https://doi.org/10.1021/ma00237a018.

(33) Wendorff, J. H. *The Structure of Amorphous Polymers*. *Polymer (Guildf).* **1982**, *23* (4), 543–557. https://doi.org/10.1016/0032-3861(82)90094-5.

(34) Renninger, A. L.; Uhlmann, D. R. *Structure of Glassy Polymers. V. Small-Angle x-Ray Scattering from Polystyrene*. *J. Polym. Sci. Polym. Phys. Ed.* **1978**, *16* (12), 2237–2244. https://doi.org/10.1002/pol.1978.180161210.

(35) Geil, P. H. *Morphology of Amorphous Polymers*. *Ind. Eng. Chem. Prod. Res. Dev.* **1975**, *14* (1), 59–71. https://doi.org/10.1021/i360053a014.

(36) *Polymers and Neutron Scattering*; Higgins, J. S., Benoit, H. C., Eds.; Oxford University Press Inc.: New York, 1994.

(37) Endo, H. *Study on Multicomponent Systems by Means of Contrast Variation SANS. Phys. B Condens. Matter* **2006**, *385–386*, 682–684. https://doi.org/10.1016/j.physb.2006.05.290.

(38) Ilavsky, J.; Zhang, F.; Allen, A. J.; Levine, L. E.; Jemian, P. R.; Long, G. G. *Ultra-Small-Angle X-Ray Scattering Instrument at the Advanced Photon Source: History, Recent Development, and Current Status*. *Metall. Mater. Trans. A* **2013**, *44* (1), 68–76. https://doi.org/10.1007/s11661-012-1431-y.

(39) Ilavsky, J.; Jemian, P. R.; Allen, A. J.; Zhang, F.; Levine, L. E.; Long, G. G. *Ultra-Small-Angle X-Ray Scattering at the Advanced Photon Source*. *J. Appl. Crystallogr.* **2009**, *42* (3), 469–479. https://doi.org/10.1107/S0021889809008802.

(40) Ilavsky, J.; Zhang, F.; Andrews, R. N.; Kuzmenko, I.; Jemian, P. R.; Levine, L. E.; Allen, A. J. *Development of Combined Microstructure and Structure Characterization Facility for in Situ and Operando Studies at the Advanced Photon Source*. *J. Appl. Crystallogr.* **2018**, *51* (3), 867–882. https://doi.org/10.1107/S160057671800643X.

(41) Pozzo, L. USAXS 48 Solid Film Holder https://www.thingiverse.com/thing:4639006/files (accessed Nov 2, 2020).

(42) Ilavsky, J. *Nika : Software for Two-Dimensional Data Reduction*. *J. Appl. Crystallogr.* **2012**, *45* (2), 324–328. https://doi.org/10.1107/S0021889812004037.

(43) Gillich, D. J.; Kovanen, A.; Danon, Y. *Deuterated Target Comparison for Pyroelectric Crystal D–D Nuclear Fusion Experiments*. *J. Nucl. Mater.* **2010**, *405* (2), 181–185. https://doi.org/10.1016/j.jnucmat.2010.08.012.

(44) Wallace, W. E.; Beck Tan, N. C.; Wu, W. L.; Satija, S. *Mass Density of Polystyrene Thin Films Measured by Twin Neutron Reflectivity*. *J. Chem. Phys.* **1998**, *108* (9), 3798–3804. https://doi.org/10.1063/1.475769.

(45) Toolan, D. T. W.; Barker, R.; Gough, T.; Topham, P. D.; Howse, J. R.; Glidle, A. *Gravimetric and Density Profiling Using the Combination of Surface Acoustic Waves and Neutron Reflectivity*. *J. Colloid Interface Sci.* **2017**, *487*, 465–474. https://doi.org/10.1016/j.jcis.2016.10.039.

(46) Hellmann, C.; Treat, N. D.; Scaccabarozzi, A. D.; Razzell Hollis, J.; Fleischli, F. D.; Bannock, J. H.; de Mello, J.; Michels, J. J.; Kim, J.-S.; Stingelin, N. *Solution Processing of Polymer Semiconductor: Insulator Blends-Tailored Optical Properties through Liquid-Liquid Phase Separation Control*. *J. Polym. Sci. Part B Polym. Phys.* **2015**, *53* (4), 304–310. https://doi.org/10.1002/polb.23656.

(47) Park, Y. D.; Lee, H. S.; Choi, Y. J.; Kwak, D.; Cho, J. H.; Lee, S.; Cho, K. *Solubility-Induced Ordered Polythiophene Precursors for High-Performance Organic Thin-Film Transistors*. *Adv. Funct. Mater.* **2009**, *19* (8), 1200–1206.

https://doi.org/10.1002/adfm.200801763.

(48) Keum, J. K.; Xiao, K.; Ivanov, I. N.; Hong, K.; Browning, J. F.; Smith, G. S.; Shao, M.; Littrell, K. C.; Rondinone, A. J.; Andrew Payzant, E.; Chen, J.; Hensley, D. K. *Solvent Quality-Induced Nucleation and Growth of Parallelepiped Nanorods in Dilute Poly(3-Hexylthiophene) (P3HT) Solution and the Impact on the Crystalline Morphology of Solution-Cast Thin Film*. *CrystEngComm* **2013**, *15* (6), 1114–1124. https://doi.org/10.1039/C2CE26666K.

(49) Liu, J.; Arif, M.; Zou, J.; Khondaker, S. I.; Zhai, L. *Controlling Poly(3-Hexylthiophene) Crystal Dimension: Nanowhiskers and Nanoribbons*. *Macromolecules 42* (24), 9390–9393. https://doi.org/10.1021/ma901955c.

(50) Bastianini, F.; Pérez, G. E.; Hobson, A. R.; Rogers, S. E.; Parnell, A. J.; Grell, M.; Gutiérrez, A. F.; Dunbar, A. D. F. *In−situ Monitoring Poly(3-Hexylthiophene) Nanowire Formation and Shape Evolution in Solution via Small Angle Neutron Scattering*. *Sol. Energy Mater. Sol. Cells* **2019**, *202*, 110128. https://doi.org/10.1016/j.solmat.2019.110128.

(51) Baghgar, M.; Labastide, J. A.; Bokel, F.; Hayward, R. C.; Barnes, M. D. *Effect of Polymer Chain Folding on the Transition from H- to J-Aggregate Behavior in P3HT Nanofibers*. *J. Phys. Chem. C* **2014**, *118* (4), 2229–2235. https://doi.org/10.1021/jp411668g.

(52) Agbolaghi, S.; Zenoozi, S. *A Comprehensive Review on Poly(3-Alkylthiophene)-Based Crystalline Structures, Protocols and Electronic Applications*. *Org. Electron. 51*, 362–403. https://doi.org/10.1016/j.orgel.2017.09.038.

(53) Merlo, J. A.; Frisbie, C. D. *Field Effect Transport and Trapping in Regioregular Polythiophene Nanofibers*. *J. Phys. Chem. B 108* (50), 19169–19179. https://doi.org/10.1021/jp047023a.

(54) Salzmann, I.; Heimel, G.; Oehzelt, M.; Winkler, S.; Koch, N. *Molecular Electrical Doping of Organic Semiconductors: Fundamental Mechanisms and Emerging Dopant Design Rules*. *Acc. Chem. Res.* **2016**, *49* (3), 370–378. https://doi.org/10.1021/acs.accounts.5b00438.

(55) Snyder, C. R.; Nieuwendaal, R. C.; DeLongchamp, D. M.; Luscombe, C. K.; Sista, P.; Boyd, S. D. *Quantifying Crystallinity in High Molar Mass Poly(3-Hexylthiophene)*. *Macromolecules* **2014**, *47* (12), 3942–3950. https://doi.org/10.1021/ma500136d.

Chapter 7. APPENDIX

7.1 PYTHON TOOLS FOR NEUTRON & X-RAY SCATTERING DATA ANALYSIS

In Chapter 6, we briefly discussed how the sasmodels[1] and Sasview[2] tools for Python were used to semi-automate the SANS fitting procedures and foster reproducible analysis for the investigation of phase conformation and self-assembly in polythiophene-polystyrene blends. The advantages of using these Python tools in our work specifically included the ability to efficiently generate combined models without having to do any additional coding of the form factors, constrain parameters with different distributions (e.g. normal vs. uniform), constrain parameters with respect to mass balances (e.g. conjugated polymer concentration), and parallelize the fitting by running the scripts on the local supercomputer at the University of Washington. The repository with all scripts and notebooks corresponding to our work presented in Chapter 6 can be found at https://github.com/pozzo-research-group/c-wolf-blends-morphology[3]. However, an additional repository with a more tutorial-based approach can be found at https://github.com/caitwolf/sas-torials as a reference guide for getting started applying sasmodels and Sasview Python tools to your own system as well as more advanced applications, such as mass balances or combined models.

7.2 A COMPREHENSIVE DATA REPOSITORY FOR SMALL-ANGLE NEUTRON SCATTERING DATA

Data science and machine learning (ML) are powerful, interdisciplinary tools with applications in a wide array of research applications.[4,5] Many equate data science with only ML tools, but the field also encompasses data management (e.g. databases) and data visualization tools.[4] Data science can not only help researchers process and manage large amounts of data automatically, but it can also provide alternative approaches to uncovering hidden information not accessible with more traditional analysis methods, or it can even improve the current workflow of scientists, helping them to work more efficiently.[4,5] For example, Gomez-Bombarelli et al. utilized machine learning to more efficiently 'discover' promising TADF emitters for lower cost OLED devices. The group started with a search space of 1.6 million potential molecules, and performing quantum calculations and manual expert sorting on all materials to narrow down the list for future synthesis would have been unfeasible. Instead, the group employed ML methods to guide the quantum calculations and researcher sorting. By continuously refining the model with quantum calculation results, it could uncover different phase spaces within the potential molecules. It then focused future quantum calculations on only molecules predicted to have the most potential for a good OLED material. In the end, the researchers synthesized four of the molecules found with their model and achieved external quantum efficiencies up to 22.0%.[6]

The X-ray scattering community has already begun to realize the potential for applications of machine learning since more data is being collected faster than ever.[7,8] For example, x-ray free electron laser experiments collect over 100,000 snapshots every hour, but only 1-10% of that data is significant. The remaining snapshots are results of misalignment or contaminant particles.[7] Yoon et al. applied machine learning sorting algorithms to help filter out the bad data. Two experts sorted the test data with a 95% agreement to each other, and the model was able to achieve a 90% agreement with the experts.[7] Using this type of model could significantly reduce the amount of manual work needed and allow researchers to focus more on the experiment. Franke et al. applied machine learning for the structural analysis of biomacromolecular solutions. They trained a classification algorithm with simulated X-ray scattering profiles of various shapes, from compact spheres to extended rods. Based on a provided scattering pattern, the model would be able to provide the closest structural conformation of the system.[9] Kiapour and coworkers used machine learning to help analyze large amounts of x-ray scattering images and label important features within the images, such as the type of isotropy present. The model was also capable of searching the dataset for similar images to one another, a characteristic that could be extremely useful in finding other samples that result in similar scattering profiles to the present sample.[8]

Large amounts of well-stored data are required to enable these powerful machine learning models. For supervised learning specifically, this data must be accurately labeled for meaningful model training. To operate at this intersection of big data and machine learning in the scattering community, we must consider database management systems. There are a few available scattering databases that provide meaningful value to research in the scattering community.[10,11] Kikhney et al. developed DARA, a database that includes over 150,000 simulated x-ray scattering patterns for protein and nucleic acid molecules found in the Protein Data Bank.[10] Researchers can utilize this database by submitting a theoretical or experimental scattering pattern, and find the nearest structural neighbors in the database. However, a particular disadvantage of these databases is their limited scope. There is an opportunity to incorporate modern data management across scattering techniques, rather than a specific research focus, and capture not only the raw scattering data but meaningful meta data that can be used to develop powerful, interdisciplinary machine learning models. The small-angle neutron scattering (SANS) community provides one opportunity for early implementation of a comprehensive repository, where large amounts of raw and meta-data are being collected but stored in a disconnected format, limiting its value. In this section, we explore the challenges and important considerations to make for such an opportunity.

7.2.1 *Raw- and Meta-Data: What Should Be Included and How?*

The question of what data to include, and in what format, is not new to the database community. More broadly, we can think about its importance for reproducibility in the scientific community. The International Union of Crystallography (IUCr) is a noteworthy organization working towards answering these questions and their efforts are outlined in the work of Kroon-Batenburg et al. In 2011, the IUCr formed the Diffraction Data Deposition Working Group to develop policies relating to the proper retention and formatting of raw and meta-data in the crystallography fields, especially as they move in the direction of open-science.[12] Moreover, access to raw data in the longer term is deemed important for not only reproducibility, but also in preparation for possible changes to standard reduction procedures in the field.[12] Trewhella and coworkers discuss the extension of these efforts into the scattering community, specifically for biomolecules. The paper outlines specific guidelines of required, suggested, and optional data for researchers to include in publications that covers information about the samples, data collection, reduction and analysis procedures, and any corresponding modelling performed.[13] When considering SANS data through these lenses, one begins to consider the large amount of data and meta-data that may, or may not, be relevant for a comprehensive database. Shown in Table 7.6 is a brief list of the data categories with examples of meta-data that are important to consider in future implementation of a comprehensive SANS repository.

Table 7.6. Raw data and meta-data classifications for small-angle neutron scattering experiments.

Data		
Raw Data (1D/2D)	Reduced Data	Model Fitting
Published Data		
Instrument Configuration		
Radiation Source	Instrument	Wavelength
Guides	Attenuators	Sample Detector Distance

Detector Type	Sample Environment	
Measurement Conditions		
Temperature	Pressure	Count Time
Samples		
Composition	Sample Cell	Activation Information
Experiment		
Users	Proposal	Experiment Dates
Instrument Scientist		

A related concern to the storage format of data is how to represent information in meaningful, specific, and concise ways. This information needs to provide adequate details to machine learning models while remaining minimal enough for scalability/storage concerns. Butler et al. discussed how the format chosen for representing data, including both numerical and non-numerical data, can significantly influence results of the model. They provide the example of lattice parameters and vectors in crystallography, and how this information is not useful for machine learning models as the coordinate system is an arbitrarily defined feature.[5] Another example lies in representing a molecular structure. Most researchers can recognize molecules in a variety of ways, such as a formula, the IUPAC name, a CAS number, or an image of the molecular structure. However, these formats would be meaningless to a machine learning model. Instead, researchers are utilizing fingerprinting methods to convert from traditional molecular structures to vector formats that a ML model can use.[5,14] An example of this is shown in the work of Wei et al. The group evaluated various fingerprinting methods in their model for predicting the products of organic chemistry reactions.[15]

7.2.2 *Value to the Scattering Community*

An important objective to keep in mind while developing this type of comprehensive repository is the added value provided to the broader scattering community. For example, a repository could enable research that would not be possible otherwise, including the previously discussed machine learning approaches that require large datasets. The work of Mounet et al. provide an excellent example of databases enabling research. By using molecular entries form the Inorganic Crystal Structure Database and Crystallographic Open Database, the group was able to discover 1800 potential two-dimensional materials from over 185,000 structures.[16] Beyond added research opportunities, other broader impacts include improved instrument use, publication tracking for facilities, easy access to past data, and sample-related queries.

To elaborate on the opportunities for added value, we have developed an example of implementing a comprehensive repository for the SANS data flow at the NCNR. Shown in Figure 4.1 is the current data flow. An incredible amount of data is already collected, including meta-data for the proposal, scheduled experiments, raw scattering data, publications, and health physics. However, this data is stored in a disconnected manner, limiting its full potential. Shown in Figure 7.2 is an envisioned improvement on the current data flow in the form of a comprehensive repository. Now, all relevant information is tied together, enabling numerous benefits. For example, by adding information about scattering and transmission measurement files taken during an experiment, one can enable future automated data reduction procedures. By including information about specific samples and the time it spent being measured on the beam, health physicists can be alerted of any significant activation concerns, improving the safety of those at the facility and the visiting researchers. By connecting information about the visiting researchers and the measurements taken, researchers can more easily find data from their past experiments. Finally, with the addition of detailed sample information, including its components, researchers can access data in new ways. For example, one could search the system for all their past measurements for one particular material, or search the system for data of related samples. Finally, this enables numerous machine learning opportunities related to neutron scattering and chemoinformatics.

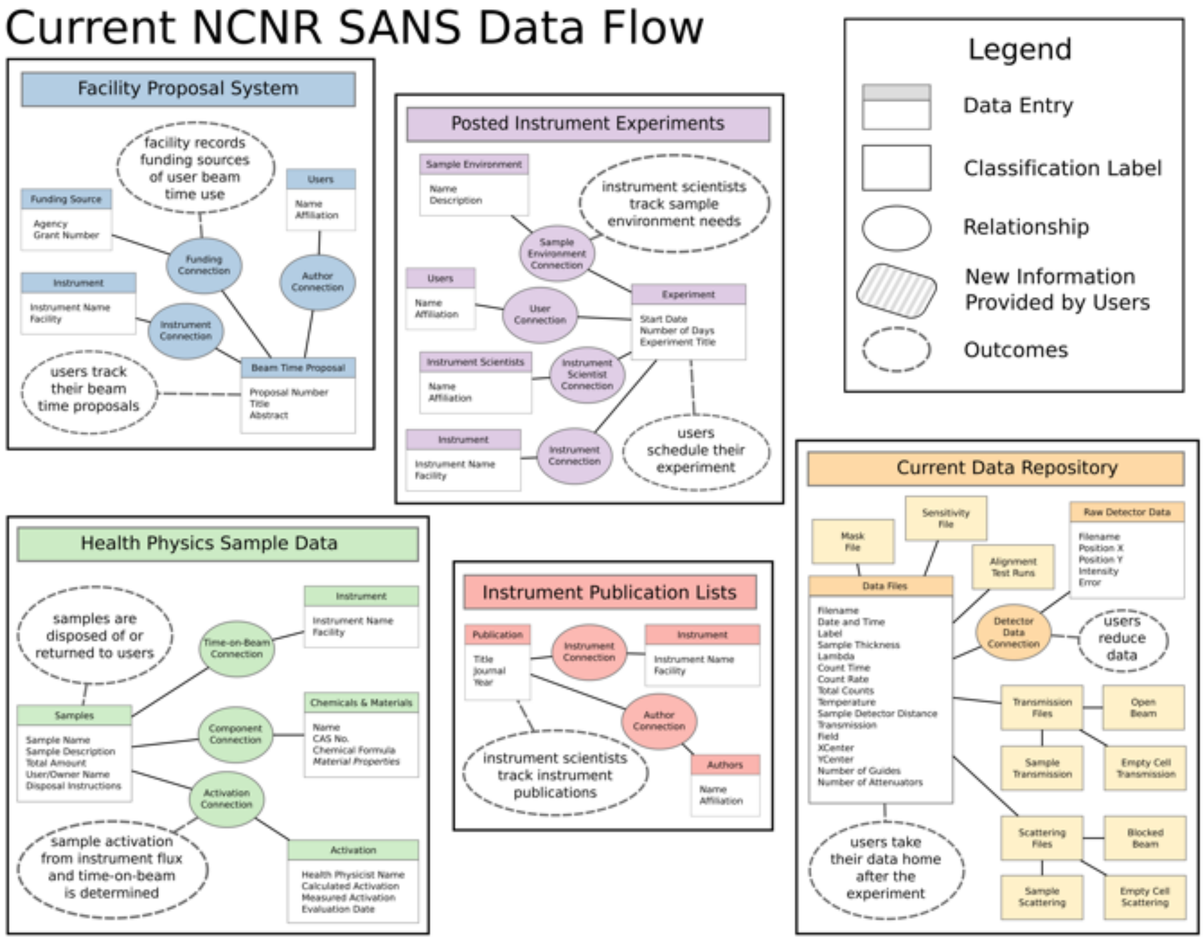

Figure 7.1. Current small-angle neutron scattering data flow at the NIST Center for Neutron Research.

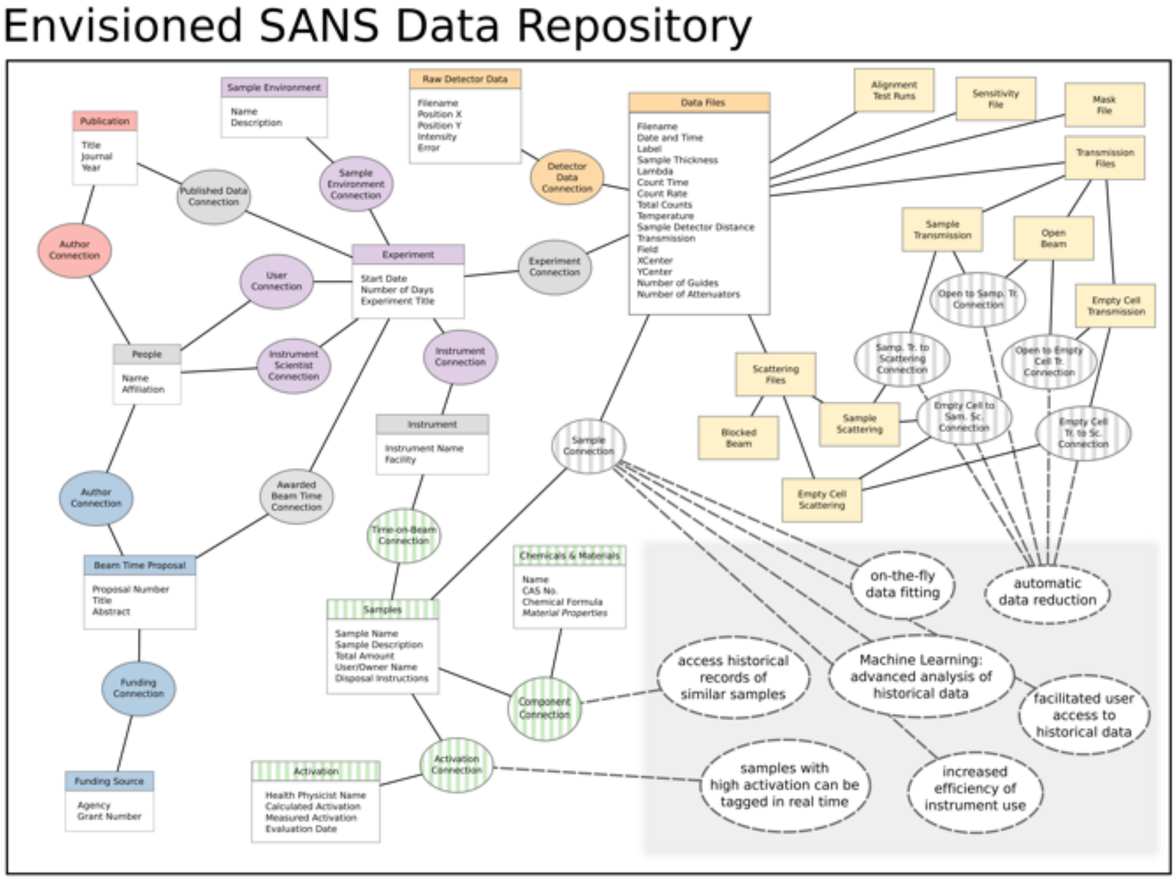

Figure 7.2. Envisioned implementation of a compressive small-angle neutron scattering repository at the NIST Center for Neutron Research.

7.3 SUPPLEMENTAL X-RAY AND NEUTRON SCATTERING DATA OF POLYTHIOPHENES

While the majority of the work focused on poly(3-hexylthiophene) (P3HT) as a model system to explore the conformation and self-assembly in pure and blended solid state films, we also explored additional polythiophenes that are known to have higher charge mobilities and differ in side-chain length, side-chain density along the backbone, and backbone variations with thienothiophene. In this section, we provide preliminary results for polymers of poly(3-dodecylthiophene) (P3DDT), poly(3-3’’’-didodecyl quarter thiophene) (PQT-12), and poly[2,5-bis(3-dodecylthiophen-2-yl)thieno[3,2-b]thiophene] (PBTTT-C12). The structure of these materials can be found in Figure 1.1 of Chapter 1. Data presented here includes including differential scanning calorimetry (DSC), wide-angle x-ray scattering (WAXS), and quasi-elastic neutron scattering (QENS) results.

7.3.1 *Differential Scanning Calorimetry*

A TA Instruments (New Castle, DE, USA) Q200 with aluminum sample was used to collect differential scanning calorimetry (DSC) data during a heat/cool/heat cycle at a rate of 5 K/min. The first heating cycle was to remove thermal history in the materials and so the second heating cycle was used for extraction of glass transition and melting temperatures, as shown in Figure 7.3. PQT-C12 shows an interesting behavior in its dual-peak melting process. In the literature, this has been defined as crystalline-to-liquid-crystalline and liquid-crystalline-to-amorphous transition points.[17,18] For P3DDT, the results correspond well to the system studied by Chen and coworkers.[19] The inflection point at 258.64 K is the glass transition temperature, while the other peak positions are attributed to various melting temperatures. Chen et al. attributes the first melting peak to the side chains of the system and the later peak to the main chain. Interestingly, two melting peaks near the main chain position appear in our results. Finally, for PBTTT-C12, a complex melting process is observed that have been attributed to liquid-crystalline properties and main chain melting processes.[20,21]

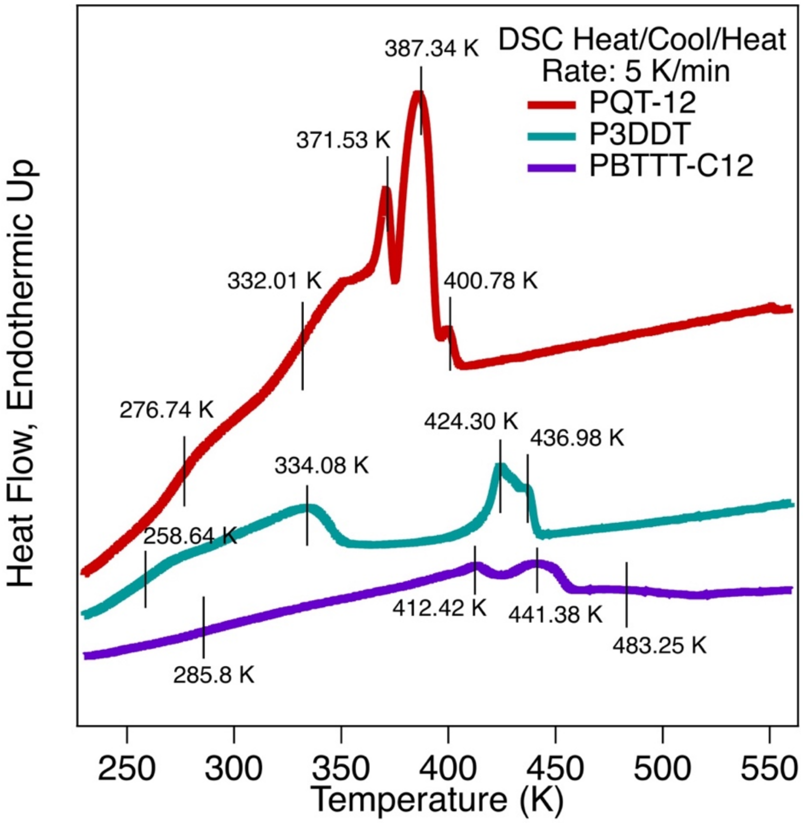

Figure 7.3. Differential scanning calorimetry (DSC) results for PQT-12, P3DDT, and PBTTT-C12. Endothermic is represented in the upwards direction and data was collected during the second heating cycle. Temperature ramping speed was set to 5 K/min.

7.3.2 *Wide-Angle X-Ray Scattering*

Wide-angle X-ray scattering data was collected following the procedure outlined in Chapter 4, and is provided in Figure 7.4 for PQT-12, P3DDT, and PBTTT-C12 at 293 K, 473 K, and 523 K (PBTTT-C12 only). The peaks at approximately 0.25 and 1.5 $Å^{-1}$ in the PQT-12 data have been attributed to lamellar and pi-stacking distances in the crystal structure[22], but the presence of additional peaks at 273 K (below the melting temperature) indicate a more complex structure of the material. Similarly, the lamellar and pi-stacking distances also appear in the P3DDT results at approximately 0.2 and 1.3 $Å^{-1}$. Finally ,the peak positions at approximately 1.4 and 1.65 $Å^{-1}$ for

PBTTT-C12 have been described in the literature as the spacing along the pi-stacking direction and the repeat units along the conjugated backbone, while peaks at lower q-values are attributed with the lamellar distance in the crystal structure.[23] An additional measurement at 523 K for PBTTT-C12 is shown as to fully melt the material. Although the sample begins melting by 473 K (see Figure 7.3), the last melting process corresponding to that of the main chains occurs after 483 K. Once melted, all materials show broad amorphous peaks in the WAXS profile that correspond to loosely correlated distances within the material.

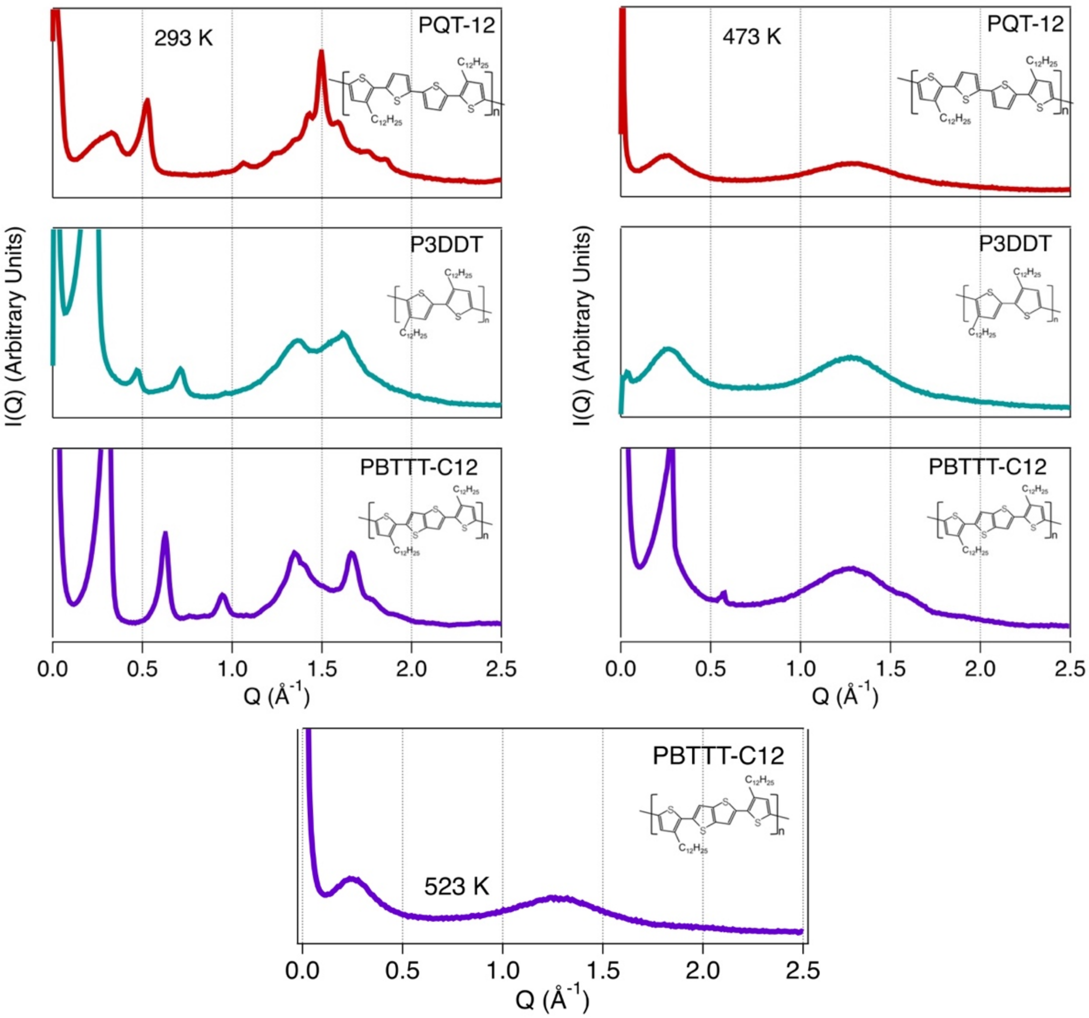

Figure 7.4. Wide-angle x-ray scattering (WAXS) results for PQT-12, P3DDT, and PBTTT-C12 taken at 273 K (left), 473 K (right) and 523 K (bottom).

7.3.3 *Quasi-Elastic Neutron Scattering*

Quasi-elastic neutron scattering (QENS) data for PQT-12, P3DDT, and PBTTT-C12 are shown in are shown in Figure 7.5, and were collected using the Disk Chopper Spectrometer (DCS)[24] at the National Institute of Standards and Technology (NIST) Center for Neutron Research (NCNR), the Backscattering Spectrometer (BASIS)[25] at the Spallation Neutron Source (SNS) at the Oak Ridge National Laboratory (ORNL), and the High-Flux Backscattering Spectrometer (HFBS)[26] at the NCNR. Measurements were collected following the QENS procedures outlined in Chapter 4. At 273 K, there is limited motion in all samples as expected from their semi-crystalline structures. Interestingly, the P3DDT sample does show the most motion at all q-values. The could be due to the large amount of side chains and their motions within this material. At 473 K, the PBTTT-C12 sample shows the least amount of motions, which can be expected from the high melting temperature (~483 K). These results, along with WAXS and DSC measurements, emphasize the influence of the backbone and side-chain structure on the system dynamics and the importance of understanding the structure-function relationship in these materials.

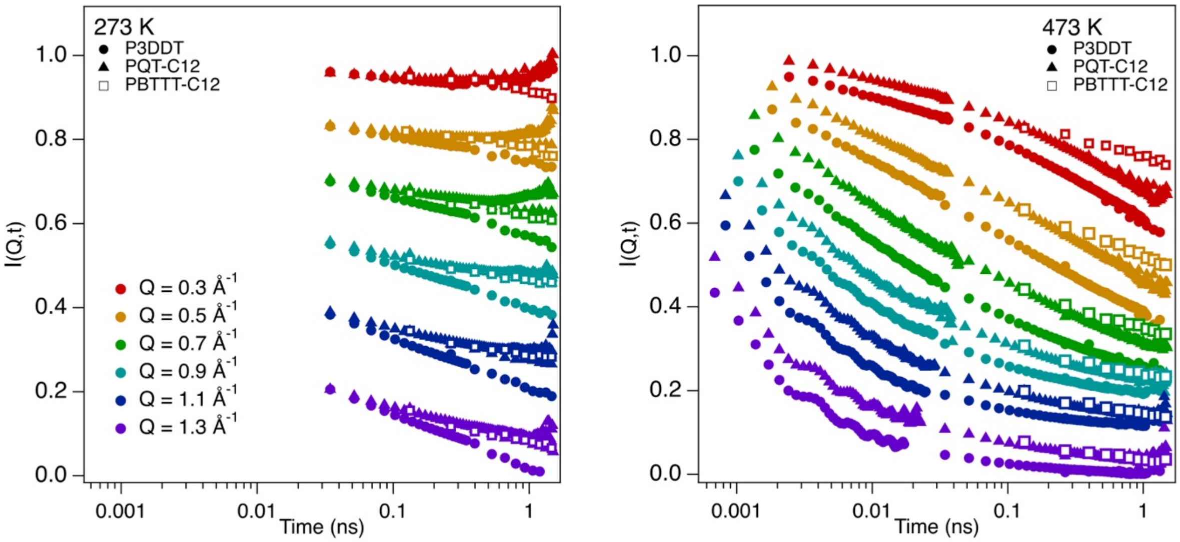

Figure 7.5. Quasi-elastic neutron scattering (QENS) results for P3DDT, PQT-12, and PBTTT-C12 taken using the Disk Chopper Spectrometer (DCS)[24] at the National Institute of Standards and Technology (NIST) Center for Neutron Research (NCNR), the Backscattering Spectrometer (BASIS)[25] at the Spallation Neutron Source (SNS) at the Oak Ridge National Laboratory (ORNL), and the High-Flux Backscattering Spectrometer (HFBS)[26] at the NCNR at 273 K (left) and 473 K (right).

7.4 REFERENCES

(1) Doucet, M.; King, S.; Butler, P.; Kienzle, P.; Parker, P.; Krzywon, J.; Jackson, A.; Richter, T.; Gonzales, M.; Nielsen, T.; Ferraz, L. R. *Sasmodels (Version 1.0.1)*. 2020.

(2) Doucet, M.; King, S.; Butler, P.; Kienzle, P.; Parker, P.; Krzywon, J.; Jackson, A.; Richter, T.; Gonzales, M.; Nielsen, T.; Ferraz, L. R. *SasView (Version 5.0.1)*. 2020.

(3) Wolf, C. pozzo-research-group/c-wolf-blends-morphology: Initial Development (Version v0.1.0) http://doi.org/10.5281/zenodo.4035166.

(4) Beck, D. A. C.; Carothers, J. M.; Subramanian, V. R.; Pfaendtner, J. *Data Science: Accelerating Innovation and Discovery in Chemical Engineering*. *AIChE J.* **2016**, *62* (5), 1402–1416. https://doi.org/10.1002/aic.15192.

(5) Butler, K. T.; Davies, D. W.; Cartwright, H.; Isayev, O.; Walsh, A. *Machine Learning for Molecular and Materials Science*. *Nature* **2018**, *559* (7715), 547–555. https://doi.org/10.1038/s41586-018-0337-2.

(6) Gómez-Bombarelli, R.; Aguilera-Iparraguirre, J.; Hirzel, T. D.; Duvenaud, D.; Maclaurin, D.; Blood-Forsythe, M. A.; Chae, H. S.; Einzinger, M.; Ha, D.-G.; Wu, T.; Markopoulos, G.; Jeon, S.; Kang, H.; Miyazaki, H.; Numata, M.; Kim, S.; Huang, W.; Hong, S. I.; Baldo, M.; Adams, R. P.; Aspuru-Guzik, A. *Design of Efficient Molecular Organic Light-Emitting Diodes by a High-Throughput Virtual Screening and Experimental Approach*. *Nat. Mater.* **2016**, *15* (10), 1120–1127. https://doi.org/10.1038/nmat4717.

(7) Yoon, C. H.; Schwander, P.; Abergel, C.; Andersson, I.; Andreasson, J.; Aquila, A.; Bajt, S.; Barthelmess, M.; Barty, A.; Bogan, M. J.; Bostedt, C.; Bozek, J.; Chapman, H. N.; Claverie, J.-M.; Coppola, N.; DePonte, D. P.; Ekeberg, T.; Epp, S. W.; Erk, B.; Fleckenstein, H.; Foucar, L.; Graafsma, H.; Gumprecht, L.; Hajdu, J.; Hampton, C. Y.; Hartmann, A.; Hartmann, E.; Hartmann, R.; Hauser, G.; Hirsemann, H.; Holl, P.; Kassemeyer, S.; Kimmel, N.; Kiskinova, M.; Liang, M.; Loh, N.-T. D.; Lomb, L.; Maia, F. R. N. C.; Martin, A. V.; Nass, K.; Pedersoli, E.; Reich, C.; Rolles, D.; Rudek, B.; Rudenko, A.; Schlichting, I.; Schulz, J.; Seibert, M.; Seltzer, V.; Shoeman, R. L.; Sierra, R. G.; Soltau, H.; Starodub, D.; Steinbrener, J.; Stier, G.; Strüder, L.; Svenda, M.; Ullrich, J.; Weidenspointner, G.; White, T. A.; Wunderer, C.; Ourmazd, A. *Unsupervised Classification of Single-Particle X-Ray Diffraction Snapshots by Spectral Clustering*. *Opt. Express* **2011**, *19* (17), 16542. https://doi.org/10.1364/OE.19.016542.

(8) Hadi Kiapour, M.; Yager, K.; Berg, A. C.; Berg, T. L. Materials Discovery: Fine-Grained Classification of X-Ray Scattering Images. In *IEEE Winter Conference on Applications of Computer Vision*; IEEE, 2014; pp 933–940. https://doi.org/10.1109/WACV.2014.6836004.

(9) Franke, D.; Jeffries, C. M.; Svergun, D. I. *Machine Learning Methods for X-Ray Scattering Data Analysis from Biomacromolecular Solutions*. *Biophys. J.* **2018**, *114* (11), 2485–2492. https://doi.org/10.1016/j.bpj.2018.04.018.

(10) Kikhney, A. G.; Panjkovich, A.; Sokolova, A. V.; Svergun, D. I. *DARA: A Web Server for Rapid Search of Structural Neighbours Using Solution Small Angle X-Ray Scattering Data*. *Bioinformatics* **2016**, *32* (4), 616–618. https://doi.org/10.1093/bioinformatics/btv611.

(11) Valentini, E.; Kikhney, A. G.; Previtali, G.; Jeffries, C. M.; Svergun, D. I. *SASBDB, a Repository for Biological Small-Angle Scattering Data*. *Nucleic Acids Res.* **2015**, *43* (D1), D357–D363. https://doi.org/10.1093/nar/gku1047.

(12) Kroon-Batenburg, L. M. J.; Helliwell, J. R.; McMahon, B.; Terwilliger, T. C. *Raw Diffraction Data Preservation and Reuse: Overview, Update on Practicalities and Metadata Requirements*. *IUCrJ* **2017**, *4* (1), 87–99. https://doi.org/10.1107/S2052252516018315.

(13) Trewhella, J.; Duff, A. P.; Durand, D.; Gabel, F.; Guss, J. M.; Hendrickson, W. A.; Hura, G. L.; Jacques, D. A.; Kirby, N. M.; Kwan, A. H.; Pérez, J.; Pollack, L.; Ryan, T. M.; Sali, A.; Schneidman-Duhovny, D.; Schwede, T.; Svergun, D. I.; Sugiyama, M.; Tainer, J. A.; Vachette, P.; Westbrook, J.; Whitten, A. E. *2017 Publication Guidelines for Structural Modelling of Small-Angle Scattering Data from Biomolecules in Solution: An Update. Acta Crystallogr. Sect. D Struct. Biol.* **2017**, *73* (9), 710–728. https://doi.org/10.1107/S2059798317011597.

(14) Duvenaud, D. K.; Maclaurin, D.; Iparraguirre, J.; Bombarell, R.; Hirzel, T.; Aspuru-Guzik, A.; Adams, R. P. *Convolutional Networks on Graphs for Learning Molecular Fingerprints*. *Adv. Neutral Inf. Process. Syst.* **2015**, *28*.

(15) Wei, J. N.; Duvenaud, D.; Aspuru-Guzik, A. *Neural Networks for the Prediction of Organic Chemistry Reactions*. *ACS Cent. Sci.* **2016**, *2* (10), 725–732. https://doi.org/10.1021/acscentsci.6b00219.

(16) Mounet, N.; Gibertini, M.; Schwaller, P.; Campi, D.; Merkys, A.; Marrazzo, A.; Sohier, T.; Castelli, I. E.; Cepellotti, A.; Pizzi, G.; Marzari, N. *Two-Dimensional Materials from High-Throughput Computational Exfoliation of Experimentally Known Compounds*. *Nat. Nanotechnol.* **2018**, *13* (3), 246–252. https://doi.org/10.1038/s41565-017-0035-5.

(17) Ong, B. S.; Wu, Y.; Li, Y.; Liu, P.; Pan, H. *Thiophene Polymer Semiconductors for Organic Thin-Film Transistors*. *Chem. - A Eur. J.* **2008**, *14* (16), 4766–4778. https://doi.org/10.1002/chem.200701717.

(18) Zhang, L.; Colella, N. S.; Liu, F.; Trahan, S.; Baral, J. K.; Winter, H. H.; Mannsfeld, S. C. B.; Briseno, A. L. *Synthesis, Electronic Structure, Molecular Packing/Morphology Evolution, and Carrier Mobilities of Pure Oligo-/Poly(Alkylthiophenes)*. *J. Am. Chem. Soc.* **2013**, *135* (2), 844–854. https://doi.org/10.1021/ja3104796.

(19) Chen, S. A.; Ni, J. M. *Structure/Properties of Conjugated Conductive Polymers. 1. Neutral Poly(3-Alkythiophene)S*. *Macromolecules* **1992**, *25* (23), 6081–6089. https://doi.org/10.1021/ma00049a001.

(20) Baklar, M.; Barard, S.; Sparrowe, D.; Wilson, R. M.; McCulloch, I.; Heeney, M.; Kreouzis, T.; Stingelin, N. *Bulk Charge Transport in Liquid-Crystalline Polymer Semiconductors Based on Poly(2,5-Bis(3-Alkylthiophen-2-Yl)Thieno[3,2-b]Thiophene). Polym. Chem.* **2010**, *1* (9), 1448–1452. https://doi.org/10.1039/c0py00056f.

(21) McCulloch, I.; Heeney, M.; Bailey, C.; Genevicius, K.; MacDonald, I.; Shkunov, M.; Sparrowe, D.; Tierney, S.; Wagner, R.; Zhang, W.; Chabinyc, M. L.; Kline, R. J.; McGehee, M. D.; Toney, M. F. *Liquid-Crystalline Semiconducting Polymers with High Charge-Carrier Mobility. Nat. Mater.* **2006**, *5* (4), 328–333. https://doi.org/10.1038/nmat1612.

(22) Ong, B. S.; Wu, Y.; Liu, P.; Gardner, S. *High-Performance Semiconducting Polythiophenes for Organic Thin-Film Transistors. J. Am. Chem. Soc.* **2004**, *126* (11), 3378–3379. https://doi.org/10.1021/ja039772w.

(23) Chabinyc, M.; Toney, M. F.; Kline, R. J.; Mcculloch, I. *X-Ray Scattering Studies of Thin-Films of Poly (2,5-Bis(3-Alkylthiophen-2-Yl)Thieno[3,2- b]Thiophene - Supplementary Materials*. **2007**, *129*.

(24) Copley, J. R. D.; Cook, J. C. *The Disk Chopper Spectrometer at NIST: A New Instrument for Quasielastic Neutron Scattering Studies. Chem. Phys.* **2003**, *292* (2–3), 477–485. https://doi.org/10.1016/S0301-0104(03)00124-1.

(25) Mamontov, E.; Herwig, K. W. *A Time-of-Flight Backscattering Spectrometer at the Spallation Neutron Source, BASIS. Rev. Sci. Instrum.* **2011**, *82* (8), 085109. https://doi.org/10.1063/1.3626214.

(26) Meyer, A.; Dimeo, R. M.; Gehring, P. M.; Neumann, D. A. *The High-Flux Backscattering Spectrometer at the NIST Center for Neutron Research. Rev. Sci. Instrum.* **2003**, *74* (5), 2759–2777. https://doi.org/10.1063/1.1568557.

Chapter 8. CONCLUSIONS

Conjugated polymers (CPs) enable low-cost, flexible organic electronic devices and are a promising material for both novel and improved technologies in the future. However, a thorough understanding of the relationship between the morphology and macroscopic electronic performance of CPs, either in pure or blended forms, is important for enabling improved materials and more efficient devices. In this work, we have shown how neutron and X-ray scattering can be used together with classical and quantum-mechanical molecular modeling for a powerful, combined experimental and theoretical approach to studying this relationship.

In Chapter 4, we performed a critical assessment[1] of five published molecular dynamics (MD) simulation force fields (Moreno et al.[2], Huang et al.[3], and Bhatta et al.[4]) for the model CP poly(3-hexylthiophene) (P3HT). These researchers provided re-parameterizations of the classical OPLS force field to account for the effects of conjugation, which included adjustments to the dihedrals potentials between monomers along the backbone and between the thiophene ring and alkyl side chain, as well as adjustments to the atomic partial charges. Variations in the approaches each of these groups followed during this re-parameterization resulted in significant differences in the *in-silico* conformation and dynamics of thiophene-thiophene distances and backbone planarity, both parameters relevant to charge transport mechanisms. All force field were able to capture structural correlations in the material when compared to wide-angle X-ray scattering (WAXS) data, but they showed a limitation at capturing dynamics at longer time scales (~1 ns) when compared to quasi-elastic neutron scattering (QENS) data, especially for the Mod. Bhatta force field. With use of a P3HT sample deuterated along the alkyl side (contrast variation), we could use QENS to further investigate the dynamics along the side-chain and backbone regimes of the chain specifically. We observed a quick relaxation of the side-chains below 200 K and a delayed relaxation of the backbone after 400 K. Unfortunately, none of the modeled systems were able to reproduce the characteristic backbone dynamics to which charge transport mechanisms are particularly sensitive. This work demonstrated the limitations of currently available force fields for conjugated polymers in capturing dynamics at time scales relevant to charge transport mechanisms.

In Chapter 5, we provided preliminary data for a set of hydrogenated and partially deuterated amorphous and semi-crystalline P3HT polymers and oligomers. We first utilize density functional theory (DFT) to highlight the current underestimation of non-bonded interactions of P3HT in the Moreno et al.[2] force field. MD simulations currently in progress are utilizing scaled Lennard-Jones parameters along the P3HT backbone to explore how increasing the strength of these interactions affect the system structure and dynamics. We also utilize QENS measurements to understand the effect of crystallinity and molecular weight in P3HT, and ongoing modeling of the QENS data using the stretched exponential fit will enable a quantitative characterization of these relationships through the extraction of characteristic relaxation times of the material. This work is important to understanding the limitations of classical molecular modeling in regards to non-bonded intermolecular interactions which are known to play an important role in the conformation and charge-transport mechanisms in CPs.

In Chapter 6, we use contrast variation small-angle neutron scattering (SANS) and wide-angle X-ray scattering (WAXS) to characterize the phase morphology and self-assembly in solid blends of polythiophenes and polystyrene (PS). A Porod analysis found that all blends, to some extent, phase separated in globular domains of aggregated conjugated polymer phase dispersed in the insulating PS matrix. Blends with amorphous, regio-random poly(3-hexylthiphene) (RRa-

P3HT) remained amorphous at all CP concentrations, but blends with semi-crystalline CPs of either poly(3-dodecylthiophene) (P3DDT) or poly(3,3'''-didodecyl[2,2':5',2'':5'',2'''-quaterthiophene]-5,5'''-diyl) (PQT-12) formed globular CP aggregates with both amorphous and crystalline sub-regimes. In samples comprised of regio-regular poly(3-hexylthiophene) (RRe-P3HT), we also observe the self-assembly of the CP into dense nanofiber networks dispersed throughout the bulk of the solid films. Moreover, modifying the solvent quality during the initial processing of these films had a significant role in the final solid-state morphology. By utilizing a moderate solvent (toluene), nanofibers could be encouraged at lower CP concentrations. Finally, the presence of nanofibers led to significant improvements to the film's conductivity, demonstrating the formation of charge transport pathways across the thickness of the sample. This work emphasizes the complexity of these systems; both polymer-polymer and polymer-solvent interactions in the solution-state influence the final solid-state phase morphology, and understanding these interactions are important for tuning the performance of these blends.

As a final note, we acknowledge the importance of open science and reproducibility in this work and in the community. All raw data that went into Chapter 4 and Chapter 6 have been provided as supplemental information in their respective publication[1] and submitted manuscript, respectively. We hope that by providing this data, we can encourage open science in the community as well as make valuable neutron and X-ray scattering data available to other researchers for new future analyses or improved molecular force fields. Moreover, all Python scripts and Jupyter notebooks used in Chapter 6 to analyze the data are openly available on GitHub. Not only did creating this repository to organize our analysis improve reproducibility across members of our own team, it also enabled semi-automation of SANS data fitting that we could then share with others in the community. Together with the raw data provided with the publication, these can be used by other researchers to apply new analysis approaches or more easily extend these methods to their own systems.

8.1 OUTLOOK

This work has provided examples of the value in combined scattering and molecular modeling approaches to understanding the conformation, dynamics, and self-assembly in conjugated polymers, but it also emphasizes the challenges associated with controlling CP morphology and also the development of accurate force fields for CPs. The bulk of this work was focused on only a single, model CP in the field, P3HT. However, hundreds of other semiconducting polymers have been studied in the literature with higher charge mobility and greater molecular complexity than that of P3HT. In Chapter 4, we saw the limited transferability of available force fields to other polythiophenes, even one as similar as P3DDT. Moreover, we saw in Chapter 7 the range in dynamics across materials of P3DDT, PQT-12 and PBTTT-C12 by use of QENS measurements. Finally, we have shown the limitations of current force fields for capturing critical backbone dynamics of P3HT, as well as the amount of experimental and theoretical data required to perform a critical assessment of these systems. This approach quickly becomes unsustainable as we begin to investigate other materials. Nevertheless, we have seen the value of using neutron and X-ray scattering data as validation metrics at time and length scales relative to charge transport mechanisms in CPs. As we consider future directions of the work presented here, we must begin approaching the problem from a broader perspective. Through the lens of data science and machine learning, we think about how these tools could help accelerate exploration of the phase space for force field parameters of different molecules by not only providing information about *which* parameters and simulations to probe next, but also taking into consideration relevant meta-data of molecular structure, physical properties, and chemical properties. In this way, we can begin to develop a more robust and sustainable approach to developing more accurate classical force fields for conjugated polymers.

8.2 REFERENCES

(1) Wolf, C. M.; Kanekal, K. H.; Yimer, Y. Y.; Tyagi, M.; Omar-Diallo, S.; Pakhnyuk, V.; Luscombe, C. K.; Pfaendtner, J.; Pozzo, L. D. *Assessment of Molecular Dynamics Simulations for Amorphous Poly(3-Hexylthiophene) Using Neutron and X-Ray Scattering Experiments*. *Soft Matter* **2019**, *15* (25), 5067–5083. https://doi.org/10.1039/C9SM00807A.

(2) Moreno, M.; Casalegno, M.; Raos, G.; Meille, S. V.; Po, R. *Molecular Modeling of Crystalline Alkylthiophene Oligomers and Polymers*. *J. Phys. Chem. B* **2010**, *114* (4), 1591–1602. https://doi.org/10.1021/jp9106124.

(3) Schwarz, K. N.; Kee, T. W.; Huang, D. M. *Coarse-Grained Simulations of the Solution-Phase Self-Assembly of Poly(3-Hexylthiophene) Nanostructures*. *Nanoscale* **2013**, *5* (5), 2017. https://doi.org/10.1039/c3nr33324h.

(4) Bhatta, R. S.; Yimer, Y. Y.; Perry, D. S.; Tsige, M. *Improved Force Field for Molecular Modeling of Poly(3-Hexylthiophene)*. *J. Phys. Chem. B* **2013**, *117* (34), 10035–10045. https://doi.org/10.1021/jp404629a.

BIBLIOGRAPHY

45-meter VSANS Instrument @ Guide NG-3 https://ncnr.nist.gov/equipment/msnew/ncnr/vsans-design-features.html (accessed May 31, 2020).

Agbolaghi, S.; Zenoozi, S. *A Comprehensive Review on Poly(3-Alkylthiophene)-Based Crystalline Structures, Protocols and Electronic Applications*. *Org. Electron. 51*, 362–403. https://doi.org/10.1016/j.orgel.2017.09.038.

Alder, B. J.; Wainwright, T. E. *Phase Transition for a Hard Sphere System*. *J. Chem. Phys.* **1957**, *27* (5), 1208–1209. https://doi.org/10.1063/1.1743957.

Allen, M. P. Introduction to Molecular Dynamics Simulation. In *Computational Soft Matter: From Synthetic Polymers to Proteins*; 23, 2004; pp 1–28.

Alvarez, A.; Costa-Fernández, J. M.; Pereiro, R.; Sanz-Medel, A.; Salinas-Castillo, A. *Fluorescent Conjugated Polymers for Chemical and Biochemical Sensing*. *TrAC Trends Anal. Chem.* **2011**, *30* (9), 1513–1525. https://doi.org/10.1016/j.trac.2011.04.017.

Anantha-Iyengar, G.; Shanmugasundaram, K.; Nallal, M.; Lee, K.-P.; Whitcombe, M. J.; Lakshmi, D.; Sai-Anand, G. *Functionalized Conjugated Polymers for Sensing and Molecular Imprinting Applications*. *Prog. Polym. Sci.* **2019**, *88*, 1–129. https://doi.org/10.1016/j.progpolymsci.2018.08.001.

Angunawela, I.; Nahid, M. M.; Ghasemi, M.; Amassian, A.; Ade, H.; Gadisa, A. *The Critical Role of Materials' Interaction in Realizing Organic Field-Effect Transistors Via High-Dilution Blending with Insulating Polymers*. *ACS Appl. Mater. Interfaces* **2020**, *12* (23), 26239–26249. https://doi.org/10.1021/acsami.0c04208.

Arbe, A.; Alvarez, F.; Colmenero, J. *Neutron Scattering and Molecular Dynamics Simulations: Synergetic Tools to Unravel Structure and Dynamics in Polymers*. *Soft Matter* **2012**, *8* (32), 8257. https://doi.org/10.1039/c2sm26061a.

Arnold, O.; Bilheux, J. C.; Borreguero, J. M.; Buts, A.; Campbell, S. I.; Chapon, L.; Doucet, M.; Draper, N.; Ferraz Leal, R.; Gigg, M. A.; Lynch, V. E.; Markvardsen, A.; Mikkelson, D. J.; Mikkelson, R. L.; Miller, R.; Palmen, K.; Parker, P.; Passos, G.; Perring, T. G.; Peterson, P. F.; Ren, S.; Reuter, M. A.; Savici, A. T.; Taylor, J. W.; Taylor, R. J.; Tolchenov, R.; Zhou, W.; Zikovsky, J. *Mantid - Data Analysis and Visualization Package for Neutron Scattering and μ SR Experiments*. *Nucl. Instruments Methods Phys. Res. Sect. A Accel. Spectrometers, Detect. Assoc. Equip.* **2014**, *764*, 156–166. https://doi.org/10.1016/j.nima.2014.07.029.

Assmus, A. Early History of X Rays http://www.slac.stanford.edu/pubs/beamline/25/2/25-2-assmus.pdf.

Azuah, R. T.; Kneller, L. R.; Qiu, Y.; Tregenna-Piggott, P. L. W.; Brown, C. M.; Copley, J. R. D.; Dimeo, R. M. *DAVE: A Comprehensive Software Suite for the Reduction, Visualization, and Analysis of Low Energy Neutron Spectroscopic Data*. *J. Res. Natl. Inst. Stand. Technol.* **2009**, *114* (6), 341. https://doi.org/10.6028/jres.114.025.

Baghgar, M.; Labastide, J. A.; Bokel, F.; Hayward, R. C.; Barnes, M. D. *Effect of Polymer Chain Folding on the Transition from H- to J-Aggregate Behavior in P3HT Nanofibers*. *J. Phys. Chem. C* **2014**, *118* (4), 2229–2235. https://doi.org/10.1021/jp411668g.

Baklar, M.; Barard, S.; Sparrowe, D.; Wilson, R. M.; McCulloch, I.; Heeney, M.; Kreouzis, T.; Stingelin, N. *Bulk Charge Transport in Liquid-Crystalline Polymer Semiconductors Based on Poly(2,5-Bis(3-Alkylthiophen-2-Yl)Thieno[3,2-b]Thiophene)*. *Polym. Chem.* **2010**, *1* (9), 1448–1452. https://doi.org/10.1039/c0py00056f.

Balko, J.; Lohwasser, R. H.; Sommer, M.; Thelakkat, M.; Thurn-Albrecht, T. *Determination of the Crystallinity of Semicrystalline Poly(3-Hexylthiophene) by Means of Wide-Angle X-Ray Scattering*. *Macromolecules* **2013**, *46* (24), 9642–9651. https://doi.org/10.1021/ma401946w.

Barker, J. G.; Glinka, C. J.; Moyer, J. J.; Kim, M. H.; Drews, A. R.; Agamalian, M. *Design and Performance of a Thermal-Neutron Double-Crystal Diffractometer for USANS at NIST*. *J. Appl. Crystallogr.* **2005**, *38* (6), 1004–1011. https://doi.org/10.1107/S0021889805032103.

Baseden, K. A.; Tye, J. W. *Introduction to Density Functional Theory: Calculations by Hand on the Helium Atom*. *J. Chem. Educ.* **2014**, *91* (12), 2116–2123. https://doi.org/10.1021/ed5004788

Bastianini, F.; Pérez, G. E.; Hobson, A. R.; Rogers, S. E.; Parnell, A. J.; Grell, M.; Gutiérrez, A. F.; Dunbar, A. D. F. *In−situ Monitoring Poly(3-Hexylthiophene) Nanowire Formation and Shape Evolution in Solution via Small Angle Neutron Scattering*. *Sol. Energy Mater. Sol. Cells* **2019**, *202*, 110128. https://doi.org/10.1016/j.solmat.2019.110128.

Beck, D. A. C.; Carothers, J. M.; Subramanian, V. R.; Pfaendtner, J. *Data Science: Accelerating Innovation and Discovery in Chemical Engineering*. *AIChE J.* **2016**, *62* (5), 1402–1416. https://doi.org/10.1002/aic.15192.

Becke, A. D. *Density‐functional Thermochemistry. III. The Role of Exact Exchange*. *J. Chem. Phys.* **1993**, *98* (7), 5648–5652. https://doi.org/10.1063/1.464913.

BENOIT, H.; DECKER, D.; HIGGINS, J. S.; PICOT, C.; COTTON, J. P.; FARNOUX, B.; JANNINK, G.; OBER, R. *Dimensions of a Flexible Polymer Chain in the Bulk and in Solution*. *Nat. Phys. Sci.* **1973**, *245* (140), 13–15. https://doi.org/10.1038/physci245013a0.

Bhatta, R. S.; Yimer, Y. Y.; Perry, D. S.; Tsige, M. *Improved Force Field for Molecular Modeling of Poly(3-Hexylthiophene)*. *J. Phys. Chem. B* **2013**, *117* (34), 10035–10045. https://doi.org/10.1021/jp404629a.

Böckmann, M.; Schemme, T.; de Jong, D. H.; Denz, C.; Heuer, A.; Doltsinis, N. L. *Structure of P3HT Crystals, Thin Films, and Solutions by UV/Vis Spectral Analysis*. *Phys. Chem. Chem. Phys.* **2015**, *17* (43), 28616–28625. https://doi.org/10.1039/C5CP03665H.

Boldon, L.; Laliberte, F.; Liu, L. *Review of the Fundamental Theories behind Small Angle X-Ray Scattering, Molecular Dynamics Simulations, and Relevant Integrated Application*. *Nano Rev.* **2015**, *6* (1), 25661. https://doi.org/10.3402/nano.v6.25661.

Boys, S. F.; Bernardi, F. *The Calculation of Small Molecular Interactions by the Differences of Separate Total Energies. Some Procedures with Reduced Errors*. *Mol. Phys.* **1970**, *19* (4), 553–566. https://doi.org/10.1080/00268977000101561.

Bronstein, H. A.; Luscombe, C. K. *Externally Initiated Regioregular P3HT with Controlled Molecular Weight and Narrow Polydispersity*. *J. Am. Chem. Soc.* **2009**, *131* (36), 12894–12895. https://doi.org/10.1021/ja9054977.

Butler, K. T.; Davies, D. W.; Cartwright, H.; Isayev, O.; Walsh, A. *Machine Learning for Molecular and Materials Science*. *Nature* **2018**, *559* (7715), 547–555. https://doi.org/10.1038/s41586-018-0337-2.

Chabinyc, M. L.; Toney, M. F.; Kline, R. J.; McCulloch, I.; Heeney, M. *X-Ray Scattering Study of Thin Films of Poly(2,5-Bis(3-Alkylthiophen-2-Yl)Thieno[3,2- b]Thiophene)*. *J. Am. Chem. Soc.* **2007**, *129* (11), 3226–3237. https://doi.org/10.1021/ja0670714.

Chang, M.; Lim, G.; Park, B.; Reichmanis, E. *Control of Molecular Ordering, Alignment, and Charge Transport in Solution-Processed Conjugated Polymer Thin Films*. *Polymers (Basel).* **2017**, *9* (12), 212. https://doi.org/10.3390/polym9060212.

Chaudhari, S. R.; Griffin, J. M.; Broch, K.; Lesage, A.; Lemaur, V.; Dudenko, D.; Olivier, Y.; Sirringhaus, H.; Emsley, L.; Grey, C. P. *Donor–Acceptor Stacking Arrangements in Bulk and Thin-Film High-Mobility Conjugated Polymers Characterized Using Molecular Modelling and MAS and Surface-Enhanced Solid-State NMR Spectroscopy*. *Chem. Sci.* **2017**, *8* (4), 3126–3136. https://doi.org/10.1039/C7SC00053G.

ChemViews. 100th Anniversary of the Discovery of X-Ray Diffraction. 2012.

Chen, S. A.; Ni, J. M. *Structure/Properties of Conjugated Conductive Polymers. 1. Neutral Poly(3-Alkythiophene)S*. *Macromolecules* **1992**, *25* (23), 6081–6089. https://doi.org/10.1021/ma00049a001.

Chen, T. A.; Rieke, R. D. *The First Regioregular Head-to-Tail Poly(3-Hexylthiophene-2,5-Diyl) and a Regiorandom Isopolymer: Nickel versus Palladium Catalysis of 2(5)-Bromo-5(2)-(Bromozincio)-3-Hexylthiophene Polymerization*. *J. Am. Chem. Soc.* **1992**, *114* (25), 10087–10088. https://doi.org/10.1021/ja00051a066.

Chiu, M.; Jeng, U.; Su, C.; Liang, K. S.; Wei, K. *Simultaneous Use of Small- and Wide-Angle X-ray Techniques to Analyze Nanometerscale Phase Separation in Polymer Heterojunction Solar Cells*. *Adv. Mater.* **2008**, *20* (13), 2573–2578. https://doi.org/10.1002/adma.200703097.

Chu, B.; Hsiao, B. S. *Small-Angle X-Ray Scattering of Polymers*. *Chem. Rev.* **2001**, *101* (6), 1727–1762. https://doi.org/10.1021/cr9900376.

Clarke, I. The History of X-Ray Crystallography https://arts.leeds.ac.uk/museum-of-hstm/research/william-thomas-astbury/the-history-of-x-ray-crystallography/.

Colmenero, J.; Arbe, A. *Recent Progress on Polymer Dynamics by Neutron Scattering: From Simple Polymers to Complex Materials*. *J. Polym. Sci. Part B Polym. Phys.* **2013**, *51* (2), 87–113. https://doi.org/10.1002/polb.23178.

Copley, J. R. D.; Cook, J. C. *The Disk Chopper Spectrometer at NIST: A New Instrument for Quasielastic Neutron Scattering Studies*. *Chem. Phys.* **2003**, *292* (2–3), 477–485. https://doi.org/10.1016/S0301-0104(03)00124-1.

Doucet, M.; King, S.; Butler, P.; Kienzle, P.; Parker, P.; Krzywon, J.; Jackson, A.; Richter, T.; Gonzales, M.; Nielsen, T.; Ferraz, L. R. *Sasmodels (Version 1.0.1)*. 2020.

Doucet, M.; King, S.; Butler, P.; Kienzle, P.; Parker, P.; Krzywon, J.; Jackson, A.; Richter, T.; Gonzales, M.; Nielsen, T.; Ferraz, L. R. *SasView (Version 5.0.1)*. 2020.

DuBay, K. H.; Hall, M. L.; Hughes, T. F.; Wu, C.; Reichman, D. R.; Friesner, R. A. *Accurate Force Field Development for Modeling Conjugated Polymers*. *J. Chem. Theory Comput.* **2012**, *8* (11), 4556–4569. https://doi.org/10.1021/ct300175w.

Duvenaud, D. K.; Maclaurin, D.; Iparraguirre, J.; Bombarell, R.; Hirzel, T.; Aspuru-Guzik, A.; Adams, R. P. *Convolutional Networks on Graphs for Learning Molecular Fingerprints*. *Adv. Neutral Inf. Process. Syst.* **2015**, *28*.

Endo, H. *Study on Multicomponent Systems by Means of Contrast Variation SANS*. *Phys. B Condens. Matter* **2006**, *385–386*, 682–684. https://doi.org/10.1016/j.physb.2006.05.290.

Etxebarria, I.; Ajuria, J.; Pacios, R. *Solution-Processable Polymeric Solar Cells: A Review on Materials, Strategies and Cell Architectures to Overcome 10%*. *Org. Electron.* **2015**, *19*, 34–60. https://doi.org/10.1016/j.orgel.2015.01.014.

Feigin, L. A.; Svergun, D. I. *Structure Analysis by Small-Angle X-Ray and Neutron Scattering*; Plenum Press: New York, 1987.

Fidanovski, K.; Mawad, D. *Conjugated Polymers in Bioelectronics: Addressing the Interface Challenge*. *Adv. Healthc. Mater.* **2019**, *8* (10), 1900053. https://doi.org/10.1002/adhm.201900053.

Fournet, G. *Scattering Functions for Geometrical Forms*. *Bull. French Soc. Mineral. Crystallogr.* **1951**, *74*.

Franke, D.; Jeffries, C. M.; Svergun, D. I. *Machine Learning Methods for X-Ray Scattering Data Analysis from Biomacromolecular Solutions*. *Biophys. J.* **2018**, *114* (11), 2485–2492. https://doi.org/10.1016/j.bpj.2018.04.018.

Frenkel, D.; Smit, B. *Understanding Molecular Simulation: From Algorithms to Applications*, 2nd ed.; Academic Press: San Diego, 2002.

Frisch, M. J.; Trucks, G. W.; Schlegel, H. B.; Scuseria, G. E.; Robb, M. A.; Cheeseman, J. R.; Scalmani, G.; Barone, V.; Petersson, G. A.; Nakatsuji, H.; Li, X.; Caricato, M.; Marenich, A. V.; Bloino, J.; Janesko, B. G.; Gomperts, R.; Mennucci, B.; Hratchian, H. P.; Ortiz, J. V.; Izmaylov, A. F.; Sonnenberg, J. L.; Williams-Young, D.; Ding, F.; Lipparini, F.; Egidi, F.; Goings, J.; Peng, B.; Petrone, A.; Henderson, T.; Ranasinghe, D.; Zakrzewski, V. G.; Gao, J.; Rega, N.; Zheng, G.; Liang, W.; Hada, M.; Ehara, M.; Toyota, K.; Fukuda, R.; Hasegawa, J.; Ishida, M.; Nakajima, T.; Honda, Y.; Kitao, O.; Nakai, H.; Vreven, T.; Throssell, K.; Montgomery Jr., J. A.; Peralta, J. E.; Ogliaro, F.; Bearpark, M. J.; Heyd, J. J.; Brothers, E. N.; Kudin, K. N.; Staroverov, V. N.; Keith, T. A.; Kobayashi, R.; Normand, J.; Raghavachari, K.; Rendell, A. P.; Burant, J. C.; Iyengar, S. S.; Tomasi, J.; Cossi, M.; Millam, J. M.; Klene, M.; Adamo, C.; Cammi, R.; Ochterski, J. W.; Martin, R. L.; Morokuma, K.; Farkas, O.; Foresman, J. B.; Fox, D. J. *Gaussian 16, Revision B.01*. Gaussian, Inc.: Wallingford CT 2016.

Furuya, H.; Mondello, M.; Yang, H.-J.; Roe, R.-J.; Erwin, R. W.; Han, C. C.; Smith, S. D. *Molecular Dynamics Simulation of Atactic Polystyrene. 2. Comparison with Neutron Scattering Data*. *Macromolecules* **1994**, *27* (20), 5674–5680. https://doi.org/10.1021/ma00098a022.

Geil, P. H. *Morphology of Amorphous Polymers*. *Ind. Eng. Chem. Prod. Res. Dev.* **1975**, *14* (1), 59–71. https://doi.org/10.1021/i360053a014.

Gillich, D. J.; Kovanen, A.; Danon, Y. *Deuterated Target Comparison for Pyroelectric Crystal D–D Nuclear Fusion Experiments*. *J. Nucl. Mater.* **2010**, *405* (2), 181–185. https://doi.org/10.1016/j.jnucmat.2010.08.012.

Glinka, C. J.; Barker, J. G.; Hammouda, B.; Krueger, S.; Moyer, J. J.; Orts, W. J. *The 30 m Small-Angle Neutron Scattering Instruments at the National Institute of Standards and Technology*. *J. Appl. Crystallogr.* **1998**, *31* (3), 430–445. https://doi.org/10.1107/S0021889897017020.

Goffri, S.; Müller, C.; Stingelin-Stutzmann, N.; Breiby, D. W.; Radano, C. P.; Andreasen, J. W.; Thompson, R.; Janssen, R. A. J.; Nielsen, M. M.; Smith, P.; Sirringhaus, H. *Multicomponent Semiconducting Polymer Systems with Low Crystallization-Induced Percolation Threshold*. *Nat. Mater.* **2006**, *5* (12), 950–956. https://doi.org/10.1038/nmat1779.

Gómez-Bombarelli, R.; Aguilera-Iparraguirre, J.; Hirzel, T. D.; Duvenaud, D.; Maclaurin, D.; Blood-Forsythe, M. A.; Chae, H. S.; Einzinger, M.; Ha, D.-G.; Wu, T.; Markopoulos, G.; Jeon, S.; Kang, H.; Miyazaki, H.; Numata, M.; Kim, S.; Huang, W.; Hong, S. I.; Baldo, M.; Adams, R. P.; Aspuru-Guzik, A. *Design of Efficient Molecular Organic Light-Emitting Diodes by a High-Throughput Virtual Screening and Experimental Approach*. *Nat. Mater.* **2016**, *15* (10), 1120–1127. https://doi.org/10.1038/nmat4717.

González, M. A. *Force Fields and Molecular Dynamics Simulations*. *École thématique la Société Française la Neutron.* **2011**, *12*, 169–200. https://doi.org/10.1051/sfn/201112009.

Green, M. A.; Dunlop, E. D.; Hohl-Ebinger, J.; Yoshita, M.; Kopidakis, N.; Ho-Baillie, A. W. Y. *Solar Cell Efficiency Tables (Version 55)*. *Prog. Photovoltaics Res. Appl.* **2020**, *28* (1), 3–15. https://doi.org/10.1002/pip.3228.

Grimme, S.; Antony, J.; Ehrlich, S.; Krieg, H. *A Consistent and Accurate Ab Initio Parametrization of Density Functional Dispersion Correction (DFT-D) for the 94 Elements H-Pu*. *J. Chem. Phys.* **2010**, *132* (15), 154104. https://doi.org/10.1063/1.3382344.

Grimme, S.; Ehrlich, S.; Goerigk, L. *Effect of the Damping Function in Dispersion Corrected Density Functional Theory*. *J. Comput. Chem.* **2011**, *32* (7), 1456–1465. https://doi.org/10.1002/jcc.21759.

Gu, K.; Snyder, C. R.; Onorato, J.; Luscombe, C. K.; Bosse, A. W.; Loo, Y.-L. *Assessing the Huang–Brown Description of Tie Chains for Charge Transport in Conjugated Polymers*. *ACS Macro Lett.* **2018**, *7* (11), 1333–1338. https://doi.org/10.1021/acsmacrolett.8b00626.

Guilbert, A. A. Y.; Urbina, A.; Abad, J.; Díaz-Paniagua, C.; Batallán, F.; Seydel, T.; Zbiri, M.; García-Sakai, V.; Nelson, J. *Temperature-Dependent Dynamics of Polyalkylthiophene Conjugated Polymers: A Combined Neutron Scattering and Simulation Study*. *Chem. Mater.* **2015**, *27* (22), 7652–7661. https://doi.org/10.1021/acs.chemmater.5b03001.

Guilbert, A. A. Y.; Zbiri, M.; Dunbar, A. D. F.; Nelson, J. *Quantitative Analysis of the Molecular Dynamics of P3HT:PCBM Bulk Heterojunction*. *J. Phys. Chem. B* **2017**, *121* (38), 9073–9080. https://doi.org/10.1021/acs.jpcb.7b08312.

Guilbert, A. A. Y.; Zbiri, M.; Finn, P. A.; Jenart, M.; Fouquet, P.; Cristiglio, V.; Frick, B.; Nelson, J.; Nielsen, C. B. *Mapping Microstructural Dynamics up to the Nanosecond of the Conjugated Polymer P3HT in the Solid State*. *Chem. Mater.* **2019**, *31* (23), 9635–9651. https://doi.org/10.1021/acs.chemmater.9b02904.

Guilbert, A. A. Y.; Zbiri, M.; Jenart, M. V. C.; Nielsen, C. B.; Nelson, J. *New Insights into the Molecular Dynamics of P3HT:PCBM Bulk Heterojunction: A Time-of-Flight Quasi-Elastic Neutron Scattering Study*. *J. Phys. Chem. Lett.* **2016**, *7* (12), 2252–2257. https://doi.org/10.1021/acs.jpclett.6b00537.

Hadi Kiapour, M.; Yager, K.; Berg, A. C.; Berg, T. L. Materials Discovery: Fine-Grained Classification of X-Ray Scattering Images. In *IEEE Winter Conference on Applications of Computer Vision*; IEEE, 2014; pp 933–940. https://doi.org/10.1109/WACV.2014.6836004.

Hammouda, B. *A New Guinier–Porod Model*. *J. Appl. Crystallogr.* **2010**, *43* (4), 716–719. https://doi.org/10.1107/S0021889810015773.

Hammouda, B. *Analysis of the Beaucage Model*. *J. Appl. Crystallogr.* **2010**, *43* (6), 1474–1478. https://doi.org/10.1107/S0021889810033856.

Hammouda, B. *Probing Nanoscale Structures - The SANS Toolbox.*; National Institute for Standards and Technology Center for Neutron Research: Gaithersburg, MD, 2016.

Han, S.; Yu, X.; Shi, W.; Zhuang, X.; Yu, J. *Solvent-Dependent Electrical Properties Improvement of Organic Field-Effect Transistor Based on Disordered Conjugated Polymer/Insulator Blends*. *Org. Electron.* **2015**, *27*, 160–166. https://doi.org/10.1016/j.orgel.2015.09.003.

Harrelson, T. F.; Moulé, A. J.; Faller, R. *Modeling Organic Electronic Materials: Bridging Length and Time Scales*. *Mol. Simul.* **2017**, *43* (10–11), 730–742. https://doi.org/10.1080/08927022.2016.1273526.

Hellmann, C.; Treat, N. D.; Scaccabarozzi, A. D.; Razzell Hollis, J.; Fleischli, F. D.; Bannock, J. H.; de Mello, J.; Michels, J. J.; Kim, J.-S.; Stingelin, N. *Solution Processing of Polymer Semiconductor: Insulator Blends-Tailored Optical Properties through Liquid-Liquid Phase Separation Control*. *J. Polym. Sci. Part B Polym. Phys.* **2015**, *53* (4), 304–310. https://doi.org/10.1002/polb.23656.

Hernandez, E. R. Molecular Dynamics: from basic techniques to applications (A Molecular Dynamics Primer).

Higgins, J. S. *Neutron Scattering from Polymers: Five Decades of Developing Possibilities*. *Annu. Rev. Chem. Biomol. Eng.* **2016**, *7* (1), 1–28. https://doi.org/10.1146/annurev-chembioeng-080615-034429.

Hockney, R. W.; Eastwood, J. W. *Computer Simulation Using Particles*, 1st ed.; Bristol: Adam Hilger, 1988.

Huang, D. M.; Faller, R.; Do, K.; Moulé, A. J. *Coarse-Grained Computer Simulations of Polymer/Fullerene Bulk Heterojunctions for Organic Photovoltaic Applications*. *J. Chem. Theory Comput.* **2010**, *6* (2), 526–537. https://doi.org/10.1021/ct900496t.

Huynh, T. P.; Sharma, P. S.; Sosnowska, M.; D'Souza, F.; Kutner, W. *Functionalized Polythiophenes: Recognition Materials for Chemosensors and Biosensors of Superior Sensitivity, Selectivity, and Detectability*. *Prog. Polym. Sci.* **2015**, *47*, 1–25. https://doi.org/10.1016/j.progpolymsci.2015.04.009.

Ilavsky, J. *Nika : Software for Two-Dimensional Data Reduction*. *J. Appl. Crystallogr.* **2012**, *45* (2), 324–328. https://doi.org/10.1107/S0021889812004037.

Ilavsky, J.; Jemian, P. R.; Allen, A. J.; Zhang, F.; Levine, L. E.; Long, G. G. *Ultra-Small-Angle X-Ray Scattering at the Advanced Photon Source*. *J. Appl. Crystallogr.* **2009**, *42* (3), 469–479. https://doi.org/10.1107/S0021889809008802.

Ilavsky, J.; Zhang, F.; Andrews, R. N.; Kuzmenko, I.; Jemian, P. R.; Levine, L. E.; Allen, A. J. *Development of Combined Microstructure and Structure Characterization Facility for in Situ and Operando Studies at the Advanced Photon Source*. *J. Appl. Crystallogr.* **2018**, *51* (3), 867–882. https://doi.org/10.1107/S160057671800643X.

Israelachvili, J. N. *Intermolecular and Surface Forces*, 3rd ed.; Elsevier Inc., 2011.

Jones, M. L.; Huang, D. M.; Chakrabarti, B.; Groves, C. *Relating Molecular Morphology to Charge Mobility in Semicrystalline Conjugated Polymers*. *J. Phys. Chem. C* **2016**, *120* (8), 4240–4250. https://doi.org/10.1021/acs.jpcc.5b11511.

Jorgensen, W. L.; Maxwell, D. S.; Tirado-Rives, J. *Development and Testing of the OLPS All-Atom Force Field on Conformational Energetics and Properties of Organic Liquids*. *J. Am. Chem. Soc.* **1996**, *118* (15), 11225–11236. https://doi.org/10.1021/ja9621760.

Jorgensen, W. L.; McDonald, N. A. *Development of an All-Atom Force Field for Heterocycles. Properties of Liquid Pyridine and Diazenes*. *J. Mol. Struct. THEOCHEM* **1998**, *424* (1–2), 145–155. https://doi.org/10.1016/S0166-1280(97)00237-6.

Jorgensen, W. L.; Tirado-Rives, J. *Potential Energy Functions for Atomic-Level Simulations of Water and Organic and Biomolecular Systems*. *Proc. Natl. Acad. Sci.* **2005**, *102* (19), 6665–6670. https://doi.org/10.1073/pnas.0408037102.

Keum, J. K.; Xiao, K.; Ivanov, I. N.; Hong, K.; Browning, J. F.; Smith, G. S.; Shao, M.; Littrell, K. C.; Rondinone, A. J.; Andrew Payzant, E.; Chen, J.; Hensley, D. K. *Solvent Quality-Induced Nucleation and Growth of Parallelepiped Nanorods in Dilute Poly(3-Hexylthiophene) (P3HT) Solution and the Impact on the Crystalline Morphology of Solution-Cast Thin Film*. *CrystEngComm* **2013**, *15* (6), 1114–1124. https://doi.org/10.1039/C2CE26666K.

Kienzle, P. A.; Krycka, J.; Patel, N.; Sahin, I. *Bumps (Version 0.7.11)*. University of Maryland: College Park, MD 2011.

Kikhney, A. G.; Panjkovich, A.; Sokolova, A. V.; Svergun, D. I. *DARA: A Web Server for Rapid Search of Structural Neighbours Using Solution Small Angle X-Ray Scattering Data*. *Bioinformatics* **2016**, *32* (4), 616–618. https://doi.org/10.1093/bioinformatics/btv611.

Kline, R. J.; McGehee, M. D. *Morphology and Charge Transport in Conjugated Polymers*. *J. Macromol. Sci. Part C Polym. Rev.* **2006**, *46* (1), 27–45. https://doi.org/10.1080/15321790500471194.

Kline, S. R. *Reduction and Analysis of SANS and USANS Data Using IGOR Pro*. *J. Appl. Crystallogr.* **2006**, *39* (6), 895–900. https://doi.org/10.1107/S0021889806035059.

Kozlov, G. Z.; Zaikov, G. E. *Structure of the Polymer Amorphous State*; Taylor & Francis Group, LLC: Boca Raton, FL, 2004.

Kroon-Batenburg, L. M. J.; Helliwell, J. R.; McMahon, B.; Terwilliger, T. C. *Raw Diffraction Data Preservation and Reuse: Overview, Update on Practicalities and Metadata Requirements*. *IUCrJ* **2017**, *4* (1), 87–99. https://doi.org/10.1107/S2052252516018315.

Kuei, B.; Gomez, E. D. *Chain Conformations and Phase Behavior of Conjugated Polymers*. *Soft Matter* **2016**, *114*, 10087–10088. https://doi.org/10.1039/C6SM00979D.

Kumar, A.; Baklar, M. A.; Scott, K.; Kreouzis, T.; Stingelin-Stutzmann, N. *Efficient, Stable Bulk Charge Transport in Crystalline/Crystalline Semiconductor-Insulator Blends*. *Adv. Mater.* **2009**, *21* (44), 4447–4451. https://doi.org/10.1002/adma.200900717.

Lan, Y.-K.; Huang, C.-I. *A Theoretical Study of the Charge Transfer Behavior of the Highly Regioregular Poly-3-Hexylthiophene in the Ordered State*. *J. Phys. Chem. B* **2008**, *112* (47), 14857–14862. https://doi.org/10.1021/jp806967x.

Lan, Y.-K.; Huang, C.-I. *Charge Mobility and Transport Behavior in the Ordered and Disordered States of the Regioregular Poly(3-Hexylthiophene)*. *J. Phys. Chem. B* **2009**, *113* (44), 14555–14564. https://doi.org/10.1021/jp904841j.

Lee, C.; Yang, W.; Parr, R. G. *Development of the Colle-Salvetti Correlation-Energy Formula into a Functional of the Electron Density*. *Phys. Rev. B* **1988**, *37* (2), 785–789. https://doi.org/10.1103/PhysRevB.37.785.

Lee, Y.-T.; Li, D. S.; Pozzo, L. D. *Kinetic Analysis of Ultrasound-Induced Oil Exchange in Oil-in-Water Emulsions through Contrast Variation Time-Resolved Small-Angle Neutron Scattering*. *Langmuir* **2019**. https://doi.org/10.1021/acs.langmuir.9b02424.

Lee, Y.-T.; Pozzo, L. D. *Contrast-Variation Time-Resolved SANS Analysis of Oil Exchange Kinetics Between Oil-in-Water Emulsions Stabilized by Anionic Surfactants*. *Langmuir* **2019**. https://doi.org/10.1021/acs.langmuir.9b02423.

Li, G.; Chang, W.-H.; Yang, Y. *Low-Bandgap Conjugated Polymers Enabling Solution-Processable Tandem Solar Cells*. *Nat. Rev. Mater.* **2017**, *2* (8), 17043. https://doi.org/10.1038/natrevmats.2017.43.

Li, T.; Xu, L.; Xiao, X.; Chen, F.; Cao, L.; Wu, W.; Tong, W.; Zhang, F. *Enhanced Spin Transport of Conjugated Polymer in the Semiconductor/Insulating Polymer Blend*. *ACS Appl. Mater. Interfaces* **2020**, *12* (2), 2708–2716. https://doi.org/10.1021/acsami.9b16602.

Li, Z.; Chueh, C.-C.; Jen, A. K.-Y. *Recent Advances in Molecular Design of Functional Conjugated Polymers for High-Performance Polymer Solar Cells*. *Prog. Polym. Sci.* **2019**, *99*, 101175. https://doi.org/10.1016/j.progpolymsci.2019.101175.

Liu, J.; Arif, M.; Zou, J.; Khondaker, S. I.; Zhai, L. *Controlling Poly(3-Hexylthiophene) Crystal Dimension: Nanowhiskers and Nanoribbons*. *Macromolecules* *42* (24), 9390–9393. https://doi.org/10.1021/ma901955c.

Liu, J.; Loewe, R. S.; McCullough, R. D. *Employing MALDI-MS on Poly(Alkylthiophenes): Analysis of Molecular Weights, Molecular Weight Distributions, End-Group Structures, and End-Group Modifications*. *Macromolecules* **1999**, *32* (18), 5777–5785. https://doi.org/10.1021/ma9905324.

Lu, G.; Blakesley, J.; Himmelberger, S.; Pingel, P.; Frisch, J.; Lieberwirth, I.; Salzmann, I.; Oehzelt, M.; Di Pietro, R.; Salleo, A.; Koch, N.; Neher, D. *Moderate Doping Leads to High Performance of Semiconductor/Insulator Polymer Blend Transistors*. *Nat. Commun.* **2013**, *4* (1), 1588. https://doi.org/10.1038/ncomms2587.

Mamontov, E.; Herwig, K. W. *A Time-of-Flight Backscattering Spectrometer at the Spallation Neutron Source, BASIS*. *Rev. Sci. Instrum.* **2011**, *82* (8), 085109. https://doi.org/10.1063/1.3626214.

Marchiori, C. F. N.; Koehler, M. *Density Functional Theory Study of the Dipole across the P3HT : PCBM Complex: The Role of Polarization and Charge Transfer*. *J. Phys. D. Appl. Phys.* **2014**, *47* (21), 215104. https://doi.org/10.1088/0022-3727/47/21/215104.

Marcon, V.; Raos, G. *Free Energies of Molecular Crystal Surfaces by Computer Simulation: Application to Tetrathiophene*. *J. Am. Chem. Soc.* **2006**, *128* (5), 1408–1409. https://doi.org/10.1021/ja056548t.

Marcon, V.; Raos, G. *Molecular Modeling of Crystalline Oligothiophenes: Testing and Development of Improved Force Fields*. *J. Phys. Chem. B* **2004**, *108* (46), 18053–18064. https://doi.org/10.1021/jp047128d.

Mardirossian, N.; Head-Gordon, M. *Thirty Years of Density Functional Theory in Computational Chemistry: An Overview and Extensive Assessment of 200 Density Functionals*. *Mol. Phys.* **2017**, *115* (19), 2315–2372. https://doi.org/10.1080/00268976.2017.1333644.

Mason, T. E.; Gawne, T. J.; Nagler, S. E.; Nestor, M. B.; Carpenter, J. M. *The Early Development of Neutron Diffraction: Science in the Wings of the Manhattan Project*. *Acta Crystallogr. Sect. A Found. Crystallogr.* **2013**, *69* (1), 37–44. https://doi.org/10.1107/S0108767312036021.

Mazzio, K. a.; Luscombe, C. K. *The Future of Organic Photovoltaics*. *Chem. Soc. Rev.* **2014**, *44* (1), 78–90. https://doi.org/10.1039/c4cs00227j.

McCulloch, B.; Ho, V.; Hoarfrost, M.; Stanley, C.; Do, C.; Heller, W. T.; Segalman, R. A. *Polymer Chain Shape of Poly(3-Alkylthiophenes) in Solution Using Small-Angle Neutron Scattering*. *Macromolecules* **2013**, *46* (5), 1899–1907. https://doi.org/10.1021/ma302463d.

McCulloch, I.; Heeney, M.; Bailey, C.; Genevicius, K.; Macdonald, I.; Shkunov, M.; Sparrowe, D.; Tierney, S.; Wagner, R.; Zhang, W.; Chabinyc, M. L.; Kline, R. J.; McGehee, M. D.; Toney, M. F. *Liquid-Crystalline Semiconducting Polymers with High Charge-Carrier Mobility*. **2006**, *5* (April).

McMahon, D. P.; Cheung, D. L.; Goris, L.; Dacuña, J.; Salleo, A.; Troisi, A. *Relation between Microstructure and Charge Transport in Polymers of Different Regioregularity*. *J. Phys. Chem. C* **2011**, *115* (39), 19386–19393. https://doi.org/10.1021/jp207026s.

Mehmood, U.; Al-Ahmed, A.; Hussein, I. A. *Review on Recent Advances in Polythiophene Based Photovoltaic Devices*. *Renew. Sustain. Energy Rev.* **2016**, *57*, 550–561. https://doi.org/10.1016/j.rser.2015.12.177.

Mei, J.; Bao, Z. *Side Chain Engineering in Solution-Processable Conjugated Polymers*. *Chem. Mater.* **2014**, *26* (1), 604–615. https://doi.org/10.1021/cm4020805.

Mei, J.; Diao, Y.; Appleton, A. L.; Fang, L.; Bao, Z. *Integrated Materials Design of Organic Semiconductors for Field-Effect Transistors*. *J. Am. Chem. Soc.* **2013**, *135* (18), 6724–6746. https://doi.org/10.1021/ja400881n.

Merlo, J. A.; Frisbie, C. D. *Field Effect Transport and Trapping in Regioregular Polythiophene Nanofibers*. *J. Phys. Chem. B 108* (50), 19169–19179. https://doi.org/10.1021/jp047023a.

Meyer, A.; Dimeo, R. M.; Gehring, P. M.; Neumann, D. A. *The High-Flux Backscattering Spectrometer at the NIST Center for Neutron Research*. *Rev. Sci. Instrum.* **2003**, *74* (5), 2759–2777. https://doi.org/10.1063/1.1568557.

Mitchell, G. R.; Windle, A. H. *Structure of Polystyrene Glasses*. *Polymer (Guildf).* **1984**, *25* (7), 906–920. https://doi.org/10.1016/0032-3861(84)90073-9.

Mo, Z.; Lee, K. B.; Moon, Y. B.; Kobayashi, M.; Heeger, A. J.; Wudl, F. *X-Ray Scattering from Poly(Thiophene): Crystallinity and Crystallographic Structure*. *Macromolecules* **1985**, *18* (10), 1972–1977. https://doi.org/10.1021/ma00152a028.

Moreno, M.; Casalegno, M.; Raos, G.; Meille, S. V.; Po, R. *Molecular Modeling of Crystalline Alkylthiophene Oligomers and Polymers*. *J. Phys. Chem. B* **2010**, *114* (4), 1591–1602. https://doi.org/10.1021/jp9106124.

Mounet, N.; Gibertini, M.; Schwaller, P.; Campi, D.; Merkys, A.; Marrazzo, A.; Sohier, T.; Castelli, I. E.; Cepellotti, A.; Pizzi, G.; Marzari, N. *Two-Dimensional Materials from High-Throughput Computational Exfoliation of Experimentally Known Compounds*. *Nat. Nanotechnol.* **2018**, *13* (3), 246–252. https://doi.org/10.1038/s41565-017-0035-5.

Munter, A. Neutron scattering lengths and cross sections https://www.ncnr.nist.gov/resources/n-lengths/ (accessed Sep 1, 2017).

Nedoma, A. J.; Robertson, M. L.; Wanakule, N. S.; Balsara, N. P. *Measurements of the Composition and Molecular Weight Dependence of the Flory−Huggins Interaction Parameter*. *Macromolecules* **2008**, *41* (15), 5773–5779. https://doi.org/10.1021/ma800698r.

Neutron Scattering https://www.iop.org/publications/iop/2011/file_47455.pdf.

Neutrons, X-Rays and Light: Scattering Methods Applied to Soft Condensed Matter, First.; Lindner, P., Zemb, T., Eds.; Elsevier Science B.V: Amsterdam, 2002.

Newbloom, G. M. Engineering the Multi-Length Scale Structure of Self-Assembled Conjugated Polymer Networks, University of Washington, 2014.

Newbloom, G. M.; Hoffmann, S. M.; West, A. F.; Gile, M. C.; Sista, P.; Cheung, H. K. C.; Luscombe, C. K.; Pfaendtner, J.; Pozzo, L. D. *Solvatochromism and Conformational Changes in Fully Dissolved Poly(3-Alkylthiophene)S*. *Langmuir* **2015**, *31* (1), 458–468. https://doi.org/10.1021/la503666x.

Newbloom, G. M.; Kim, F. S.; Jenekhe, S. A.; Pozzo, D. C. *Mesoscale Morphology and Charge Transport in Colloidal Networks of Poly(3-Hexylthiophene)*. *Macromolecules* **2011**, *44* (10), 3801–3809. https://doi.org/10.1021/ma2000515.

NREL Best Research-Cell Efficiency Chart https://www.nrel.gov/pv/cell-efficiency.html (accessed Jun 11, 2020).

Obrzut, J.; Page, K. A. *Electrical Conductivity and Relaxation in Poly(3-Hexylthiophene)*. *Phys. Rev. B* **2009**, *80* (19), 195211. https://doi.org/10.1103/PhysRevB.80.195211.

Ong, B. S.; Wu, Y.; Li, Y.; Liu, P.; Pan, H. *Thiophene Polymer Semiconductors for Organic Thin-Film Transistors*. *Chem. - A Eur. J.* **2008**, *14* (16), 4766–4778. https://doi.org/10.1002/chem.200701717.

Ong, B. S.; Wu, Y.; Liu, P.; Gardner, S. *High-Performance Semiconducting Polythiophenes for Organic Thin-Film Transistors*. *J. Am. Chem. Soc.* **2004**, *126* (11), 3378–3379. https://doi.org/10.1021/ja039772w.

Onsager, L. *The Effects of Shape on the Interaction of Colloidal Particles*. *Ann. N. Y. Acad. Sci.* **1949**, *51* (4), 627–659.

Pandey, M.; Kumari, N.; Nagamatsu, S.; Pandey, S. S. *Recent Advances in the Orientation of Conjugated Polymers for Organic Field-Effect Transistors*. *J. Mater. Chem. C* **2019**, *7* (43), 13323–13351. https://doi.org/10.1039/C9TC04397G.

Park, Y. D.; Lee, H. S.; Choi, Y. J.; Kwak, D.; Cho, J. H.; Lee, S.; Cho, K. *Solubility-Induced Ordered Polythiophene Precursors for High-Performance Organic Thin-Film Transistors*. *Adv. Funct. Mater.* **2009**, *19* (8), 1200–1206. https://doi.org/10.1002/adfm.200801763.

Parnell, A. J.; Cadby, A. J.; Mykhaylyk, O. O.; Dunbar, A. D. F.; Hopkinson, P. E.; Donald, A. M.; Jones, R. A. L. *Nanoscale Phase Separation of P3HT PCBM Thick Films As Measured by Small-Angle X-Ray Scattering*. *Macromolecules* **2011**, *44* (16), 6503–6508. https://doi.org/10.1021/ma2007706.

Pedersen, J. S. *Analysis of Small-Angle Scattering Data from Colloids and Polymer Solutions: Modeling and Least-Squares Fitting*. *Adv. Colloid Interface Sci.* **1997**, *70*.

Pellegrini, E.; Calligari, P.; Calandrini, V.; Hinsen, K.; Kneller, G. R. *NMOLDYN User's Guide Version 3.4*; 2009.

Plimpton, S. *Fast Parallel Algorithms for Short-Range Molecular Dynamics*. *J. Comput. Phys.* **1995**, *117* (1), 1–19, http://lammps.sandia.gov. https://doi.org/10.1006/jcph.1995.1039.

Polymers and Neutron Scattering; Higgins, J. S., Benoit, H. C., Eds.; Oxford University Press Inc.: New York, 1994.

Porod, G. *Die Röntgenkleinwinkelstreuung von Dichtgepackten Kolloiden Systemen*. *Kolloid-Zeitschrift* **1951**, *124* (2), 83–114. https://doi.org/10.1007/BF01512792.

Pozzo, L. USAXS 48 Solid Film Holder https://www.thingiverse.com/thing:4639006/files (accessed Nov 2, 2020).

Prosa, T. J.; Winokur, M. J.; Moulton, J.; Smith, P.; Heeger, A. J. *X-Ray Structural Studies of Poly(3-Alkylthiophenes): An Example of an Inverse Comb*. *Macromolecules* **1992**, *25* (17), 4364–4372. https://doi.org/10.1021/ma00043a019.

Qiu, L.; Lee, W. H.; Wang, X.; Kim, J. S.; Lim, J. A.; Kwak, D.; Lee, S.; Cho, K. *Organic Thin-Film Transistors Based on Polythiophene Nanowires Embedded in Insulating Polymer*. *Adv. Mater.* **2009**, *21* (13), 1349–1353. https://doi.org/10.1002/adma.200802880.

Qiu, L.; Wang, X.; Lee, W. H.; Lim, J. A.; Kim, J. S.; Kwak, D.; Cho, K. *Organic Thin-Film Transistors Based on Blends of Poly(3-Hexylthiophene) and Polystyrene with a Solubility-Induced Low Percolation Threshold*. *Chem. Mater.* **2009**, *21* (19), 4380–4386. https://doi.org/10.1021/cm900628j.

Renninger, A. L.; Uhlmann, D. R. *Structure of Glassy Polymers. V. Small-Angle x-Ray Scattering from Polystyrene*. *J. Polym. Sci. Polym. Phys. Ed.* **1978**, *16* (12), 2237–2244. https://doi.org/10.1002/pol.1978.180161210.

Richter, D.; Monkenbusch, M.; Arbe, A.; Colmenero, J. *Neutron Spin Echo in Polymer Systems*; Springer Berlin Heidelberg: Berlin, Heidelberg, 2005. https://doi.org/10.1007/b106578.

Rivnay, J.; Jimison, L. H.; Northrup, J. E.; Toney, M. F.; Noriega, R.; Lu, S.; Marks, T. J.; Facchetti, A.; Salleo, A. *Large Modulation of Carrier Transport by Grain-Boundary Molecular Packing and Microstructure in Organic Thin Films*. *Nat. Mater.* **2009**, *8* (12), 952–958. https://doi.org/10.1038/nmat2570.

Roe, R. J.; Curro, J. J. *Small-Angle x-Ray Scattering Study of Density Fluctuation in Polystyrene Annealed below the Glass Transition Temperature*. *Macromolecules* **1983**, *16* (3), 428–434. https://doi.org/10.1021/ma00237a018.

Rosov, N.; Rathgeber, S.; Monkenbusch, M. Neutron Spin Echo Spectroscopy at the NIST Center for Neutron Research. In *Scattering from polymers: characterization by x-rays, neutrons, and light*; Cebe, P., Hsaio, B. S., Lohse, D. J., Eds.; American Chemical Society: Washington, D.C., 2000; pp 103–116.

Rush, J. J.; Cappelletti, R. L. The NIST Center for Neutron Research: Over 40 Years Serving NIST/NBS and the Nation.

Russell, T. P.; Ito, H.; Wignall, G. D. *Neutron and X-Ray Scattering Studies on Semicrystalline Polymer Blends*. *Macromolecules* **1988**, *21* (6), 1703–1709. https://doi.org/10.1021/ma00184a029.

Sakai, V. G.; Arbe, A. *Quasielastic Neutron Scattering in Soft Matter*. *Curr. Opin. Colloid Interface Sci.* **2009**, *14* (6), 381–390. https://doi.org/10.1016/j.cocis.2009.04.002.

Salzmann, I.; Heimel, G.; Oehzelt, M.; Winkler, S.; Koch, N. *Molecular Electrical Doping of Organic Semiconductors: Fundamental Mechanisms and Emerging Dopant Design Rules*. *Acc. Chem. Res.* **2016**, *49* (3), 370–378. https://doi.org/10.1021/acs.accounts.5b00438.

Samanta, K.; Guenet, J.-M.; Malik, S. *Intermingled Network of Syndiotactic Polystyrene/Poly(3-Hexylthiophene)*. *Macromolecules* **2019**, *52* (22), 8569–8576. https://doi.org/10.1021/acs.macromol.9b01512.

Schmit, J. D.; Levine, A. J. *Statistical Model for Intermolecular Adhesion π-Conjugated Polymers*. *Phys. Rev. Lett.* **2008**, *100* (19), 198303. https://doi.org/10.1103/PhysRevLett.100.198303.

Schwarz, K. N.; Kee, T. W.; Huang, D. M. *Coarse-Grained Simulations of the Solution-Phase Self-Assembly of Poly(3-Hexylthiophene) Nanostructures*. *Nanoscale* **2013**, *5* (5), 2017. https://doi.org/10.1039/c3nr33324h.

Sears, V. F. *Neutron Scattering Lengths and Cross Sections*. *Neutron News* **1992**, *3* (3), 26–37. https://doi.org/10.1080/10448639208218770.

Sekine, C.; Tsubata, Y.; Yamada, T.; Kitano, M.; Doi, S. *Recent Progress of High Performance Polymer OLED and OPV Materials for Organic Printed Electronics*. *Sci. Technol. Adv. Mater.* **2014**, *15* (3), 034203. https://doi.org/10.1088/1468-6996/15/3/034203.

Sekine, C.; Tsubata, Y.; Yamada, T.; Kitano, M.; Doi, S. *Recent Progress of High Performance Polymer OLED and OPV Materials for Organic Printed Electronics*. *Sci. Technol. Adv. Mater.* **2014**, *15* (3), 034203. https://doi.org/10.1088/1468-6996/15/3/034203.

Selivanova, M.; Chuang, C.-H.; Billet, B.; Malik, A.; Xiang, P.; Landry, E.; Chiu, Y.-C.; Rondeau-Gagné, S. *Morphology and Electronic Properties of Semiconducting Polymer and Branched Polyethylene Blends*. *ACS Appl. Mater. Interfaces* **2019**, *11* (13), 12723–12732. https://doi.org/10.1021/acsami.8b22746.

Simon, S.; Duran, M.; Dannenberg, J. J. *How Does Basis Set Superposition Error Change the Potential Surfaces for Hydrogen‐bonded Dimers? J. Chem. Phys.* **1996**, *105* (24), 11024–11031. https://doi.org/10.1063/1.472902.

Sirringhaus, H. *25th Anniversary Article: Organic Field-Effect Transistors: The Path Beyond Amorphous Silicon*. *Adv. Mater.* **2014**, *26* (9), 1319–1335. https://doi.org/10.1002/adma.201304346.

Snyder, C. R.; Nieuwendaal, R. C.; DeLongchamp, D. M.; Luscombe, C. K.; Sista, P.; Boyd, S. D. *Quantifying Crystallinity in High Molar Mass Poly(3-Hexylthiophene)*. *Macromolecules* **2014**, *47* (12), 3942–3950. https://doi.org/10.1021/ma500136d.

Someya, T.; Bao, Z.; Malliaras, G. G. *The Rise of Plastic Bioelectronics*. *Nature* **2016**, *540* (7633), 379–385. https://doi.org/10.1038/nature21004.

Song, H. H.; Roe, R. J. *Structural Change Accompanying Volume Change in Amorphous Polystyrene as Studied by Small and Intermediate Angle X-Ray Scattering*. *Macromolecules* **1987**, *20* (11), 2723–2732. https://doi.org/10.1021/ma00177a016.

Sutmann, G. Classical Molecular Dynamics. In *Quantum Simulations of Complex Many-Body Systems: From Theory to Algorithms, Lecture Notes*; Grotendorst, J., Marx, D., Muramatsu, A., Eds.; 2002; pp 211–254.

T., R.; K., M.; K., H.; Kneller, G. R. *NMoldyn : A Program Package for a Neutron Scattering*. *J. Comput. Chem.* **2003**, *24* (5), 657–667. https://doi.org/10.1002/jcc.10243.

Tapping, P. C.; Clafton, S. N.; Schwarz, K. N.; Kee, T. W.; Huang, D. M. *Molecular-Level Details of Morphology-Dependent Exciton Migration in Poly(3-Hexylthiophene) Nanostructures*. *J. Phys. Chem. C* **2015**, *119* (13), 7047–7059. https://doi.org/10.1021/acs.jpcc.5b00705.

Toolan, D. T. W.; Barker, R.; Gough, T.; Topham, P. D.; Howse, J. R.; Glidle, A. *Gravimetric and Density Profiling Using the Combination of Surface Acoustic Waves and Neutron Reflectivity*. *J. Colloid Interface Sci.* **2017**, *487*, 465–474. https://doi.org/10.1016/j.jcis.2016.10.039.

Trewhella, J.; Duff, A. P.; Durand, D.; Gabel, F.; Guss, J. M.; Hendrickson, W. A.; Hura, G. L.; Jacques, D. A.; Kirby, N. M.; Kwan, A. H.; Pérez, J.; Pollack, L.; Ryan, T. M.; Sali, A.; Schneidman-Duhovny, D.; Schwede, T.; Svergun, D. I.; Sugiyama, M.; Tainer, J. A.; Vachette, P.; Westbrook, J.; Whitten, A. E. *2017 Publication Guidelines for Structural Modelling of Small-Angle Scattering Data from Biomolecules in Solution: An Update*. *Acta Crystallogr. Sect. D Struct. Biol.* **2017**, *73* (9), 710–728. https://doi.org/10.1107/S2059798317011597.

Vakhshouri, K.; Smith, B. H.; Chan, E. P.; Wang, C.; Salleo, A.; Wang, C.; Hexemer, A.; Gomez, E. D. *Signatures of Intracrystallite and Intercrystallite Limitations of Charge Transport in Polythiophenes*. *Macromolecules* **2016**, *49* (19), 7359–7369. https://doi.org/10.1021/acs.macromol.6b01086.

Valentini, E.; Kikhney, A. G.; Previtali, G.; Jeffries, C. M.; Svergun, D. I. *SASBDB, a Repository for Biological Small-Angle Scattering Data*. *Nucleic Acids Res.* **2015**, *43* (D1), D357–D363. https://doi.org/10.1093/nar/gku1047.

VSANS Detectors https://ncnr.nist.gov/equipment/msnew/ncnr/vsans-detectors.html (accessed May 31, 2020).

Wallace, W. E.; Beck Tan, N. C.; Wu, W. L.; Satija, S. *Mass Density of Polystyrene Thin Films Measured by Twin Neutron Reflectivity*. *J. Chem. Phys.* **1998**, *108* (9), 3798–3804. https://doi.org/10.1063/1.475769.

Wang, M.; Baek, P.; Akbarinejad, A.; Barker, D.; Travas-Sejdic, J. *Conjugated Polymers and Composites for Stretchable Organic Electronics*. *J. Mater. Chem. C* **2019**, *7* (19), 5534–5552. https://doi.org/10.1039/C9TC00709A.

Wei, J. N.; Duvenaud, D.; Aspuru-Guzik, A. *Neural Networks for the Prediction of Organic Chemistry Reactions*. *ACS Cent. Sci.* **2016**, *2* (10), 725–732. https://doi.org/10.1021/acscentsci.6b00219.

Wendorff, J. H. *The Structure of Amorphous Polymers*. *Polymer (Guildf).* **1982**, *23* (4), 543–557. https://doi.org/10.1016/0032-3861(82)90094-5.

Wolf, C. M.; Kanekal, K. H.; Yimer, Y. Y.; Tyagi, M.; Omar-Diallo, S.; Pakhnyuk, V.; Luscombe, C. K.; Pfaendtner, J.; Pozzo, L. D. *Assessment of Molecular Dynamics Simulations for Amorphous Poly(3-Hexylthiophene) Using Neutron and X-Ray Scattering Experiments*. *Soft Matter* **2019**, *15* (25), 5067–5083. https://doi.org/10.1039/C9SM00807A.

Wolf, C. pozzo-research-group/c-wolf-blends-morphology: Initial Development (Version v0.1.0) http://doi.org/10.5281/zenodo.4035166.

Xi, Y.; Li, D. S.; Newbloom, G. M.; Tatum, W. K.; O'Donnell, M.; Luscombe, C. K.; Pozzo, L. D. *Sonocrystallization of Conjugated Polymers with Ultrasound Fields*. *Soft Matter* **2018**, *14* (24), 4963–4976. https://doi.org/10.1039/C8SM00905H.

Xi, Y.; Pozzo, L. D. *Electric Field Directed Formation of Aligned Conjugated Polymer Fibers*. *Soft Matter* **2017**, *13* (21), 3894–3908. https://doi.org/10.1039/C7SM00485K.

Xi, Y.; Wolf, C. M.; Pozzo, L. D. *Self-Assembly of Donor–Acceptor Conjugated Polymers Induced by Miscible 'Poor' Solvents*. *Soft Matter* **2019**, *15* (8), 1799–1812. https://doi.org/10.1039/C8SM02517G.

Yimer, Y. Y.; Tsige, M. *Static and Dynamic Properties of Poly(3-Hexylthiophene) Films at Liquid/Vacuum Interfaces*. *J. Chem. Phys.* **2012**, *137* (20), 204701. https://doi.org/10.1063/1.4767395.

Yoon, C. H.; Schwander, P.; Abergel, C.; Andersson, I.; Andreasson, J.; Aquila, A.; Bajt, S.; Barthelmess, M.; Barty, A.; Bogan, M. J.; Bostedt, C.; Bozek, J.; Chapman, H. N.; Claverie, J.-M.; Coppola, N.; DePonte, D. P.; Ekeberg, T.; Epp, S. W.; Erk, B.; Fleckenstein, H.; Foucar, L.; Graafsma, H.; Gumprecht, L.; Hajdu, J.; Hampton, C. Y.; Hartmann, A.; Hartmann, E.; Hartmann, R.; Hauser, G.; Hirsemann, H.; Holl, P.; Kassemeyer, S.; Kimmel, N.; Kiskinova, M.; Liang, M.; Loh, N.-T. D.; Lomb, L.; Maia, F. R. N. C.; Martin, A. V.; Nass, K.; Pedersoli, E.; Reich, C.; Rolles, D.; Rudek, B.; Rudenko, A.; Schlichting, I.; Schulz, J.; Seibert, M.; Seltzer, V.; Shoeman, R. L.; Sierra, R. G.; Soltau, H.; Starodub, D.; Steinbrener, J.; Stier, G.; Strüder, L.; Svenda, M.; Ullrich, J.; Weidenspointner, G.; White, T. A.; Wunderer, C.; Ourmazd, A. *Unsupervised Classification of Single-Particle X-Ray Diffraction Snapshots by Spectral Clustering*. *Opt. Express* **2011**, *19* (17), 16542. https://doi.org/10.1364/OE.19.016542.

Zhan, P.; Zhang, W.; Jacobs, I. E.; Nisson, D. M.; Xie, R.; Weissen, A. R.; Colby, R. H.; Moulé, A. J.; Milner, S. T.; Maranas, J. K.; Gomez, E. D. *Side Chain Length Affects Backbone Dynamics in Poly(3-Alkylthiophene)S. J. Polym. Sci. Part B Polym. Phys.* **2018**, *56* (17), 1193–1202. https://doi.org/10.1002/polb.24637.

Zhang, L.; Colella, N. S.; Liu, F.; Trahan, S.; Baral, J. K.; Winter, H. H.; Mannsfeld, S. C. B.; Briseno, A. L. *Synthesis, Electronic Structure, Molecular Packing/Morphology Evolution, and Carrier Mobilities of Pure Oligo-/Poly(Alkylthiophenes). J. Am. Chem. Soc.* **2013**, *135* (2), 844–854. https://doi.org/10.1021/ja310ww4796.

Zhugayevych, A.; Mazaleva, O.; Naumov, A.; Tretiak, S. *Lowest-Energy Crystalline Polymorphs of P3HT. J. Phys. Chem. C* **2018**, *122* (16), 9141–9151. https://doi.org/10.1021/acs.jpcc.7b11271.

CURRICULUM VITAE

Caitlyn Wolf

Education

University of Washington **Seattle, WA**
Ph.D. Candidate in Chemical Engineering: Advanced Data Science **December 2020**
Thesis Title: Molecular Conformation and Dynamics of Conjugated Polymers using Neutron and X-ray Scattering and Simulations
GPA: 3.82/4.00

M.S. in Chemical Engineering **March 2018**
GPA: 3.84/4.00

University of North Dakota **Grand Forks, ND**
B.S. in Chemical Engineering, Minor in Mathematics **May 2015**
GPA: 4.00/4.00

Research & Professional Experience

Graduate Student Research Assistant **September 2015 –Present**
University of Washington, Department of Chemical Engineering Seattle, WA
Advisor: Professor Lilo Pozzo

- Utilizing quasi-elastic neutron scattering to explore molecular dynamics in conjugated polymers and oligomers.
- Evaluating non-bonded parameters of force fields for molecular dynamics simulations of conjugated polymers using neutron scattering and density functional theory
- Exploring morphology-function relationships in conjugated and non-conjugated polymer blends.
- Performed neutron scattering experiments at the NIST Center for Neutron Research and ORNL Spallation Neutron Source using both small-angle and spectrometer instruments.
- Validated molecular dynamics simulation force fields for conjugated polymers using neutron and X-ray scattering.
- Skilled in utilizing the University of Washington supercomputing cluster, Hyak, for running molecular dynamics simulations and processing large quantities of data efficiently.

23rd Center for High Resolution Neutron Scattering "Summer School on Methods and Applications of Neutron Spectroscopy" **June 19-23, 2017**
NIST Center for Neutron Research,
National Institute of Standards and Technology Gaithersburg, MD

- Participated in an intensive one-week training school on neutron methods accessing molecular-scale dynamics, including Neutron Spin Echo, Disk Chopper Spectrometer, and Triple-Axis Spectrometer instruments.

Engineering Intern **May – August 2015**
ComDel Innovation & Heartland Precision Wahpeton, ND

- Developed testing and new quality control procedures to optimize efficiency, lower cost, and improve product quality in metal finishing processes, and performed sensitivity analyses on wastewater treatment lines.

Research, Development & Innovation Intern **May – August 2014**
Andersen Windows, Adhesives & Hardware Team Bayport, MN

- Developed project plans and validation testing for line optimization projects related to adhesive components.

Undergraduate Student Researcher **January – November 2013**
University of North Dakota, Department of Chemical Engineering Grand Forks, ND
Advisor: Professor Gautham Krishnamoorthy

- Performed computational fluid dynamics to study radiative heat transfer in oxy-fuel combustion systems.

Publications

C. M. Wolf, L. Guio, S. C. Scheiwiller, R. P. O'Hara, C. K. Luscombe, L. D. Pozzo, "Blend Morphology in Polythiophene-Polystyrene Composites from Neutron and X-ray Scattering", 2020. *Submitted.*

C. D. Curtis, **C. M. Wolf**, and D. A. C. Beck, "Enrichment of Student Learning and Homework Management with use of GitHub in an Introductory Cross-disciplinary Engineering Course Series on Software Engineering and Data Science", *Chemical Engineering Education*, 2020, 54 (4). DOI: 10.18260/2-1-370.660-119316.

C. M. Wolf*, K. H. Kanekal*, Y. Y. Yimer, M. Tyagi, S. Omar-Diallo, V. Pakhnyuk, C. K. Luscombe, J. Pfaendtner, and L. D. Pozzo, "Assessment of Molecular Dynamics Simulations for Amorphous Poly(3-hexylthiophene) using Neutron and X-ray Scattering Experiments", *Soft Matter,* 2019, 15 (25), 5067-5083. DOI: 10.1039/C9SM00807A
*These authors contributed equally to this work.

Y. Xi, **C. M. Wolf**, and L. D. Pozzo, "Self-assembly of donor–acceptor conjugated polymers induced by miscible 'poor' solvents", *Soft Matter*, 2019, 15 (8), 1799–1812. DOI: 10.1039/C8SM02517G

G. Krishnamoorthy and **C. M. Wolf**, "Assessing the Role of Particles in Radiative Heat Transfer during Oxy-Combustion of Coal and Biomass Blends", *Journal of Combustion,* 2015, 1–15. DOI: 10.1155/2015/793683

Presentations & Posters

C. M. Wolf, L. Guio, C. Luscombe and L. D. Pozzo, "Structural Analysis of Polythiophene-Polystyrene Blends via Small-Angle Neutron Scattering" **Presentation** **July 14, 2020**
2020 American Conference on Neutron Scattering (ACNS)

C. M. Wolf and L. D. Pozzo, "Assessment of Molecular Dynamics Force Fields for Conjugated Polymers Using Neutron and X-Ray Scattering" **Presentation** **November 11, 2019**
2019 American Institute of Chemical Engineers (AIChE) Annual Meeting

C. M. Wolf, R. O'Hara and L. D. Pozzo, "Molecular Conformation and Dynamics of Conjugated Polymers using Neutron Scattering" **Presentation** **September 19, 2019**
12th Annual Chemical Engineering Graduate Student Symposium
Department of Chemical Engineering, University of Washington

C. M. Wolf and L. D. Pozzo, "Structure-function relationship of conjugated and non-conjugated polymer blends" **Presentation** **June 19, 2019**
93rd ACS Colloid & Surface Science Symposium

C. M. Wolf and L. D. Pozzo, "A comprehensive data repository for neutron scattering and improved molecular models" **Seminar** **November 20, 2018**
eScience Institute Community Seminar, University of Washington

C. M. Wolf and L. D. Pozzo, "Neutron Scattering and Computational Analysis of Molecular Conformation and Dynamics in Conductive Poly(3-hexylthiophene)" **Presentation** **June 26, 2018**
American Conference on Neutron Scattering

C. M. Wolf and L. D. Pozzo*, "Building a Comprehensive Repository for Small-Angle Neutron Scattering Data" **Presentation** **June 26, 2018**
American Conference on Neutron Scattering
*Presented at the conference by L. D. Pozzo.

C. M. Wolf and L. D. Pozzo, "Dynamics of conjugated polymers from neutron scattering and molecular simulation" **Presentation** **July 10, 2017**
91st ACS Colloid & Surface Science Symposium

C. M. Wolf, K. Kanekal, Y. Yimer and L. D. Pozzo, "Force Field Development for Conjugated Polymers: Optimization with Scattering Methods" **Poster** **September 7, 2016**
Orcas 2016: International Conference on Energy Conversion & Storage

C. M. Wolf, K. Kanekal, Y. Yimer and L. D. Pozzo, "Force Field Development for Conjugated Polymers: Molecular Dynamics Validation with Neutron and X-ray Scattering" **Poster** **August 29, 2018**
Theory and Applications of Computational Chemistry

Leadership Experience

Pozzo Research Group Lab Manager **June 2017 – June 2019**
Faculty Advisor: Professor Lilo Pozzo Seattle, WA

- Ensured safety compliance of the Pozzo Research Group lab spaces, and coordinated with the University of Washington's Environmental Health & Safety for annual safety inspections.
- Performed lab safety training for new group members and manage training records.
- Managed the weekly group meeting location and schedule. Assigned lab members to the lab cleanup rotation.

9th Annual Distinguished Young Scholars Seminar

Planning Committee **April – September 2019**
Department of Chemical Engineering, University of Washington Seattle, WA

- As lead TA, ensured that the planning committee met critical deadlines in planning a summer seminar series for visiting graduate students and postdoctoral researchers.
- Coordinated and directed a large team of graduate students for an NSF-style review panel of seminar applications. With the planning committee, developed and hosted a bias training session for the panelists prior to aid in fair application review.
- Assisted the planning committee in the summer seminar schedule, visiting speaker itineraries and day-of logistics.

Teaching & Mentorship

Undergraduate Research Mentor **March 2019 – March 2020**
Department of Chemical Engineering, University of Washington

- Mentored one undergraduate chemical engineering student focused on molecular properties and behavior of conjugated and non-conjugated polymer blends.

Teaching Assistant for Professor David Beck **January - March 2019 & 2020**
Department of Chemical Engineering, University of Washington

- ChemE 545: Data Science Methods for Clean Energy Research
- ChemE 546: Software Engineering for Molecular Data Scientists
- Prepared lecture *"Database Management Systems: Relational Databases & SQL"*for ChemE 545.

Research Computing Club Mentorship Program **October 2018 - June 2019**
University of Washington

- Mentored two undergraduate computer science & engineering students on developing machine learning classification algorithms and automated reduction visualizations for small-angle neutron scattering data.
- Poster Presentation: M. Doerr*, Y. Y. Low*, **C. M. Wolf** and L. D. Pozzo, "Machine Learning for the Automated Classification and Reduction of Small-Angle Neutron Scattering Data"
  22nd Annual Undergraduate Research Symposium, University of Washington, May 17, 2019 – Accepted
  *Presented by M. Doerr and Y. Y. Low; these authors contributed equally to this work.

Research Experiences for Undergraduates (REU) Mentor **June – August 2017**
Clean Energy Bridge to Research Program, University of Washington

- Mentored a visiting undergraduate chemistry student focused on validating molecular modeling of conjugated polymers in organic solvent with experimental neutron scattering data.

Research Experiences for Teachers (RET) Mentor **June – July 2017**
University of Washington

- Mentored a visiting faculty member from Green River College to develop molecular modeling tools that can be used for class demonstrations and lab sessions with students.

Involvement & Outreach

WChE Industry Event Planning Committee **May – November 2017, 2018 and 2019**
Women in Chemical Engineering (WChE), University of Washington
Faculty Advisor: Professor Elizabeth Nance

- Selected as part of a committee of undergraduate and graduate students to plan the annual WChE Industry Event.
- Invited 20+ professional chemical engineers annually from across the U.S. to serve as panelists on sessions focused on Data Science, Energy, PhD/MS/BS – Paths to Industry, and Diversity.
- Coordinated with local professionals and alumni on nine different workshops held during the most recent event focused on Strategies for Better Leadership, How to Combat Self Doubt, How to Sell Your Strengths and others.
- Gained experience in managing logistics of event location, panel and keynote schedules, registration, volunteer assignments, and catering.

Women in Chemical Engineering (WChE) **September 2016 - Present**
University of Washington
Faculty Advisor: Professor Elizabeth Nance

- **Vice President April 2017 – 2018:** Planned WChE events, including "Building Skills for Inclusive Leadership" developed with UW Theater for Change. Supported the president as needed with their duties.

Seattle-Limbe Sewing Circle **July 2018 – July 2019**
Seattle-Limbe Sister City Association

- Sewed and assembled feminine hygiene kits that were then sent to young women attending school in Cameroon.

Walk-on-Water, University of Washington Discovery Days **April 2016, 2017, 2018, 2019**
Pozzo Research Group, Department of Chemical Engineering, University of Washington

- Demonstrate shear-thickening fluids by preparing a tub of cornstarch and water mixture that K-12 students can walk across at an annual 2-day UW Engineering outreach event.
- Managed the 2018 demo by finding volunteers, procuring 500 lbs of cornstarch required, and leading the setup, operation and cleanup.

Awards & Achievements

University of Washington Society of Women Engineers Outstanding Female Award	January 2020
2020 ACS National Excellence in Graduate Polymer Research Symposium	November 2019
2020 Clean Energy Institute Graduate Fellow, University of Washington	September 2019 – June 2020
2018 Krieger-Brocker Travel Award, University of Washington Dept. of Chemical Engineering	April 2019

NSF IGERT in Big Data and Data Science Fellow, University of Washington	August 2016 – June 2019
Dean’s Fellowship, University of Washington, College of Engineering	September 2015
Outstanding Student Award, North Dakota Society of Professional Engineers	Feb 2014 & 2015
Tau Beta Pi Scholar Recipient	June 2014
Barry M. Goldwater Scholarship Honorable Mention	April 2014